

# University of Alberta

## Library Release Form

**Name of Author:** Steven John Lyster

**Title of Thesis:** Simulation of Geologic Phenomena Using Multiple-Point Statistics in a Gibbs Sampler Algorithm

**Degree:** Doctor of Philosophy

**Year this Degree Granted:** 2009

Permission is hereby granted to the University of Alberta Library to reproduce single copies of this thesis and to lend or sell such copies for private, scholarly or scientific research purposes only.

The author reserves all other publication and other rights in association with the copyright in the thesis, and except as herein before provided, neither the thesis nor any substantial portion thereof may be printed or otherwise reproduced in any material form whatsoever without the author's prior written permission.

---

*Signature*

**University of Alberta**

Simulation of Geologic Phenomena Using Multiple-Point Statistics in a  
Gibbs Sampler Algorithm

by

Steven John Lyster

A thesis submitted to the Faculty of Graduate Studies and Research  
in partial fulfillment of the requirements for the degree of

Doctor of Philosophy

in

Mining Engineering

Department of Civil and Environmental Engineering

Edmonton, Alberta

Spring 2009

# University of Alberta

## Faculty of Graduate Studies and Research

The undersigned certify that they have read, and recommend to the Faculty of Graduate Studies and Research for acceptance, a thesis entitled **Simulation of Geologic Phenomena Using Multiple-Point Statistics in a Gibbs Sampler Algorithm** submitted by **Steven John Lyster** in partial fulfillment of the requirements for the degree of **Doctor of Philosophy in Mining Engineering**.

---

Dr. Clayton V. Deutsch (Supervisor)

---

Dr. Rick Chalaturnyk (Chair and Examiner)

---

Dr. Jef Caers (External Examiner)

---

Dr. Ivan Mizera (Examiner)

---

Dr. Oy Leuangthong (Examiner)

---

Dr. Ali Nouri (Examiner)

Date: \_\_\_\_\_

To Michelle,

I never could have gone as far without your support. I love you.

I told you I'd graduate someday.

To my family,

Thank you for believing that this whole thing would lead somewhere eventually.

Now you can say there's a doctor in the family.

To my friends,

Thank you for providing a distraction when I needed one most.

And by distraction I mean beer.

## **Abstract**

Geostatistical modeling of geological bodies for earth sciences applications often involves simulation of categorical variables such as facies or rock types. Many geological settings have features that are not easily captured and reproduced by traditional variogram-based methods. Multiple-point statistics can be used to create realizations of geology that better match a conceptual model of geology, also called a training image.

This dissertation develops a new simulation algorithm, called MPS-GS, using multiple-point statistics in a Gibbs sampler framework. The Gibbs sampler is a Markov chain Monte Carlo method and is used as a theoretical foundation. MPS-GS is an iterative algorithm that visits every location many times, converging on a simulated realization resembling the training image using conditional distributions. Multiple-point statistics are utilized to determine the conditional distributions. To overcome the problem of dimensionality associated with multiple-point statistics, multiple-point events are used. The indicators of multiple-point events are nonlinear data that are used in a linear estimate similar to indicator kriging.

Iterative algorithms have a number of computational limitations and problems with artifacts. MPS-GS uses modifications to the conditional distributions, noise reduction, multiple grids, and a servosystem to reduce the problems associated with iterative methods. A number of features are implemented, including automatic convergence detection, automatic template creation, and a multiple servosystem approach for reproducing locally varying proportions.

Several case studies are considered to demonstrate the effectiveness of MPS-GS. The results show visual improvement compared to a traditional geostatistical method, SISIM. Lower-order statistics such as indicator variograms are reproduced well by MPS-GS and high-order measures such as multiple-point histograms are better reproduced when compared to SISIM. The improved visual and statistical quality of the realizations leads to a more precise quantification of uncertainty without sacrificing accuracy.

## **Acknowledgements**

I would like to thank my supervisor Dr. Clayton V. Deutsch for his advice and support. During meetings in his office Clayton can make the most difficult concepts sound easy and make sense of the mountains of ideas conceived during this research.

Financial support for this research was provided by the industrial sponsors of the Centre for Computational Geostatistics and by the National Science and Engineering Research Council of Canada.

The data for the reservoir case study was provided by ConocoPhillips, who also presented me with a very interesting and rewarding internship opportunity.

Thanks also to all of my colleagues at the Centre for Computational Geostatistics for providing opinions, insights, and suggestions. The Friday afternoon poker games were good too.

# Table of Contents

<b>1</b>	<b>Introduction.....</b>	<b>1</b>
	1.1 Problem Setting .....	1
	1.2 Proposed Approach.....	5
	1.3 Dissertation Outline .....	7
<b>2</b>	<b>Literature Review .....</b>	<b>9</b>
	2.1 Geostatistical Modeling .....	9
	2.1.1 Categorical Variables .....	11
	2.1.2 Conventional Facies Modeling Techniques .....	13
	2.2 Multiple-Point Statistics .....	17
	2.2.1 Multiple-Point Histograms .....	18
	2.2.2 Connectivity Functions.....	19
	2.2.3 Training Images.....	20
	2.2.4 Dimensionality .....	20
	2.2.5 Applications of MPS .....	21
	2.3 MPS Algorithms .....	22
	2.3.1 Single Normal Equation .....	22
	2.3.2 Markov Chain Monte Carlo Methods.....	24
	2.3.3 Pattern-Based Geostatistics .....	26
	2.4 Gibbs Sampling .....	30
	2.4.1 Markov Chains .....	30
	2.4.2 Two-Dimensional Gibbs Sampler .....	37
	2.4.3 Multi-Dimensional Gibbs Sampler.....	39
	2.4.4 Markov Random Fields .....	45
<b>3</b>	<b>MPS-GS Theory .....</b>	<b>47</b>
	3.1 Conditional Distributions.....	47
	3.1.1 Multiple-Point Events.....	49
	3.1.2 Relation to the Single Normal Equation.....	52
	3.1.3 Properties of the Conditional Distributions .....	53
	3.1.4 Singularity of the System .....	55
	3.1.5 Markov Random Fields .....	61

3.2	Statistical Inference .....	61
3.2.1	Selection of the MPS Template .....	62
3.2.2	Examples .....	63
3.3	Example .....	66
3.4	Initial States .....	71
3.5	Pattern Simulation .....	72
<b>4</b>	<b>Algorithm Implementation .....</b>	<b>75</b>
4.1	Modifications to Conditional Distributions .....	75
4.1.1	Single-Point Indicators .....	75
4.1.2	Two-Part Conditional Probability .....	78
4.1.3	Univariate Proportions.....	78
4.1.4	Image Cleaning.....	92
4.2	Multiple Grids.....	97
4.2.1	Grid Discretization .....	99
4.2.2	Conditioning Data .....	99
4.2.3	Populating Multiple Grids .....	100
4.3	Stopping Criteria.....	102
4.3.1	Number of Changes per Loop .....	103
4.3.2	Minimum Number of Changes .....	105
4.3.3	Maximum Number of Loops .....	106
4.4	Simulation Path.....	106
4.4.1	Spiral Path .....	106
4.4.2	Random Path .....	106
4.4.3	Conditioning Data Artifacts .....	107
4.5	Edge Effects.....	110
4.5.1	Exact Solutions.....	112
4.5.2	Grid Wrapping.....	112
4.5.3	Grid Reflection .....	114
4.5.4	Grid Expansion.....	115
4.6	Long-term Convergence Properties .....	116
4.7	Evaluating Results .....	117
4.7.1	Lower-Order Statistics.....	118

4.7.2 Multiple-Point Statistics .....	118
4.7.3 Response Characteristics .....	119
<b>5 Case Studies.....</b>	<b>120</b>
5.1 Braided Channels.....	120
5.1.1 Data and Training Image .....	120
5.1.2 Unconditional Simulation.....	123
5.1.3 Conditional Simulation.....	130
5.1.4 SNESIM Realizations.....	137
5.2 Eolian Sandstone .....	140
5.2.1 Data and Training Image .....	140
5.2.2 Unconditional Simulation.....	145
5.2.3 Conditional Simulation.....	151
5.3 Petroleum Reservoir .....	157
5.3.1 Training Images.....	158
5.3.2 Unconditional Simulation.....	170
5.3.3 Conditional Simulation with a Vertical Trend .....	179
5.4 Conclusions.....	189
<b>6 Conclusions.....</b>	<b>190</b>
6.1 Areas of Application.....	191
6.2 Future Areas of Research.....	192
<b>Bibliography .....</b>	<b>194</b>
<b>A Symbols and Selected Terms .....</b>	<b>203</b>
<b>B MPS-GS Software.....</b>	<b>210</b>
B.1 GSLIB Conventions .....	210
B.2 Workflow .....	212
B.3 Parameter File .....	215
B.4 Template and MPS Files .....	218
B.5 FORTRAN Files .....	221
B.6 Example .....	221

## List of Tables

Table 2.1: Dimension of statistics characterizing $K$ facies and $N$ points. ....	21
Table 2.2: Probability of bankruptcy or winning from each initial state in the finite coin-flipping game.....	37
Table 2.3: Summary statistics for three two-dimensional Gibbs samplers simulated to $t=1000$ using bivariate Gaussian conditional distributions.....	39
Table 2.4: Stationary distribution of the multi-dimensional Gibbs sampler example. ....	43
Table 2.5: Stationary distribution of the conditional multi-dimensional Gibbs sampler example. ....	45
Table 4.1: Simulated channel proportions using varying $\mu$ and $P_{channel}$ parameters. ....	81
Table 4.2: Connectivity probabilities for the four facies in the TI in Figure 4.3. ....	93
Table 4.3: Connectivity corrections for the four facies in the TI in Figure 4.3. ....	94
Table 5.1: CPU time required to create the templates and calculate MPS for the braided channel study.....	123
Table 5.2: CPU time required to simulate twenty unconditional realizations for the braided channel study. ....	124
Table 5.3: CPU time required to simulate twenty conditional realizations for the braided channel study.....	131
Table 5.4: CPU time required to create the templates and calculate MPS for the eolian sandstone study.....	144
Table 5.5: CPU time required to simulate twenty unconditional realizations for the eolian sandstone study. ....	145
Table 5.6: CPU time required to simulate twenty conditional realizations for the eolian sandstone study.....	151
Table 5.7: Absolute MPH differences of the petroleum reservoir TIs from the well data. ....	169

Table 5.8: CPU time required to create the templates and calculate MPS for the petroleum reservoir case study.....	170
Table 5.9: CPU time required to simulate ten unconditional realizations for the petroleum reservoir study.....	170
Table 5.10: CPU time required to simulate ten conditional realizations for the petroleum reservoir case study.....	180
Table B.1: An example GSLIB data file.....	211
Table B.2: An example parameter file for MPESIM. ....	217
Table B.3: An example template file for MPESIM. ....	219
Table B.4: An example MPS file for MPESIM. ....	220
Table B.5: A list of the FORTRAN files required for MPESIM. ....	221
Table B.6: The MPESIM parameter file used in the example. ....	223

## List of Figures

Figure 1.1: Twenty facies data typical of a fluvial-type petroleum reservoir. ....	2
Figure 1.2: An expert geological interpretation of the field containing the twenty data shown in Figure 1.1. ....	3
Figure 1.3: Two object-based realizations of the domain containing the Figure 1.1 data. Realizations 1 and 2 have mismatch from the sample data of 15% and 10%. ....	4
Figure 1.4: Two SIS realizations of the area containing the data in Figure 1.1. Both realizations reproduce all data locations but do not display the correct geological structure. ....	5
Figure 2.1: A realization of three facies created using SISIM (Deutsch and Journal, 1998). ....	14
Figure 2.2: A SGS realization of a standard normal RV created using SGSIM (Deutsch and Journal, 1998). ....	15
Figure 2.3: A standard normal distribution partitioned into three facies codes for TGS. ....	15
Figure 2.4: A TGS realization created using the SGS realization in Figure 2.2, the thresholds in Figure 2.3, and the GTSIM program (Deutsch and Journal, 1998). ....	16
Figure 2.5: An example of a four-point MPH template and patterns with two indicator values. ....	19
Figure 2.6: A channel-type TI (Journal, 2004, Liu, 2006, Strebelle, 2002, among others). ....	20
Figure 2.7: An example using the SNE equation to calculate conditional distributions using MPS. ....	23
Figure 2.8: An example of a simple neural network with eight neurons and three layers (input layer, hidden layer, output layer). ....	26
Figure 2.9: An example of the Growthsim algorithm. Clockwise from left: Data locations with the template size and possible locations shown; pattern	

inserted into the simulated field; state of the realization after several more patterns have been inserted. ....	28
Figure 2.10: An example of the SIMPAT workflow. Left to right: Conditioning data; primal template pattern; dual template pattern.....	29
Figure 2.11: An example of three possible filters for classification of patterns in Filtersim. ....	29
Figure 2.12: An example of the Filtersim workflow. Left to right: Conditioning data; pattern prototype; pattern from TI.....	30
Figure 2.13: An example of a one dimensional discrete state space over the integers -10 through +10. ....	31
Figure 2.14: An example of a simple one-dimensional random walk in the form of a coin-flipping game. Four Markov chains are shown.....	34
Figure 2.15: A histogram of the values of 50 coin-flipping games after 20 flips ( $t=20$ ). ....	35
Figure 2.16: Transition matrix of the finite state space coin-flipping game. All values not shown are zero. ....	36
Figure 2.17: Results of three two-dimensional Gibbs samplers simulated to $t=1000$ using bivariate Gaussian conditional distributions. ....	39
Figure 2.18: The state space of the example with the communicating states shown as connected and the MPH class of each state labeled. ....	41
Figure 2.19: Covariance model used in the example. ....	41
Figure 2.20: Transition matrix for the example Gibbs sampler. ....	42
Figure 2.21: The state space of the conditional example with the upper left corner frozen as facies 1 (white). ....	44
Figure 2.22: Transition matrix for the example conditional Gibbs sampler. ....	44
Figure 2.23: An example of a Markov random field in area $A$ with point of interest $i$ and local neighbourhood $\partial i$ . ....	46
Figure 3.1: A single class for a 24-point MPH that shows no discernible geological structure. ....	49

Figure 3.2: A 24-point MPH class (center) and six discrete multiple-point events containing the same data.....	50
Figure 3.3: A channel-type TI with a number of five-point templates and the scanning border superimposed.....	62
Figure 3.4: A simple 160x160 TI made up of 10x10 black and white squares (left); two-point spatial entropy of the TI in a 21-by-21 square template (right). ....	64
Figure 3.5: A 256x256 three-facies fluvial TI (left); two-point spatial entropy of the TI in a 21-by-21 square template (right).....	64
Figure 3.6: A 256x256 TI with two distinct ellipsoidal structures (left); two-point spatial entropy of the TI in a 21-by-21 square template (right).....	65
Figure 3.7: A 200x100 five-facies complex TI (Deutsch, 1992) (left); two-point spatial entropy of the TI in a 21-by-21 square template (right).....	66
Figure 3.8: A section of the three-facies fluvial TI for the example.....	67
Figure 3.9: A MPS template of four, four-point MPEs for the example.....	68
Figure 3.10: A graph of the four MPHs of the MPEs in the example, sorted from greatest to least frequencies.....	69
Figure 3.11: A graph of the 324 eigenvalues in the linear system of the example, sorted from greatest to least.....	70
Figure 3.12: A graph of the optimal linear weights for the example, sorted in the same order as the MPHs in Figure 3.10. ....	71
Figure 3.13: A 25-point MPS template with a five-point central event and five four-point MPEs as data. ....	74
Figure 4.1: An example of the effect of $\mu$ and varying target facies proportions. Left column to right: target $P_{channel}=0.1, 0.3, 0.5$ ; Top to bottom: $\mu=0.0, 0.5, 1.0, 2.0$ . ....	80
Figure 4.2: Fluvial TI used for the local proportion example (Hoffman et al, 2005, Boisvert, 2007).....	84
Figure 4.3: Vertical proportion curve used for the local proportion example.....	85

Figure 4.4: An unconditional realization using the additive method for reproducing the vertical proportion curve.....	86
Figure 4.5: An unconditional realization using the multiplicative method for reproducing the vertical proportion curve.....	87
Figure 4.6: An unconditional realization using the permanence of ratios method for reproducing the vertical proportion curve. ....	88
Figure 4.7: An unconditional realization using the multiple servosystem method for reproducing the vertical proportion curve. ....	89
Figure 4.8a: Facies 1 vertical proportion curve reproduction for the four methods shown in the example. ....	90
Figure 4.8b: Facies 2 vertical proportion curve reproduction for the four methods shown in the example. ....	90
Figure 4.8c: Facies 3 vertical proportion curve reproduction for the four methods shown in the example. ....	91
Figure 4.8d: Facies 4 vertical proportion curve reproduction for the four methods shown in the example. ....	91
Figure 4.9: An example of the connectivity at a location “?”. The white facies has a connectivity $C_{white}=4$ and the grey facies has $C_{grey}=2$ . ....	93
Figure 4.10: Left: an MPS-GS realization using no noise reduction. Right: an MPS-GS realization using the frozen cells method and no other noise reduction. ....	95
Figure 4.11: Four MPS-GS realizations using the noise reduction factor and freezing of converged cells. Top row: $NRF=0.2$ and $NRF=0.4$ ; Bottom row: $NRF=0.6$ and $NRF=0.8$ . ....	96
Figure 4.12: Four MPS-GS realizations using the connectivity correction and freezing of converged cells. Top row: $\eta=0.2$ and $\eta=0.4$ ; Bottom row: $\eta=0.6$ and $\eta=0.8$ .....	97
Figure 4.13: An example of the multiple grid approach used in MPS-GS, three successively finer grids clockwise from top left. Grey squares are those	

cells in the current grid, black are frozen cells from previously-simulated grids.....	98
Figure 4.14: An example of the assigning of conditioning data to cells on progressively finer grids. The striped square is a sampled location; black squares are frozen cells; grey squares are active cells on the current grid.....	100
Figure 4.15: An example of the method used to populate finer grids in MPS-GS. ....	101
Figure 4.16: Four MPS-GS realizations using different numbers of multiple grids. Top row: $G=1$ and $G=2$ ; Bottom row: $G=3$ and $G=4$ . ....	102
Figure 4.17: A graph of the number of changes per loop (black lines) and the correlation coefficients as in Equation 4.16 (grey lines) for ten realizations. The black dots mark the first occurrences of positive correlation coefficients.....	104
Figure 4.18: A graph showing the number of changes per loop (red lines) and the number of points remaining in the random path (black lines) for ten realizations. ....	105
Figure 4.19: Three different types of artifacts seen near strings of conditioning data.....	107
Figure 4.20: Training image (top) and true data (bottom) used to demonstrate conditioning data artifacts.....	108
Figure 4.21: An example of the MPS-GS algorithm using a spiral path. One realization is shown after 10, 50, and 100 loops. ....	109
Figure 4.22: An example of the MPS-GS algorithm using a random path. One realization is shown after 10, 50, and 100 loops. ....	110
Figure 4.23: An MPS template near the edge of a simulated domain.....	111
Figure 4.24: An MPS-GS realization with edge effects.....	111
Figure 4.25: An MPS template being wrapped at the edge of a domain.....	113
Figure 4.26: An MPS-GS realization using grid wrapping. The same realization is repeated four times to demonstrate the wallpaper artifact.....	113
Figure 4.27: An MPS template being reflected at the edge of a domain. ....	114

Figure 4.28: An MPS-GS realization using grid reflection (top left). The same realization is mirrored to demonstrate the effects of reflection. ....	115
Figure 4.29: An MPS-GS realization using grid expansion and reflection.....	116
Figure 4.30: Four conditional MPS-GS realizations created using the same parameters and run through a specified number of loops. Top left: 1 loop. Top right: 10 loops. Lower left: 100 loops. Lower right: 1000 loops.....	117
Figure 5.1: The TI used for the braided channel study (Journel, 2004, Liu, 2006, Strebelle, 2002, among others). ....	121
Figure 5.2: The nine-point histogram of the braided channel TI. ....	122
Figure 5.3: 50 data points extracted from the braided channel TI. ....	122
Figure 5.4a: Two unconditional MPS-GS realizations using $M=32$ and $N=2$ . ....	125
Figure 5.4b: The indicator variograms of the TI (red line), data (black dots) and 20 MPS-GS realizations (blue lines) in the east-west (left) and north-south (right) directions. ....	125
Figure 5.4c: The MPH reproduction of 20 MPS-GS realizations. Bars: reference TI MPH; solid line: median MPH frequencies; dashed lines: P5 and P95 MPH frequencies.....	125
Figure 5.5a: Two unconditional MPS-GS realizations using $M=16$ and $N=4$ . ....	126
Figure 5.5b: The indicator variograms of the TI (red line), data (black dots) and 20 MPS-GS realizations (blue lines) in the east-west (left) and north-south (right) directions. ....	126
Figure 5.5c: The MPH reproduction of 20 MPS-GS realizations. Bars: reference TI MPH; solid line: median MPH frequencies; dashed lines: P5 and P95 MPH frequencies.....	126
Figure 5.6a: Two unconditional MPS-GS realizations using $M=10$ and $N=6$ . ....	127
Figure 5.6b: The indicator variograms of the TI (red line), data (black dots) and 20 MPS-GS realizations (blue lines) in the east-west (left) and north-south (right) directions. ....	127

Figure 5.6c: The MPH reproduction of 20 MPS-GS realizations. Bars: reference TI MPH; solid line: median MPH frequencies; dashed lines: P5 and P95 MPH frequencies.....	127
Figure 5.7a: Two unconditional MPS-GS realizations using $M=8$ and $N=8$ . .....	128
Figure 5.7b: The indicator variograms of the TI (red line), data (black dots) and 20 MPS-GS realizations (blue lines) in the east-west (left) and north-south (right) directions. ....	128
Figure 5.7c: The MPH reproduction of 20 MPS-GS realizations. Bars: reference TI MPH; solid line: median MPH frequencies; dashed lines: P5 and P95 MPH frequencies.....	128
Figure 5.8a: Two SISIM realizations.....	129
Figure 5.8b: The indicator variograms of the TI (red line), data (black dots) and 20 SISIM realizations (blue lines) in the east-west (left) and north-south (right) directions.....	129
Figure 5.8c: The MPH reproduction of 20 SISIM realizations. Bars: reference TI MPH; solid line: median MPH frequencies; dashed lines: P5 and P95 MPH frequencies.....	129
Figure 5.9: A graph of the absolute MPH differences for each case of the braided channel study between twenty realizations and the TI. Bars: P50 realization difference; lines: P5 and P95 realizations. ....	130
Figure 5.10a: Two conditional MPS-GS realizations using $M=32$ and $N=2$ . ....	131
Figure 5.10b: The simulated proportions of sand for 20 conditional MPS-GS realizations. ....	131
Figure 5.11a: Two conditional MPS-GS realizations using $M=16$ and $N=4$ . ....	132
Figure 5.11b: The simulated proportions of sand for 20 conditional MPS-GS realizations. ....	132
Figure 5.12a: Two conditional MPS-GS realizations using $M=10$ and $N=6$ . ....	133
Figure 5.12b: The simulated proportions of sand for 20 conditional MPS-GS realizations. ....	133
Figure 5.13a: Two conditional MPS-GS realizations using $M=8$ and $N=8$ . ....	134

Figure 5.13b: The simulated proportions of sand for 20 conditional MPS-GS realizations. ....	134
Figure 5.14a: Two conditional SISIM realizations. ....	135
Figure 5.14b: The simulated proportions of sand for 20 conditional SISIM realizations. ....	135
Figure 5.15: Accuracy plot for the braided channel conditional simulations. ....	136
Figure 5.16: Precision of the braided channel conditional simulations. ....	137
Figure 5.17a: Two unconditional SNESIM realizations. ....	138
Figure 5.17b: The indicator variograms of the TI (red line), data (black dots) and 20 SNESIM realizations (blue lines) in the east-west (left) and north-south (right) directions. ....	138
Figure 5.18a: Two conditional SNESIM realizations. ....	139
Figure 5.18b: The simulated proportions of sand for 20 conditional SNESIM realizations. ....	139
Figure 5.19: The reference dataset (left) and cleaned image (right) used as the true data for the eolian sandstone study. ....	140
Figure 5.20: The reference dataset (top) and cleaned image (bottom) used as the TI in the eolian sandstone study. ....	142
Figure 5.21: 100 data points extracted from the eolian sandstone true dataset. ....	143
Figure 5.22: Indicator variograms of the eolian sandstone true dataset (red line), sample data (black dots), and TI (black line). ....	143
Figure 5.23: The four-point histograms of the true dataset and TI for the eolian sandstone study. ....	144
Figure 5.24a: Two unconditional MPS-GS realizations using $M=32$ and $N=2$ . ....	146
Figure 5.24b: The indicator variograms of the true dataset (red line), sample data (black dots), TI (black line) and 10 MPS-GS realizations (blue lines) in the X (left) and Y (right) directions for facies 1 (top), facies 2 (middle) and facies 3 (bottom). ....	146
Figure 5.25a: Two unconditional MPS-GS realizations using $M=16$ and $N=4$ . ....	147

Figure 5.25b: The indicator variograms of the true dataset (red line), sample data (black dots), TI (black line) and 10 MPS-GS realizations (blue lines) in the X (left) and Y (right) directions for facies 1 (top), facies 2 (middle) and facies 3 (bottom). .....	147
Figure 5.26a: Two unconditional MPS-GS realizations using $M=8$ and $N=6$ . .....	148
Figure 5.26b: The indicator variograms of the true dataset (red line), sample data (black dots), TI (black line) and 10 MPS-GS realizations (blue lines) in the X (left) and Y (right) directions for facies 1 (top), facies 2 (middle) and facies 3 (bottom). .....	148
Figure 5.27a: Two unconditional SISIM realizations. ....	149
Figure 5.27b: The indicator variograms of the true dataset (red line), sample data (black dots), TI (black line) and 10 SISIM realizations (blue lines) in the X (left) and Y (right) directions for facies 1 (top), facies 2 (middle) and facies 3 (bottom). .....	149
Figure 5.28: A graph of the absolute MPH differences for each case of the eolian sandstone study between twenty realizations and the TI. Bars: P50 realization difference; lines: P5 and P95 realizations. ....	150
Figure 5.29a: Two conditional MPS-GS realizations using $M=32$ and $N=2$ . ....	152
Figure 5.29b: The simulated proportions of facies 1 (top left), facies 2 (top right), and facies 3(bottom) for 20 conditional MPS-GS realizations. ....	152
Figure 5.30a: Two conditional MPS-GS realizations using $M=16$ and $N=4$ . ....	153
Figure 5.30b: The simulated proportions of facies 1 (top left), facies 2 (top right), and facies 3(bottom) for 20 conditional MPS-GS realizations. ....	153
Figure 5.31a: Two conditional MPS-GS realizations using $M=8$ and $N=6$ . ....	154
Figure 5.31b: The simulated proportions of facies 1 (top left), facies 2 (top right), and facies 3(bottom) for 20 conditional MPS-GS realizations. ....	154
Figure 5.32a: Two conditional SISIM realizations. ....	155
Figure 5.32b: The simulated proportions of facies 1 (top left), facies 2 (top right), and facies 3(bottom) for 20 conditional SISIM realizations. ....	155
Figure 5.33: Accuracy plot for the eolian sandstone conditional simulations. ....	156

Figure 5.34: Precision of the eolian sandstone conditional simulations. ....	157
Figure 5.35a: TI #1 for the petroleum reservoir case study. ....	160
Figure 5.35b: The MPH of the well data (bars) and TI #1 (line). The MPH patterns are shown under the horizontal axis. ....	160
Figure 5.35c: Indicator variograms for the well data (points) and TI #1 (line) in the X, Y, and Z directions (left to right) for the four facies, top to bottom: facies 1 (white), facies 2 (light grey), facies 3 (dark grey), and facies 4 (black). ....	161
Figure 5.36a: TI #2 for the petroleum reservoir case study. ....	162
Figure 5.36b: The MPH of the well data (bars) and TI #2 (line). The MPH patterns are shown under the horizontal axis. ....	162
Figure 5.36c: Indicator variograms for the well data (points) and TI #2 (line) in the X, Y, and Z directions (left to right) for the four facies, top to bottom: facies 1 (white), facies 2 (light grey), facies 3 (dark grey), and facies 4 (black). ....	163
Figure 5.37a: TI #3 for the petroleum reservoir case study. ....	164
Figure 5.37b: The MPH of the well data (bars) and TI #3 (line). The MPH patterns are shown under the horizontal axis. ....	164
Figure 5.37c: Indicator variograms for the well data (points) and TI #3 (line) in the X, Y, and Z directions (left to right) for the four facies, top to bottom: facies 1 (white), facies 2 (light grey), facies 3 (dark grey), and facies 4 (black). ....	165
Figure 5.38a: TI #4 for the petroleum reservoir case study. ....	166
Figure 5.38b: The MPH of the well data (bars) and TI #4 (line). The MPH patterns are shown under the horizontal axis. ....	166
Figure 5.38c: Indicator variograms for the well data (points) and TI #4 (line) in the X, Y, and Z directions (left to right) for the four facies, top to bottom: facies 1 (white), facies 2 (light grey), facies 3 (dark grey), and facies 4 (black). ....	167
Figure 5.39a: TI #5 for the petroleum reservoir case study. ....	168

Figure 5.39b: The MPH of the well data (bars) and TI #5 (line). The MPH patterns are shown under the horizontal axis. ....	168
Figure 5.39c: Indicator variograms for the well data (points) and TI #5 (line) in the X, Y, and Z directions (left to right) for the four facies, top to bottom: facies 1 (white), facies 2 (light grey), facies 3 (dark grey), and facies 4 (black). ....	169
Figure 5.40a: Slices from one unconditional MPS-GS realization created using TI #1 in the petroleum reservoir case study. ....	172
Figure 5.40b: The indicator variograms of TI #1 (red line), sample data (black dots), and 5 MPS-GS realizations (blue lines) in the (left to right) X, Y, and Z directions for (top to bottom) facies 1, facies 2, facies 3, and facies 4. ....	173
Figure 5.41a: Slices from one unconditional MPS-GS realization created using TI #3 in the petroleum reservoir case study. ....	174
Figure 5.41b: The indicator variograms of TI #3 (red line), sample data (black dots), and 5 MPS-GS realizations (blue lines) in the (left to right) X, Y, and Z directions for (top to bottom) facies 1, facies 2, facies 3, and facies 4. ....	175
Figure 5.42a: Slices from one unconditional MPS-GS realization created using TI #4 in the petroleum reservoir case study. ....	176
Figure 5.42b: The indicator variograms of TI #4 (red line), sample data (black dots), and 5 MPS-GS realizations (blue lines) in the (left to right) X, Y, and Z directions for (top to bottom) facies 1, facies 2, facies 3, and facies 4. ....	177
Figure 5.43a: Slices from one unconditional SISIM realization in the petroleum reservoir case study. ....	178
Figure 5.43b: The modeled indicator variograms, sample data (black dots), and 5 SISIM realizations (blue lines) in the (left to right) X, Y, and Z directions for (top to bottom) facies 1, facies 2, facies 3, and facies 4. ....	179
Figure 5.44: Vertical trend model used in the petroleum reservoir case study. ....	180

Figure 5.45: Slices from one conditional MPS-GS realization created using TI #1 in the petroleum reservoir case study.....	182
Figure 5.46: Slices from one conditional MPS-GS realization created using TI #3 in the petroleum reservoir case study.....	183
Figure 5.47: Slices from one conditional MPS-GS realization created using TI #4 in the petroleum reservoir case study.....	184
Figure 5.48: Slices from one conditional SISIM realization in the petroleum reservoir case study.....	185
Figure 5.49a: Trend model reproduction of the conditional simulations for facies 1 in the petroleum reservoir case study. ....	186
Figure 5.49b: Trend model reproduction of the conditional simulations for facies 2 in the petroleum reservoir case study. ....	186
Figure 5.49c: Trend model reproduction of the conditional simulations for facies 3 in the petroleum reservoir case study. ....	187
Figure 5.49d: Trend model reproduction of the conditional simulations for facies 4 in the petroleum reservoir case study. ....	187
Figure 5.50: Accuracy plot of the petroleum reservoir conditional simulations based on the jackknife cross-validation data. ....	188
Figure 5.51: Precision of the petroleum reservoir conditional simulations. ....	188
Figure B.1: An example of GSLIB grid indexing. The origin cell is marked with a dot.....	211
Figure B.2: An example of GSLIB cell geometry definitions. ....	212
Figure B.3: MPESIM workflow for creating a template and calculating MPS. ....	213
Figure B.4: MPESIM workflow for preparing for simulation. ....	214
Figure B.5: MPESIM workflow for performing simulation. ....	215
Figure B.6: The data in TRUE.DAT (top left), DATA.DAT (top right), and TI.DAT (bottom).....	222
Figure B.7: The first two realizations produced by MPESIM using the data in Figure B.6 and the parameters in Table B.6. ....	223



# 1 Introduction

Mineral resources are important to the Canadian economy. Engineering and geoscience methods are used to help decide what resource extraction projects are worth undertaking to realize a profit for the operator, royalties for the owner, and minimum environmental impact. A part of the decision-making process is determination of the subsurface geology. This involves creating one or more models of the geology. In this dissertation a model is a geologic description in numerical format at a specified scale for the purposes of engineering calculations. Models are created for petroleum reservoirs, ore deposits, or other geologic sites that are of interest.

Due to the incomplete information available about the subsurface, uncertainty in a model is inevitable. In this context uncertainty is the probability distribution of possible outcomes such as oil or mineral production. Uncertainty occurs because a number of valid but different models may be created by the same method by varying input parameters such as a random number seed value, simulation path, or spatial statistics. Quantifying the uncertainty allows an assessment to be made of the economic feasibility and financial risk of a project or specific development strategy.

Geostatistics is a tool that is used for quantifying subsurface uncertainty and making it meaningful for application to mine design, petroleum reservoir evaluation, production planning, or other natural resources characterization.

## 1.1 Problem Setting

Models of geologic sites are created over a specified domain. A domain typically ranges in size from several hundred metres to several kilometres horizontally and tens to hundreds of metres vertically.

Creating models of geology involves different rock types or facies and modeling them over the domain. Facies are distinguished from one another at the sampling scale by grain size, geometry, diagenetic alteration, or some combination of these factors. Each facies has distinct subsurface architectural features because of the geological process. Examples of distinct geological architectural events are channel sands, levee sands, and floodplain shale in fluvial-type deposits; and mineralized veins and non-mineralized host rock in ore deposits.

Categorical models of facies may be constructed in several ways: deterministic interpretation by an expert; simulation of geologic bodies or processes meant to mimic the formation of the deposit; and simulation by geostatistical methods that use the spatial structure inferred from the available data. As an illustrative example, consider the twenty data points shown in Figure 1.1. There are three different types of facies typical of a fluvial reservoir: an impermeable shale matrix, channel sand, and different quality levee sand.

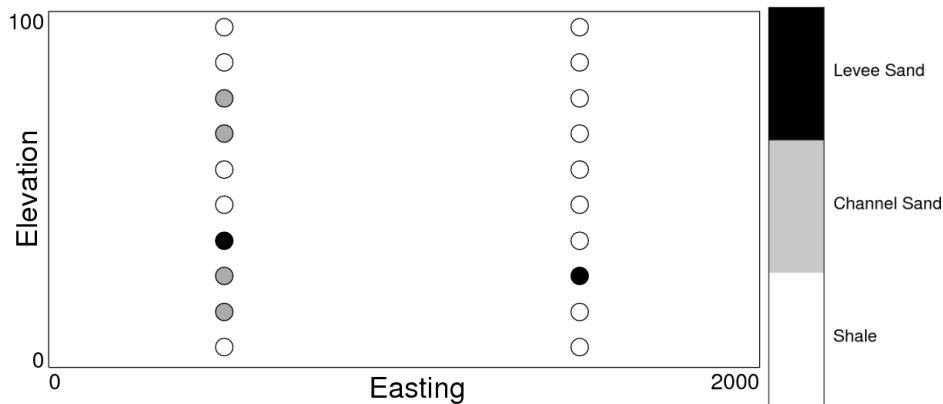


Figure 1.1: Twenty facies data typical of a fluvial-type petroleum reservoir.

Expert geological interpretation may yield results that are representative of the phenomena under study; however, this approach is neither repeatable nor reproducible. Different experts, given the same data, will certainly produce different models. Moreover, an expert with the same set of data would not generate the same model twice. It is expensive and time consuming to generate many deterministic models, making them unattractive as a method to assess uncertainty. Figure 1.2 shows one possible expert interpretation of the samples from Figure 1.1. This interpretation reproduces the data and

may be plausible, but it would be laborious to create a number of such cases to quantify the uncertainty of the deposit.

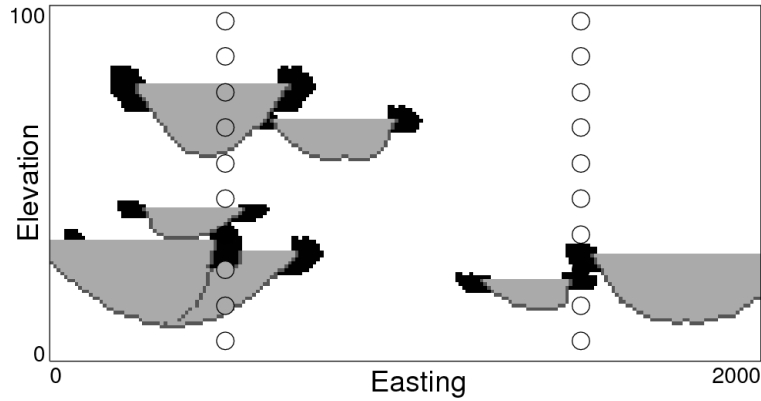


Figure 1.2: An expert geological interpretation of the field containing the twenty data shown in Figure 1.1.

Stochastic or random simulation using object-based or process-mimicking techniques can produce a number of models or realizations that may be used to assess uncertainty. Object-based methods place geometric objects in the domain until the data are reproduced and the target proportion of each facies have been reached. Process-mimicking methods start with an empty model and populate the domain in a similar way to the actual geologic progression. If done properly these methods will give results that are similar to the true geology and match what an expert's interpretation might look like. Object- and process-based methods require fine tuning of many parameters, can understate the uncertainty, and often have trouble reproducing densely sampled data. Figure 1.3 shows two object-based realizations that have the same geologic structure as the expert interpretation. It is relatively easy to quickly generate a number of realizations using this method, but placing the geo-objects in a random way results in some mismatch to the sample data. The mismatches in the example realizations are 15% and 10%.

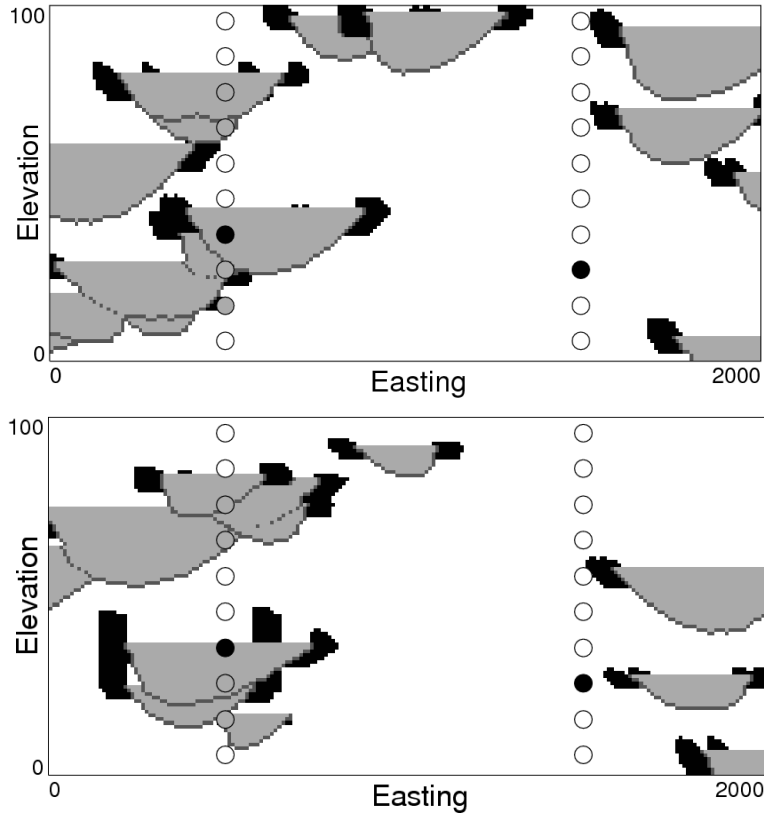


Figure 1.3: Two object-based realizations of the domain containing the Figure 1.1 data. Realizations 1 and 2 have mismatch from the sample data of 15% and 10%.

Pixel-based simulation methods such as sequential indicator simulation (SIS) and truncated Gaussian simulation are fast, can incorporate many data sources, and use spatial statistics that are inferable from sparse data. Second-order spatial statistics such as covariance functions or semivariograms are well-defined and have a relatively long history of use in geostatistical modeling. The main drawback of this family of techniques is that the results do not appear geologically realistic. The simple statistics used do not contain enough information to explicitly define the geological structures and geometric shapes present. Figure 1.4 shows two realizations that were created using SIS. The spatial correlation of the different facies is correct and all of the sample data are reproduced; however, the structure does not resemble actual geology as it would be interpreted by an expert. While this type of simulation approach is mathematically attractive, the results are unrealistic from a geological perspective. Many realizations can be created quickly to quantify uncertainty; however, uncertainty from an unrealistic model may not be useful for engineering purposes.

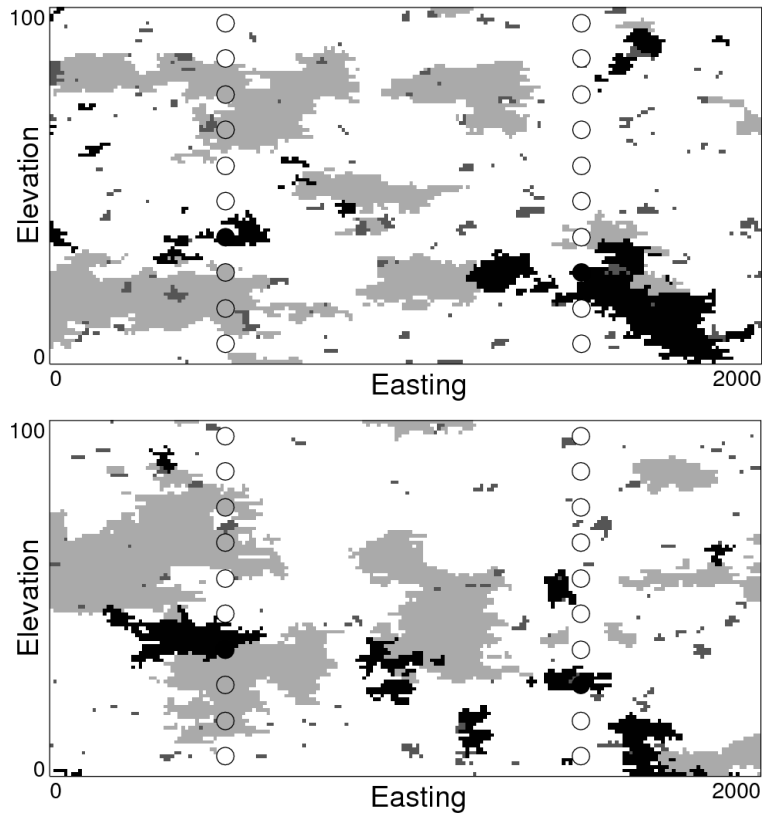


Figure 1.4: Two SIS realizations of the area containing the data in Figure 1.1. Both realizations reproduce all data locations but do not display the correct geological structure.

## 1.2 Proposed Approach

More sophisticated stochastic simulation methods have been proposed in recent years. A number of these methods use what is called multiple-point statistics (MPS). MPS refers to spatial moments that are of order greater than two and therefore contain more information than covariance functions or semivariograms. The term MPS is also sometimes used to refer to methods or families of methods that use these higher-order spatial moments.

The amount of information contained within MPS defines more geologically realistic structures than SIS. Rather than inferring the spatial statistics directly from data, MPS are derived from a conceptual model of geology called a training image (TI). An expert's

interpretation such as that shown in Figure 1.2 is an example of what could be used as a TI. This approach leads to a compromise between ease of simulation and geologic realism of the results. A challenge for MPS is how to best extract the MPS from a TI and then use them effectively in producing realizations.

This dissertation proposes a novel method for incorporating MPS in facies simulation. The workflow used by the proposed algorithm is as follows:

1. Start with a randomly-populated field on the coarsest grid;
2. At a random unsampled location:
  - a. Calculate the conditional probability of each facies;
  - b. Adjust the probabilities to account for secondary information and global facies proportions;
  - c. Apply noise reduction or cleaning and correct the probabilities to sum to 1.0;
  - d. Draw a new facies value from the corrected distribution and assign it to the current location;
  - e. Move to another unsampled location and repeat Step 2;
3. After every unsampled location has been visited, check for convergence:
  - a. If there is no convergence yet, repeat Step 2;
  - b. If the convergence criteria are met, populate the next-coarsest grid and repeat from Step 2;
4. After the finest grid has been simulated write out the results and proceed to the next realization if necessary.

Simulation methods that use MPS have several issues to consider. One issue is selection of a TI that is representative of the geology in the domain of interest. A great deal of information is extracted from a TI; therefore, the appropriateness of a particular TI has a large impact on the results. This aspect has been studied elsewhere and will not be discussed in detail in this dissertation.

Another issue is how to extract, store, and use the MPS contained within a TI. Unlike traditional geostatistical tools such as the semivariogram, MPS cannot be expressed as a simple mathematical function. All spatial relations must be stored and retrieved as needed; in sequential simulation methods the infinite possible data configurations can

lead to difficulties in inference and storage of the MPS. An iterative framework, called a Gibbs sampler, is proposed to simplify the data configuration issue.

In a Gibbs sampler, all locations are assigned values at the beginning of the simulation, so there are no data configuration issues. The algorithm starts with a random field reproducing the hard conditioning data and any secondary information, and then modifies (or perturbs) facies at locations in the realization using the current state of the surrounding locations as conditioning data. Using the theoretical properties of the Gibbs sampler, the image should converge to a realization that reproduces the data as well as the MPS obtained from the TI.

The conditional distributions used to perturb the facies at each location could be based on a variety of methods as there is no theoretical constraint. A basic concept of the Gibbs sampler is that the final image will converge to the statistics that are input to the algorithm. Deviations from Gibbs sampler theory that are required for practical implementation may affect the theoretical convergence properties of the algorithm.

The Gibbs sampler put forward in this dissertation will explicitly reproduce facies and trend data and utilize the conceptual geological interpretation. The output realizations of this algorithm may then be used to quantify the uncertainty in the facies modeling of natural resource deposits. This, in turn, improves the assessment of risk inherent to projects exploiting these resources.

There are a number of existing methods that utilize MPS for simulation; there has even been commercial implementation. Each method has its own advantages and disadvantages and areas of applicability. Most work has focused on one particular method and on applying ad-hoc modifications to increase functionality. A different theoretical foundation may provide better insights into MPS and expand the field as a whole.

## **1.3 Dissertation Outline**

**Chapter 2** provides an overview of geostatistical simulation for quantifying uncertainty and how this is applied to modeling of categorical variables such as rock types. Different methods for modeling of geological bodies are presented. The background and previous implementations of MPS are reviewed. The theory of Markov chains and the Gibbs sampler is presented.

**Chapter 3** presents the theoretical underpinnings of the proposed algorithm, including its application to geological modeling, the incorporation of MPS into estimation of the conditional distributions, and the background of some of the numerical methods that are used to accomplish this.

**Chapter 4** covers the implementation issues encountered with the proposed algorithm. Artifact prevention, computational speed, selection of a random path, stopping criteria, matching of lower-order statistics, and integration of multiple data types are some of the topics covered.

**Chapter 5** looks at case studies implementing the algorithm to assess uncertainty in a model as it would proceed for a practical project. Three cases are considered: a braided channel system; an eolian sandstone; and a petroleum reservoir.

**Chapter 6** gives conclusions with closing discussion on the applications and potential for the presented algorithm.

**Appendix A** provides a list of the symbols and selected terms used in the dissertation.

**Appendix B** discusses the FORTRAN code developed to implement the proposed algorithm.

## 2 Literature Review

This chapter presents a background of theory relevant to this thesis and to the methodology that will be developed in later chapters. Section 2.1 introduces the concept of geostatistical modeling of regionalized variables and explains how this is applied in simulation of categorical variables such as facies. Section 2.2 provides an overview of multiple-point statistics (MPS), the theory of high-order spatial moments, and application to geostatistics. Section 2.3 reviews previous work on the implementation of MPS in geostatistics. The background of the Gibbs sampler (GS) is reviewed in Section 2.4.

### 2.1 Geostatistical Modeling

In any earth sciences application there is a limited amount of direct data measurements available with which to quantify the phenomena being studied. Small-scale data such as core and well log data are used to characterize the spatial structure of the geological variables of interest and then the inferred parameters are applied to estimate or simulate at the field scale (Chiles and Delfiner, 1999, Deutsch, 2002, Deutsch and Journel, 1998, Goovaerts, 1997, Isaaks and Srivastava, 1990, Journel and Huijbregts, 1978, Wackernagel, 2003).

The important variables in geostatistical modeling at an engineering project scale are those that control the valuable and/or deleterious characteristics of the resource deposit. These variables can include ore grade and concentration of contaminants in hard rock mining projects; porosity, permeability, and proportion of shale in oil reservoirs; and percent bitumen, sulphur, water, and fine material in oil sands mining deposits. These variables affect engineering-related decisions on extraction methods, recovery potential, and environmental remediation. The engineering-related variables may be expressed as continuous numbers with any possible value, up to the measurement accuracy. The values

of these continuous variables must be defined at all locations for engineering purposes. Values must be generated by some method at unsampled locations. Geostatistical methods use spatial structure inferred from the sample data for prediction.

The application of interpreted spatial structure to unsampled locations is justified through the theory of regionalized variables (RV) (Journel and Huijbregts, 1978). A RV is a spatially distributed random variable with some form of correlation or relationships between locations. In geostatistics the relation between two locations is most often expressed by a covariance or a semivariogram, often shortened to just variogram. The variogram is considered easier to infer from sparse data than the covariance, but is converted to covariance for use in geostatistical methods. The spatial covariance between two locations, separated by lag vector  $\mathbf{h}$ , of a RV  $Z$ , with stationary mean  $m_z$ , may be expressed as:

$$Cov\{Z(\mathbf{u}), Z(\mathbf{u} + \mathbf{h})\} = E\left\{\left[Z(\mathbf{u}) - m_z\right] \cdot \left[Z(\mathbf{u} + \mathbf{h}) - m_z\right]\right\} \quad (2.1)$$

The variogram value between two locations,  $\mathbf{u}$  and  $\mathbf{u} + \mathbf{h}$ , can be calculated as:

$$\begin{aligned} 2 \cdot \gamma(\mathbf{h}) &= E\left\{\left[Z(\mathbf{u}) - Z(\mathbf{u} + \mathbf{h})\right]^2\right\} \\ &= 2 \cdot \sigma_z^2 - 2 \cdot Cov\{Z(\mathbf{u}), Z(\mathbf{u} + \mathbf{h})\} \end{aligned} \quad (2.2)$$

A linear estimate of a RV at unsampled location  $\mathbf{u}$ , using the  $n$  sample data at locations  $\mathbf{u}_i$ ,  $i=1, \dots, n$ , may be formulated using the equation:

$$Z^*(\mathbf{u}) = \sum_{i=1}^n \lambda_i \cdot \left[Z(\mathbf{u}_i) - m_z\right] + m_z \quad (2.3)$$

where  $\lambda_i$  is the linear estimation weight assigned to  $Z(\mathbf{u}_i)$ ,  $i=1, \dots, n$ .

In Equation 2.3, the residual value of the variable is being estimated; that is, the mean  $m_z$  is assumed to be constant and known and the difference is being estimated. The residual of the variable  $Z(\mathbf{u})$  can be expressed as  $Y(\mathbf{u})$ ; the residual has a number of useful properties that make estimating unknown locations easier:

$$\begin{aligned} Y(\mathbf{u}) &= Z(\mathbf{u}) - m_z \\ m_y &= 0 \\ \sigma_y^2 &= \sigma_z^2 \end{aligned} \quad (2.4)$$

$$Cov\{Y(\mathbf{u}), Y(\mathbf{u} + \mathbf{h})\} = Cov\{Z(\mathbf{u}), Z(\mathbf{u} + \mathbf{h})\}$$

These properties show that  $Y$  has the same variance and spatial covariance structure as  $Z$ . With the mean removed, the calculation of error variance becomes simpler. The

variance of the error can be expressed in terms of the linear estimation weights, as follows:

$$\begin{aligned}
\sigma_E^2 &= E\left\{\left[Z^*(\mathbf{u}) - Z(\mathbf{u})\right]^2\right\} = E\left\{\left[Y^*(\mathbf{u}) - Y(\mathbf{u})\right]^2\right\} \\
&= E\left\{\left[Y^*(\mathbf{u})\right]^2\right\} - 2 \cdot E\left\{Y^*(\mathbf{u}) \cdot Y(\mathbf{u})\right\} + E\left\{\left[Y(\mathbf{u})\right]^2\right\} \\
&= \sum_{i=1}^n \sum_{j=1}^n \lambda_i \cdot \lambda_j \cdot E\left\{Y(\mathbf{u}_i) \cdot Y(\mathbf{u}_j)\right\} - 2 \cdot \sum_{i=1}^n \lambda_i \cdot E\left\{Y(\mathbf{u}_i) \cdot Y(\mathbf{u})\right\} + \sigma_y^2 \quad (2.5) \\
&= \sum_{i=1}^n \sum_{j=1}^n \lambda_i \cdot \lambda_j \cdot Cov\left\{Y(\mathbf{u}_i), Y(\mathbf{u}_j)\right\} - 2 \cdot \sum_{i=1}^n \lambda_i \cdot C\left\{Y(\mathbf{u}_i), Y(\mathbf{u})\right\} + \sigma_y^2
\end{aligned}$$

Equation 2.5 shows the error variance of the estimate as a quadratic function of the linear estimation weights. If the covariance structure of the variable  $Z$ , and therefore the residuals  $Y$ , is positive definite then there is a single unique minimum value for the  $n$ -dimensional quadratic function. This minimum may be found by taking the partial derivatives with respect to the weights, and then setting the derivatives to zero and solving the resulting system of equations:

$$\frac{\partial \sigma_E^2}{\partial \lambda_i} = 2 \cdot \sum_{j=1}^n \lambda_j \cdot Cov\left\{Y(\mathbf{u}_i), Y(\mathbf{u}_j)\right\} - 2 \cdot Cov\left\{Y(\mathbf{u}_i), Y(\mathbf{u})\right\} \quad i = 1, \dots, n \quad (2.6)$$

$$\sum_{j=1}^n \lambda_j \cdot Cov\left\{Y(\mathbf{u}_i), Y(\mathbf{u}_j)\right\} = Cov\left\{Y(\mathbf{u}_i), Y(\mathbf{u})\right\} \quad i = 1, \dots, n \quad (2.7)$$

The system of  $n$  equations in Equation 2.7 is known as the kriging system of equations; the weights found from the solution of this system are called the kriging weights and the estimate from Equation 2.3 using those weights is called the kriging (or kriged) estimate. This particular form of kriging, with a known mean, is called simple kriging.

### 2.1.1 Categorical Variables

In many cases the variables of engineering interest are controlled by categorical facies in the deposit, and modeling the facies can improve the predictive power of the model (Deutsch, 2002). The facies have different spatial structure than the continuous variables and are categorized mathematically into discrete integer values for modeling purposes. Each integer value represents one facies that has its own set of properties. The facies can

be modeled by indicators, or transformed values of zero or one corresponding to the  $K$  different facies values:

$$I(k; \mathbf{u}) = \begin{cases} 1, & \text{if facies } k \text{ is present at location } \mathbf{u} \\ 0, & \text{otherwise} \end{cases} \quad (2.8)$$

The indicators are exhaustive and exclusive, meaning that every location has an indicator value equal to one and  $K-1$  equal to zero; no location has two non-zero indicator values:

$$\sum_{k=1}^K I(k; \mathbf{u}) = 1 \quad (2.9)$$

$$I(k; \mathbf{u}) \cdot I(k'; \mathbf{u}) = 0, \quad k \neq k' \quad (2.10)$$

Indicator transforms of the facies can be viewed as RVs with the mean equal to the proportion of facies  $k$  and a variance expressible as a function of the mean:

$$\begin{aligned} E\{I(k; \mathbf{u})\} &= P(k) \\ \text{Var}\{I(k; \mathbf{u})\} &= \sigma_k^2 = E\{I(k; \mathbf{u})^2\} - E\{I(k; \mathbf{u})\}^2 = P(k) - P(k)^2 \\ &= P(k) \cdot [1 - P(k)] \end{aligned} \quad (2.11)$$

The spatial covariance of indicators may also be calculated in a similar way to other RVs as in Equation 2.1:

$$\begin{aligned} \text{Cov}\{I(k; \mathbf{u}), I(k; \mathbf{u} + \mathbf{h})\} &= E\{[I(k; \mathbf{u}) - P(k)] \cdot [I(k; \mathbf{u} + \mathbf{h}) - P(k)]\} \\ &= E\{I(k; \mathbf{u}) \cdot I(k; \mathbf{u} + \mathbf{h})\} - P(k)^2 \end{aligned} \quad (2.12)$$

In practice the indicator variogram is often calculated instead of the indicator covariance; this does not require the global probability of the facies  $P(k)$  to be known (Deutsch, 2002):

$$\begin{aligned} 2 \cdot \gamma(k; \mathbf{h}) &= E\{[I(k; \mathbf{u}) - I(k; \mathbf{u} + \mathbf{h})]^2\} \\ &= 2 \cdot \sigma_k^2 - 2 \cdot \text{Cov}\{I(k; \mathbf{u}), I(k; \mathbf{u} + \mathbf{h})\} \end{aligned} \quad (2.13)$$

Under the assumption of second-order stationarity, the indicator covariance may be calculated from the indicator variogram (Journel and Huijbregts, 1978):

$$\text{Cov}\{I(k; \mathbf{u}), I(k; \mathbf{u} + \mathbf{h})\} = \sigma_k^2 - \gamma(k; \mathbf{h}) \quad (2.14)$$

## 2.1.2 Conventional Facies Modeling Techniques

There are a number of alternative techniques for stochastic simulation of facies. Some of these methods are variogram-based, where the facies categorical values are directly simulated pixel-by-pixel; others model geo-objects as geometric shapes; and some methods mimic the underlying geologic processes that form resource deposits.

### Variogram-Based Methods

Simulating cell-by-cell using a variogram/spatial covariance as user-specified structure is a popular option for facies modeling for a number of reasons (Deutsch, 2002):

1. Sample data is explicitly reproduced by these methods;
2. Variograms/covariances are relatively easy to infer from wells or drillholes;
3. Secondary data or trends may be incorporated;
4. The results are realistic in cases where no clear geometries may be inferred for the facies.

There are two main variogram-based methods for simulating categorical variables: sequential indicator simulation (SIS) and truncated Gaussian simulation (TGS). SIS uses the indicator transform in Equation 2.7 to express the facies in a manner that is similar to the RV formalism presented earlier. TGS simulates a continuous standard normal variable that is then discretized into facies based on thresholds.

The probability of a facies  $k$  at an unsampled location  $\mathbf{u}$  can be found by using a linear estimate of indicator data:

$$I^*(k; \mathbf{u}) = \sum_{i=1}^n \lambda_i \cdot [I(k; \mathbf{u}_i) - P(k)] + P(k) \quad (2.15)$$

This is the same linear estimate as in Equation 2.3. Minimizing the error variance of the estimate leads to the simple indicator kriging system of equations:

$$\sum_{j=1}^n \lambda_j \cdot Cov\{I(k; \mathbf{u}_i), I(k; \mathbf{u}_j)\} = Cov\{I(k; \mathbf{u}_i), I(k; \mathbf{u})\} \quad i = 1, \dots, n \quad (2.16)$$

The covariances in the system of Equations 2.16 are the indicator covariance as defined in Equation 2.12. Using this approach, the probability of each facies may be calculated at an unsampled location. A value could be drawn from the conditional distribution by Monte Carlo simulation. The SIS algorithm then proceeds to the next unsampled location on a random path and uses both the sample data and previously-

simulated locations as conditioning data. One of the most well-known implementations of SIS is the SISIM program (Deutsch and Journel, 1998). An example of a three-facies SIS realization is shown in Figure 2.1.

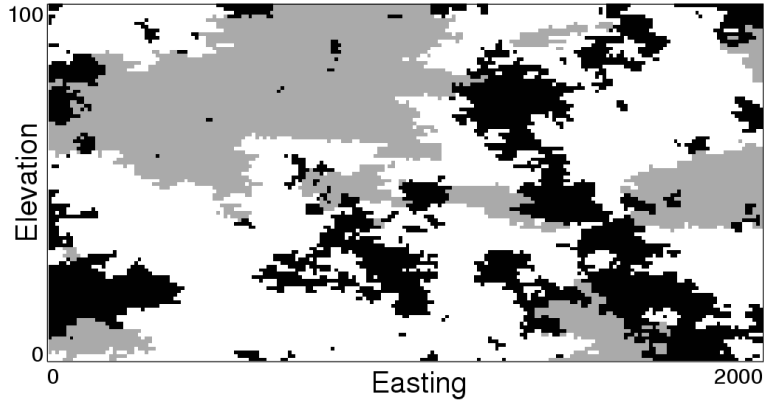


Figure 2.1: A realization of three facies created using SISIM (Deutsch and Journel, 1998).

The TGS method uses a Gaussian realization of a continuous standard normal variable and discretizes the values based on a series of thresholds into facies categories. A common Gaussian simulation algorithm is sequential Gaussian simulation (SGS). The idea of SGS is to sample conditional distributions in sequence and generate realizations that honour the spatial covariance structure and univariate statistics; kriging estimates do not reproduce these statistics (Chiles and Delfiner, 1999, Deutsch, 2002, Journel and Huijbregts, 1978, Goovaerts, 1997, Isaaks and Srivastava, 1990, among others).

A common software program that implements SGS is SGSIM (Deutsch and Journel, 1998). An example of a RV simulated using SGSIM is shown in Figure 2.2.

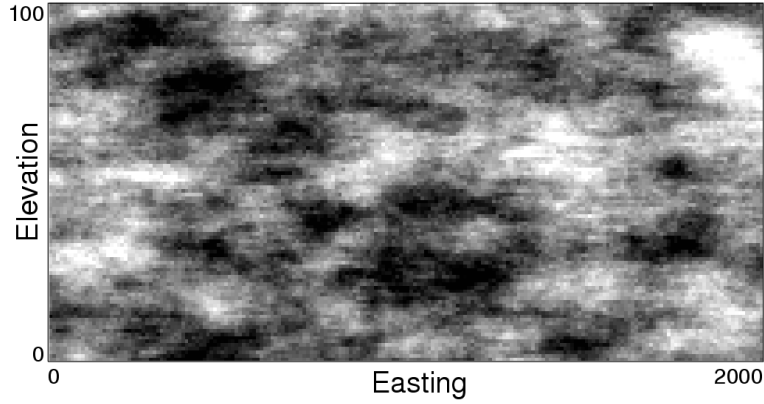


Figure 2.2: A SGS realization of a standard normal RV created using SGSIM (Deutsch and Journel, 1998).

Once a RV with a standard normal distribution has been simulated with SGS or by another method, the realization is discretized into facies categories by applying thresholds. The values within each range are assigned the same facies value. An example of this is shown in Figure 2.3. The thresholds can be specified by the target global proportions for each facies. The resulting realization displays clear ordering of the facies; an example is shown in Figure 2.4.

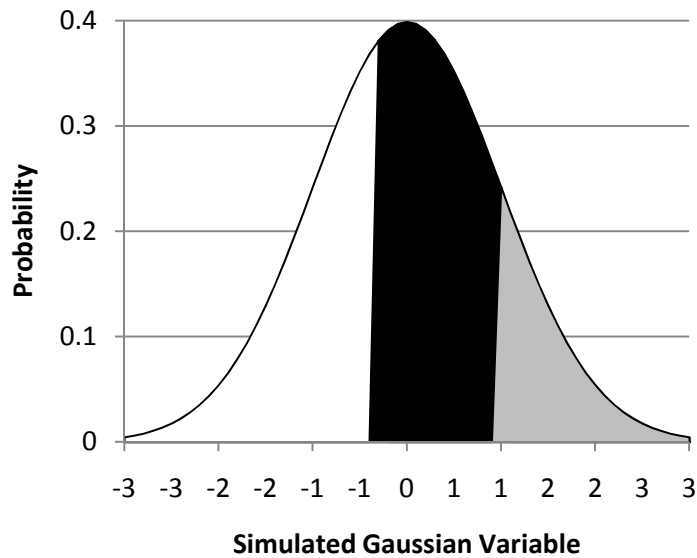


Figure 2.3: A standard normal distribution partitioned into three facies codes for TGS.

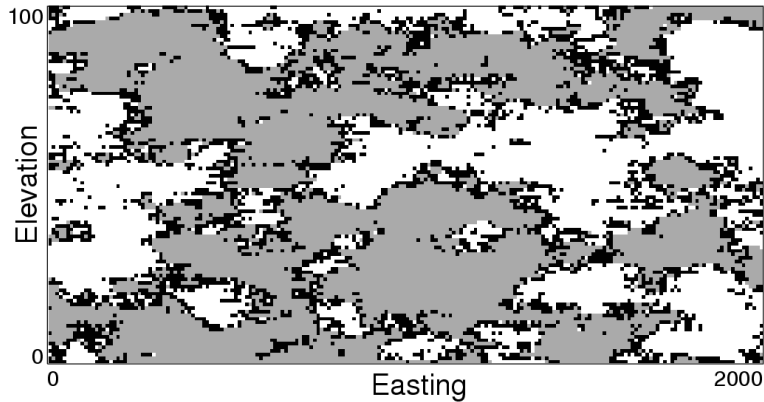


Figure 2.4: A TGS realization created using the SGS realization in Figure 2.2, the thresholds in Figure 2.3, and the GTSIM program (Deutsch and Journel, 1998).

Variogram-based (or covariance-based) methods have become ubiquitous in modern geostatistics due to the relative ease of calculating variograms from sparse data and the simplicity of the Gaussian formalism. From a facies modeling perspective, these methods have drawbacks: SIS produces images that are patchy and TGS shows distinct ordering of facies that amounts to a significant modeling decision.

### **Object-Based Modeling**

As an alternative to variogram-based simulation of facies is to insert entire geo-objects into the simulated field. This approach is called object-based modeling (Allard et al, 2004, Deutsch, 2002, Deutsch and Wang, 1996, Holden et al, 1998). Petroleum reservoirs made up of fluvial channels and associated features, particularly those reservoirs located in the North Sea, are a common type of model to be constructed using object-based methods.

The strengths of object-based models are that they can create realistic-looking realizations, can account for complex interactions between facies structures, and successfully reproduce long-range curvilinear connectivity that cannot be captured by variogram-based methods.

One drawback of object-based modeling is the reliance on user-specified parameters for the geological setting, relevant object types, and geometry of the objects. Object-based methods also have difficulty honouring dense well data.

## Event-Based Methods

Variogram- and object-based methods for simulating geological facies have the drawback of being very dependent on user-defined parameters for the spatial relations and structure. The variogram model and object parameters specify the structure so that the only variations in the realizations are ergodic fluctuations (unless parameter uncertainty is expressly accounted for). Event-based methods simulate the physical formation of geology based on the progression seen in nature (Cojan et al, 2004, Pyrcz, 2004, Pyrcz and Deutsch, 2004).

For fluvial depositional systems, this entails simulating streamlines to represent the central axes of channels. The streamlines are then modified and operated on to create further architectural elements of the depositional system such as abandoned channel fill, crevasse splays, and levees.

To simulate deepwater depositional systems, surface- or flow-based events are used (Pyrcz, 2004, Pyrcz et al, 2005). Successive surfaces representing sedimentary accumulations are simulated by stochastically choosing the source location for the flow events, the path for the deepwater flow, and the geometry of the individual events. The resulting surface architecture is used to assign facies such as turbidite lobes and shales.

## 2.2 Multiple-Point Statistics

Variogram-based methods cannot reproduce complex geologic features. Object- and process-based methods are more sophisticated in their ability to construct realistic models but have difficulty integrating data, are limited in application to certain geologic scenarios, and involve significant fine tuning of parameters. Multiple-point statistics are an attempt to use produce realistic-looking realizations in a pixel-by-pixel manner.

The idea of using non-Gaussian models for spatial statistics was first proposed by Journel and Alabert in 1989. In 1992 and 1993 the first practical algorithm for MPS simulation of facies was proposed by Guardiano and Srivastava. Other early implementations of MPS include Deutsch, 1992, and Srivastava, 1992.

Multiple-point statistics include spatial moments or probabilities involving more than two locations. It is difficult to express these statistics in the form of functions like the covariance or variogram. Two types of MPS that may be expressed in some analytical form are the multiple-point histogram and connectivity functions; those two statistics will

be discussed below. Also of relevance to MPS are the concepts of training images and dimensionality. Practical applications of MPS to geostatistical problems will be discussed.

## 2.2.1 Multiple-Point Histograms

The multiple-point histogram (MPH) is an extension of the univariate histogram. A MPH is the probability or frequency of all possible combinations of a set of indicators at many locations simultaneously. In most uses this means categorical variables such as facies but continuous variables divided into thresholds could be expressed in a MPH as well.

The value of a MPH class is the joint probability of  $N$  indicators occurring simultaneously at a defined set of  $N$  locations,  $\mathbf{u}_n$ . For  $k=1,\dots,K$  facies and  $n=1,\dots,N$  points, this is:

$$P(\mathbf{u}_1 = k_1, \mathbf{u}_2 = k_2, \dots, \mathbf{u}_N = k_N) \quad (2.17)$$

$$\forall k_1, \dots, k_N = 1, \dots, K$$

There are  $K^N$  classes in a MPH. The MPH has been a central idea of MPS methods since the first algorithms were proposed. In the cases where a MPH is explicitly used (Boisvert, 2007, Deutsch, 1992, Ortiz et al, 2006, Wang, 1996), a one-dimensional index is assigned to each combination of facies:

$$\alpha = 1 + \sum_{n=1}^N [k(n) - 1] \cdot K^{n-1} \quad (2.18)$$

$\alpha$  is the index,  $N$  is the number of points in the template,  $k(n)$  is the facies value at point  $n$ , and  $K$  is the total number of facies values. The indices are assigned from  $\alpha=1,\dots,K^N$ . The facies, points and indices can be rearranged to count from zero instead of one with no practical changes. An example of a MPH template and the corresponding patterns is shown in Figure 2.5. The template is 2x2 pixels for a total of four points; there are two indicator values, white (one) and black (two); the total number of classes is  $K^N=16$ .

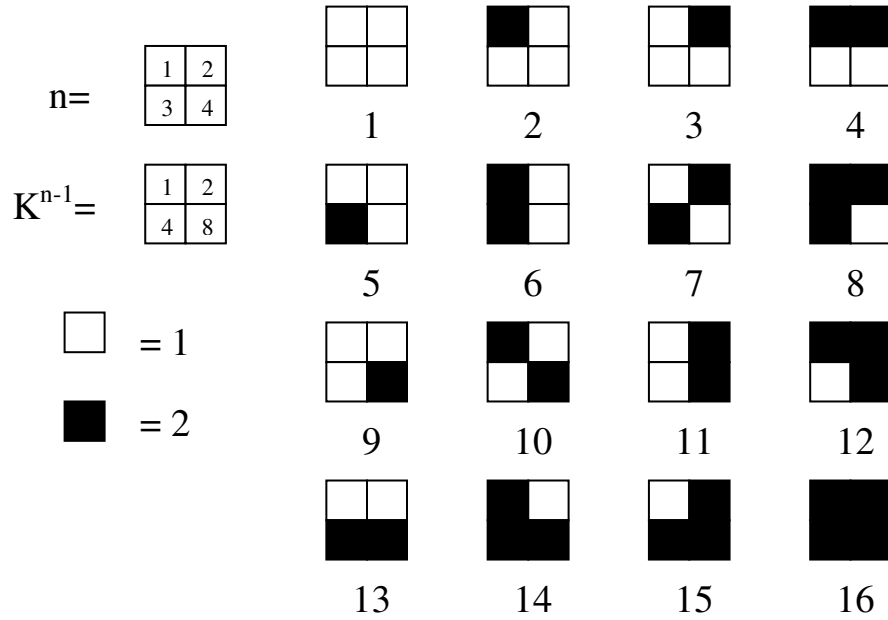


Figure 2.5: An example of a four-point MPH template and patterns with two indicator values.

## 2.2.2 Connectivity Functions

Indicator covariances and variograms were defined above in Equations 2.12 and 2.13. They quantify the probability of two points separated by a given lag having the same facies value. They are two-point statistics and deal only with the locations at either end of the lag vector  $h$ . These relations can be extended to the  $N$ -point case (Deutsch, 2002, Journel and Alabert, 1989) for facies  $k$  and a given arrangement of points  $u_n$ :

$$\phi(k; N) = E \left\{ \prod_{n=1}^N I(k; \mathbf{u}_n) \right\} \quad (2.19)$$

This  $N$ -point statistic is called a connectivity function; it is the probability of all points in the template having the indicator value  $k$ . Typically the template for a connectivity function is a straight line and so the arguments in Equation 2.19 can be simplified to a vector of length  $N$  in a specified direction. A straight-line connectivity function has been explored in several sources and is sometimes referred to as runs (Boisvert, 2007, Ortiz, 2003, Ortiz and Deutsch, 2004).

The connectivity function has also been extended by Krishnan and Journel, 2003, to include curvilinear connectivity. This concept captures the nonlinear nature of many geological features such as fluvial channels or ore veins.

### 2.2.3 Training Images

Most MPS methods use spatial statistics that are too complex to infer directly from sparse sampling data. For this reason, training images (TIs) are used. A TI is a fully-populated model that is representative of the conceptual geology of the area under study, and can be viewed as the prior model of spatial structure (Journel, 2006). By using a TI any statistics that are needed for a stochastic algorithm may be inferred, even third-, fourth-, or higher-order spatial moments. Figure 2.6 shows an example of a typical TI for a two-dimensional braided channel system.

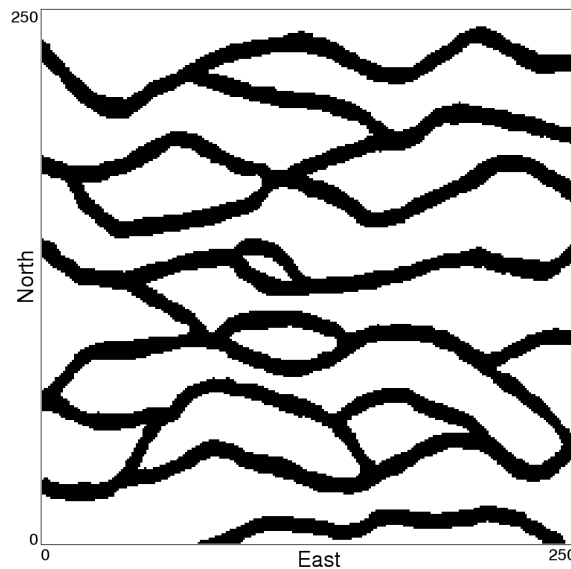


Figure 2.6: A channel-type TI (Journel, 2004, Liu, 2006, Strebelle, 2002, among others).

Using a TI for statistical inference has several advantages over alternative function-based methods: there is no grouping or averaging of scattered data into lags; there is no assumption of Gaussian spatial structure; and, complex relations between facies may be calculated. A TI is a subjective choice; however, a TI could be refuted by a qualified geomodeler, whereas an inferred variogram is much more difficult to dispute on geological grounds (Journel, 2004).

### 2.2.4 Dimensionality

The main reason for using higher-order spatial moments is to increase the information content of the statistics and thus the complexity of the geology that may be characterized

and reproduced in stochastic algorithms. However, as the order of the statistics increases the dimensionality of the problem becomes an intractable problem.

In geostatistical facies modeling the order of the statistics is equal to the number of categories raised to the power of the number of points in the statistics, or  $K^N$ . As the number of facies increases the order or dimension increases very rapidly; an example of this is shown in Table 2.1. The order of the statistics is also the total number of classes in the MPH.

Table 2.1: Dimension of statistics characterizing  $K$  facies and  $N$  points.

	<b>K=2</b>	<b>K=3</b>	<b>K=4</b>	<b>K=5</b>
<b>N=1</b>	2	3	4	5
<b>N=2</b>	4	9	16	25
<b>N=3</b>	8	27	64	125
<b>N=4</b>	16	81	256	625
<b>N=5</b>	32	243	1,024	3,125
<b>N=10</b>	1,024	59,049	1,048,576	9,765,625
<b>N=15</b>	32,768	14,348,907	1,073,741,824	30,517,578,125
<b>N=20</b>	1,048,576	3,486,784,401	1,099,511,627,776	95,367,431,640,625

Multiple-point statistics typically use ten or more points and we would like to go as high as a hundred points or more. From Table 2.1 it is obvious that the dimensionality of these statistics becomes unwieldy. This issue is mitigated by the fact that nearly any desired statistics can be calculated from a TI; however, when the order of the MPS exceeds the size of the TI the inferred statistics may be unreliable.

## 2.2.5 Applications of MPS

There have been a number of applications of MPS methods in geostatistical modeling. MPS originated in the petroleum industry, where interest in global uncertainty has driven the development of algorithms and commercial software. Applications of MPS to reservoir modeling may be found in Strebelle et al, 2002; Strebelle et al, 2003; Maharaja, 2004; Strebelle, 2005; and Zhang et al, 2006a. Integration of MPS simulation with methods for history matching of production data is described in Caers, 2003 and Hoffman et al, 2005.

Non-petroleum applications of MPS methods have also been published. The use of MPS in a mining setting is discussed in Ortiz, 2003 and Ortiz and Deutsch, 2004. The potential use of MPS in other mining settings is discussed in Boisvert, 2007.

Okabe and Blunt, 2004 and 2005 apply MPS simulation to pore space reconstruction at a scale of micrometers to millimeters, in a variety of settings such as petroleum, environmental, and groundwater flow.

## 2.3 MPS Algorithms

Since the introduction of MPS as a field of geostatistics, there have been a number of algorithms proposed and/or implemented that use higher-order spatial moments inferred from TIs for facies modeling. The algorithms are divided here into three categories: the single normal equation approach using direct inference of conditional distributions; Markov chain Monte Carlo algorithms; and pattern-based methods.

### 2.3.1 Single Normal Equation

The original concept for reproducing high-order structure in geologic realizations was proposed by Guardiano and Srivastava in 1992 and 1993. The algorithm used for this approach is a sequential simulation method with a similar workflow to SIS; however, when determining the probability of each facies  $k$  at an unsampled location  $u$  given the surrounding indicator data  $D$  a single normal equation (SNE), or Bayes' Law, is used instead of IK:

$$P(k; \mathbf{u} | D) = \frac{P(k \cap D)}{P(D)} \quad (2.20)$$

In Equation 2.20 the numerator is the probability of both  $k$  and  $D$  occurring simultaneously and the denominator is the probability of  $D$  occurring regardless of the value at  $\mathbf{u}$ . These probabilities are calculated directly from a TI of size  $n_{xyz}$  by counting the number of times,  $n$ , each configuration occurs:

$$\frac{P(k \cap D)}{P(D)} = \frac{n(k \cap D)/n_{xyz}}{n(D)/n_{xyz}} = \frac{n(k \cap D)}{n(D)} \quad (2.21)$$

Figure 2.7 shows an example of the SNE as it is used to calculate the conditional probabilities of three facies using five data. The “?” value is the unsampled location to be

populated. The numerators in the SNEs are six-point statistics ( $N=6$ ) and the denominators are five-point statistics ( $N=5$ ). All of the joint probabilities shown in the equations in Figure 2.7 could be calculated directly from a TI given the arrangement of data locations and the facies values.

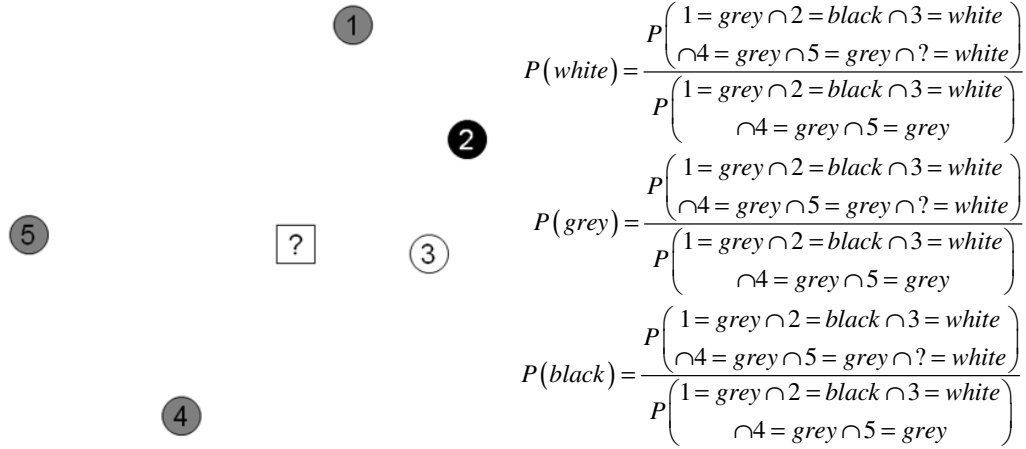


Figure 2.7: An example using the SNE equation to calculate conditional distributions using MPS.

In the original implementation by Guardiano and Srivastava the TI was scanned at each unsampled location to find the values for Equation 2.21. This caused the algorithm to be very slow for large TIs and ultimately impractical. An important advancement of the SNE method was made when Strebelle used the concept of search trees to store facies configurations from the TI while only scanning the TI once (Strebelle and Journel, 2000, Strebelle and Journel, 2001, Strebelle, 2002). This method was named SNESIM by Strebelle and this term is now used to describe the different versions of the SNE approach.

Significant research effort has been put into the SNESIM workflow. Implementation aspects and parameter uncertainty were explored in several publications (Liu, 2006, Zhang, 2002). Integration of secondary data such as seismic has been explored and implemented (Strebelle, 2005, Strebelle et al, 2002, Strebelle et al, 2003). Dynamic data integration has been put into practice by way of history matching (Caers, 2003, Hoffman et al, 2005). Hierarchical simulation of facies reduces the effective value of  $K$  and hence helps with the problem of dimensionality (Maharaja and Journel, 2005).

### 2.3.2 Markov Chain Monte Carlo Methods

Iterative methods for geostatistical simulation have been used in a number of cases. As opposed to sequential simulation methods, iterative algorithms have no data configuration issues; do not require a search of scattered data; and do not require solving a system of equations or looking up spatial statistics from a table or search tree at every unsampled location. However, iterative methods can produce artifacts near conditioning data; have issues with edge effects; and require sometimes subjective stopping criteria.

There have been three different iterative simulation algorithms developed to some extent that use MPS for facies simulation. All of these algorithms use some form of Markov chain Monte Carlo (MCMC) method (Robert and Casella, 2004) as a theoretical background. The three MCMC algorithms that have used MPS are simulated annealing, the Gibbs sampler, and a neural network in a Metropolis-Hastings algorithm.

#### Simulated Annealing

Simulated annealing (SA) is an optimization method that minimizes an objective function to match a set of target statistics (Deutsch, 1992). The objective function is representative of the energy state of the realization; in physical annealing, heated metal is cooled slowly until crystals form in a near-optimal manner with minimum energy. For MPS simulation the objective function may be set as the sum of the square differences between the MPH of the TI and the current MPH of the simulated realization:

$$O = \sum_{\alpha=1}^{K^N} [P^{TI}(\alpha) - P^{SIM}(\alpha)]^2 \quad (2.22)$$

The SA algorithm proceeds by visiting all unsampled locations along a random path. Every location is assigned a value, whether hard conditioning data, a randomly-chosen facies, or a previously simulated value. A new facies is selected for the unsampled location; then, the new value is accepted with the probability:

$$P(\text{accept}) = \min \left\langle 1, \exp \left\{ -\frac{\Delta O}{T} \right\} \right\rangle \quad (2.23)$$

The  $T$  parameter in Equation 2.23 is a control temperature that is analogous to the temperature of heated metal in annealing. If the objective function is lowered the change is always accepted and the simulation moves closer to the target statistics. If the objective function is raised, there is a chance that the simulation will move farther away from the

target to a less-optimal solution; this allows the algorithm to avoid local minima that may trap greedy optimization methods. The temperature is lowered as the simulation proceeds until the objective function cannot be lowered any further from the current state.

## **Gibbs Sampler**

The Gibbs sampler is a statistical resampling algorithm used to draw samples from complex multivariate joint distributions using only the conditional distributions (Geman and Geman, 1984, Casella and George, 1992). A geostatistical Gibbs sampler starts with a field, fully-populated with conditioning data or random values, and visits every unsampled location in a random path. At each location the conditional probabilities of the facies is calculated based on the current state of the nearby locations; then a new value is drawn from this distribution and assigned to the unsampled location.

This concept was implemented by Srivastava, 1992, using ordinary IK (Deutsch, 2002) to determine the conditional distributions. The Gibbs sampler algorithm was found to be ten times faster than SIS for simulation of a two-dimensional binary sand/shale reservoir. The application of MPS in the Gibbs sampler was also briefly explored using a SNE to determine the conditional distributions. The use of MPS allowed reproduction of complex structure that was not possible using only second-order statistics. However, the idea was not explored any further. This previous work by Srivastava was the inspiration behind this thesis.

## **Neural Networks**

A neural network (NN) is a programming method that is widely used in optimization (Chong and Zak, 2001). The idea behind NN is to use a number of simulated “neurons” in several layers to produce non-linear output values. Each neuron has an “activation function” that specifies its output based on the input variables. The combination of the neurons and their activation functions produces a complex system that accounts for many interactions. The optimal parameters for the activation functions are found by training on known data, such as a TI – making NN a natural fit for MPS. The use of a NN system in MPS simulation was first proposed by Caers and Journel in 1998 and further developed in Caers, 2001. An example of a simple NN for geostatistical simulation is shown in Figure 2.8. The example has three layers: an input layer with three facies data, a hidden

layer with four neurons, and an output layer that produces the conditional facies probabilities at an unsampled location.

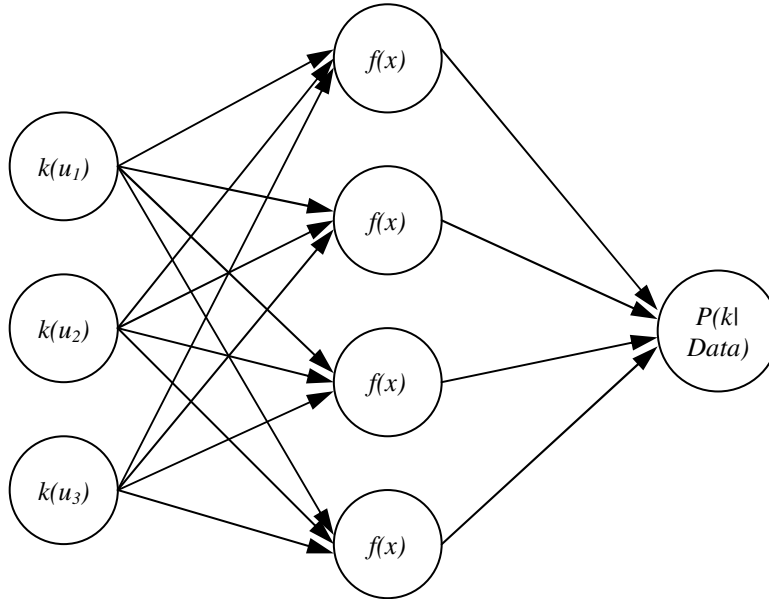


Figure 2.8: An example of a simple neural network with eight neurons and three layers (input layer, hidden layer, output layer).

The NN algorithm as implemented by Caers and Journel, 1998, and Caers, 2001, is an iterative simulation method that uses a Metropolis-Hastings accept/reject step (Metropolis et al, 1953, Hastings, 1970) to ensure the final simulated image honours the input statistics determined from the TI. In this type of algorithm a new facies (not equal to the current state of the unsampled location) is proposed. The value at that location is then changed to the proposal value with the probability:

$$P(\text{accept}) = \min \left\langle 1, \frac{P(k_{new} | Data)}{P(k_{old} | Data)} \cdot \frac{P(k_{old})}{P(k_{new})} \right\rangle \quad (2.24)$$

If the change is rejected then the facies value is left the same. The algorithm moves to the next unsampled location and repeats the process.

### 2.3.3 Pattern-Based Geostatistics

The MPS algorithms mentioned previously visit all unsampled locations and use nearby data as high-order information to produce a probability distribution for the single location

being considered. There has been a movement in recent year towards taking entire patterns from the TI and inserting them into the simulated field (Journel, 2004). In this instance a pattern is a group of cells with a specific structure; structures seen a number of times in a consistent and repeating TI are the patterns that should be seen in a geological model reproducing the features of that TI. There have been three pattern-based MPS simulation methods developed: Growthsim (Eskandaridavand, 2008), SIMPAT (Arpat and Caers, 2007), and Filtersim (Zhang et al, 2006b).

## **Growthsim**

The original implementation of the Growthsim algorithm was not pattern-based, but used MP configurations of data to assign new facies values at unsampled locations (Wang, 1996). All unsampled locations are assigned as the “background” or most “unimportant” facies (i.e. shale, non-mineralized zone). The locations immediately next to the existing facies of importance (i.e. channel sands, ore veins) are then visited and the conditional probability of changing facies calculated using a SNE with probabilities calculated from the TI. One pixel at a time is then changed to the net or “important” facies, thus “growing” the geo-objects.

Further development of the Growthsim idea has been performed by Eskandaridavand, 2008. This more recent implementation of the Growthsim method uses a similar approach, but does not assign the background values initially, rather proceeding in a fully sequential manner. The uninformed locations near conditioning data (samples or previously simulated) are visited and the TI is scanned to determine which patterns match the existing values; one of those patterns is then selected using a SNE and inserted into the simulated field. An example of this algorithm is shown in Figure 2.9.

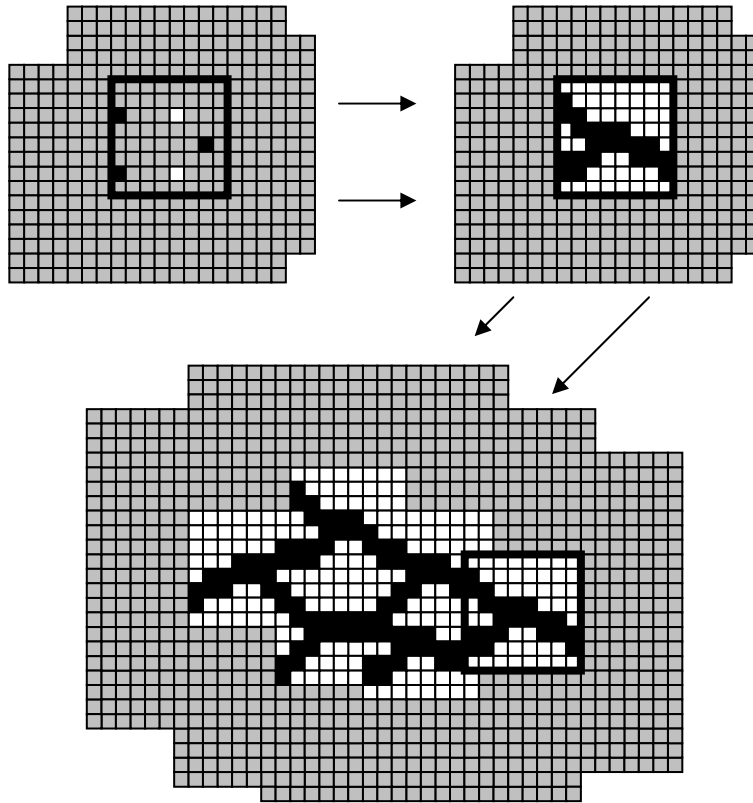


Figure 2.9: An example of the Growthsim algorithm. Clockwise from left: Data locations with the template size and possible locations shown; pattern inserted into the simulated field; state of the realization after several more patterns have been inserted.

## SIMPAT

A sequential algorithm designed to use the concept of patterns for MPS simulation was developed by Arpat and Caers, 2004 (see also Arpat and Caers, 2007). This method is called SIMPAT (SIMulation using PATterns). The workflow begins by visiting an unsampled location on a coarse grid near conditioning data or previously-simulated values. A pattern on a coarse or “primal” template is then selected from the TI based on the data and a pattern is inserted using a finer or “dual” template.

Figure 2.10 shows an example of this workflow. The use of primal and dual templates reduces the dimension of the patterns to be selected; the patterns are chosen based on the coarse primal template, which in the example has 16 points ( $N=16$ ). The dual template that is inserted into the image has more points and therefore contains finer structure; in the example the dual template has 64 points ( $N=64$ ).

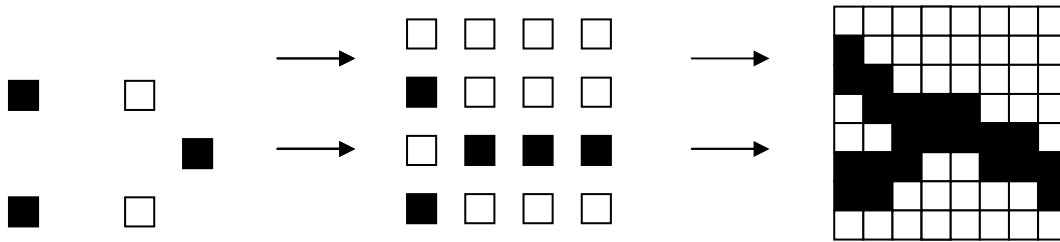


Figure 2.10: An example of the SIMPAT workflow. Left to right: Conditioning data; primal template pattern; dual template pattern.

### Filtersim

One of the most pressing problems with pattern-based geostatistics is the high dimension of the spatial moments represented by TI patterns (the problem of dimensionality). SIMPAT reduces the dimension by using primal and dual templates. An alternate approach put forth by Zhang et al in 2004 is to use “filters” to reduce a large template ( $N$  between 10 and 100) to a smaller number of values, or “scores”. Examples of three 2D filters are shown in Figure 2.11. Patterns in the TI with similar scores for every filter are grouped together in the same “prototype” pattern.

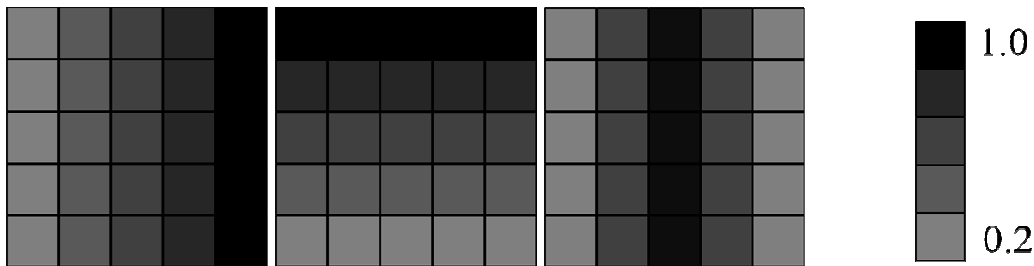


Figure 2.11: An example of three possible filters for classification of patterns in Filtersim.

The Filtersim algorithm proceeds at an unsampled location by searching for nearby data and finding the prototype pattern or patterns that match the filter scores of the data the closest; from these prototypes one is selected and then a single pattern within that prototype is patched in to place in the simulated field. This process is repeated until all unsampled locations have been populated. An example of the Filtersim workflow is shown in Figure 2.12.

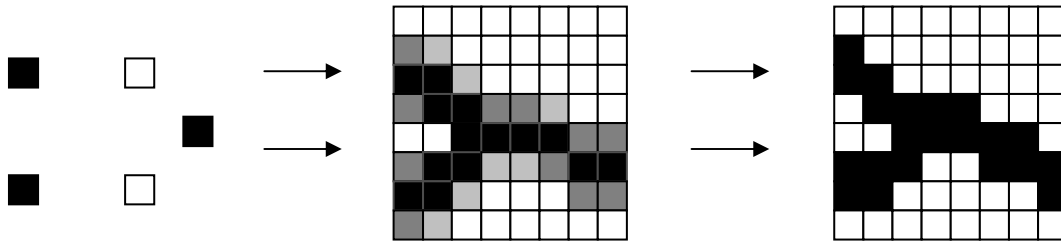


Figure 2.12: An example of the Filtersim workflow. Left to right: Conditioning data; pattern prototype; pattern from TI.

Since the original publication of Filtersim, there has been significant further development of the algorithm; see Wu et al, 2008a, Wu et al, 2008b, Zhang et al 2006a, and Zhang et al, 2006b.

## 2.4 Gibbs Sampling

The concept of Gibbs sampling originated in the field of image processing (Geman and Geman, 1984) and was first derived as a variation of the Metropolis-Hastings algorithm (Metropolis et al, 1953, Hastings, 1970). The Gibbs sampler uses the concept of Markov chains to produce random values from complex multivariate joint distributions that cannot be simulated directly, without having to use (or even know) the posterior density function (Casella and George, 1992, Gelfand and Smith, 1990, Smith and Gelfand, 1992).

This section explains the background of Markov chains and Markov chain Monte Carlo (MCMC) methods that were mentioned in Section 2.3.2 as the basis for some MPS algorithms. The Gibbs sampler method is explained for the two-dimensional case and for the extension to the multivariate case.

### 2.4.1 Markov Chains

A Markov chain is made up of a number of values for a random variable as it changes in time. The value (or state) of a Markov chain,  $X$ , at a given point in time,  $t$ , is dependent upon the past values of the chain; the specific property of interest for a Markov chain is the Markov property. The Markov property is that the next state depends only on the current state; the history can be ignored without affecting the results. The Markov property can be expressed mathematically as:

$$P(X_{t+1} | X_t, X_{t-1}, \dots, X_1, X_0) = P(X_{t+1} | X_t) \quad (2.25)$$

In Equation 2.25,  $X_t$  is the state of random variable  $X$  at time  $t$ . All previous values for time less than  $t$  can be disregarded due to the Markov property.

The values a random variable can take are collectively called the state space (Robert and Casella, 2004). A state space can be finite or infinite, continuous or discrete, and of any dimension. This thesis will consider primarily finite and discrete state spaces; geostatistical facies models have both of these properties.

A Markov chain can be thought of as exploring the state space by visiting one state after another. The movement from state to state is expressed by a transition probability (Lawler, 2006). Figure 2.13 shows an example of a one dimensional discrete state space over the integers -10 through +10. A Markov chain on this state space could take 21 different values.

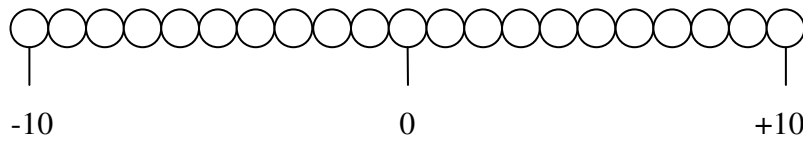


Figure 2.13: An example of a one dimensional discrete state space over the integers -10 through +10.

## Exploration of the State Space

Markov chains take values in the state space and move about the state space in a manner that is controlled by the transition probabilities, that is, the probability of moving from any given state to any other state. A transition probability from state  $\alpha$  to state  $\beta$  in a single step can be expressed in the form (Robert and Casella, 2004):

$$P(X_{t+1} = \beta | X_t = \alpha) = P_{\alpha\beta} \quad (2.26)$$

The rules and probabilities governing the movement of a Markov chain about its state space, taken collectively, are referred to as a “transition kernel” (Robert and Casella, 2004). For finite and discrete state spaces the transition kernel can be expressed as a matrix containing all of the transition probabilities:

$$P(X_{t+1} = \beta | X_t = \alpha) = \begin{bmatrix} P_{\alpha\beta} \end{bmatrix} \quad \forall \alpha, \beta \quad (2.27)$$

To determine the probability of moving from state  $\alpha$  to state  $\beta$  in a given time  $t$ , the transition matrix can be raised to the power  $t$  (Lawler, 2006):

$$P(X_t = \beta | X_0 = \alpha) = P_{\alpha\beta}^t = \left[ P_{\alpha\beta} \right]^t \quad (2.28)$$

The movement of a Markov chain from state to state can be thought of as exploration of the state space. If the chain can move directly from one state to another in a single time step ( $P_{\alpha\beta} > 0$ ), they are said to be neighbouring states. If a Markov chain can move from one state to another in any given time  $t$  with a non-zero probability ( $P_{\alpha\beta}^t > 0$ ), then the two states are said to be in communication, or communicating states. If all states in the space are in communication, then the Markov chain is referred to as irreducible. If not all states in a space communicate, they can be grouped into distinct communicating classes where the chain cannot move from one class to another. In those cases the initial state becomes an important consideration.

## Convergence Properties

A property that makes Markov chains interesting for a number of applications is the limiting distribution. Over a long period of time the current state of the Markov chain will tend to be certain values more often than others. The likelihood of one state over another is controlled by the transition kernel. At a large enough time, the probability distribution over all of the states will approach a limiting distribution; the limit distribution may or may not be explicit from the transition kernel, and could be unknown.

Using the transition matrix  $P_{\alpha\beta}$  it is possible to analytically determine the stationary distribution of a Markov chain (if it exists) by solving the system of equations (Lawler, 2006):

$$\left[ \pi_\alpha \right] \left[ P_{\alpha\beta} \right] = \left[ P_{\alpha\beta} \right] \quad (2.29)$$

In Equation 2.29  $\pi$  is the stationary limiting distribution for all states  $\alpha$  that are in the state space. Equation 2.29 shows that at some large time the probability of being in any individual state no longer changes as time increases, thus the distribution is stationary. As an alternative to solving Equations 2.29 it is possible to take the limit (Lawler, 2006):

$$[\pi_\alpha] = \lim_{t \rightarrow \infty} [\varphi_\alpha] \left[ P_{\alpha\beta} \right]^t \quad (2.30)$$

The probability vector  $\varphi$  is any initial state. This will produce the same results as solving Equations 2.29. Irreducible Markov chains will reach the stationary distribution regardless of the initial state; however, a distribution of initial states may need to be considered for Markov chains that have separate classes.

States that have stationary values greater than zero are called positive. A state  $\alpha$  is called “recurrent” if a return to that state in a finite amount of time is certain, that is, the probability of the time to return to  $\alpha$  being finite is one. Equivalently, the expected number of visits to a recurrent state over a large amount of time is infinite. For chains with finite state spaces all positive states are recurrent and vice versa. If a state is not recurrent then it is said to be “transient”, that is, at some point the chain can be expected to leave that state and never return.

In a finite state space communicating classes of states are always positive and recurrent. If the initial state,  $X_0$ , is in one of those classes the chain will remain in that class and never escape; this severely limits the exploration of the state space. If the initial state is in a transient class it may explore the space for a large number of iterations before entering a communicating class, but will eventually leave the transient states and explore only a single class of recurrent states.

For certain cases a Markov chain can be used to produce samples from a limiting distribution that is difficult to define or simulate from, and this is where MCMC methods have found favour. If the state space is finite but exceedingly large it is not possible to solve Equations 2.29 for the stationary distribution. For example, in a geomodel there is often on the order of  $10^6$  cells; for three possible facies values there are then  $3^{1,000,000} \approx 10^{477,121}$  states in the space. While finite, this is exceptionally large and most states are transient as there is a certain geologic structure to be expected and those that vary greatly from this structure are impossible. Ensuring that the entire state space is sampled requires a random starting state.

### **Example: 1D Random Walk**

A simple example of a Markov chain is known as a random walk (Lawler, 2006, Robert and Casella, 2004). A random walk is a simple exploration of a state space where the

Markov chain can move to any adjacent state from the current one, and satisfies the equation

$$X_{t+1} = X_t + \varepsilon_t \quad (2.31)$$

If the epsilon values in Equation 2.31 are independently generated then the sequence of variables  $X_t$  is a random walk (Robert and Casella, 2004). An example of this is a simple coin-flipping game where the player wins a dollar every time a heads is flipped and loses a dollar every time tails is flipped:

$$X_{t+1} = \begin{cases} X_t + 1 & \text{if heads} \\ X_t - 1 & \text{if tails} \end{cases} \quad (2.32)$$

This coin-flipping game is a 1D random walk Markov chain; the first example has an infinite state space consisting of all the integers. The initial state is  $X_0=0$  and the value of the chain at any time may be seen as the profit (if positive) or loss (if negative) of the player. Other cases have been considered elsewhere such as unfair coins (Robert and Casella, 2004). Examples of the values of four random walk coin-flipping games are shown in Figure 2.14.

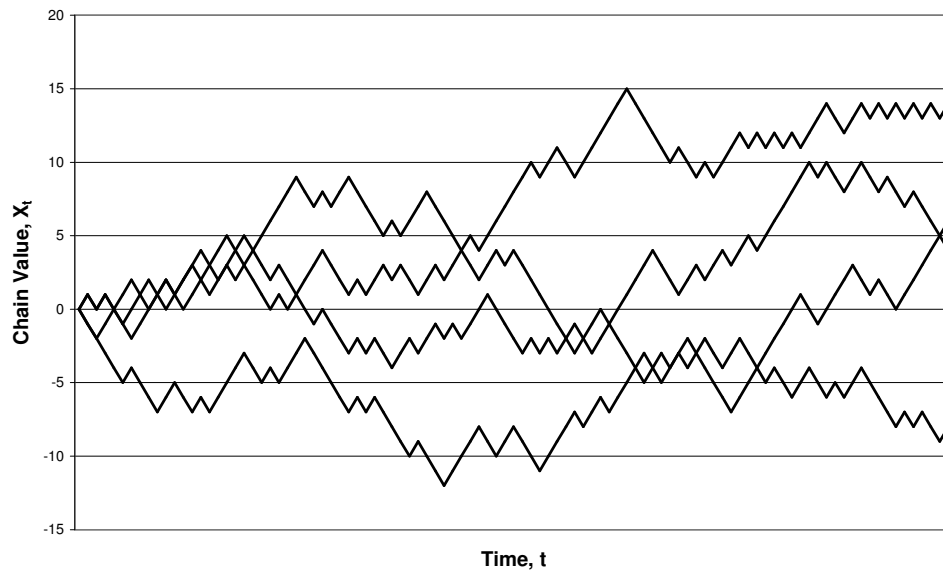


Figure 2.14: An example of a simple one-dimensional random walk in the form of a coin-flipping game. Four Markov chains are shown.

At a large time the values of the coin-flipping game will approach a Gaussian underlying stationary distribution; simulating a large enough sample size of this random walk will make this clear. Figure 2.15 shows a histogram of the value of 50 coin-flipping games after 20 flips.

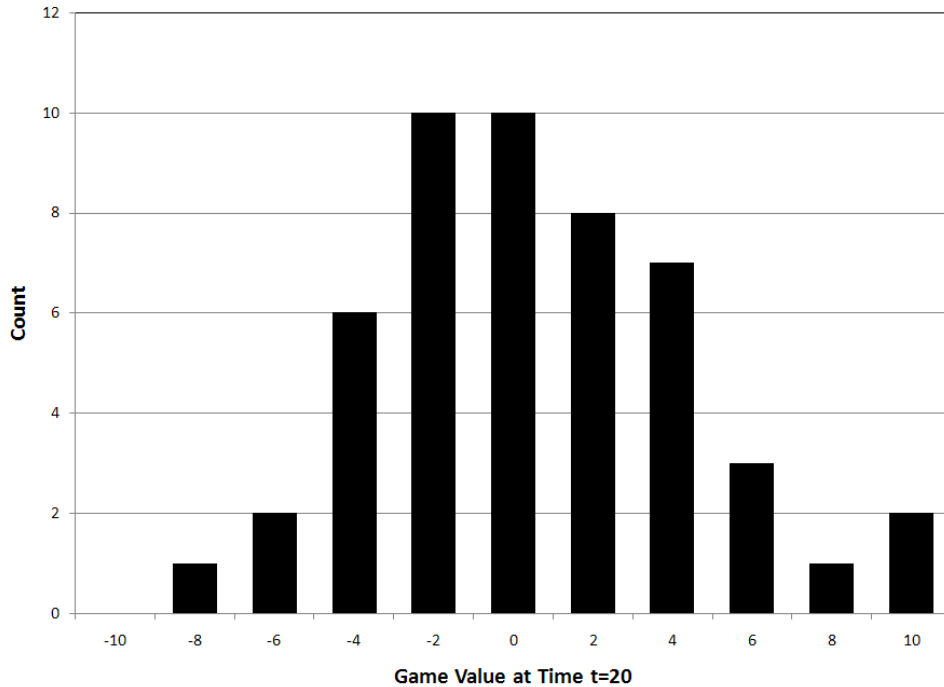


Figure 2.15: A histogram of the values of 50 coin-flipping games after 20 flips ( $t=20$ ).

If the coin-flipping game is modified such that the player either goes bankrupt at -10 or stops playing and keeps the winnings at +10 the state space includes only the 21 integers from -10 to +10, as shown in Figure 2.13. With a finite and discrete state space the transition kernel can now be expressed as a matrix, as shown in Figure 2.16. There are 21 states and thus the matrix is  $21 \times 21$ ; from each state there is a 50% chance of moving to a higher value and a 50% chance of moving to a lower value, with no chance of staying the same or moving more than one at a time. The states at -10 and +10 are called absorbing states because they do not allow the chain to move once it has reached those values.

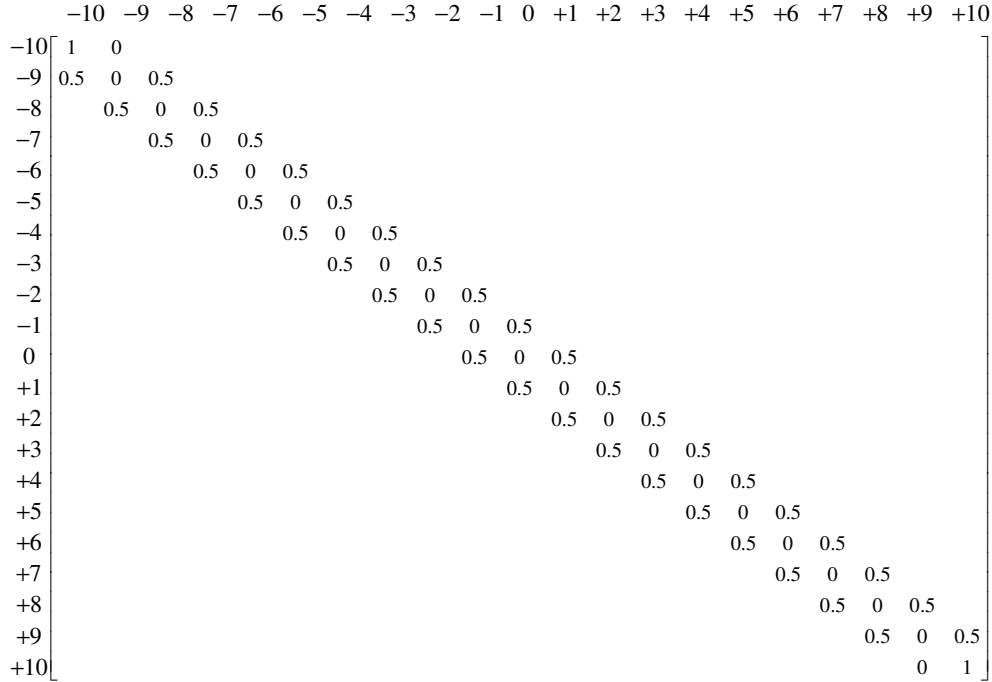


Figure 2.16: Transition matrix of the finite state space coin-flipping game. All values not shown are zero.

The system of Equations 2.29 that give the stationary distribution of this Markov chain is singular; the viable solutions are any states that satisfy

$$\begin{aligned} \pi_{-10} + \pi_{+10} &= 1.0 \\ \pi_i &= 0.0, \quad i \neq -10, +10 \end{aligned} \tag{2.33}$$

Using Equation 2.30 and an initial state of  $X_0=0$  (or  $\varphi_0=1, \varphi_{i \neq 0}=0$  in vector form), taking the limit given the stationary distribution

$$\pi = [0.5 \ 0.5]$$

This solution satisfies Equations 2.29 and suggests that in a coin-flipping game with absorbing states that are equal distances from the initial state, the game will eventually end up at -10 or +10 with equal probability. Using different initial states from -10 to +10 and taking the limit in Equation 2.30, the probability of the player going bankrupt ( $X=-10$ ) or winning ( $X=+10$ ) can be calculated. Table 2.2 shows the results for all 21 initial states.

Table 2.2: Probability of bankruptcy or winning from each initial state in the finite coin-flipping game.

Initial State	P(Bankrupt)	P(Winner)
-10	1.0	0.0
-9	0.95	0.05
-8	0.90	0.10
-7	0.85	0.15
-6	0.80	0.20
-5	0.75	0.25
-4	0.70	0.30
-3	0.65	0.35
-2	0.60	0.40
-1	0.55	0.45
0	0.50	0.50
+1	0.45	0.55
+2	0.40	0.60
+3	0.35	0.65
+4	0.30	0.70
+5	0.25	0.75
+6	0.20	0.80
+7	0.15	0.85
+8	0.10	0.90
+9	0.05	0.95
+10	0.0	1.0

The significant result demonstrated in Table 2.2 is that when there are a large number of transient states and several distinct communicating recurrent classes, the initial state is an important consideration.

### 2.4.2 Two-Dimensional Gibbs Sampler

A GS can only be used for multidimensional variables; the simplest form of the Gibbs sampler is the two-dimensional case. A two-dimensional Gibbs sampler selects the next state in the chain by changing one dimension of the variable conditional to the other dimension. If the two dimensions of a variable are  $x$  and  $y$ , then a two-dimensional Gibbs sampler proceeds as follows:

$$\begin{aligned} x_{t+1} &= f(x | y_t) \\ y_{t+1} &= f(y | x_{t+1}) \end{aligned} \tag{2.34}$$

The two-dimensional Gibbs sampler has a number of interesting properties as a Markov chain. Each dimension of the Gibbs sampler chain,  $X$  and  $Y$ , form Markov chains

of their own; that is,  $X_{t+1}$  is independent of all  $X$  before time  $t$  and  $Y_{t+1}$  is independent of all  $Y$  before time  $t$  (Robert and Casella, 2004). Both subchains will converge as the overall bivariate chain converges.

### Example: Bivariate Gaussian Distribution

To demonstrate a two-dimensional Gibbs sampler, consider the case of a bivariate Gaussian distribution in the variables  $X$  and  $Y$ . The conditional distributions for the variables are:

$$f(x|y) = N(\rho y, 1 - \rho^2) = \frac{e^{-\frac{(x-\rho y)^2}{2(1-\rho^2)}}}{\sqrt{2\pi(1-\rho^2)}} \quad (2.35)$$

$$f(y|x) = N(\rho x, 1 - \rho^2) = \frac{e^{-\frac{(y-\rho x)^2}{2(1-\rho^2)}}}{\sqrt{2\pi(1-\rho^2)}}$$

The initial state for this example is  $(X,Y)=(0,0)$ . Three chains were run from this initial state to time  $t=1000$  with a correlation coefficient  $\rho=0.5$ . Convergence for this Markov chain means that the chain values at a large enough time should approximate samples from the underlying bivariate distribution; all of the values of the chain taken together should therefore show the characteristics of the bivariate Gaussian distribution. Figure 2.17 shows all 3000 points in the three chains; the distribution is bivariate Gaussian. Table 2.3 shows the summary statistics of the three chains. The means of  $X$  and  $Y$  are close to zero and the correlation coefficients are close to the target value of 0.5.

The joint bivariate Gaussian distribution was not used explicitly in this example, but the Gibbs sampler produced a two-dimensional Markov chain that successfully sampled from the joint distribution.

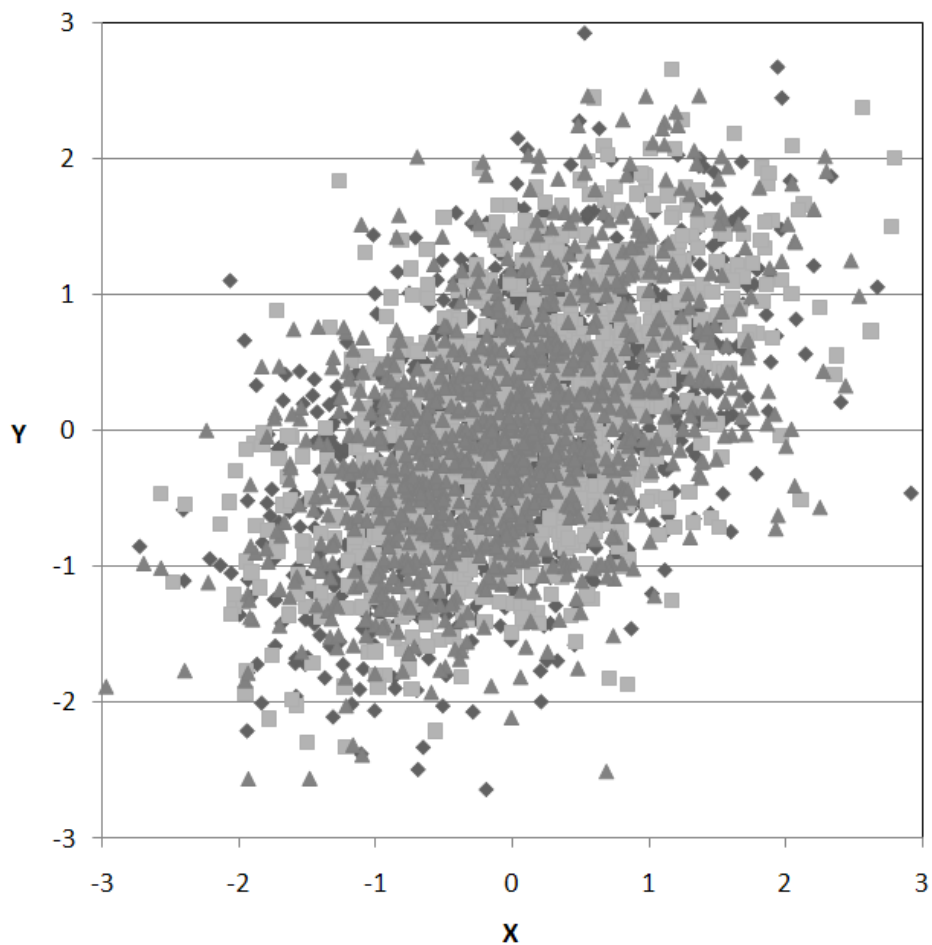


Figure 2.17: Results of three two-dimensional Gibbs samplers simulated to  $t=1000$  using bivariate Gaussian conditional distributions.

Table 2.3: Summary statistics for three two-dimensional Gibbs samplers simulated to  $t=1000$  using bivariate Gaussian conditional distributions.

	Chain 1	Chain 2	Chain 3
$E\{X\}$	0.017	0.074	-0.011
$E\{Y\}$	0.000	0.079	-0.006
$\rho_{xy}$	0.478	0.517	0.488

### 2.4.3 Multi-Dimensional Gibbs Sampler

A two-dimensional simulation is useful in many cases; however, for earth sciences applications the distributions of interest are of much larger dimensions. Markov chains

can be used to model these higher-dimensional variables. A multidimensional variable  $X$  at time  $t$  is expressed as

$$X_t = (x_1, x_2, \dots, x_{n-1}, x_n)_t \quad (2.36)$$

$$X_{t+1} \sim \frac{f(x_1, x_2, \dots, x_i, \dots, x_{n-1}, x_n)_t}{\sum_{k=1}^K f(x_1, x_2, \dots, x_i, \dots, x_{n-1}, x_n)_t} \quad (2.37)$$

### Example: Four-point Domain, Two Facies

Consider the case of a four-cell model in a two-by-two arrangement with two possible facies values (as in the MPH shown in Figure 2.5). Considering this as a geomodel,  $K=2$  and  $N_{xyz}=4$  so there are a total of  $2^4=16$  states in the space of the Markov chain. This is a very small geomodel; the size allows an analytical analysis to be performed. The variable for this example is expressed as:

$$X_t = (x_1, x_2, x_3, x_4)_t \quad (2.38)$$

The individual components,  $x_i$ , are the facies values at each location for a given state and can take the facies values of one or two. Each state is numbered as a MPH class  $\alpha$ . To move from state to state one location at a time is changed conditional to the other three locations; note that it is possible for the chain to remain in the same state if the selected value for  $x_i$  is equal to the current value. The new value for the four-dimensional variable  $X$  is drawn from the distribution:

$$X_{t+1} \sim f(x_i | x_j, j \neq i)_t \quad (2.39)$$

In Equation 2.39, there is no restriction on which one of the four points is to be changed at each step; for the purposes of this example one will be selected at random. Figure 2.18 illustrates the state space of this example, with states that are adjacent to one another connected by lines and each state numbered by its corresponding MPH class. Figure 2.18 is arranged by univariate proportions, with the entirely white (facies one) state at the top and the entirely black (facies two) state at the bottom, and fractional proportions between the two. The state space is symmetric as each state has an opposite state with all four values switched. Opposing states are distributed symmetrically about the center of Figure 2.18 that is located in the space between states 7 and 10. Opposite states cannot communicate with one another in fewer than four steps.



For any location that is to be modified there is always one diagonal location and two adjacent; setting the diagonal location as data point one and the two adjacent locations as data points two and three, the simple IK system is then:

$$\begin{bmatrix} 1 & 0.5 & 0.5 \\ 0.5 & 1 & 0.2 \\ 0.5 & 0.2 & 1 \end{bmatrix} \begin{bmatrix} \lambda_1 \\ \lambda_2 \\ \lambda_3 \end{bmatrix} = \begin{bmatrix} 0.2 \\ 0.5 \\ 0.5 \end{bmatrix} \quad (2.40)$$

Solving this system, the optimal linear weights are:

$$\begin{bmatrix} \lambda_1 \\ \lambda_2 \\ \lambda_3 \end{bmatrix} = \begin{bmatrix} -0.3714 \\ 0.5714 \\ 0.5714 \end{bmatrix} \quad (2.41)$$

Using global proportions of 0.4 for facies 1 (white) and 0.6 for facies 2 (black) and randomly selecting the location to be changed, the transition matrix for this Gibbs sampler is shown in Figure 2.20. From each state the chain can move to five potential states: the four adjacent states in Figure 2.18 or the same state, i.e.  $X_{t+l}=X_t$ .

$$P_{\alpha\beta} = \begin{bmatrix} 0.8628 & 0.0343 & 0.0343 & 0 & 0.0343 & 0 & 0 & 0 & 0.0343 & 0 & 0 & 0 & 0 & 0 & 0 \\ 0.2157 & 0.4300 & 0 & 0.1771 & 0 & 0.1771 & 0 & 0 & 0 & 0 & 0 & 0 & 0 & 0 & 0 \\ 0.2157 & 0 & 0.4300 & 0.1771 & 0 & 0 & 0 & 0 & 0 & 0 & 0.1771 & 0 & 0 & 0 & 0 \\ 0 & 0.0729 & 0.0729 & 0.6857 & 0 & 0 & 0 & 0.0843 & 0 & 0 & 0 & 0.0843 & 0 & 0 & 0 \\ 0.2157 & 0 & 0 & 0 & 0.4300 & 0.1771 & 0 & 0 & 0 & 0 & 0 & 0 & 0.1771 & 0 & 0 \\ 0 & 0.0729 & 0 & 0 & 0.0729 & 0.6857 & 0 & 0.0843 & 0 & 0 & 0 & 0 & 0 & 0.8429 & 0 \\ 0 & 0 & 0.2500 & 0 & 0.2500 & 0 & 0 & 0.2500 & 0 & 0 & 0 & 0 & 0 & 0 & 0.2500 \\ 0 & 0 & 0 & 0.1657 & 0 & 0.1657 & 0 & 0.4414 & 0 & 0 & 0 & 0 & 0 & 0 & 0.2271 \\ 0.2157 & 0 & 0 & 0 & 0 & 0 & 0 & 0 & 0.4300 & 0 & 0.1771 & 0 & 0.1771 & 0 & 0 \\ 0 & 0.2500 & 0 & 0 & 0 & 0 & 0 & 0 & 0.2500 & 0 & 0 & 0.2500 & 0 & 0.2500 & 0 \\ 0 & 0 & 0.0729 & 0 & 0 & 0 & 0 & 0 & 0.0729 & 0 & 0.6857 & 0.0843 & 0 & 0 & 0.0843 \\ 0 & 0 & 0 & 0.1657 & 0 & 0 & 0 & 0 & 0 & 0 & 0.1657 & 0.4414 & 0 & 0 & 0.2271 \\ 0 & 0 & 0 & 0 & 0.0729 & 0 & 0 & 0 & 0.0729 & 0 & 0 & 0.6857 & 0.0843 & 0.0843 & 0 \\ 0 & 0 & 0 & 0 & 0 & 0.1657 & 0 & 0 & 0 & 0 & 0 & 0.1657 & 0.4414 & 0 & 0.2271 \\ 0 & 0 & 0 & 0 & 0 & 0 & 0 & 0 & 0 & 0 & 0.1657 & 0 & 0.1657 & 0 & 0.4414 \\ 0 & 0 & 0 & 0 & 0 & 0 & 0 & 0.0229 & 0 & 0 & 0 & 0.0229 & 0 & 0.0229 & 0.9086 \end{bmatrix}$$

Figure 2.20: Transition matrix for the example Gibbs sampler.

It is notable that two states (7 and 10) have no probability of being visited from any other state, and so these two states are clearly transient, as they can only occur as the initial state and will never be visited again by the Markov chain. These two states are those for which the diagonal locations have the same facies; that arrangement disagrees with the structure suggested by the covariance model and therefore the transience of these states is sensible. The properties of the other states are less clear.

Taking the limit in Equation 2.30 for the transition matrix, the stationary distribution,  $f(X)$ , of the Markov chain can be calculated. Table 2.4 shows the stationary joint

distribution. States 7 and 10 do indeed have zero probability in the full joint distribution and are therefore transient as mentioned above. The states with higher proportions of black values always have higher frequencies than the opposite states with higher proportions of white values due to the different global univariate proportions.

Table 2.4: Stationary distribution of the multi-dimensional Gibbs sampler example.

Class	Frequency
1	0.1689
2	0.0268
3	0.0268
4	0.0653
5	0.0268
6	0.0653
7	0
8	0.0332
9	0.0268
10	0
11	0.0653
12	0.0332
13	0.0653
14	0.0332
15	0.0332
16	0.3299

The limiting distribution in Table 2.4 is for an unconditional simulation, that is, there are no conditioning data. In earth sciences applications there are always some data, and one important data type is hard conditioning data from core samples, drillholes, or another analytical sampling method. A Gibbs sampler can easily accommodate conditioning data by freezing the appropriate locations. Figure 2.21 shows a state space for the same simulated domain as that shown in Figure 2.18, but with the upper left location frozen as facies 1 (white). Only odd-numbered classes can occur with this particular conditioning datum, as shown in Figure 2.21.

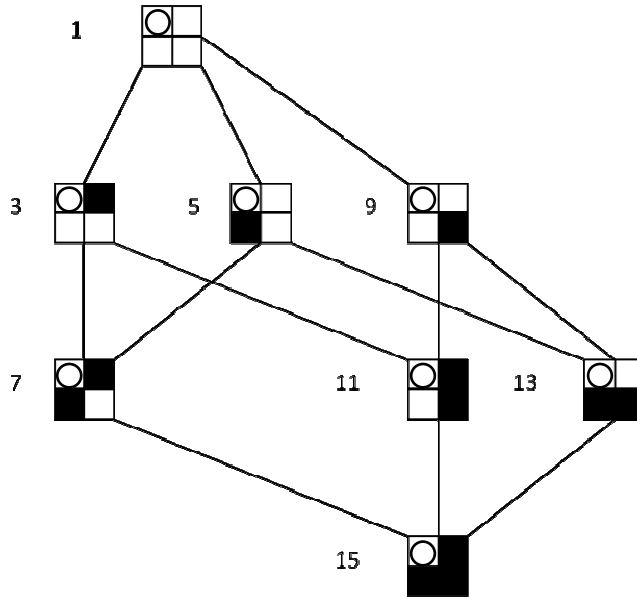


Figure 2.21: The state space of the conditional example with the upper left corner frozen as facies 1 (white).

The transition probabilities are the same as for the previous example; however, if the upper left location is selected to be modified it must always end up as white. An alternative is to set it as white and never modify that location, but considering all 16 states allows a demonstration of transient states. Figure 2.22 shows the new transition matrix for the conditional simulation case.

$$P_{\alpha\beta} = \begin{bmatrix} 0.8971 & 0 & 0.0343 & 0 & 0.0343 & 0 & 0 & 0 & 0.0343 & 0 & 0 & 0 & 0 & 0 & 0 & 0 \\ 0.2500 & 0.3957 & 0 & 0.1771 & 0 & 0.1771 & 0 & 0 & 0 & 0 & 0 & 0 & 0 & 0 & 0 & 0 \\ 0.2157 & 0 & 0.6072 & 0 & 0 & 0 & 0 & 0 & 0 & 0 & 0.1771 & 0 & 0 & 0 & 0 & 0 \\ 0 & 0.0729 & 0.2500 & 0.5086 & 0 & 0 & 0 & 0.0843 & 0 & 0 & 0.0843 & 0 & 0 & 0 & 0 & 0 \\ 0.2157 & 0 & 0 & 0 & 0.6072 & 0 & 0 & 0 & 0 & 0 & 0 & 0.1771 & 0 & 0 & 0 & 0 \\ 0 & 0.0729 & 0 & 0 & 0.2500 & 0.5086 & 0 & 0.0843 & 0 & 0 & 0 & 0 & 0 & 0.8429 & 0 & 0 \\ 0 & 0 & 0.2500 & 0 & 0.2500 & 0 & 0.2500 & 0 & 0 & 0 & 0 & 0 & 0 & 0 & 0.2500 & 0 \\ 0 & 0 & 0 & 0.1657 & 0 & 0.1657 & 0.2500 & 0.1914 & 0 & 0 & 0 & 0 & 0 & 0 & 0 & 0.2271 \\ 0.2157 & 0 & 0 & 0 & 0 & 0 & 0 & 0 & 0.4300 & 0 & 0.1771 & 0 & 0.1771 & 0 & 0 & 0 \\ 0 & 0.2500 & 0 & 0 & 0 & 0 & 0 & 0 & 0.2500 & 0 & 0 & 0.2500 & 0 & 0.2500 & 0 & 0 \\ 0 & 0 & 0.0729 & 0 & 0 & 0 & 0 & 0 & 0.0729 & 0 & 0.7700 & 0 & 0 & 0 & 0.0843 & 0 \\ 0 & 0 & 0 & 0.1657 & 0 & 0 & 0 & 0 & 0 & 0 & 0.2500 & 0.3572 & 0 & 0 & 0 & 0.2271 \\ 0 & 0 & 0 & 0 & 0.0729 & 0 & 0 & 0 & 0.0729 & 0 & 0 & 0 & 0.7700 & 0 & 0.0843 & 0 \\ 0 & 0 & 0 & 0 & 0 & 0.1657 & 0 & 0 & 0 & 0 & 0 & 0 & 0.2500 & 0.3572 & 0 & 0.2271 \\ 0 & 0 & 0 & 0 & 0 & 0 & 0 & 0 & 0 & 0 & 0.1657 & 0 & 0.1657 & 0 & 0.6686 & 0 \\ 0 & 0 & 0 & 0 & 0 & 0 & 0 & 0.0229 & 0 & 0 & 0 & 0.0229 & 0 & 0.0229 & 0.2500 & 0.6814 \end{bmatrix}$$

Figure 2.22: Transition matrix for the example conditional Gibbs sampler.

Because of the conditioning datum all even-numbered states must be transient; however, it is possible for the chain to remain in the transient states for some time, moving from one transient state to another before entering the recurring class of the odd-numbered states. Table 2.5 shows the results of taking the limit in Equation 2.30 for the conditional example. All of the even-numbered states are indeed transient and over a long enough time the chain will leave those states and never return to that part of the state space. State 7 is also transient, as it was for the unconditional example.

Table 2.5: Stationary distribution of the conditional multi-dimensional Gibbs sampler example.

Class	Frequency
1	0.4088
2	0
3	0.065
4	0
5	0.065
6	0
7	0
8	0
9	0.065
10	0
11	0.158
12	0
13	0.158
14	0
15	0.0804
16	0

#### 2.4.4 Markov Random Fields

The example in Section 2.4.3 demonstrates a very small case. Real models of geology are much larger and more complex: there are often on the order of  $10^6$  cells in a geomodel and each cell has an assigned facies value. The probability of moving from one state to another should theoretically be the full conditional probability of the facies at one location given the current facies at all other locations as per Equation 2.37.

The full conditional distributions are of an order only one less than the full joint distribution of all locations. To reduce the dimension of the statistics to a manageable

level that is both inferable and useable, the concept of Markov random fields can be used (Kindermann and Snell, 1980). In a Markov random field, the Markov property (Equation 2.25) is applied spatially rather than in time. If a variable  $X$  has a number of dimensions as in Equation 2.36 and these dimensions are distributed spatially, then the conditional distribution of a single dimension or location is only dependent on those nearby locations:

$$f(x_i | x_j, j \in A, j \neq i) = f(x_i | x_j, j \in \partial i, \partial i \in A) \quad (2.42)$$

In Equation 2.42 the part of variable  $X$  being considered is at location  $i$ ;  $A$  is the entire area covered by  $X$ ; and  $\partial i$  is the local neighbourhood around location  $i$ . This is similar in principle to the Markov property in Equation 2.25 in that information can be disregarded without changing the conditional distribution. Rather than separation in time, the information separated from  $i$  in space is ignored. Figure 2.23 shows an example of a Markov random field.

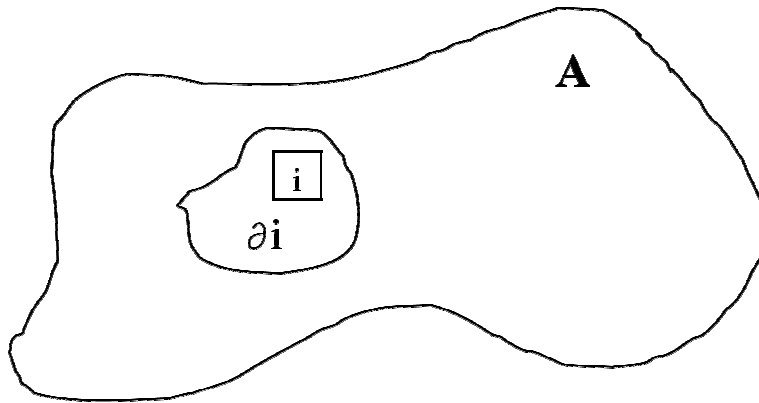


Figure 2.23: An example of a Markov random field in area  $A$  with point of interest  $i$  and local neighbourhood  $\partial i$ .

The concept of Markov random fields is used implicitly in many geostatistical algorithms. The use of limited search radii when finding scattered data in a sequential algorithm is a common practice (Deutsch and Journel, 1998). Discarding data outside a limited radius amounts to the implicit assumption of a Markov random field (Journel and Huijbregts, 1978).

## 3 MPS-GS Theory

The application of a Gibbs sampler (GS) to earth sciences problems requires a number of modeling decisions. The determination of conditional distributions, inference of statistics used, and selection of the initial states are all important considerations in a Gibbs sampler. Using multiple-point statistics (MPS) in a GS can lead to problems with storage of information caused by dimensionality (Strebelle, 2002), selection of an MPS template (Barrera et al, 2004), and the measurement of how well MPS are reproduced.

This chapter develops the theory for an algorithm, called MPS-GS, that has been implemented to use MPS in a GS framework. The conditional distributions used in MPS-GS are presented in Section 3.1. Section 3.2 discusses statistical inference from a training image (TI). Section 3.3 shows an example of the inference and use of MPS to determine conditional distributions. Section 3.4 discusses the topic of initial states in MPS-GS. Section 3.5 provides a framework for the use of multiple-point patterns in the MPS-GS algorithm.

### 3.1 Conditional Distributions

The transition matrix of a GS for earth science applications is largely controlled by the conditional distributions used by the algorithm. Using simple statistics such as univariate proportions and variograms will produce transition probabilities that result in simulated images that have low-order structure. Sequential algorithms exist (see Chapter 2) that can reproduce such structure, negating the need for an iterative method.

Higher-order statistics (i.e. MPS) can be used to determine the conditional distributions in a GS; that is the goal of this thesis. Within the framework of a GS on a Cartesian grid, it is not necessary to search for nearby data or consider different configurations; this lends itself naturally to the use of templates for calculating statistics,

storing information, and determining conditional distributions. A limited template size can be justified by assuming a Markov random field where the template is the local neighbourhood  $\partial i$ . A decision must be made on how to best use a MPS template for calculating conditional distributions.

One such possible decision is to use a single normal equation and Bayes' Law (see Equation 2.21) in a similar manner to SNESIM. This conditional distribution would result in realizations that honour the MPH of the template. A problem that arises when using this approach is the dimensionality of a MPH for large MPS templates.

For a simulation with  $K$  facies and an MPS template with  $N$  points, there are  $K^N$  classes in the MPH. A training image can provide at most  $N_{ti}$  occurrences of MPH classes. If the TI size is on the order of  $N_{ti}=10^6$ , there are  $K=3$  facies, and  $N=40$  points in the template, then at most only one in every  $1.21 \times 10^{13}$  MPH classes could be informed. In a sequential algorithm this problem is avoided by using only a limited number of surrounding data points (not filling the entire template) and dropping the furthest data locations in cases where the data configuration is not seen in any informed MPH class.

In an iterative algorithm such as a GS every location is informed and therefore there are no data configuration issues. This is one of the main advantages of iterative methods (Srivastava, 1992). Starting from a random initial state the vast majority of the MPH classes seen in a simulated realization will not show any quantifiable structure, and will not occur in the TI. Figure 3.1 shows an example of a 24-point MPH class that does not display any patterns that are commonly associated with geological structure. Points could be dropped similar to SNESIM to reduce the dimension of the statistics until the lower-order MPH class is informed; the problem with this approach is that the dimension of the statistic must be reduced so much that little of the high-order structure is preserved, and it is difficult to determine the final order of the statistics that are being reproduced.

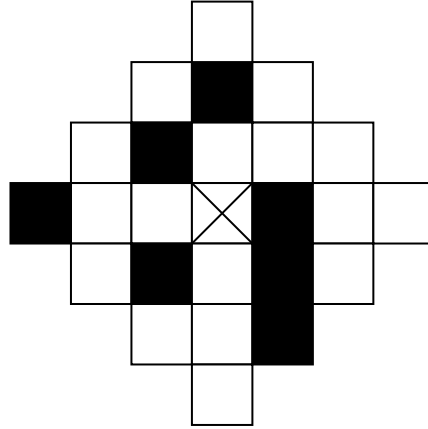


Figure 3.1: A single class for a 24-point MPH that shows no discernible geological structure.

The solution proposed in this thesis is to divide a MPS template into a number,  $M$ , of discrete multiple-point events (MPEs), each containing  $N$  points. Each MPE contains lower-order information than an entire MPS template and is easier to infer from a TI. A number of MPEs considered together can be used to introduce high-order structure into the transition probabilities of a GS.

### 3.1.1 Multiple-Point Events

A multiple-point event is defined here as a discrete set of  $N$  points distributed spatially within a MPS template. Figure 3.2 shows an example of a 24-point template, with the same arrangement of facies as in Figure 3.1, broken down into  $M=6$  discrete MPEs with  $N=4$ .

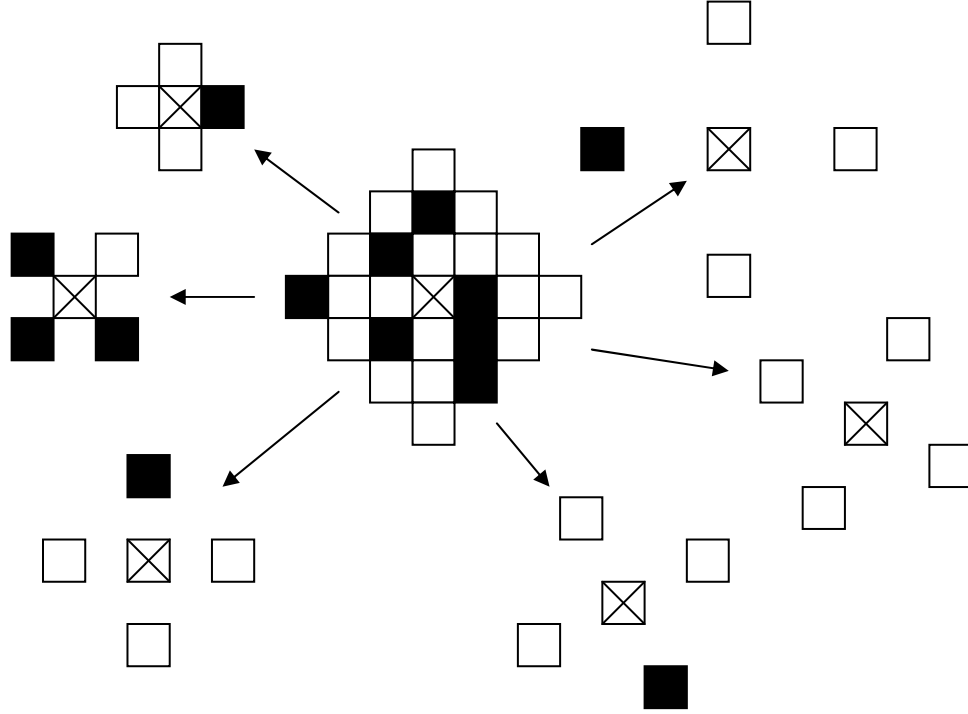


Figure 3.2: A 24-point MPH class (center) and six discrete multiple-point events containing the same data.

A MPE can be used as a template for calculating a MPH, and the indicators of the MPH classes used as data for estimating a conditional probability of a facies:

$$P^*(k) = P(k) + \sum_{i=1}^M \sum_{\alpha=1}^{K^N} \lambda_{i,\alpha}^k \cdot [I(E_i^\alpha) - P(E_i^\alpha)] \quad (3.1)$$

In Equation 3.1,  $P^*(k)$  is the estimated probability of facies  $k$  given the nearby data;  $P(k)$  is the global probability of facies  $k$ ;  $E_i^\alpha$  represents class  $\alpha$  of MPE  $i$ ;  $M$  is the number of MPEs used in the estimate;  $N$  is the number of points in each MPE;  $I(E_i^\alpha)$  is the indicator of  $E_i^\alpha$  occurring;  $P(E_i^\alpha)$  is the global probability of  $E_i^\alpha$ ; and  $\lambda_{i,\alpha}^k$  is the linear weight assigned to  $E_i^\alpha$ . Equation 3.1 is a linear estimate similar to the simple indicator kriging estimate (Equation 2.14) but uses non-linear data (i.e. MPEs) rather than the indicators of univariate information.

The error variance of an estimated facies probability found using Equation 3.1 can be calculated, as is the case for any linear estimate:

$$\sigma_E^2 = E \left\{ \left[ \sum_{i=1}^M \sum_{\alpha=1}^{K^N} \lambda_{i,\alpha}^k \cdot [I(E_i^\alpha) - P(E_i^\alpha)] - [I(k) - P(k)] \right]^2 \right\} - \left[ E \left\{ \sum_{i=1}^M \sum_{\alpha=1}^{K^N} \lambda_{i,\alpha}^k \cdot [I(E_i^\alpha) - P(E_i^\alpha)] - [I(k) - P(k)] \right\} \right]^2 \quad (3.2)$$

Expanding the squared terms in Equation 3.2, the error variance then becomes:

$$\begin{aligned} \sigma_E^2 = E & \left\{ \sum_{i=1}^M \sum_{\alpha=1}^{K^N} \sum_{j=1}^M \sum_{\beta=1}^{K^N} \lambda_{i,\alpha}^k \lambda_{j,\beta}^k \cdot [I(E_i^\alpha) - P(E_i^\alpha)] \cdot [I(E_j^\beta) - P(E_j^\beta)] \right\} \\ & - 2 \cdot E \left\{ \sum_{i=1}^M \sum_{\alpha=1}^{K^N} \lambda_{i,\alpha}^k \cdot [I(E_i^\alpha) - P(E_i^\alpha)] \cdot [I(k) - P(k)] \right\} \\ & + E \left\{ [I(k) - P(k)]^2 \right\} \end{aligned} \quad (3.3)$$

Taking the expected values and changing the notation to probabilities then gives:

$$\begin{aligned} \sigma_E^2 = & \sum_{i=1}^M \sum_{\alpha=1}^{K^N} \sum_{j=1}^M \sum_{\beta=1}^{K^N} \lambda_{i,\alpha}^k \lambda_{j,\beta}^k \cdot [P(E_i^\alpha \cap E_j^\beta) - P(E_i^\alpha) \cdot P(E_j^\beta)] \\ & - 2 \cdot \sum_{i=1}^M \sum_{\alpha=1}^{K^N} \lambda_{i,\alpha}^k \cdot [P(E_i^\alpha \cap k) - P(E_i^\alpha) \cdot P(k)] \\ & + [P(k) - P(k)^2] \end{aligned} \quad (3.4)$$

To find the optimal linear estimation weights using Equation 3.4, it is necessary to first define the multiple-point covariance:

$$\begin{aligned} Cov\{E_i^\alpha, E_j^\beta\} &= E\{I(E_i^\alpha) \cdot I(E_j^\beta)\} - E\{I(E_i^\alpha)\} \cdot E\{I(E_j^\beta)\} \\ &= P(E_i^\alpha \cap E_j^\beta) - P(E_i^\alpha) \cdot P(E_j^\beta) \end{aligned} \quad (3.5)$$

A MP covariance is similar to an indicator covariance or cross-covariance, but is generalized to allow for MPEs. If each event has only a single point then Equation 3.5 becomes the definition of an indicator covariance for a defined lag. A MP covariance is a spatial statistic of order  $2N$ . It is also possible to define the covariance between a MPE and a single-point indicator, a statistic of order  $N+1$ :

$$\begin{aligned} Cov\{E_i^\alpha, k\} &= E\{I(E_i^\alpha) \cdot I(k)\} - E\{I(E_i^\alpha)\} \cdot E\{I(k)\} \\ &= P(E_i^\alpha \cap k) - P(E_i^\alpha) \cdot P(k) \end{aligned} \quad (3.6)$$

Substituting MP covariances into Equation 3.4,

$$\sigma_E^2 = \sum_{i=1}^M \sum_{\alpha=1}^{K^N} \sum_{j=1}^M \sum_{\beta=1}^{K^N} \lambda_{i,\alpha}^k \lambda_{j,\beta}^k \cdot Cov\{E_i^\alpha, E_j^\beta\} - 2 \cdot \sum_{i=1}^M \sum_{\alpha=1}^{K^N} \lambda_{i,\alpha}^k \cdot Cov\{E_i^\alpha, k\} + \sigma_k^2 \quad (3.7)$$

Equation 3.7 is a quadratic function with the linear estimation weights as the independent variables. If the MP covariance model used is positive definite then there exists a unique global minimum to Equation 3.7. To minimize the function value, the partial derivatives with respect to all of the linear weights can be taken:

$$\frac{\partial \sigma_E^2}{\partial \lambda_{i,\alpha}^k} = 2 \cdot \sum_{j=1}^M \sum_{\beta=1}^{K^N} \lambda_{j,\beta}^k \cdot Cov\{E_i^\alpha, E_j^\beta\} - 2 \cdot Cov\{E_i^\alpha, k\} \quad i = 1, \dots, M, \quad \alpha = 1, \dots, K^N \quad (3.8)$$

The point at which the partial derivatives are all zero gives the global minimum for the error variance:

$$\frac{\partial \sigma_E^2}{\partial \lambda_{i,\alpha}^k} = 0 \quad \forall i, \alpha \quad (3.9)$$

Setting Equation 3.8 equal to zero and rearranging gives a system of linear equations:

$$\sum_{j=1}^M \sum_{\beta=1}^{K^N} \lambda_{j,\beta}^k \cdot Cov\{E_i^\alpha, E_j^\beta\} = Cov\{E_i^\alpha, k\} \quad i = 1, \dots, M, \quad \alpha = 1, \dots, K^N \quad (3.10)$$

The Equations 3.10 are a system with  $MK^N$  equations and unknowns. Solving the system and substituting the optimal weights back into Equation 3.1 results in an optimal linear estimate using the MPEs as defined in the given MPS template.

### 3.1.2 Relation to the Single Normal Equation

The MPE estimator in Equation 3.1 provides a way of linking the linear estimates in traditional covariance- or variogram-based geostatistics with the concept of high-order statistical moments. This approach is similar to the justification of the use of a SNE for calculating conditional distributions. If only a single MPE is in the template ( $M=1$ ) and only the MPH class  $\alpha$  that is seen in the nearby data is used as conditioning information ( $I(E_i^\alpha)=1$ ), then the estimate in Equation 3.1 becomes (Strebelle and Journel, 2001):

$$P^*(k) = P(k) + \lambda_{i,\alpha}^k \cdot \left[ 1 - P(E_i^\alpha) \right] \quad (3.11)$$

There is only a single data point and a single linear weight in this case. The system of Equations 3.10 is then only one equation with one unknown:

$$\lambda_{i,\alpha}^k \cdot Cov\{E_i^\alpha, E_i^\alpha\} = Cov\{E_i^\alpha, k\} \quad (3.12)$$

It is a simple matter of rearranging Equation 3.12 and using the definition of a multiple-point covariance to find the value of  $\lambda_{i,\alpha}^k$ :

$$\begin{aligned} \lambda_{i,\alpha}^k &= \frac{Cov\{E_i^\alpha, k\}}{Cov\{E_i^\alpha, E_i^\alpha\}} = \frac{P(E_i^\alpha \cap k) - P(E_i^\alpha) \cdot P(k)}{P(E_i^\alpha \cap E_i^\alpha) - P(E_i^\alpha) \cdot P(E_i^\alpha)} \\ &= \frac{P(E_i^\alpha \cap k) - P(E_i^\alpha) \cdot P(k)}{[1 - P(E_i^\alpha)] \cdot P(E_i^\alpha)} \end{aligned} \quad (3.13)$$

Substituting the linear weight in Equation 3.13 back into Equation 3.11, the estimate for the probability of facies  $k$  becomes:

$$\begin{aligned} P^*(k) &= P(k) + \frac{P(E_i^\alpha \cap k) - P(E_i^\alpha) \cdot P(k)}{[1 - P(E_i^\alpha)] \cdot P(E_i^\alpha)} \cdot [1 - P(E_i^\alpha)] \\ &= P(k) + \frac{P(E_i^\alpha \cap k) - P(E_i^\alpha) \cdot P(k)}{P(E_i^\alpha)} \\ &= P(k) + \frac{P(E_i^\alpha \cap k)}{P(E_i^\alpha)} - \frac{P(E_i^\alpha) \cdot P(k)}{P(E_i^\alpha)} \\ &= \frac{P(E_i^\alpha \cap k)}{P(E_i^\alpha)} \end{aligned} \quad (3.14)$$

This is the definition of the SNE as shown in Equation 2.21.

### 3.1.3 Properties of the Conditional Distributions

The estimated conditional distributions in Equation 3.1 have a number of mathematical properties that must be considered when solving the system of Equations 3.10. The first of these properties involves the summation of all MPH classes for a given MPE:

$$\sum_{\alpha=1}^{K^N} P(E_i^\alpha) = 1 \quad (3.15)$$

The sum of the probabilities of all combinations of facies  $\alpha$  in a given spatial configuration  $i$  is always equal to one. Some combination of facies must exist for each configuration. Another property involves the joint probability of two MPEs:

$$\sum_{\alpha=1}^{K^N} P(E_i^\alpha \cap E_j^\beta) = P(E_j^\beta) \quad (3.16)$$

In words, Equation 3.16 states that for a defined configuration of facies  $\beta$  in spatial arrangement  $j$ , some configuration of facies  $\alpha$  must always occur at the spatial locations defined by MPE  $i$ . Using the properties in Equations 3.15 and 3.16,

$$\begin{aligned} \sum_{\alpha=1}^{K^N} Cov\{E_i^\alpha, E_j^\beta\} &= \sum_{\alpha=1}^{K^N} P(E_i^\alpha \cap E_j^\beta) - \sum_{\alpha=1}^{K^N} P(E_i^\alpha) \cdot P(E_j^\beta) \\ &= P(E_j^\beta) - P(E_j^\beta) \cdot \sum_{\alpha=1}^{K^N} P(E_i^\alpha) \\ &= P(E_j^\beta) - P(E_j^\beta) \cdot 1 \\ &= 0 \end{aligned} \quad (3.17)$$

This shows that the sum of all MP covariances involving a specific class for one MPE must be zero; positive covariances must be balanced by negative covariances. A similar property is held for the covariances between MPEs and single-point indicators:

$$\begin{aligned} \sum_{k=1}^K Cov\{E_i^\alpha, k\} &= \sum_{k=1}^K P(E_i^\alpha \cap k) - \sum_{k=1}^K P(E_i^\alpha) \cdot P(k) \\ &= P(E_i^\alpha) - P(E_i^\alpha) \cdot \sum_{k=1}^K P(k) \\ &= P(E_i^\alpha) - P(E_i^\alpha) \cdot 1 \\ &= 0 \end{aligned} \quad (3.18)$$

Recalling the system of Equations 3.10 and using the properties in Equations 3.17 and 3.18, it can be shown that the sum of the linear weights given to a particular class  $\beta$  of one MPE  $j$  is zero:

$$\begin{aligned} \sum_{j=1}^M \sum_{\beta=1}^{K^N} \lambda_{j,\beta}^k \cdot Cov\{E_i^\alpha, E_j^\beta\} &= Cov\{E_i^\alpha, k\} \\ \sum_{k=1}^K \sum_{j=1}^M \sum_{\beta=1}^{K^N} \lambda_{j,\beta}^k \cdot Cov\{E_i^\alpha, E_j^\beta\} &= \sum_{k=1}^K Cov\{E_i^\alpha, k\} \\ \sum_{j=1}^M \sum_{\beta=1}^{K^N} Cov\{E_i^\alpha, E_j^\beta\} \cdot \sum_{k=1}^K \lambda_{j,\beta}^k &= 0 \\ \sum_{k=1}^K \lambda_{j,\beta}^k &= 0 \end{aligned} \quad (3.19)$$

This property is useful for checking the solutions for the optimal weights; any positive weights assigned to a MPE class must be exactly offset by negative weights. It

also makes logical sense: if a specified event  $E_i^\alpha$  suggests the presence of one facies (i.e. adds to the probability by a positive weight) then it inherently suggests that some other facies must be less likely to occur. Taking the property in Equation 3.19 for all facies, it can be shown that the sum of all of the estimates from Equation 3.1 is one:

$$\begin{aligned}
\sum_{k=1}^K P^*(k) &= \sum_{k=1}^K P(k) + \sum_{k=1}^K \sum_{i=1}^M \sum_{\alpha=1}^{K^N} \lambda_{i,\alpha}^k \cdot [I(E_i^\alpha) - P(E_i^\alpha)] \\
&= 1 + \sum_{i=1}^M \sum_{\alpha=1}^{K^N} [I(E_i^\alpha) - P(E_i^\alpha)] \cdot \sum_{k=1}^K \lambda_{i,\alpha}^k \\
&= 1
\end{aligned} \tag{3.20}$$

Although the sum must be one there is no constraint that the estimated probabilities  $P^*(k)$  are between zero and one.

### 3.1.4 Singularity of the System

Equation 3.17 shows that the system of Equations 3.10 must be a singular system; there are  $MK^N$  equations and variables, but only at most  $M(K^N-1)$  independent variables as the sum of any  $K^N-1$  covariances (or weights) for any MPE is equal to zero minus the remaining covariance (or weight). The quadratic function in Equation 3.7 is positive semidefinite and there are an infinite number of solutions to the system of Equations 3.10 (Anderson et al, 1999). The system of equations cannot be solved by the typical means such as Gaussian elimination (Deutsch and Journel, 1998). A resolution of this problem can be found by looking at the system of equations in matrix form.

### Matrix Form of the Equations

Recall the system of Equations 3.10:

$$\sum_{j=1}^M \sum_{\beta=1}^{K^N} \lambda_{j,\beta}^k \cdot Cov\{E_i^\alpha, E_j^\beta\} = Cov\{E_i^\alpha, k\} \quad i = 1, \dots, M, \quad \alpha = 1, \dots, K^N$$

The left-hand-side [LHS] covariances of the system of equations can be expressed as a symmetric  $MK^N$ -by- $MK^N$  matrix:

$$\begin{aligned}
& \left[ \begin{array}{c} LHS \end{array} \right] = \\
& \left[ \begin{array}{ccc|ccc}
Cov\{E_1^1, E_1^1\} & \cdots & Cov\{E_1^1, E_1^{K^N}\} & & Cov\{E_1^1, E_M^1\} & \cdots & Cov\{E_1^1, E_M^{K^N}\} \\
\vdots & \ddots & \vdots & \cdots & \vdots & \ddots & \vdots \\
Cov\{E_1^{K^N}, E_1^1\} & \cdots & Cov\{E_1^{K^N}, E_1^{K^N}\} & & Cov\{E_1^{K^N}, E_M^1\} & \cdots & Cov\{E_1^{K^N}, E_M^{K^N}\} \\
\hline
& \vdots & & \ddots & & & \vdots \\
Cov\{E_M^1, E_1^1\} & \cdots & Cov\{E_M^1, E_1^{K^N}\} & & Cov\{E_M^1, E_M^1\} & \cdots & Cov\{E_M^1, E_M^{K^N}\} \\
\vdots & \ddots & \vdots & \cdots & \vdots & \ddots & \vdots \\
Cov\{E_M^{K^N}, E_1^1\} & \cdots & Cov\{E_M^{K^N}, E_1^{K^N}\} & & Cov\{E_M^{K^N}, E_M^1\} & \cdots & Cov\{E_M^{K^N}, E_M^{K^N}\}
\end{array} \right] \\
& \tag{3.21}
\end{aligned}$$

Each of the submatrices (separated by dashed lines) within the full [LHS] represents the covariances between all MPH classes of two particular MPEs, and each submatrix is  $K^N$ -by- $K^N$  with a rank no greater than  $K^N-1$ . An easier way to visualize the indices of [LHS] is shown below:

$$\begin{aligned}
& \begin{array}{c} \overbrace{\hspace{10em}}^{j=1,\dots,M} \\ \underbrace{\hspace{3em}}_{\beta=1,\dots,K^N} \quad \underbrace{\hspace{3em}}_{\beta=1,\dots,K^N} \quad \underbrace{\hspace{3em}}_{\beta=1,\dots,K^N} \end{array} \\
& \left\{ \begin{array}{l} \alpha = 1, \dots, K^N \\ \alpha = 1, \dots, K^N \\ \alpha = 1, \dots, K^N \end{array} \right\} \left[ \begin{array}{ccc|ccc}
\ddots & & \vdots & & \ddots & & \\
\cdots & & Cov\{E_i^\alpha, E_j^\beta\} & & \cdots & & \\
\ddots & & \vdots & & \ddots & & \\
\end{array} \right] \\
& \tag{3.22}
\end{aligned}$$

The [LHS] matrix is the same for all facies probabilities  $P(k)$ ,  $k=1,\dots,K$ . The right-hand-side [RHS] of Equation 3.10 is different for each facies; however, in matrix form a single [RHS] made up of  $K$  column vectors can be constructed:

$$\left[ \begin{array}{c} RHS \end{array} \right] = \left[ \begin{array}{c|c|c} \begin{array}{c} Cov\{E_1^1, 1\} \\ \vdots \\ Cov\{E_1^{K^N}, 1\} \\ \vdots \\ Cov\{E_M^1, 1\} \\ \vdots \\ Cov\{E_M^{K^N}, 1\} \end{array} & \begin{array}{c} \dots \\ \dots \\ \dots \end{array} & \begin{array}{c} Cov\{E_1^1, K\} \\ \vdots \\ Cov\{E_1^{K^N}, K\} \\ \vdots \\ Cov\{E_M^1, K\} \\ \vdots \\ Cov\{E_M^{K^N}, K\} \end{array} \end{array} \right] \quad (3.23)$$

The [RHS] matrix has size  $MK^N$ -by- $K$ ; each column is made up of the covariances between a single facies indicator and all MPE classes. The subvectors of [RHS] (separated by dashed lines in Equation 3.23) all sum to zero as per Equation 3.18. Equation 3.24 shows [RHS] in a form that makes it easier to visualize the indices:

$$\left. \begin{array}{l} \alpha = 1, \dots, K^N \\ \alpha = 1, \dots, K^N \\ \alpha = 1, \dots, K^N \end{array} \right\} \begin{array}{c} i = 1, \dots, M \left\{ \begin{array}{c|c|c} \begin{array}{c} \dots \\ \vdots \\ \dots \end{array} & \begin{array}{c} \dots \\ Cov\{E_i^\alpha, k\} \\ \dots \end{array} & \begin{array}{c} \dots \\ \vdots \\ \dots \end{array} \\ \hline \dots & Cov\{E_i^\alpha, k\} & \dots \\ \hline \begin{array}{c} \dots \\ \vdots \\ \dots \end{array} & \begin{array}{c} \dots \\ \vdots \\ \dots \end{array} & \begin{array}{c} \dots \\ \vdots \\ \dots \end{array} \end{array} \right. \quad (3.24)$$

The linear weights in Equation 3.10 can be expressed as a matrix the same size and shape as [RHS]:

$$\left[ \begin{array}{c} \lambda \end{array} \right] = \left[ \begin{array}{c|c|c} \begin{array}{c} \lambda_{1,1}^1 \\ \vdots \\ \lambda_{1,K^N}^1 \\ \vdots \\ \lambda_{M,1}^1 \\ \vdots \\ \lambda_{M,K^N}^1 \end{array} & \begin{array}{c} \dots \\ \dots \\ \dots \end{array} & \begin{array}{c} \lambda_{1,1}^K \\ \vdots \\ \lambda_{1,K^N}^K \\ \vdots \\ \lambda_{M,1}^K \\ \vdots \\ \lambda_{M,K^N}^K \end{array} \end{array} \right] \quad (3.25)$$

The size of this matrix is  $MK^N$ -by- $K$ . From Equation 3.19 each row of the weight matrix sums to zero, as opposed to the columns in [RHS]. Equation 3.26 shows the linear weight matrix with the indices labeled:



## Eigenvalue Decomposition

The [LHS] matrix is both real and symmetric; because of these properties, it is possible to break down [LHS] into its eigenvalues and eigenvectors (Anderson et al, 1999):

$$\begin{bmatrix} LHS \end{bmatrix} = \begin{bmatrix} V \end{bmatrix} \begin{bmatrix} \omega \end{bmatrix} \begin{bmatrix} V \end{bmatrix}^T \quad (3.33)$$

In Equation 3.33,  $[\omega]$  is a matrix of the same size as [LHS] with the diagonal entries being the eigenvalues of [LHS] and all other entries zero:

$$\begin{bmatrix} \omega \end{bmatrix} = \begin{bmatrix} \omega_1 & & 0 \\ & \ddots & \\ 0 & & \omega_{M \cdot K^N} \end{bmatrix} \quad (3.34)$$

As show by Equation 3.17, [LHS] is singular and has a rank no greater than  $M(K^N-1)$ . The singular matrix will therefore have at least  $M$  eigenvalues equal to zero. The number of eigenvalues that are equal to zero is exactly  $M$  if all MPH classes for all MPEs have non-zero probabilities; uninformed classes create null rows and columns in the matrix that are redundant information. If a large proportion of MPH classes are uninformed [LHS] will be very sparse and the redundant zero columns and rows may be dropped without changing its properties.

In Equation 3.33, the columns of [V] are the orthonormal eigenvectors of [LHS], meaning the vector lengths are equal to one and the transpose of V is also its inverse:

$$\begin{bmatrix} V \end{bmatrix} \begin{bmatrix} V \end{bmatrix}^T = \begin{bmatrix} I \end{bmatrix} \quad (3.35)$$

The inverse of [LHS] can be found by rearranging Equation 3.33:

$$\begin{bmatrix} LHS \end{bmatrix}^{-1} = \begin{bmatrix} V \end{bmatrix} \begin{bmatrix} 1/\omega \end{bmatrix} \begin{bmatrix} V \end{bmatrix}^T \quad (3.36)$$

In Equation 3.36, [V] and  $[V]^T$  are the same as in Equation 3.33; however, the middle term is the inverse of  $[\omega]$ . The inverse is found by taking the reciprocal of each diagonal term in the matrix and leaving the rest as zero:

$$\begin{bmatrix} 1/\omega \end{bmatrix} = \begin{bmatrix} 1/\omega_1 & & 0 \\ & \ddots & \\ 0 & & 1/\omega_{M \cdot K^N} \end{bmatrix} \quad (3.37)$$

The zeros in  $[\omega]$  are accounted for by leaving those terms as zero and not taking the reciprocal. This is similar to the procedure for singular value decomposition (Anderson et al, 1999) but using the symmetry of [LHS] to simplify the calculations. The solution to the matrix Equation 3.32 is then:

$$\begin{bmatrix} \lambda \end{bmatrix} = \begin{bmatrix} V \end{bmatrix} \begin{bmatrix} 1/\omega \end{bmatrix} \begin{bmatrix} V \end{bmatrix}^T \begin{bmatrix} RHS \end{bmatrix} \quad (3.38)$$

Because [LHS] is singular, there is no single inverse and thus there exist an infinite number of solutions of the optimal linear weights. The matrix procedure as outlined above produces the pseudoinverse of the system. A pseudoinverse is a solution to the system of equations that has the minimum norm of the resulting weights. The minimum norm property of this solution is desirable because it consequently avoids any extreme linear weights while minimizing the variance of the estimate. Other solutions are mathematically valid from a minimum-variance perspective but one cannot be justified over another in an objective way. The pseudoinverse solution is unique and because of the minimum-norm property is justifiable compared to any other solution.

The problem with uninformed MPH classes is solved by using this approach. Each uninformed class is represented in [LHS] as a row and column of zeros, reducing the rank of the matrix by one. Solving the linear estimation system using Equation 3.38 will result in weights of zero being assigned to uninformed classes; alternatively, these classes could be assigned weights of zero and excluded from the system to reduce the CPU and memory requirements. An optimal solution is still found using the reduced system and assigning uninformed classes weights of zero seems reasonable and is mathematically valid. An example of using the eigenvalue / singular value decomposition approach to solving the system of equations will be shown in Section 3.3.

### 3.1.5 Markov Random Fields

The MPS-GS algorithm uses the concept of Markov random fields (MRFs) primarily to justify using a limited search radius; however, there are several deviations from a true MRF. In a standard MRF application, a model is formulated and then sampled from using a MCMC method. A major difficulty is in determining the model parameters. In MPS-GS the conditional distributions are not explicitly defined by a model but rather are estimated as shown above; the least-squares approach differs from standard MRFs that use maximum likelihood estimators. This estimation approach reflects the uncertainty in the TI and the high-order statistics that are inferred. Uninformed MPH classes and conditional probabilities outside the interval [0,1] force approximations to be made that make the MPS-GS algorithm not a true MRF.

An implementation of Markov random fields was developed to use high-order statistical moments (Tjelmeland and Besag, 1998). That methodology uses the concept of cliques (similar to MPEs) to determine conditional probabilities of colours on a two-dimensional hexagonal grid, then simulates using the Metropolis-Hastings algorithm. Controlling the conditional probabilities is difficult and sensitive to selection of parameters. The MPS-GS algorithm takes a more practical approach at the expense of some theoretical rigor.

## 3.2 Statistical Inference

High-order spatial moments and MPS are too complex to infer directly from limited sample data. Training images, reviewed in Section 2.2.3, are used to calculate the necessary statistics such as the probabilities in Equation 3.1 and the MP covariances in Equation 3.10. As discussed above, the size of a TI  $N_{ti}$  is often significantly smaller than the number of combinations possible in a MPS template,  $K^N$ .

In practice, the full extents of the TI cannot be scanned using a MPS template and the effective size is less than  $N_{ti}$  locations. Because of the nature of a template with fixed size and shape, the template cannot go outside the grid. Figure 3.3 shows an example of this: the TI from Figure 2.6 is shown, with a five-point template superimposed in several locations. One template is too far to the right in the TI and cannot be used. Any template with its central location outside of the outlined square cannot be fully informed; the

square is the erosion limits of the TI for that template, or the border to which the TI may be scanned.

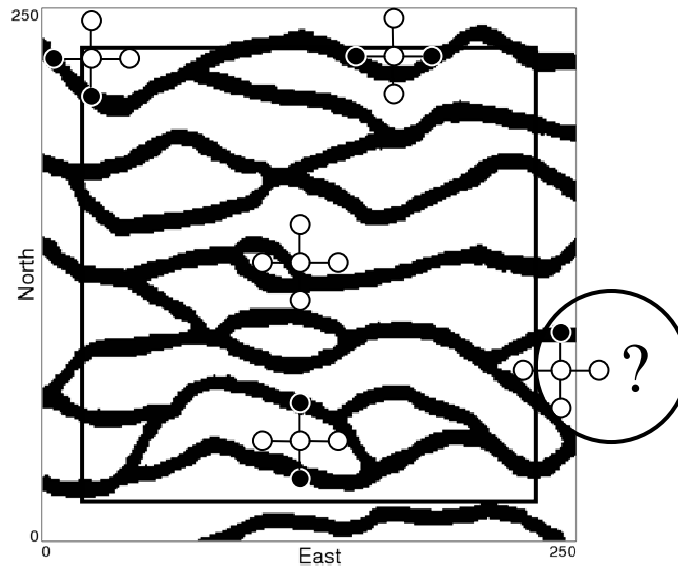


Figure 3.3: A channel-type TI with a number of five-point templates and the scanning border superimposed.

This erosion changes some of the statistics such as univariate proportions and MP covariances; not accounting for the edge effects causes the system of Equations 3.10 / 3.32 to be unstable and not necessarily positive semidefinite. Accounting for the edge effects entails using only those frequencies that are seen in the locations that can be scanned; this may lead to identically-shaped MPEs having different MPHs if different patterns occur near different edges of the TI.

Classes of MPEs that occur only once or twice in a TI may have significantly different frequencies if the edges are or are not accounted for. If multiple grids (Deutsch and Journel, 1998) are used in the simulation then the coarsest template may erode so much of the TI that there are insufficient locations remaining to inform the MP covariances.

### 3.2.1 Selection of the MPS Template

The template that is used for statistical inference and simulation is an important consideration. It is possible to use a simple ellipsoidal template (Liu, 2006); the

anisotropy can be changed to match the approximate anisotropy of the geometric features in the TI. As an alternative, it is possible to characterize the values of offsets within the template by some measure other than Euclidean distance: one possibility that has been explored elsewhere is covariances (Barrera et al, 2004; Eskandaridavand, 2008). The disadvantage of covariances is when there are more than two facies, weighting the different covariances and cross covariances or choosing a single facies to use for a representative template is an additional modeling decision.

For MPS-GS it is necessary not only to select  $MN$  points for the template but also to group the points into discrete events. In this thesis it is proposed to use spatial entropy (Journel and Deutsch, 1993) as a measure to characterize and rank locations at specified lag vectors, then build a template based on this measure. Entropy is a measure of spatial disorder, so higher entropy suggests more randomness and less spatial structure. Low entropy suggests more information content between two locations. For a specified lag vector  $\mathbf{u}$ , the two-point spatial entropy can be calculated as:

$$H_{\mathbf{u}} = -\sum_{k=1}^K \sum_{k'=1}^K P_{kk'} \cdot \ln(P_{kk'}) \quad (3.39)$$

In Equation 3.39,  $H_{\mathbf{u}}$  is the entropy of location  $\mathbf{u}$  in a template (or at lag vector  $\mathbf{u}$ ) and  $P_{kk'}$  is short form for  $P(k(\mathbf{u}_0)=k, k(\mathbf{u}_0+\mathbf{u})=k')$ , or the probability that the facies at the central location is  $k$  and the facies at offset  $\mathbf{u}$  is  $k'$ . At an offset of zero,  $P_{kk'}=P_k$  for  $k=k'$  and is zero otherwise. The minimum entropy occurs at an offset of zero. If  $k$  and  $k'$  are entirely unrelated, then  $P_{kk'}=P_k \cdot P_{k'}$  and the entropy is maximized at large offsets where there is no spatial relation. This is similar to zero correlation beyond the range of a variogram.

Entropy thus has minimum value at  $\mathbf{u}=0$  and maximum value at very large  $\mathbf{u}$ . These endpoints are the same as those for variogram values. Locations that are in between these two extremes can be sorted based on entropy, providing a ranking measure that does not depend on the number of facies or any weighting of components.

### 3.2.2 Examples

The left side of Figure 3.4 shows a simple conceptual TI made up of ten-by-ten black and white squares ( $K=2$ ); the right side shows a 21-by-21 square template, with the null offset in the center, and the spatial entropy of every location within the template. The maximum offsets are ten units in the X and/or Y directions, the same as the size of the squares; it

can be observed in the spatial entropy map that there is a repeating pattern in the image at that distance.

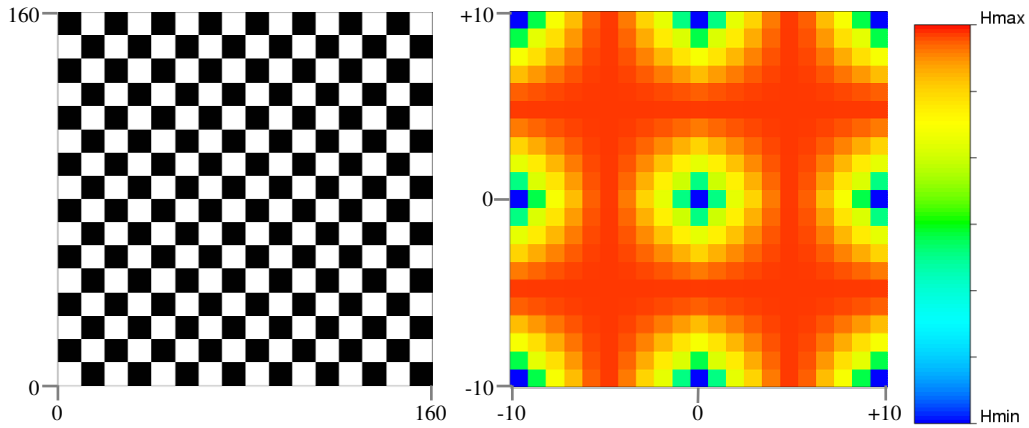


Figure 3.4: A simple 160x160 TI made up of 10x10 black and white squares (left); two-point spatial entropy of the TI in a 21-by-21 square template (right).

Figure 3.5 shows a more realistic case featuring a three-facies TI with a fluvial channel structure; and the map of two-point entropy for a 21-by-21 template, again with zero offset in the center of the template. The entropy map in Figure 3.5 shows strong east-west structure with shorter range north-south; there is also a slight northeast-southwest slant. An image with three (or more) facies does not present a problem when calculating spatial entropy.

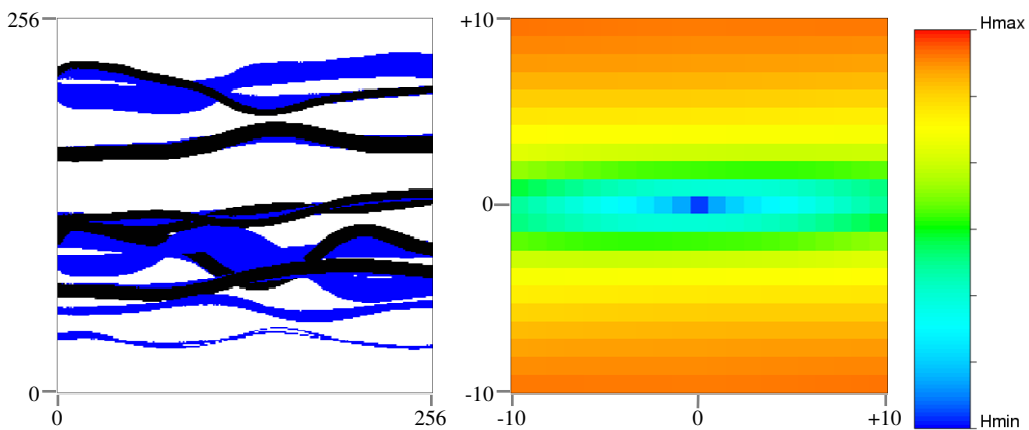


Figure 3.5: A 256x256 three-facies fluvial TI (left); two-point spatial entropy of the TI in a 21-by-21 square template (right).

In a fluvial TI such as the one shown in Figure 3.5, all of the facies have similar anisotropy. In more complex cases it is possible that there could be structures with significantly different geometries and directions of continuity. Figure 3.6 shows a TI with two very different ellipsoidal structures, and a 21-by-21 template of spatial entropies. The two ellipsoid structures are both captured and represented in the entropy map; both directions of anisotropy are visible.

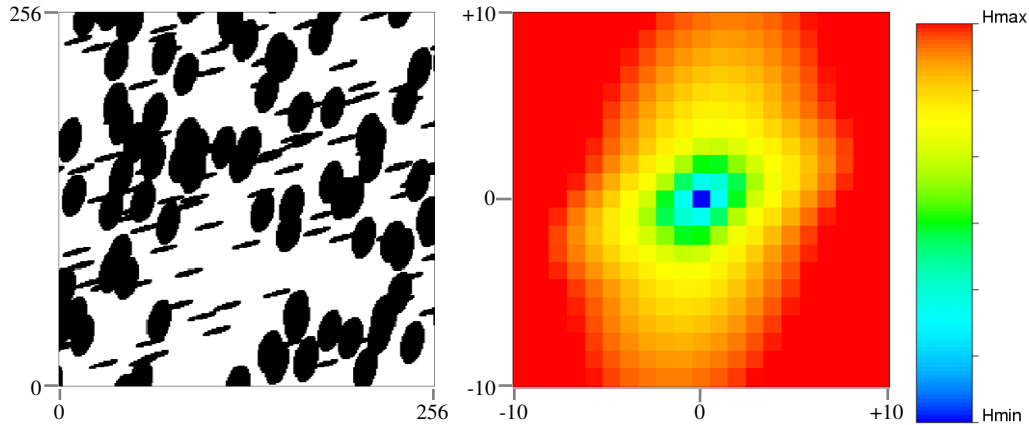


Figure 3.6: A 256x256 TI with two distinct ellipsoidal structures (left); two-point spatial entropy of the TI in a 21-by-21 square template (right).

Spatial entropy can be used for cases where different anisotropic structures are represented by different facies; Figure 3.7 shows such a case. The left side of Figure 3.7 is a complex TI with five facies, all with different anisotropies (Deutsch, 1992); the right side shows the entropies of the TI in a 21-by-21 template. Three of the facies have east-west structure, and this is seen in the entropy map. One facies has a very distinct northwest-southeast structure, and this is seen in the entropy map; points in the template that are northwest or southeast of the null vector contain significant information about whether or not the central location is likely to be the green facies.

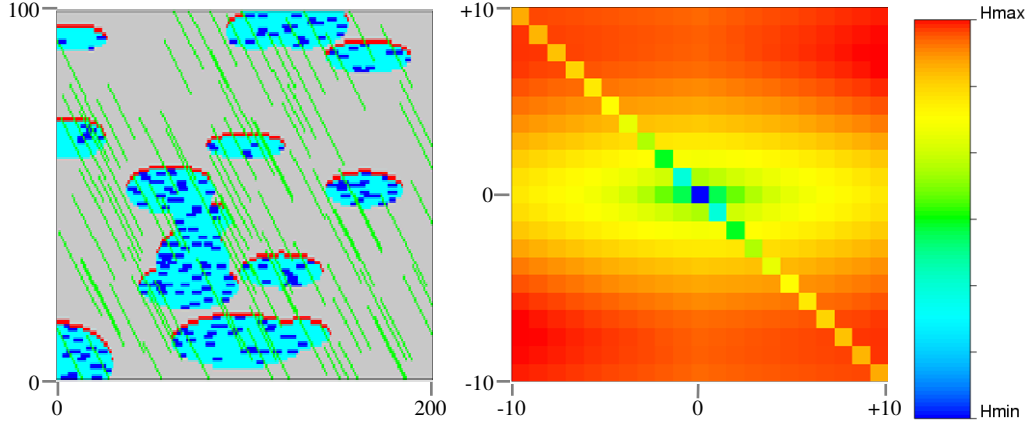


Figure 3.7: A 200x100 five-facies complex TI (Deutsch, 1992) (left); two-point spatial entropy of the TI in a 21-by-21 square template (right).

The examples shown above for the spatial entropy have used relatively simple two-point entropy. Spatial entropy can be extended to statistics in an  $N$ -point template by considering the MPH frequencies instead of two-point probabilities. The  $N$ -point entropy of a MPE  $i$  can be calculated as:

$$H_i = -\sum_{\alpha=1}^{K^N} P(E_i^\alpha) \cdot \ln \left[ P(E_i^\alpha) \right] \quad (3.40)$$

For classes  $\alpha$  in Equation 3.40 that have probabilities of zero, the logarithm function is undefined; the limit value of the entropy contribution is zero. Using the  $N$ -point entropy instead of two-point entropy accounts for the arrangement of points in a template instead of just individual locations one at a time. The  $N$ -point MPE containing the most information is not necessarily made up of the  $N$  points that have the lowest two-point entropy, and Equation 3.40 suggests a more robust measure for measuring MPE information content. An example of a template created using the MP spatial entropy will be shown in Section 3.3.

### 3.3 Example

This Section demonstrates the creation of MPEs with minimal entropy from a TI and the solution of the matrix equations using eigenvalue decomposition as outlined above. The TI that is used for the example has a fluvial channel structure with east-west continuity and three facies,  $K=3$  (background, channels, crevasse splays). The TI is very large ( $>10^6$  cells in two dimensions); this ensures full inference of all MPH classes. Figure 3.8 shows

a small section of the TI. The background (white) facies has a univariate proportion of approximately 0.5; the channel (black) facies 0.4; and the crevasse splay (blue) facies 0.1.

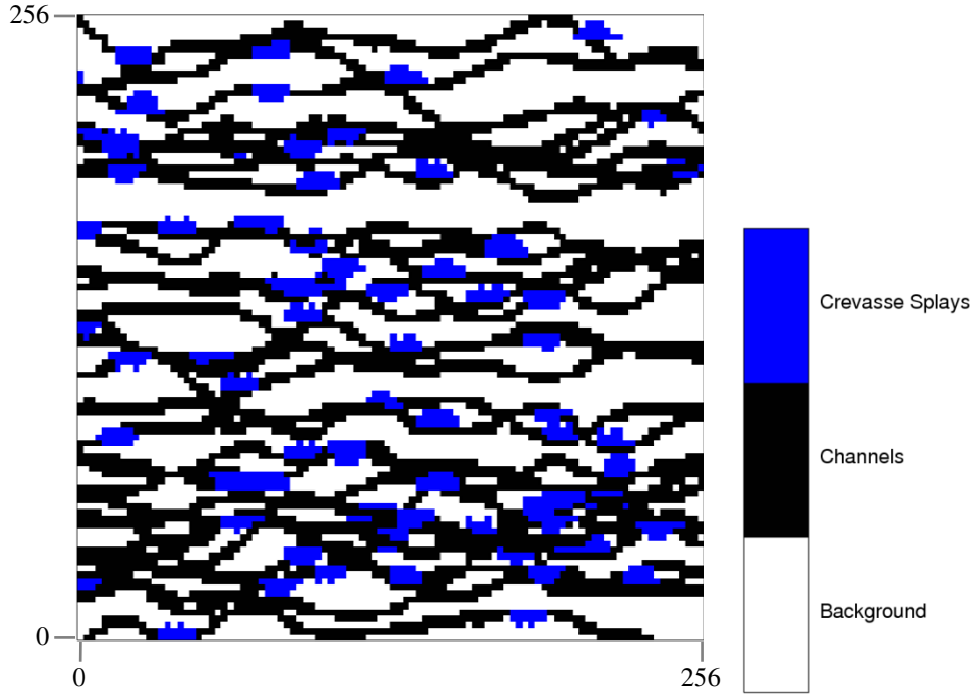


Figure 3.8: A section of the three-facies fluvial TI for the example.

For the example, four MPEs are used ( $M=4$ ) with four points each ( $N=4$ ). The total size of the linear system in Equations 3.10 / 3.32 is then  $MK^N=324$ . This size is large enough for the example but small enough to be manageable from a visualization and calculation perspective.

To use the  $N$ -point entropy shown in Equation 3.40, the offsets  $\mathbf{u}$  and  $-\mathbf{u}$  were retained that had the lowest three-point entropy when taken together with the null offset; then, the five-point entropy was calculated for the null offset, the two retained points, and a number of potential offsets (as well as their opposites). The MPEs after the first were calculated using the same procedure but not including any of the same offsets within the potential template. This does not guarantee minimum-entropy MPEs, but does ensure the minimum-entropy offsets are matched with optimal additional points. Figure 3.9 shows the four MPEs that were calculated from the TI using this method as well as the five-point entropy associated with each.

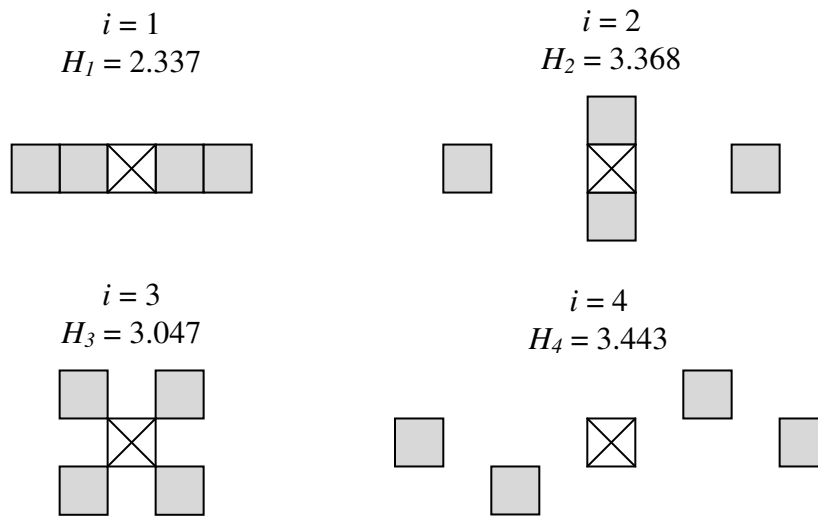


Figure 3.9: A MPS template of four, four-point MPEs for the example.

Each MPE has  $K^N=81$  possible combinations of facies; in this example all MPH classes are informed for all four MPEs. Figure 3.10 shows the MPHs of the four MPEs, with each MPH sorted from greatest to least class frequency for ease of visualization.

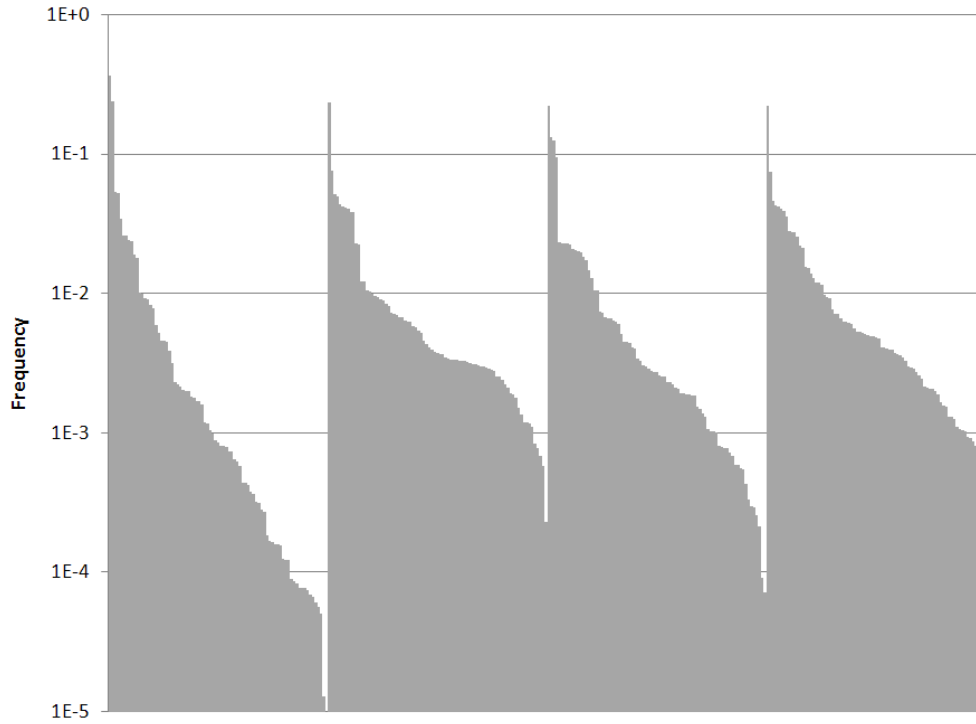


Figure 3.10: A graph of the four MPHs of the MPEs in the example, sorted from greatest to least frequencies.

The 324-by-324 [LHS] matrix of the system is calculated, and the rank of [LHS] found to be  $M(K^N-1)=320$  or exactly what is predicted as per the theory in Section 3.1.4. Four eigenvalues of [LHS] are exactly equal to zero and several more are very close to zero. Double precision real numbers had to be retained to produce the correct results; using single precision storage made the [LHS] matrix unstable. Figure 3.11 shows a graph of the eigenvalues of [LHS] sorted from greatest to least. The properties in Equations 3.17 and 3.18 are confirmed to be true.

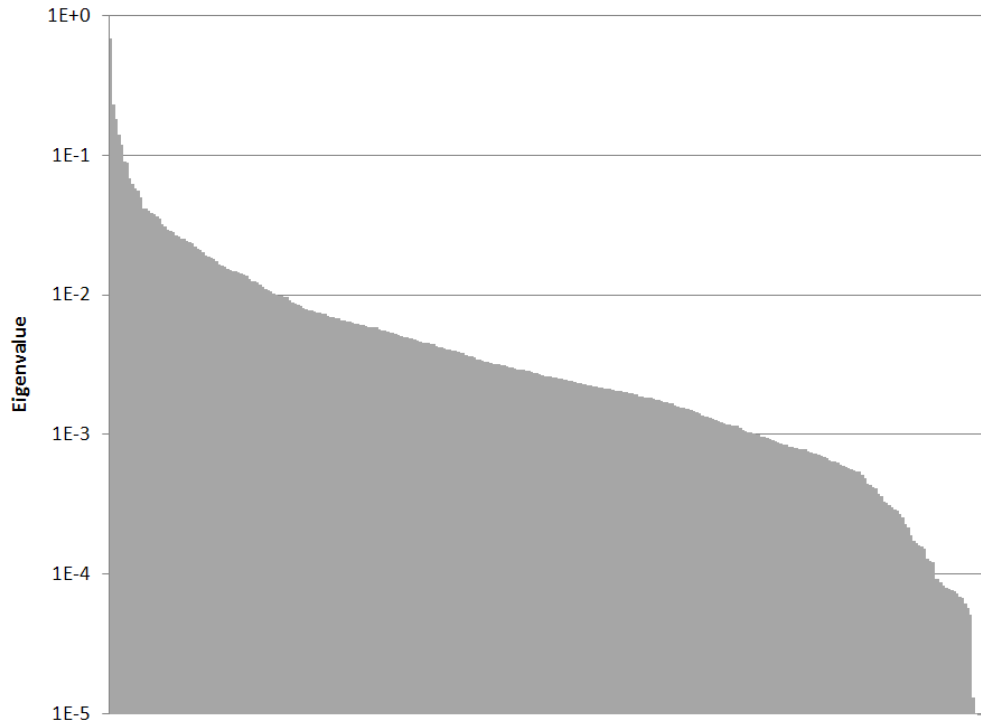


Figure 3.11: A graph of the 324 eigenvalues in the linear system of the example, sorted from greatest to least.

The optimal linear weights were calculated using Equation 3.38. The weights were found to satisfy Equation 3.20 as the weights for any single class of a MPE do indeed sum to exactly zero. Figure 3.12 shows a graph of the optimal linear weights for the example. It can be seen that the positive and negative weights exactly match one another for all of MPH classes of each MPE.

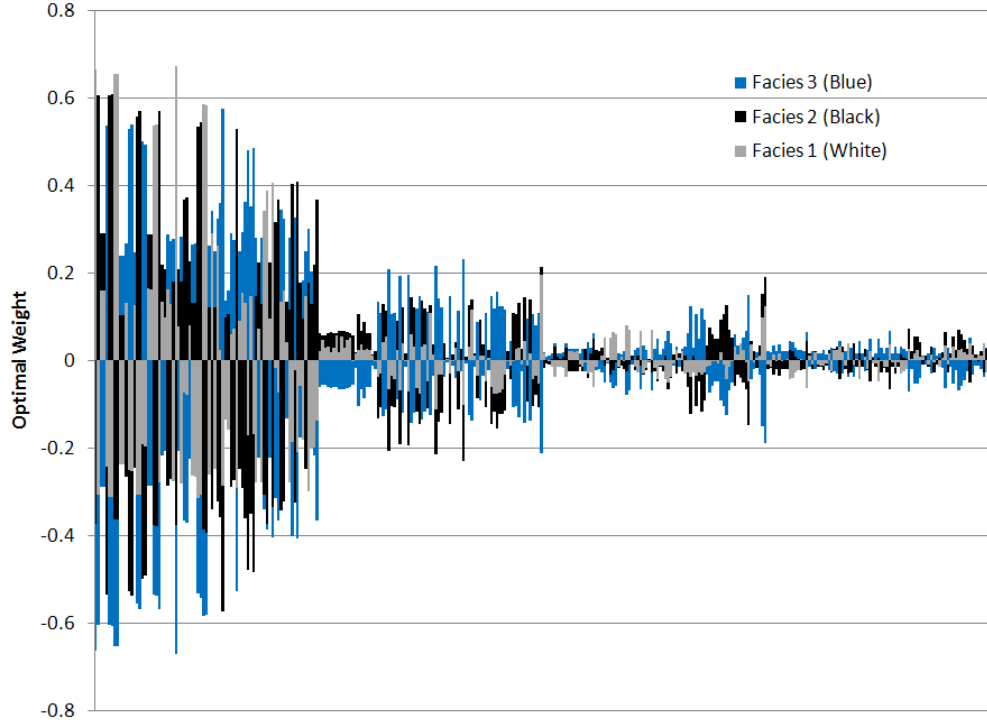


Figure 3.12: A graph of the optimal linear weights for the example, sorted in the same order as the MPHs in Figure 3.10.

### 3.4 Initial States

Recall Equation 2.27, the definition of a transition matrix:

$$P(X_{t+1} = \beta | X_t = \alpha) = \begin{bmatrix} P_{\alpha\beta} \end{bmatrix} \quad \forall \alpha, \beta$$

The transition matrix can be broken down into submatrices made up of the transition matrix of each irreducible recurrent class,  $P_r$ ,  $r=1, \dots, R$ ; the transition matrix within the transient classes,  $Q$ ; and the transition probabilities from the transient states to the recurrent states,  $S$  (Lawler, 2006):

$$\begin{bmatrix} P_{\alpha\beta} \end{bmatrix} = \begin{bmatrix} P_1 & & 0 & | & \\ & \ddots & & | & 0 \\ 0 & & P_R & | & \\ \hline & S & & | & Q \end{bmatrix} \quad (3.41)$$

As shown in Equation 2.30, the stationary distribution  $\pi$  of a Markov chain with transition probabilities  $P_{\alpha\beta}$  is found by taking the limit of the transition matrix as time

goes to infinity. Substituting in Equation 3.41 and using the properties of a reducible transition matrix (Lawler, 2006) gives the result:

$$\begin{aligned}
 [\pi_\alpha] &= \lim_{t \rightarrow \infty} [\varphi_\alpha] \begin{bmatrix} P_1 & & 0 & | & \\ & \ddots & & & 0 \\ 0 & & P_R & | & \\ \hline & S & & | & Q \end{bmatrix}^t \\
 &= \lim_{t \rightarrow \infty} [\varphi_\alpha] \begin{bmatrix} P_1^t & & 0 & | & \\ & \ddots & & & 0 \\ 0 & & P_R^t & | & \\ \hline & 0 & & | & 0 \end{bmatrix}^t
 \end{aligned} \tag{3.42}$$

In Equation 3.42 the submatrices  $P_r$  each form their own irreducible Markov chains; if the chain over the whole state space starts in recurrent class  $r$  then the chain will always remain in that class and will not explore the full state space. Chains that start in transient states will eventually end up in a recurrent class; which class is dependent on the transition probabilities  $S$ . The initial state  $\varphi$  will exert some control over the recurrent class that the Markov chain ends up in over a long time period.

State spaces in earth sciences applications are finite but extremely large, so it is impossible to analytically scrutinize the transition probabilities in the MPS-GS algorithm. The existence of transient states was demonstrated in the small example in Section 2.4.3, and distinct recurrent classes would be expected to exist for a state space with over  $10^{100,000}$  classes. Selecting initial states by using other simulation methods such as SIS or TGS (see Section 2.1.2) would reduce the distance between the initial state and the high-probability recurrent states. This could lead to a bias if the initial states are consistently in one recurrent class; the recurrent states in other classes would never (or rarely) be explored by the Markov chain. For this reason MPS-GS uses a random initial state to ensure an unbiased exploration of the entire state space.

### 3.5 Pattern Simulation

The idea of pattern-based geostatistics was mentioned in Section 2.3.3. The process of placing (or patching) entire patterns into a simulation grid instead of a single point at a time extends the concept of MPS from data used for inference of conditional distributions to the distributions themselves. All of the statistics inferred from a TI can be of any

arbitrary order set by the modeler. There is no practical or theoretical constraint preventing entire patterns from being used instead of individual points (Journel, 2004).

The MPS-GS algorithm can be extended to include patterns by the same logic as using MPEs instead of univariate information as data. Equation 3.1, the linear estimate of conditional distributions for facies using the indicators of MPEs, can be modified to estimate the probabilities of MPH classes for a given MPE:

$$P^*(E_0^\gamma) = P(E_0^\gamma) + \sum_{i=1}^M \sum_{\alpha=1}^{K^N} \lambda_{i,\alpha}^\gamma \cdot [I(E_i^\alpha) - P(E_i^\alpha)] \quad (3.43)$$

The MPH classes for MPE zero are the patterns to be patched into the domain. The event  $E_0$  is the central MPE in the template and takes the place of the null vector. There is no theoretical constraint as to how many points  $N_0$  the central MPE contains, and it need not be the same as  $N$ . Similarly there is no requirement for the data MPEs to have the same number of points and in fact each MPE  $E_i$  could have a different number of points  $N_i$ ; the case where all of the statistics are of the same order has been used here for ease of notation.

The optimal linear weights in Equation 3.43 can be found by using the same procedure as before, with the difference that the [RHS] statistics are now of order  $N+N_0$  instead of  $N+1$ :

$$\sum_{j=1}^M \sum_{\beta=1}^{K^N} \lambda_{j,\beta}^\gamma \cdot Cov\{E_i^\alpha, E_j^\beta\} = Cov\{E_i^\alpha, E_0^\gamma\} \quad i = 1, \dots, M, \quad \alpha = 1, \dots, K^N \quad (3.44)$$

Another difference is that there are now  $K^{N_0}$  columns in the [RHS] matrix and  $K^{N_0}$  probabilities to estimate. The properties of [LHS] do not change when using patterns. The MPS template used for calculating and storing information must be modified to include a central MPE instead of the null vector; Figure 3.13 shows an example template with a central pattern.

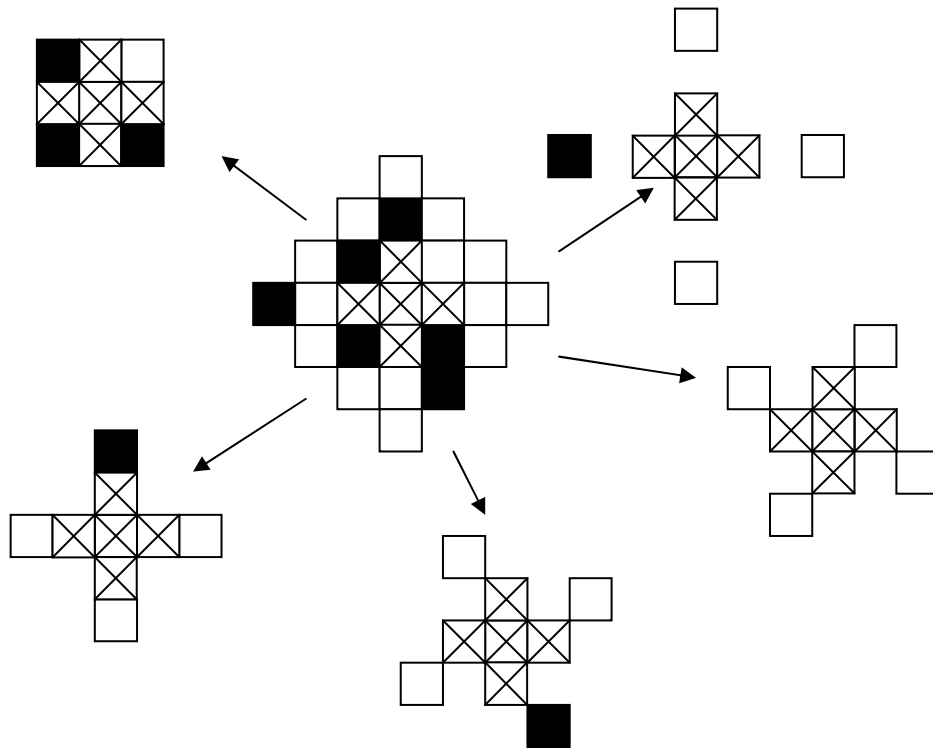


Figure 3.13: A 25-point MPS template with a five-point central event and five four-point MPEs as data.

## 4 Algorithm Implementation

The MPS-GS algorithm developed in Chapter 3 presents a number of issues that relate to computational efficiency and a risk of numerical artifacts. This Chapter addresses these important implementation challenges. Section 4.1 presents modifications to be applied to the conditional distributions calculated using multiple-point events (MPEs). Section 4.2 explains the need for a multiple-grid approach in MPS simulation and outlines how this is accomplished. Section 4.3 describes the criteria used for stopping the MPS-GS algorithm. Section 4.4 compares two alternatives for the path followed when visiting all locations; each visitation of all unsampled locations is termed a loop. Section 4.5 presents a solution to the issue of edge effects. Section 4.7 reviews a number of methods for evaluating the results of MPS simulation.

### 4.1 Modifications to Conditional Distributions

The conditional distributions calculated using MPEs are used in MPS-GS to explore the state space. Problems arise if the conditional distributions are used directly in MPS-GS; relatively simple adjustments can be used to rectify these problems. This section describes the required changes including the use of single-point indicators in addition to the MPE data; the division of the conditional distributions into two parts; a servosystem approach to reproduce global and local univariate proportions; and noise reduction methods to speed convergence and improve the appearance of the final realizations.

#### 4.1.1 Single-Point Indicators

The linear estimate in Equation 3.1 uses a number of  $N$ -point events to determine conditional probabilities for the  $K$  facies. The statistics used in determining the linear

weights in Equation 3.10 are of order  $K^{2N}$ . The higher the order of the spatial statistics, the more difficult it is to infer them reliably. Large MPEs are desirable as they contain more information; however, using a random initial state for the Gibbs sampler and large MPEs will lead to many patterns that are not informed from the training image (TI) and therefore must be discarded without contributing to the conditional distributions. This slows down convergence of the MPS-GS algorithm.

A solution to this problem is to use single-point indicators in addition to large MPEs to improve the conditional distributions early in the simulation. Once some structure has been established, more MPEs will be informed from the TI. The informed MPEs then dominate the information provided by single-point data because the single-point events are redundant with the MPEs; this redundancy is demonstrated below.

There is no theoretical constraint against using events of different sizes. The conditional probability of facies  $k$  is written below simultaneously using  $N$ -point MPEs and single-point indicators:

$$P^*(k) = P(k) + \sum_{i=1}^M \sum_{\alpha=1}^{K^N} \lambda_{i,\alpha}^k \cdot [I(E_i^\alpha) - P(E_i^\alpha)] + \sum_{u=1}^{MN} \sum_{\kappa=1}^K \chi_{u,\kappa}^k \cdot [I(\kappa;u) - P(\kappa;u)] \quad (4.1)$$

In Equation 4.1,  $I(\kappa;u)$  is the indicator of facies  $\kappa$  at offset location  $u$  within the MPS template;  $P(\kappa;u)$  is the global probability of facies  $\kappa$  at location  $u$  (nominally the same as  $P(\kappa)$  but not necessarily due to erosion of the TI); and  $\chi_{u,\kappa}^k$  is the linear weight assigned to  $I(\kappa;u)$ . The system of equations is expanded from  $MK^N$  equations to  $MK^N+MKN$ ; the new [LHS] matrix becomes:

$$\left[ \begin{array}{c} LHS \end{array} \right] = \left[ \begin{array}{cc|cc} \text{Cov}\{E_i^\alpha, E_j^\beta\} & & \text{Cov}\{E_i^\alpha, I_v^\psi\} & \\ \hline & & \text{Cov}\{I_u^\kappa, E_j^\beta\} & \text{Cov}\{I_u^\kappa, I_v^\psi\} \end{array} \right] \quad (4.2)$$

In Equation 4.2,  $I_u^\kappa$  is used as shorthand notation for  $I(\kappa;u)$ . The [RHS] matrix is expanded to have dimensions of  $MK^N+MKN$ -by- $K$ :

$$\left[ \begin{array}{c} RHS \end{array} \right] = \left[ \begin{array}{c} Cov\{E_i^\alpha, k\} \\ \hline Cov\{I_u^\kappa, k\} \end{array} \right] \quad (4.3)$$

The  $[\lambda]$  matrix is also expanded to the same size as [RHS]:

$$\left[ \begin{array}{c} \lambda \end{array} \right] = \left[ \begin{array}{c} \lambda_{i,\alpha}^k \\ \hline \lambda_{u,\kappa}^k \end{array} \right] \quad (4.4)$$

Using single-point indicators in the estimator provides additional information in cases where not all MPEs  $E_i^\alpha$  are informed. When the MPEs are informed, the single-point indicators contained within provide no additional information and do not affect the estimated conditional distributions. As a demonstration, consider the relations between single-point indicators and MPEs:

$$I(\kappa, u) = \begin{cases} 1 & \forall i, \alpha | u \in E_i, \kappa \in E_i^\alpha \\ 0 & \forall i, \alpha | u \in E_i, \kappa \notin E_i^\alpha \\ [0,1] & \forall i, \alpha | u \notin E_i \end{cases} \quad (4.5)$$

For single-point indicators located spatially within a specified MPE  $E_i$ , the value is always defined as zero or one. The covariance between  $I_u^\kappa$  and  $E_i^\alpha$  for the case of  $u \in E_i$  can be rearranged as:

$$\begin{aligned} Cov\{I_u^\kappa, E_j^\beta\} &= P(I_u^\kappa \cap E_j^\beta) - P(I_u^\kappa) \cdot P(E_j^\beta) \\ &= P(I_u^\kappa | E_j^\beta) \cdot P(E_j^\beta) - P(I_u^\kappa) \cdot P(E_j^\beta) \\ &= P(I_u^\kappa | E_j^\beta) \cdot \sum_{\alpha=1}^{K^N} P(E_i^\alpha \cap E_j^\beta) - \sum_{\alpha=1}^{K^N} P(I_u^\kappa | E_i^\alpha) \cdot P(E_i^\alpha) \cdot P(E_j^\beta) \\ &= \sum_{\alpha=1}^{K^N} P(I_u^\kappa | E_i^\alpha) \cdot [P(E_i^\alpha \cap E_j^\beta) - P(E_i^\alpha) \cdot P(E_j^\beta)] \\ &= \sum_{\alpha=1}^{K^N} P(I_u^\kappa | E_i^\alpha) \cdot Cov\{E_i^\alpha, E_j^\beta\} \end{aligned} \quad (4.6)$$

This shows that the covariance values in the lower-left submatrix of [LHS] can be expressed as linear combinations of terms within the upper-left submatrix with

coefficients equal to the conditional probability of the single-point indicators given the MPE classes; these conditional probabilities are known from Equation 4.5. The redundancy of the single-point indicators means that the rank of the [LHS] matrix is unchanged by their inclusion and  $P^*(k)$  is not changed.

### 4.1.2 Two-Part Conditional Probability

The conditional probability of all facies must be calculated at each location visited by the MPS-GS algorithm; however, only the indicators change from one location to the next; the global probability terms are constant. For this reason, it is possible to determine a base or intermediate probability,  $P^+(k)$ , for every facies  $k$  at the start of the simulation:

$$P^+(k) = P(k) - \sum_{i=1}^M \sum_{\alpha=1}^{K^N} \lambda_{i,\alpha}^k \cdot P(E_i^\alpha) - \sum_{u=1}^{MN} \sum_{\kappa=1}^K \chi_{u,\kappa}^k \cdot P(\kappa; u) \quad (4.7)$$

The base probabilities do not account for any indicator values equal to one and are equivalent to every indicator having a value of zero. To update the base values to the full conditional distributions, the linear weights of the indicators that have values of one are added:

$$P^*(k) = P^+(k) + \sum_{i=1}^M \lambda_{i,\alpha}^k \{ \forall \alpha | I(E_i^\alpha) = 1 \} + \sum_{u=1}^{MN} \chi_{u,\kappa}^k \{ \forall \kappa | I(\kappa; u) = 1 \} \quad (4.8)$$

This reduces the number of arithmetic operations necessary at each location from  $MK^N + MKN$  to  $M + MN$ . This is a significant computational saving for large grids.

### 4.1.3 Univariate Proportions

The proportions of the facies are important in the response characteristics of a natural resource model; as such, reproducing the univariate proportions of facies is important. Algorithms that use high-order statistics often do not accurately reproduce univariate statistics (Strebelle and Journel, 2001). Problems with univariate proportions are also encountered when order relations problems exist (Ortiz, 2003); resetting facies probabilities to be within [0,1] amounts to changing the conditional probabilities and can lead to deviations from the target global distribution.

Assuming stationarity in the mean of the indicator variables, the proportions are constant over the entire domain. In practice, there are often trends in facies proportions

that come from vertical proportion curves or secondary data, and these local univariate proportions must be accounted for in MPS-GS.

## Servosystem Correction

Other MPS algorithms have used the concept of a servosystem correction to correct the global facies proportions (Strebelle and Journel, 2001, Liu, 2006). A servosystem adds the difference between the (target) global proportions and the current simulated proportions to the conditional probability:

$$P'(k) = P^*(k) + \mu \cdot [P^{TARG}(k) - P^{SIM}(k)] \quad (4.9)$$

$P^{TARG}(k)$  is the target proportion of facies  $k$ , and is not necessarily the same as the TI proportion  $P(k)$ . The factor  $\mu$  is a control parameter used to tune the impact of the servosystem; values of  $\mu$  greater than one put more weight on the univariate proportions, while  $\mu=0.0$  removes the servosystem correction. The effect of  $\mu$  is demonstrated in the example below. Recall the TI shown in Figure 2.6, a channelized TI that is 250x250 (62,500 cells) with two facies, channel and background. The channels have a proportion of 0.30 in the TI.

MPS-GS is used to create a number of realizations with varying values of  $\mu$ . The parameters for all realizations were:  $G=4$ ;  $M=16$ ;  $N=4$ . The TI and all realizations for the example are 250x250 cells. Four servosystem parameters are used,  $\mu=0.0, 0.5, 1.0,$  and  $2.0$ . Five target channel proportion values are used,  $P_{channel}=0.1, 0.3, 0.5, 0.7,$  and  $0.9$ . Figure 4.1 shows one realization from twelve cases.

For  $\mu=0.0$  there is no effect from the servosystem and the resulting realizations have channel proportions of approximately 0.3, close to the TI proportions. For  $\mu>0.0$ , the effect of the servosystem can be seen visually. There appears to be little change for different values of  $\mu$ ; the actual simulated proportions for the 20 cases are shown in Table 4.1.

There is no significant difference between  $\mu$  values for target channel proportions close to the TI value of 0.3. As the target proportions vary, the servosystem becomes more prominent and the simulated proportions differ more from the target.

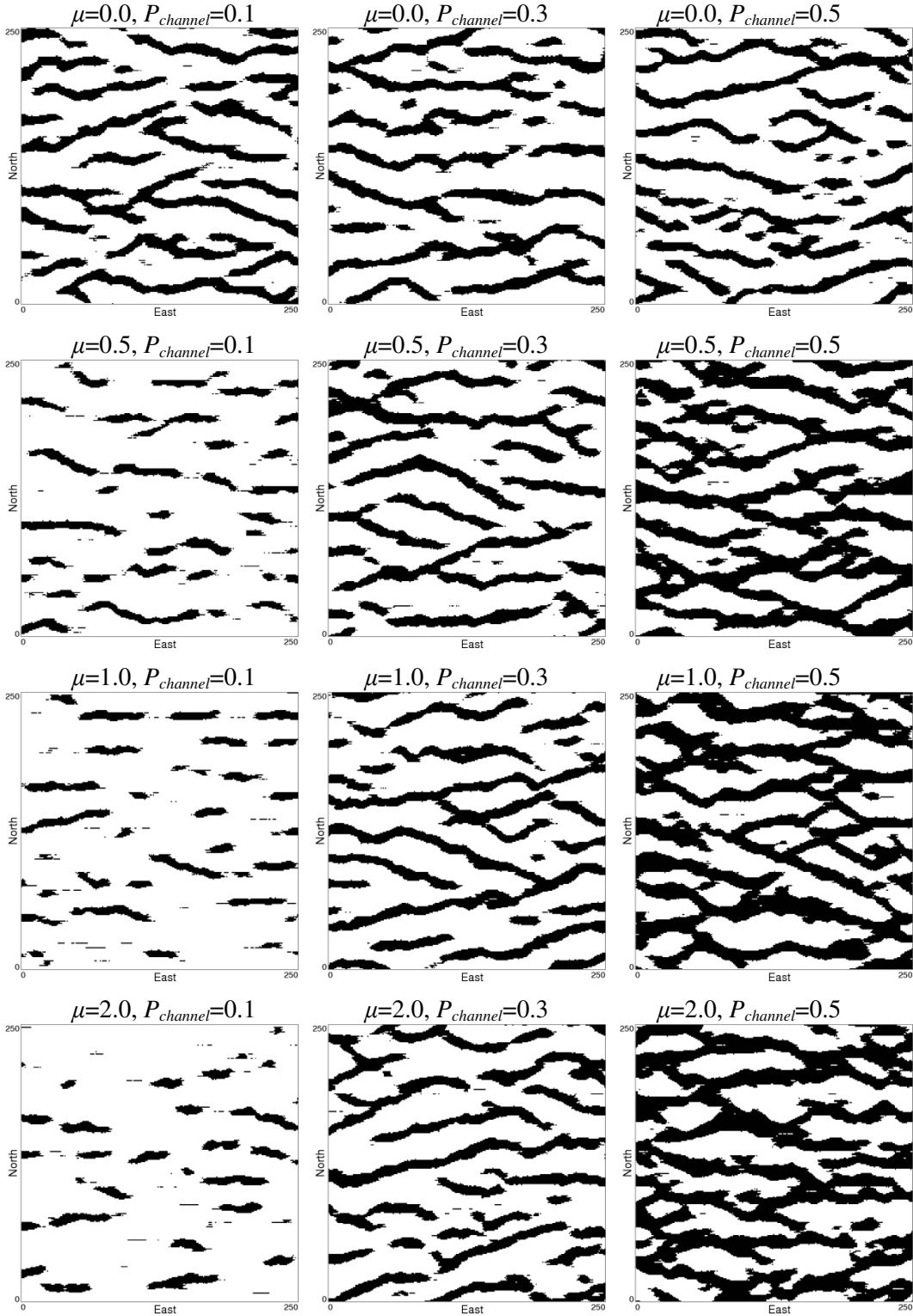


Figure 4.1: An example of the effect of  $\mu$  and varying target facies proportions. Left column to right: target  $P_{channel}=0.1, 0.3, 0.5$ ; Top to bottom:  $\mu=0.0, 0.5, 1.0, 2.0$ .

Table 4.1: Simulated channel proportions using varying  $\mu$  and  $P_{channel}$  parameters.

		Target Channel Proportions				
		0.1	0.3	0.5	0.7	0.9
Servosystem Parameter $\mu$	0.0	0.288	0.263	0.283	0.275	0.274
	0.5	0.131	0.275	0.436	0.576	0.746
	1.0	0.108	0.283	0.459	0.668	0.853
	2.0	0.092	0.283	0.482	0.704	0.893

## Local Proportions

Facies proportions in local neighbourhoods or at individual locations can come from vertical proportion curves, areal proportion maps, secondary information, or expert interpretation. Local proportions could be viewed as likelihood data while the conditional distributions using hard data or a model of spatial structure (i.e. variogram, TI) could be considered prior information.

With these definitions, the estimated conditional probability  $P^*(k)$  is the prior distribution; the local facies proportions are the likelihood distribution, and are denoted by  $P^{LOC}(k)$ ; and the combined or updated distribution accounting for hard and soft data is represented by  $P'(k)$ . There are a number of methods to integrate the prior and likelihood information into an updated distribution. Those that are considered here are the additive method or servosystem (Strebelle and Journel, 2001); the multiplicative method or Bayesian updating (Deutsch, 2002); permanence of ratios (Journel, 2002); and a multiple servosystem approach developed for MPS-GS.

The servosystem method for using secondary information adds the difference between the local and global proportions to the conditional probability; if this is combined with the global servosystem in Equation 4.9, the overall correction becomes:

$$\begin{aligned}
 P'(k) &= P^*(k) + \mu \cdot \left[ \left( P^{LOC}(k) - P(k) \right) + \left( P(k) - P^{SIM}(k) \right) \right] \\
 &= P^*(k) + \mu \cdot \left[ P^{LOC}(k) - P^{SIM}(k) \right]
 \end{aligned} \tag{4.10}$$

The parameter  $\mu$  is a control parameter, but now applies to both the local proportion and servosystem corrections. The two corrections could be separated. Assuming the prior distribution and likelihood distribution each sum to one, the updated proportions will also sum to exactly one. A drawback to the additive correction for local facies proportions is that zeros and ones are not reproduced exactly; a facies with a local proportion of zero

would not necessarily have an updated probability of zero. Also, there is no guarantee that the updated proportions will be bounded by zero and one.

Using Bayesian updating in a multiplicative method for reproducing local proportions is an alternative to the additive method. This correction is:

$$P'(k) = P^*(k) \cdot \left( \frac{P^{LOC}(k)}{P(k)} \right)^\tau \quad (4.11)$$

In Equation 4.11  $\tau$  is a control parameter, with a value of zero removing all effect of the local proportions. The multiplicative approach to reproducing local proportions has the benefits of exactly reproducing zero values and never returning any negative updated probabilities. However, this method does not guarantee that the updated probabilities will have an upper bound of one and restandardization is required.

Another approach to combining prior and likelihood information is the permanence of ratios. This updating procedure is as follows:

$$\frac{1 - P'(k)}{P'(k)} = \frac{1 - P^*(k)}{P^*(k)} \cdot \left( \frac{1 - P^{LOC}(k)}{P^{LOC}(k)} \cdot \frac{P(k)}{1 - P(k)} \right)^\tau \quad (4.12)$$

In Equation 4.12, the parameter  $\tau$  is a control parameter. The permanence of ratios approach has the significant benefit in that the updated probabilities will sum to one and will be bounded by zero and one. Local facies proportions of zero and one are also exactly reproduced.

The additive, multiplicative, and permanence of ratios methods were all tested with MPS-GS. The TI is shown in Figure 4.2; it is a representation of fluvial geological architecture with a background shale facies (facies 1, white), two different lobe facies (facies two and three, light and dark grey), and a channel facies (facies four, black). This TI has been shown in other MPS papers in the past (Hoffman et al, 2007, Boisvert, 2007). The TI is 78x59x116 (533,832) cells. The proportions of the four facies in the TI are 50%, 12.5%, 9%, and 28.5% respectively.

Figure 4.3 shows the vertical proportion curve used to test the local proportion methods above. There are two distinct regions with lower proportions of the shale facies; of these, the upper has higher proportions of the lobe facies and the lower has a higher proportion of the channel facies. The very top and bottom of the vertical proportion curve represent zones of primarily shale facies. The proportions are assumed to have no areal variations.

Figures 4.4 through 4.6 show one unconditional realization created using MPS-GS with the additive, multiplicative, and permanence of ratios corrections, respectively, for matching local proportions. The control parameter is set to  $\mu=1.0$  or  $\tau=1.0$  in each case. All three realizations are similar in that they have grossly distorted vertical proportions; the region of higher lobe facies proportions has nearly all lobe facies, the region of higher channel facies proportions has nearly all channel facies, and the other layers have almost no facies other than shale. The source of this problem is that the updating procedure is applied every time an unsampled location is visited. Over several iterations, the updating dominates the conditional distribution  $P'(k)$ . Reducing the control parameter slightly does not mitigate this effect; the difference between a value of  $\mu$  that results in the problem in Figures 4.4 to 4.6 and one that does not reproduce the local facies proportions is very small and would be unpractical to find in practical cases.

A proposed solution to this problem is to divide the local facies proportions into a number,  $N_B$ , of discrete bins,  $B_k$ . The bins are equally distributed between the minimum nonzero local proportion of  $k$ ,  $P^{MIN}(k)$ , and the maximum local proportion of  $k$  less than one,  $P^{MAX}(k)$ . The bins are numbered from 1 to  $N_B$  and the bin for facies  $k$  at a specified location can be found by using the equation:

$$B_k = \text{int} \left( \frac{P^{LOC}(k) - P^{MIN}(k)}{P^{MAX}(k) - P^{MIN}(k) + \varepsilon} \cdot N_B \right) + 1 \quad (4.13)$$

The value of  $\varepsilon$  is a small constant used to prevent divide-by-zero errors. The conditional probabilities of each facies are updated to match the global proportions within each bin using a servosystem. The zeros in the local distributions are reproduced by setting the probability of that facies to zero on each visit to the unsampled location; the ones are reproduced by assigning the facies  $k$  with a local probability of one to that location and not revisiting it in the simulation path.

Using multiple servosystems in this way, the updated conditional probability is:

$$P'(k) = P^*(k) + \mu \cdot [P^{LOC}(k) - P^{SIM}(k; B_k)] \quad (4.14)$$

$P^{SIM}(k; B_k)$  is the current simulated proportion of facies  $k$  within bin  $B_k$  and the other variables are as before. Figure 4.7 shows an MPS-GS realization created using the multiple servosystem approach; the distinct zones with high probabilities of lobe and channel facies are clear and yet the local proportions do not dominate the realization. Ten bins are used for the local proportions. Figure 4.8 shows a graph of the vertical proportion

curve reproduction for the four different methods. The multiple servosystem method is clearly better than the other three approaches.

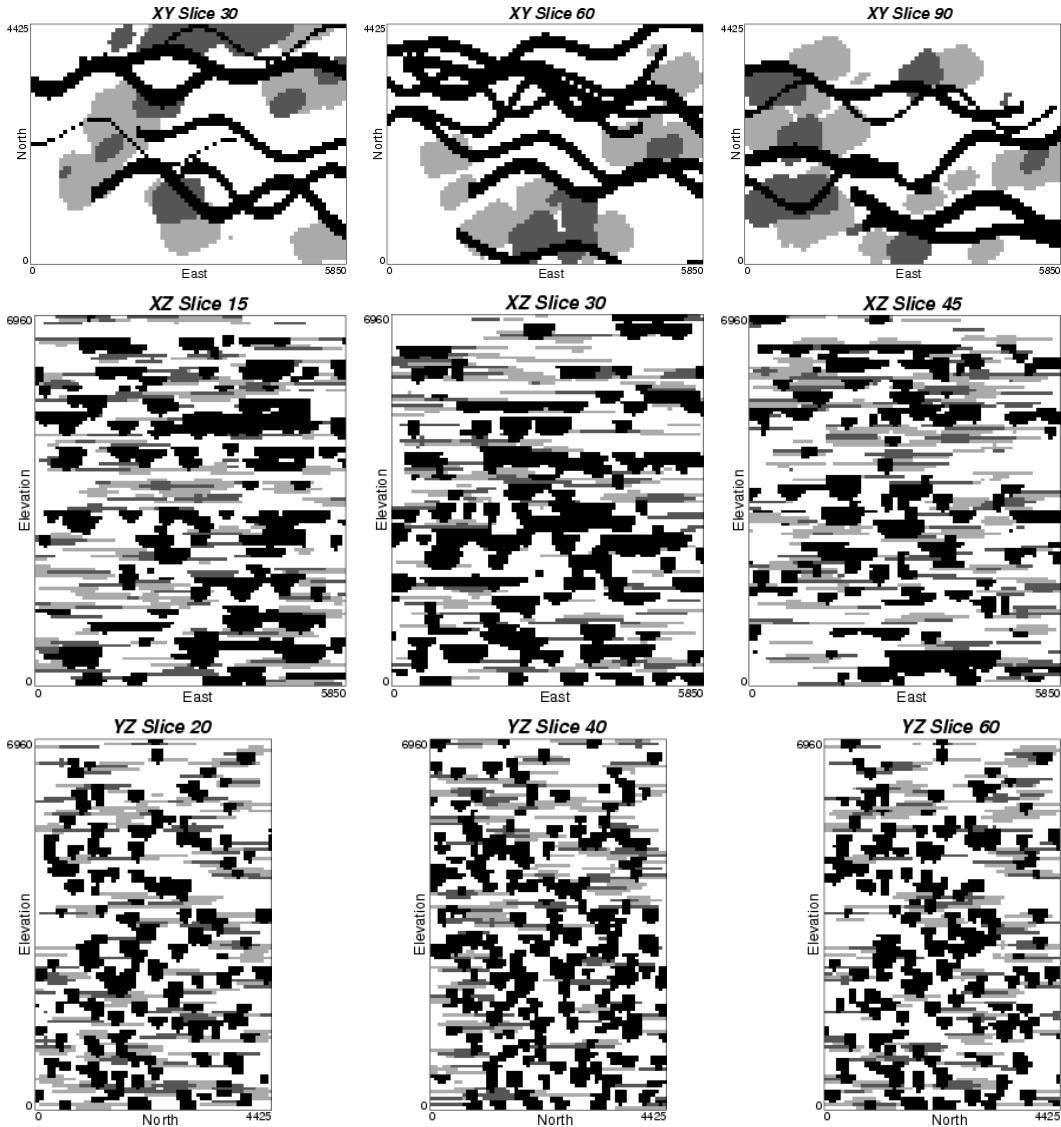


Figure 4.2: Fluvial TI used for the local proportion example (Hoffman et al, 2005, Boisvert, 2007).

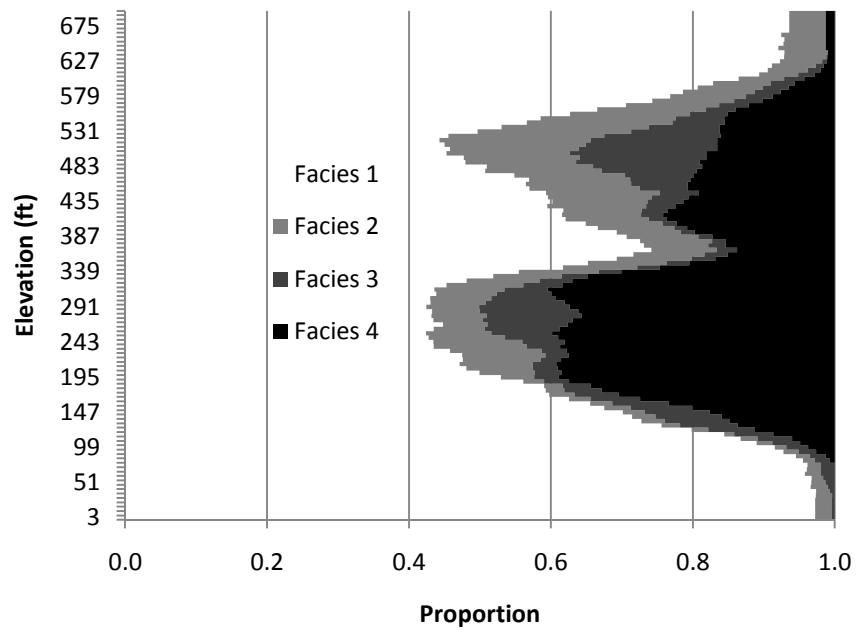


Figure 4.3: Vertical proportion curve used for the local proportion example.

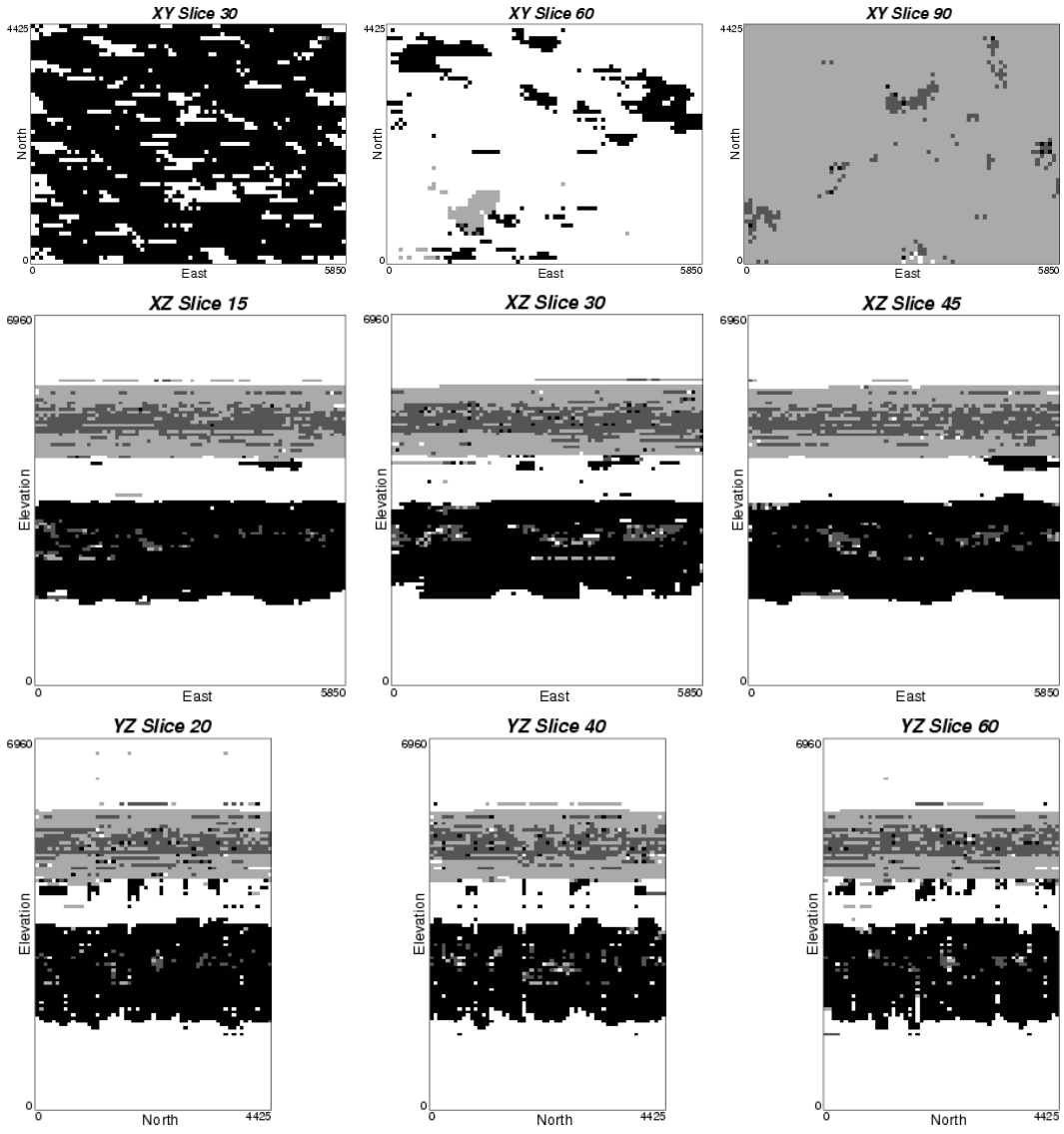


Figure 4.4: An unconditional realization using the additive method for reproducing the vertical proportion curve.

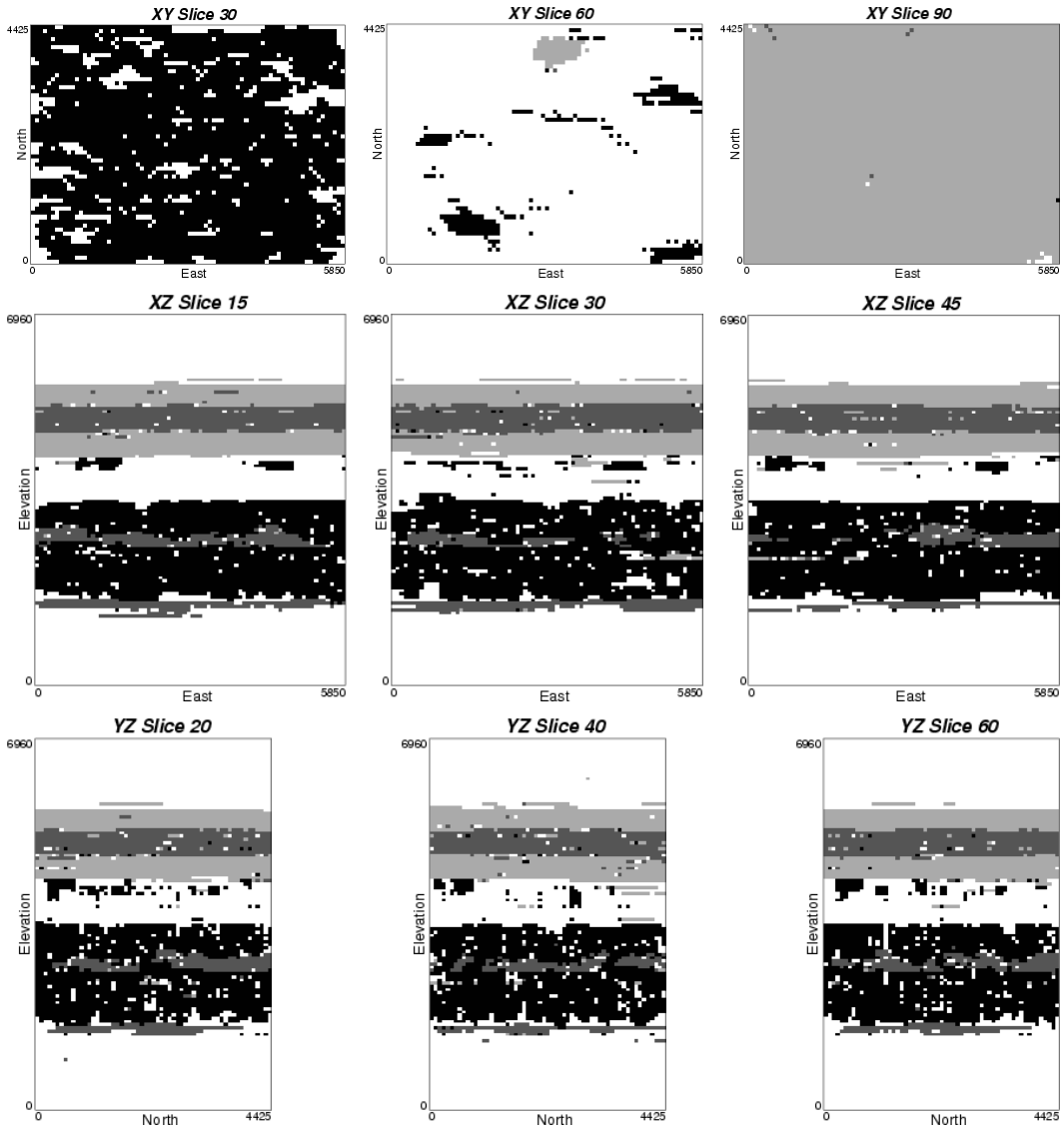


Figure 4.5: An unconditional realization using the multiplicative method for reproducing the vertical proportion curve.

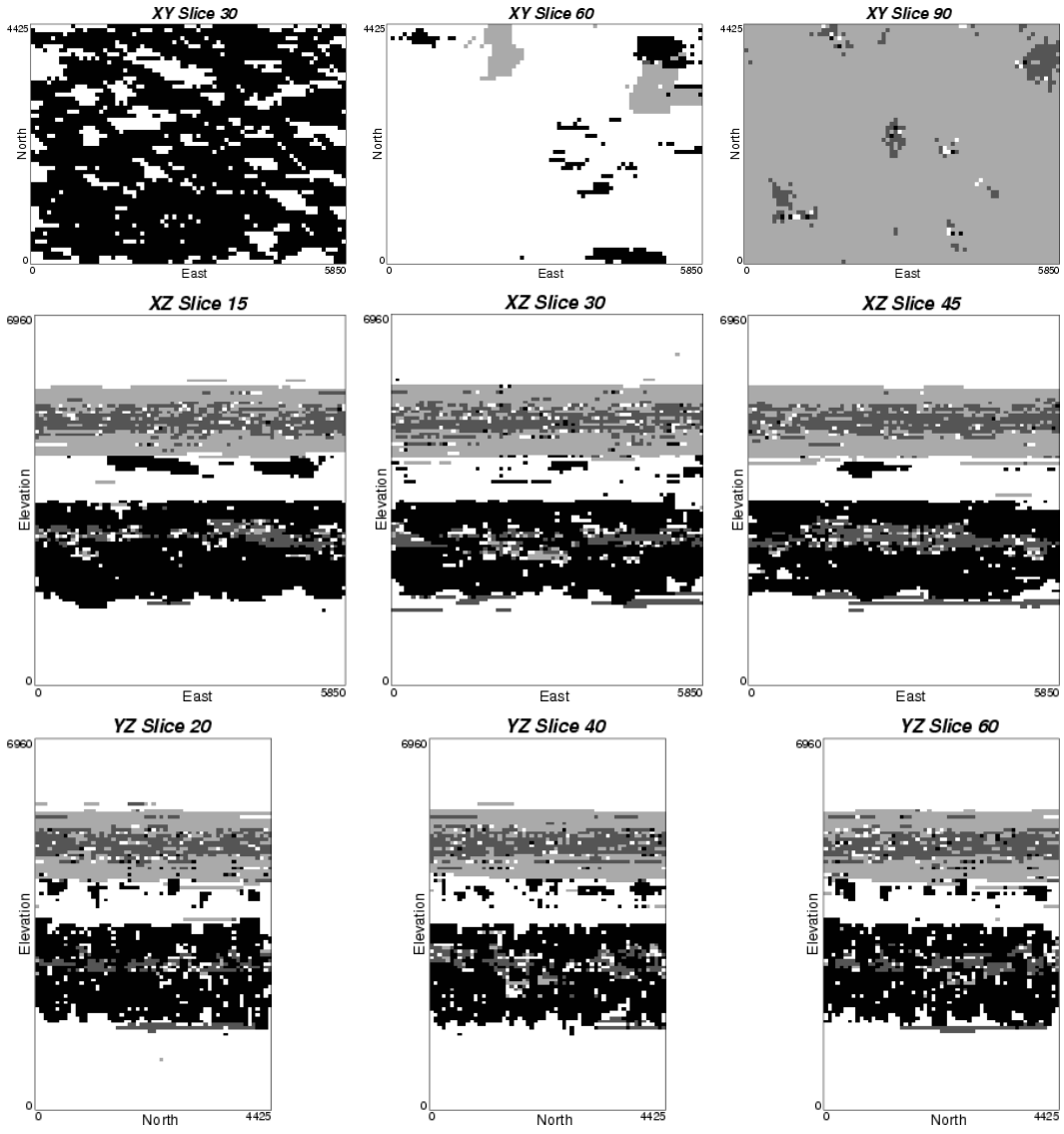


Figure 4.6: An unconditional realization using the permanence of ratios method for reproducing the vertical proportion curve.

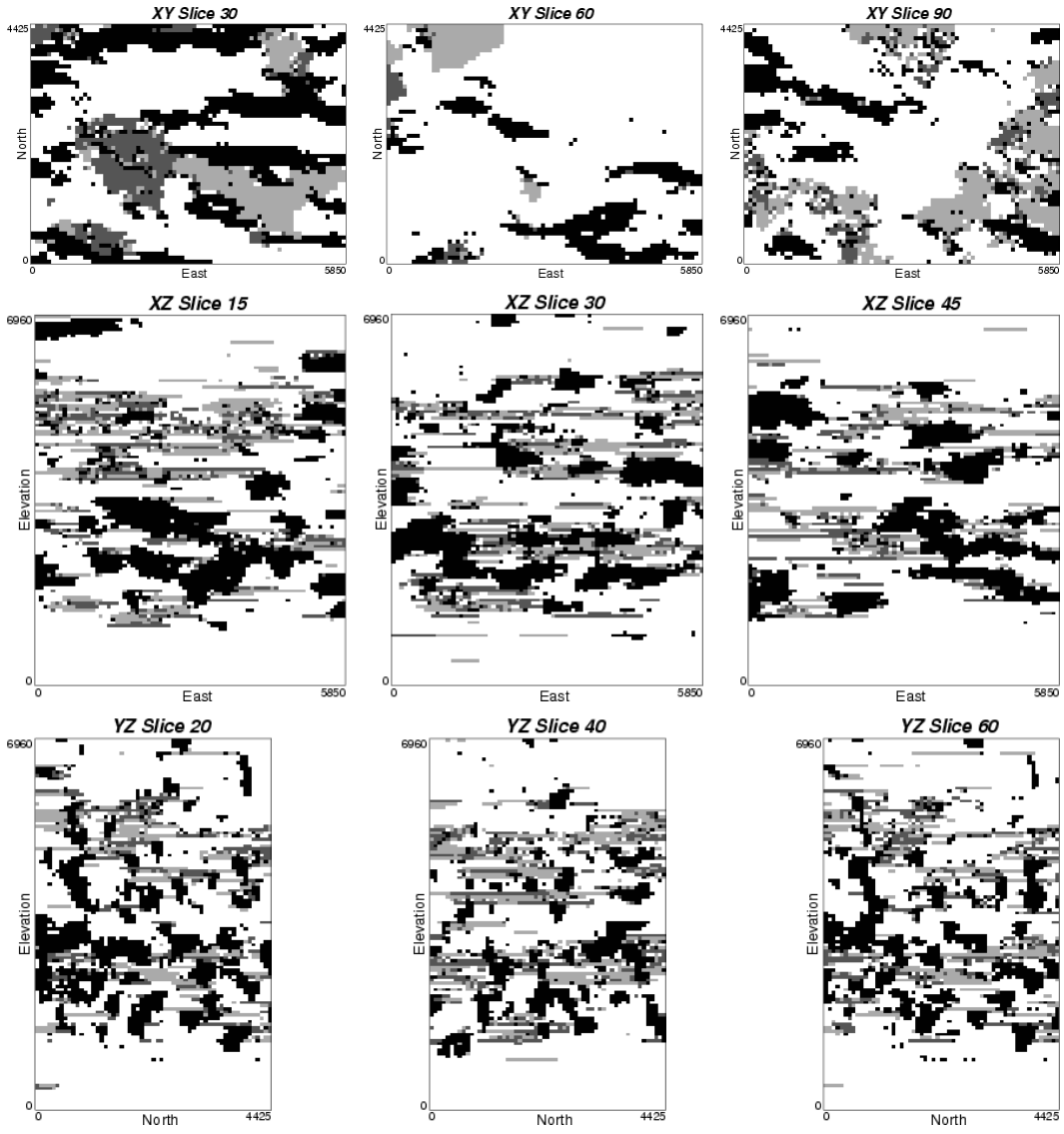


Figure 4.7: An unconditional realization using the multiple servosystem method for reproducing the vertical proportion curve.

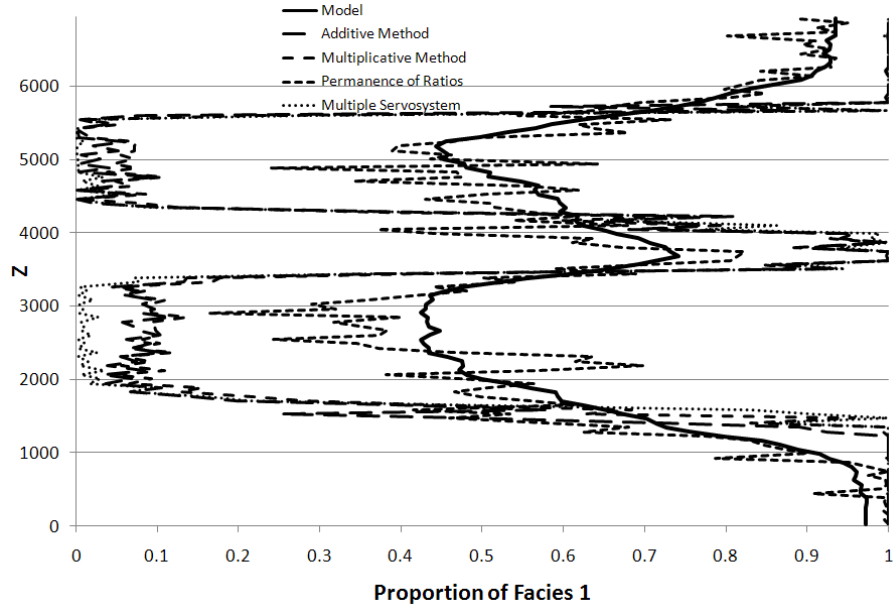


Figure 4.8a: Facies 1 vertical proportion curve reproduction for the four methods shown in the example.

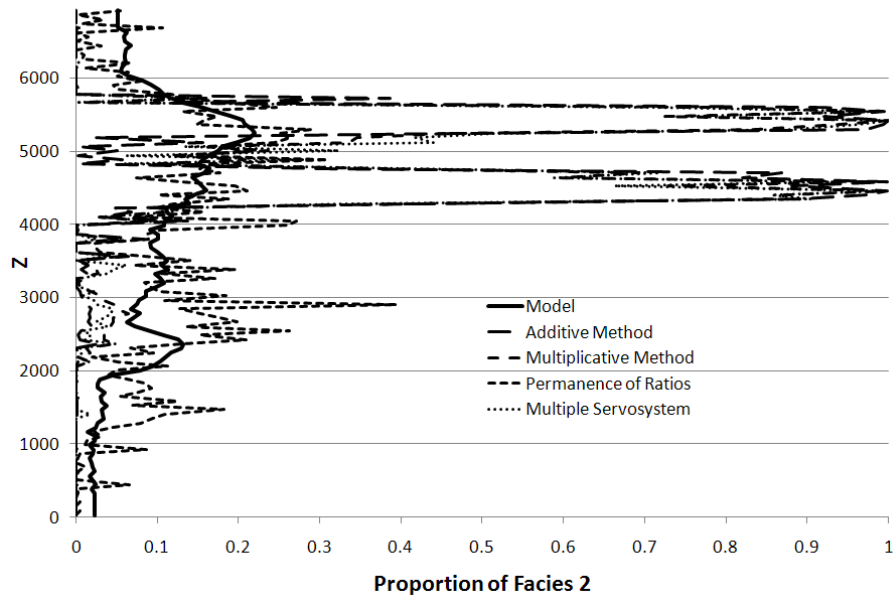


Figure 4.8b: Facies 2 vertical proportion curve reproduction for the four methods shown in the example.

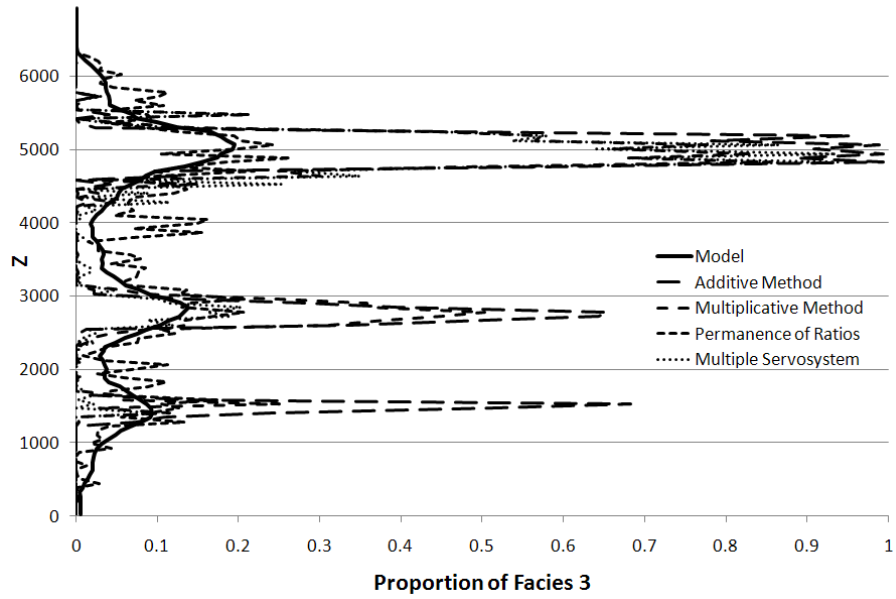


Figure 4.8c: Facies 3 vertical proportion curve reproduction for the four methods shown in the example.

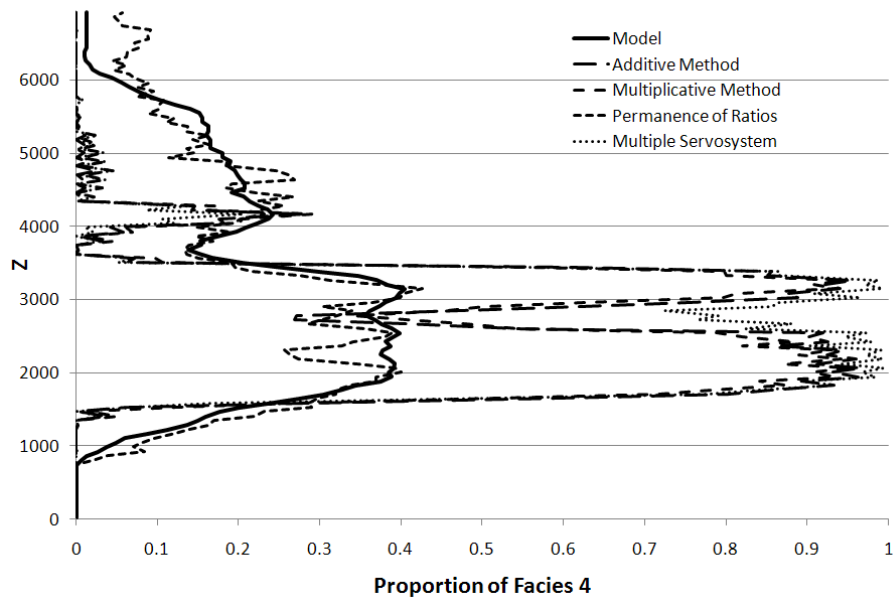


Figure 4.8d: Facies 4 vertical proportion curve reproduction for the four methods shown in the example.

#### 4.1.4 Image Cleaning

As the MPS-GS algorithm proceeds, structure and order is introduced into the realization. Often there are regions where the convergence to geological structures resembling the TI is slow, and there is significant randomness left in a realization. For this reason, image cleaning is implemented during the MPS-GS algorithm to speed convergence and improve the continuity of the realizations. Two methods for image cleaning, the noise reduction factor and connectivity correction, involve modifications to the conditional distributions that are calculated at unsampled locations visited along the simulation path.

##### Noise Reduction Factor

One of the ways randomness is injected into a simulated domain is through small probabilities of facies occurring at unlikely locations. A small conditional probability for a facies, say 0.01, suggests that that facies is very unlikely at the location being considered. In a large domain with many thousands or millions of cells these small probabilities result in many of these facies being selected where they are unlikely. This randomness is propagated through the domain as nearby locations are visited. Eliminating the facies with these small probabilities would therefore reduce the randomness in the simulated domain and the both reduce CPU time and improve the final realizations.

This is accomplished through the use of a noise reduction factor,  $NRF$ :

$$P''(k) = \begin{cases} 0 & \text{if } P'(k) < NRF \cdot P^{LOC}(k) \\ P'(k) & \text{otherwise} \end{cases} \quad (4.15)$$

The second updated conditional probability  $P''(k)$  is then used for selection of the new facies at the current location. The parameter  $NRF$  is typically set between 0.2 and 0.4, although some fine tuning is required. The effect of the noise reduction factor is shown in an example below.

##### Connectivity Correction

The randomness that can occur in realizations is a problem in part because it breaks up the continuity or connectivity of the facies. This property is important as it can greatly influence the response characteristics of the realization and affect the uncertainty associated with the geomodel. It is therefore desirable to match the connectivity properties of the TI to reduce the randomness without creating a too-ordered realization.

The connectivity of a facies  $k$  at a given location is denoted as  $C_k$  and is equal to the number of immediately neighbouring locations that have the same facies. In 2D  $C_k$  can take a value from zero to four and in 3D can take a value from zero to six. An example of this is shown in Figure 4.9. The connectivity distribution for each facies can be calculated from the TI; the connectivity probabilities from the TI in Figure 4.3 are shown in Table 4.2.

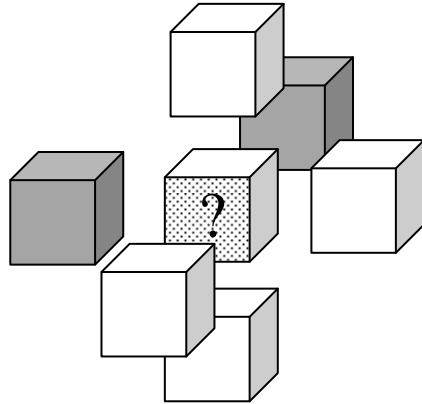


Figure 4.9: An example of the connectivity at a location “?”. The white facies has a connectivity  $C_{white}=4$  and the grey facies has  $C_{grey}=2$ .

Table 4.2: Connectivity probabilities for the four facies in the TI in Figure 4.3.

		Facies			
		1	2	3	4
Connected Cells	0	0.001	0.002	0.002	0.000
	1	0.005	0.014	0.016	0.004
	2	0.030	0.110	0.130	0.020
	3	0.080	0.181	0.187	0.152
	4	0.158	0.379	0.433	0.212
	5	0.332	0.255	0.179	0.303
	6	0.393	0.058	0.054	0.310

Using the probability of facies  $k$  having connectivity  $C_k$ , the corrected conditional probability is adjusted as follows:

$$P''(k) = P'(k) + \eta \cdot [P(C_k) - E\{P(C_k) | P(C_k) > 0\}] \quad (4.16)$$

The value of  $\eta$  is a control parameter;  $E\{P(C_k) | P(C_k) > 0\}$  is the expected value of the connectivity values that are found at least once in the TI. The maximum possible value of

the expected value if all connectivity configuration are seen in the TI is 0.25 in 2D and 0.166 in 3D; it is greater if not all configurations are seen in the TI. For example, facies 4 in the TI in Figure 4.3 is never found with zero connectivity, as shown in Table 4.2. Using Equation 4.16, the connectivity corrections for the TI shown in Figure 4.3 are shown in Table 4.3. It can be seen that facies 2 and 3 are most likely to have four connected cells, and facies 1 and 4 are most likely to have five or six connected cells.

Table 4.3: Connectivity corrections for the four facies in the TI in Figure 4.3.

		<b>Facies</b>			
		<b>1</b>	<b>2</b>	<b>3</b>	<b>4</b>
<b>Connected Cells</b>	<b>0</b>	-0.142	-0.140	-0.141	-0.167
	<b>1</b>	-0.137	-0.129	-0.127	-0.163
	<b>2</b>	-0.112	-0.033	-0.013	-0.147
	<b>3</b>	-0.063	0.039	0.044	-0.015
	<b>4</b>	0.015	0.237	0.290	0.046
	<b>5</b>	0.189	0.112	0.036	0.136
	<b>6</b>	0.250	-0.085	-0.089	0.144

The connectivity correction parameter  $\eta$  should be set to a low value to avoid interfering with the MPS in the conditional probabilities. A value of 0.1 to 0.2 is typically found to be adequate; the effects of different  $\eta$  values are shown in an example below.

## Freezing Cells

In a large domain, it is possible that for a realization generated using MPS-GS different regions will converge at different rates. Near conditioning data or in areas with highly constraining secondary data, there is less freedom for the facies to change due to the influence of the data. Far away from conditioning data or in areas with no secondary information, the exploration of the state space in the local area will take longer to converge to high-probability states. This differential rate of convergence causes problems; stopping the MPS-GS algorithm when some areas are converged and correctly match the TI structure will leave randomness in other areas of the domain, while running the algorithm too long wastes CPU resources.

A solution to the problem of differential convergence is to freeze those cells that have converged locally. This also reduces the noise in a realization; those cells will not have

the small chance of changing values to less-ordered structure later in the simulation. In MPS-GS, if the sum of the conditional probabilities is greater than or equal to 1.0 after the servosystem and noise reduction or connectivity updating is applied, the value of that cell is frozen and it is not visited again. This is not done until after the first loop over all locations to prevent random artifacts from appearing in a totally random image.

### Example

To demonstrate the effect of the different noise reduction methods, consider the TI shown in the Figure 4.1. A number of MPS-GS simulations were performed using this TI. The parameters for all simulations were:  $G=4$ ;  $M=16$ ;  $N=4$ . The TI and all realizations for the example are 250x250 cells. The left of Figure 4.10 shows a MPS-GS realization using no noise reduction. It is clear that the channel structure is not reproduced in any meaningful way, and the long-range connectivity that is desirable in this case is not seen. The right of Figure 4.10 shows a realization using the frozen cells approach and no other noise reduction; there is a clear benefit to freezing cells once they have converged.

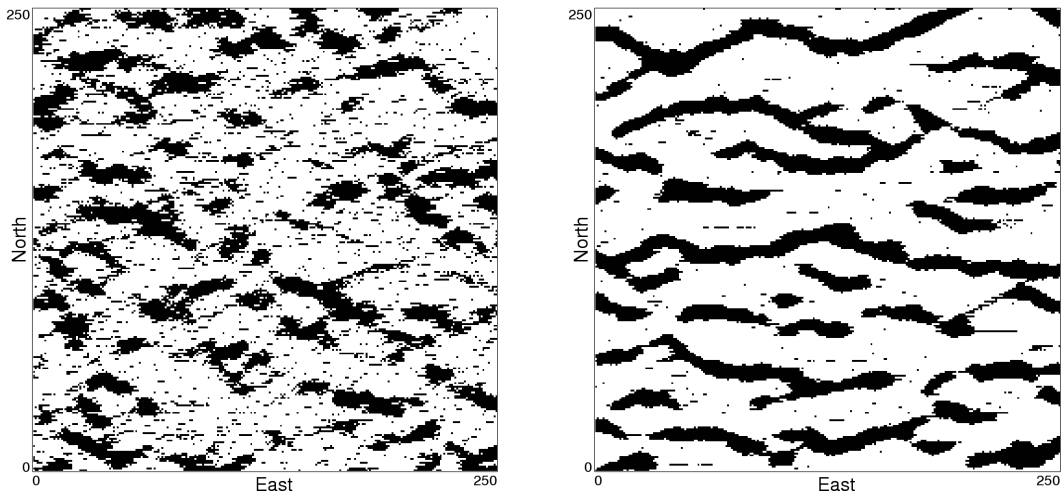


Figure 4.10: Left: an MPS-GS realization using no noise reduction. Right: an MPS-GS realization using the frozen cells method and no other noise reduction.

Figure 4.11 shows four MPS-GS realizations using the TI in Figure 4.1. The only difference between these realizations and the one at the bottom of Figure 4.10 is that a noise reduction factor was applied. Four different control parameter values were used,  $NRF=0.2$ , 0.4, 0.6, and 0.8. With  $NRF=0.2$  there appears to be little improvement over

using only the freezing of cells;  $NRF=0.6$  or  $0.8$  shows too much straight-line east-west or diagonal connectivity and little curvilinearity. The noise reduction factor leaves some random channel facies in the middle of non-channel areas; this is not seen in the TI.

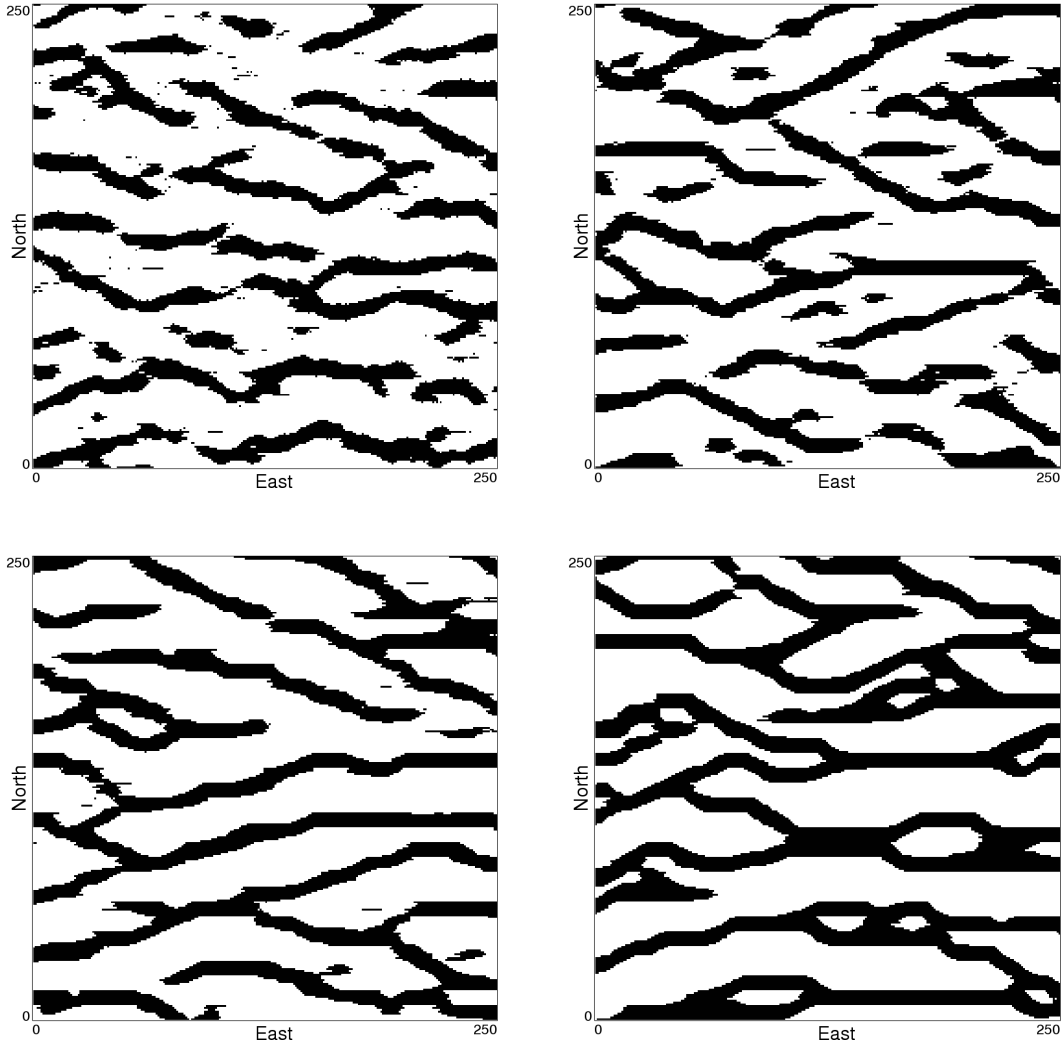


Figure 4.11: Four MPS-GS realizations using the noise reduction factor and freezing of converged cells. Top row:  $NRF=0.2$  and  $NRF=0.4$ ; Bottom row:  $NRF=0.6$  and  $NRF=0.8$ .

Figure 4.12 shows four MPS-GS realizations using the TI in Figure 4.1 and the connectivity correction of Equation 4.16. Four different control parameter values were used,  $\eta=0.2, 0.4, 0.6,$  and  $0.8$ . The long-range connectivity is improved noticeably for low values of  $\eta$  while higher values significantly straighten the channels; in particular, for  $\eta=0.6$  there is one channel that is nearly straight east-west across the domain. Using the

connectivity correction with a low value of  $\eta$  produces the best results with the fewest artifacts and best reproduction of the TI features.

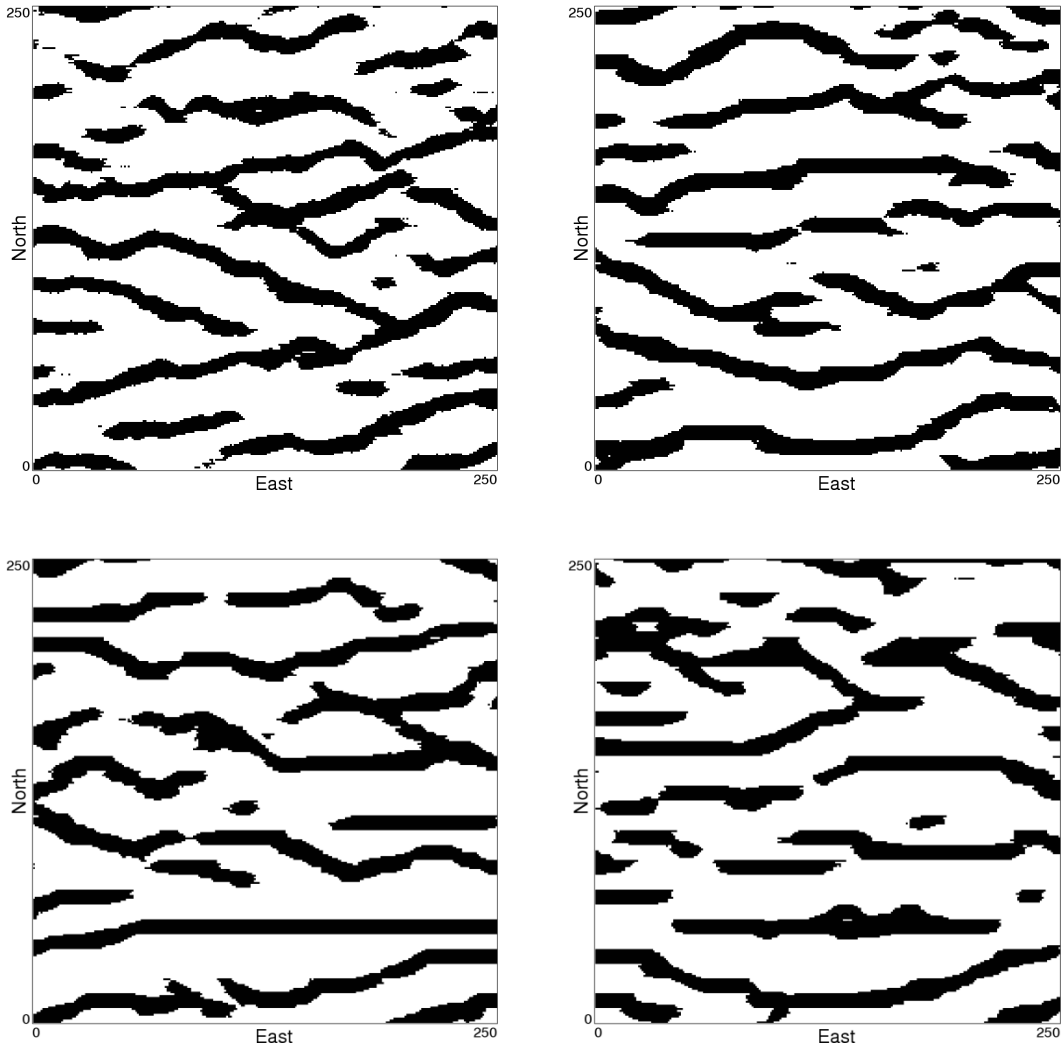


Figure 4.12: Four MPS-GS realizations using the connectivity correction and freezing of converged cells. Top row:  $\eta=0.2$  and  $\eta=0.4$ ; Bottom row:  $\eta=0.6$  and  $\eta=0.8$ .

## 4.2 Multiple Grids

Multiple-point statistics are complex and require a significant amount of CPU time to calculate and memory to store, and this limits the size of a MPS template that can be used. This problem is somewhat mitigated by the use of MPEs; however, the spatial extent of the template is still too limited to cover the full size of geobodies that are typically simulated. For this reason, multiple grids are used in simulation; that is, a subset

of the cells in the domain on a regular grid are simulated first then frozen in place and used as conditioning data for subsequent finer grids within the domain. The last grid will include every cell in the domain. This approach is used successfully by other algorithms such as SNESIM (Liu, 2006) and SISIM (Deutsch and Journel, 1998). An example of the multiple grid approach is shown in Figure 4.13.

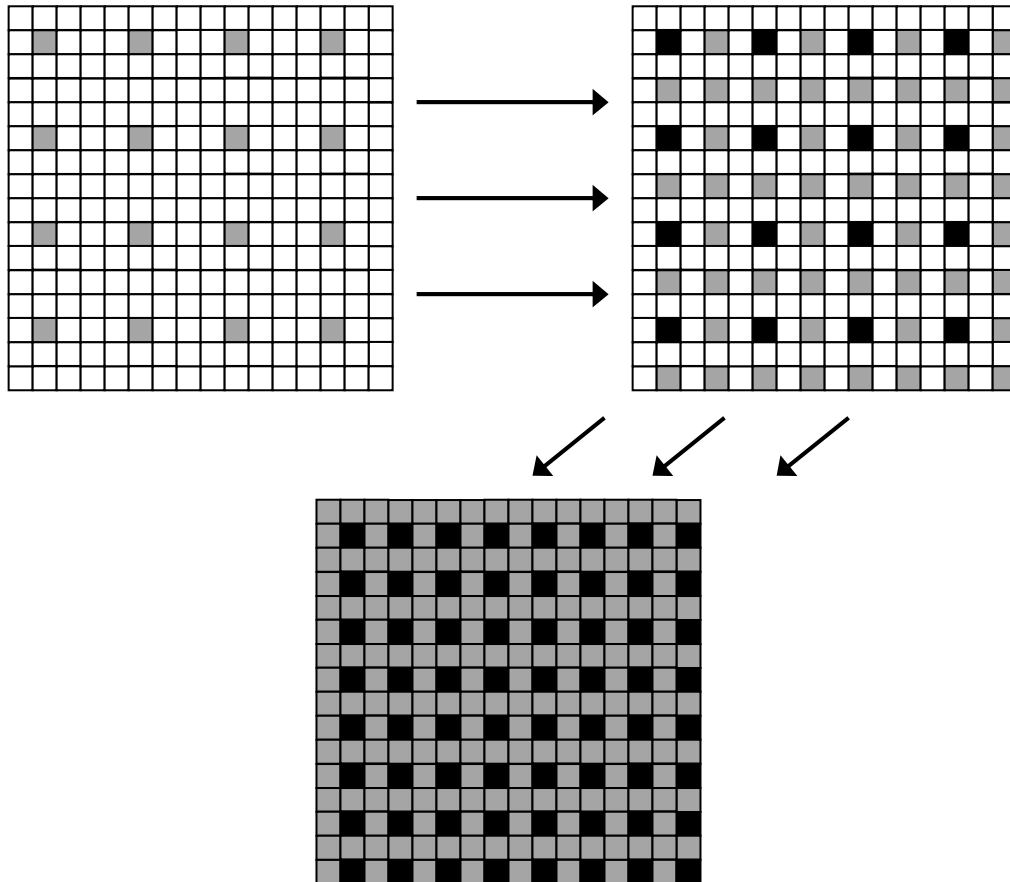


Figure 4.13: An example of the multiple grid approach used in MPS-GS, three successively finer grids clockwise from top left. Grey squares are those cells in the current grid, black are frozen cells from previously-simulated grids.

Using multiple grids reduces the relative size of the domain, speeding convergence at the coarser grids. Because of the relatively large amount of conditioning data available, structure on the finer grids is formed quicker and thus convergence is also faster on the finer grids. If there are  $g=1, \dots, G$  grids used, with  $g=1$  being the finest grids, and every  $d^{\text{th}}$  cell is used in the grid discretization then the domain on grid  $g$  is only  $1/d^{2(g-1)}$  the size of

the full domain in 2D or  $1/d^{3(g-1)}$  in 3D. It is possible to discretize the domain differently along the X, Y, and Z axes but this will not be considered here.

### **4.2.1 Grid Discretization**

The discretization of the grid  $d$  could be any integer value. Other algorithms use  $d=2$  (SNESIM, Liu, 2006, FILTERSIM, Zhang et al, 2006b) or  $d=4$  (SISIM, Deutsch and Journel, 1998). The MPS-GS algorithm uses a discretization of 2; this has the advantage of every cell in the current grid being no farther than one cell away from the nearest previously-simulated location. The coarse grids thus have the maximum influence on the progressively finer grids.

### **4.2.2 Conditioning Data**

Hard conditioning data are typically available when simulation is being carried out. The locations of these data are seldom aligned with the current simulation grid. The conditioning data are normally assigned to the nearest grid location and that cell is frozen; however, when using multiple grids this becomes more complicated. A solution is to assign the conditioning data to the nearest cells on the coarsest grid, then reassign the data to the nearest cells on each successively finer grid. The cells that were conditioning points on coarser grids need to be unfrozen and re-simulated to avoid artifacts. If a cell on a coarse grid is frozen with a hard data value and then left with that value as the conditioning datum is reassigned, two points (or more) will end up being frozen as that facies value near the conditioning data. This leads to artifacts and poor reproduction of small scale structure. Figure 4.14 shows an example of how hard conditioning data are assigned to multiple grid locations.

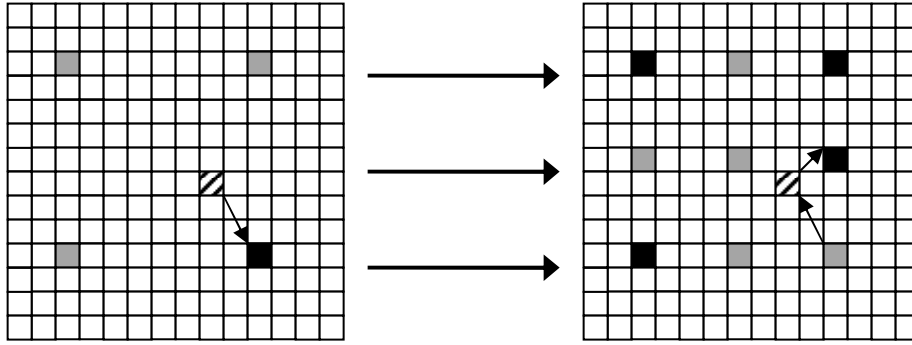


Figure 4.14: An example of the assigning of conditioning data to cells on progressively finer grids. The striped square is a sampled location; black squares are frozen cells; grey squares are active cells on the current grid.

### 4.2.3 Populating Multiple Grids

As each successive grid is simulated, every cell on the next finer grid must be populated. One-quarter (in 2D) or one-eighth (in 3D) of the cells in a grid (other than the first one) are populated by frozen locations from the previous coarser grid. The remaining cells must be populated somehow. Randomly populating finer grids using local univariate proportions can overwhelm the long-range structure imposed by the multiple grid procedure by breaking up continuous geo-objects.

It is proposed instead to populate finer multiple grids ( $g < G$ ) by replicating the large cell values to all smaller cells on the next-finer grid. The locations that are on the coarser grid are frozen while the remaining cells are assigned the same facies value. This approach maintains the structure that is formed at coarse grid discretizations and allows the fine structure to form gradually on each grid. There is also the advantage of reducing CPU time requirements; starting from a coarse structure results in faster convergence than starting from a random initial image because the initial state in the space is closer to a high-probability region than a random state.

Figure 4.15 shows an example of the population of multiple grids in the MPS-GS algorithm. The large cells on a coarse grid have large-scale structure but do not contain small-scale features such as smooth curves. The finer scale grid injects the smaller-scale smoothly varying channels into the realization.

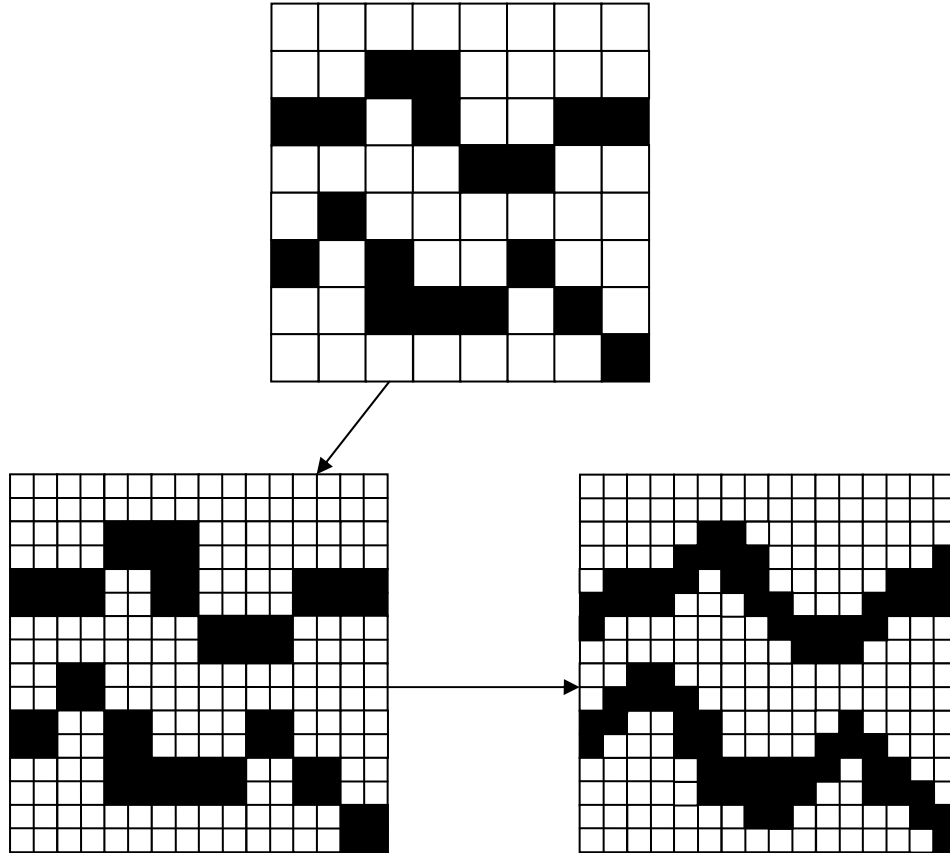


Figure 4.15: An example of the method used to populate finer grids in MPS-GS.

### Example

Figure 4.16 shows four realizations using different numbers of grids,  $G=1, 2, 3,$  and  $4$ . The TI in Figure 4.8 was used for inference of MPS; the TI and all realizations are  $250 \times 250$  cells in size; sixteen four-point MPEs were used in the MPS template; the finer grids were populated using the method outlined in Section 4.2.3; the local convergence freezing of cells from Section 4.1.4 was implemented; a connectivity correction was used with  $\eta=0.2$ .

The consequence of not using multiple grids is apparent from Figure 4.16. With a template of size  $M=16$  and  $N=4$  for a total of 64 points (65 including the null vector), there is not enough long-range structure captured to effectively reproduce channel features. For  $G=2$  there are more distinct objects but still too little long-range continuity. The case of  $G=3$  shows more continuity but none of the channels span the full width of the simulated domain. Using four grids,  $G=4$ , reproduces the long-range continuity to a

large extent, with a number of channel features extending the full size of the domain in the east-west direction.

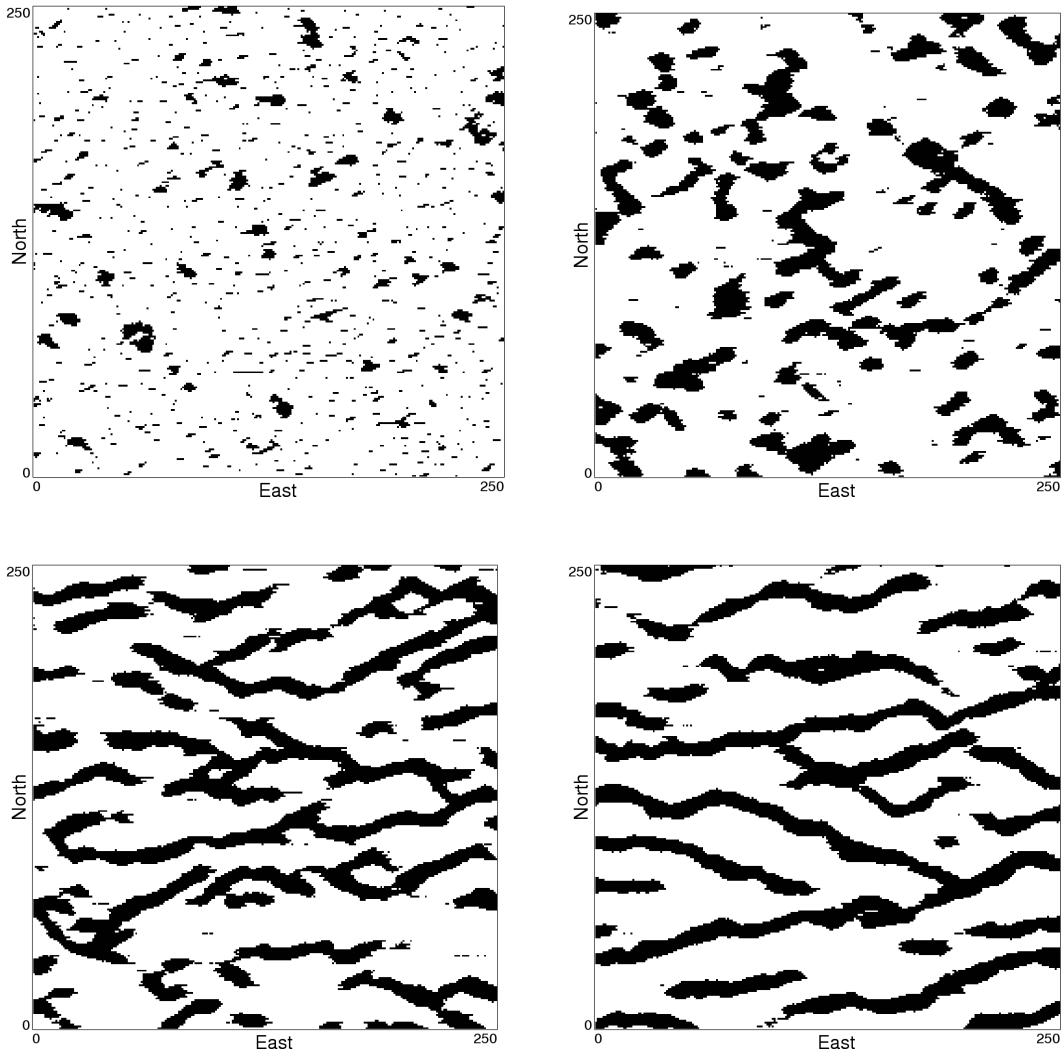


Figure 4.16: Four MPS-GS realizations using different numbers of multiple grids. Top row:  $G=1$  and  $G=2$ ; Bottom row:  $G=3$  and  $G=4$ .

### 4.3 Stopping Criteria

Some measure is needed to stop MPS-GS at a point in time at which the diminishing return in the improvement of a simulated realization makes it not worth the CPU time to continue. Some objective and easy to calculate measure is needed to diagnose when the

image has converged to an acceptable state and it is no longer worth continuing the algorithm.

Three criteria are used to check for convergence in the MPS-GS algorithm: the number of changes per loop over the simulation path stabilizes; the number of changes in a loop is below a threshold; and a specified maximum number of loops is reached.

### 4.3.1 Number of Changes per Loop

At the start of the MPS-GS algorithm there is a significant mismatch between the TI and the simulated realization. This results in changes at a large number of locations early in the algorithm as structure is formed, then eventually stabilization to a relatively constant or small number of changes. This point can be detected by calculating the slope of the number of changes versus loop number; when the slope becomes positive the curve has leveled off or turned upwards slightly (Srivastava, 1992). An increase in the number of changes can be found when small variations in the number of changes are greater than the slope.

An equivalent measure of the slope is the correlation coefficient between the loop number and the number of changes. The correlation coefficient has the advantage of being unitless and always within the range negative one to one. Using the most recent five loops to diagnose convergence, the correlation coefficient is calculated as:

$$\rho = \frac{\sum_{i=1}^5 i \cdot Nch_i - 3 \cdot \sum_{i=1}^5 Nch_i}{\sqrt{10 \cdot \left[ \sum_{i=1}^5 Nch_i^2 - \frac{1}{5} \cdot \left( \sum_{i=1}^5 Nch_i \right)^2 \right]}} \quad (4.16)$$

In Equation 4.16,  $Nch_i$  is the number of changes made in loop  $i$ ; the loops are numbered from one to five. Figure 4.15 shows a graph of the number of changes and correlation coefficients for ten realizations of the MPS-GS algorithm. On the first loop the initial image is random and so there are a large number of changes as structure forms quickly; then there is a significant drop in the number of changes until about loop 10-15 in all realizations. The correlation coefficients increase rapidly after loop 15 and the first non-negative occurrence for each realization is marked by a black dot; these are the points at which the algorithm would have been stopped. The number of changes per loop

continues to decline slowly beyond this point; however, the incremental gains in the image quality are not noticeable.

The graphs in Figure 4.17 are very typical of the results seen in other examples. This characteristic shape, with a steep decline and a leveling off between 10 and 30 loops, is consistent for a large variety of TIs, template, and parameters. The correlation coefficient in Equation 4.16 is used as the primary stopping criterion for the MPS-GS algorithm.

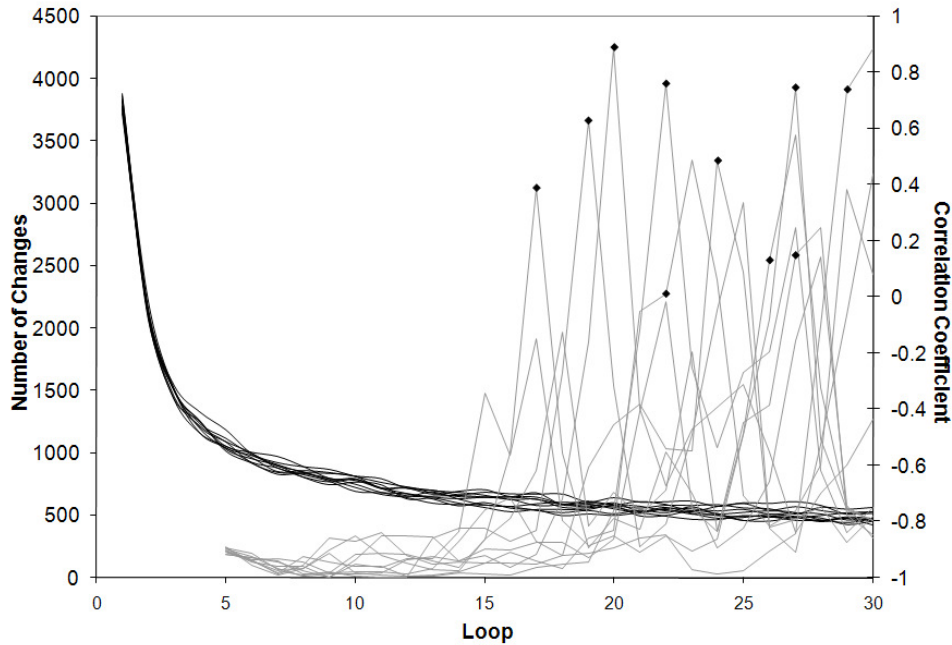


Figure 4.17: A graph of the number of changes per loop (black lines) and the correlation coefficients as in Equation 4.16 (grey lines) for ten realizations. The black dots mark the first occurrences of positive correlation coefficients.

### Effect of Freezing Cells and Multiple Grids

The correlation coefficient criterion for stopping the MPS-GS algorithm can be affected by the freezing of cells as described in Section 4.1.4 and the non-random population of multiple grids from Section 4.2.3. The existing spatial structure of the geo-objects from coarser grids changes the early behavior of the number of changes; freezing cells changes the number of potential changes that could be made. Figure 4.18 shows a graph of the number of changes per loop and the number of non-frozen points remaining in the simulation path for ten MPS-GS realizations.

A notable feature in this case is the spike in the number of changes that occurs in the second loop before the steep decline in the number of changes. The spike is caused by relatively few changes occurring early in the algorithm due to the large-scale structure introduced by multiple grids, followed by a larger number of changes made as the finer details of the geo-objects are resolved and the right angles and blocky features are smoothed out. Like the previous results, the characteristic behaviour of the number of changes is consistent for a variety of TIs and parameters.

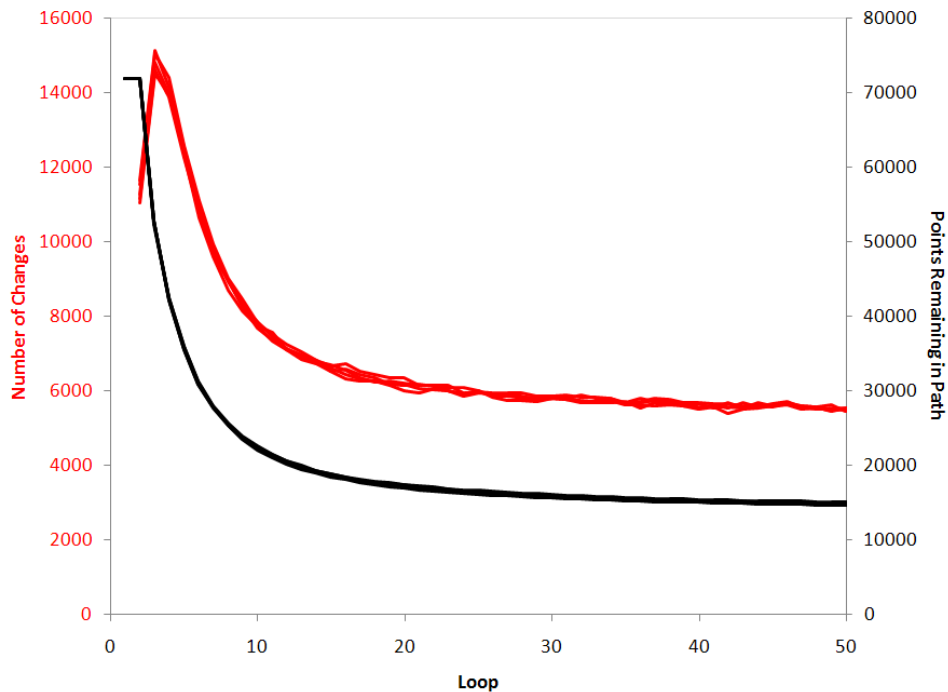


Figure 4.18: A graph showing the number of changes per loop (red lines) and the number of points remaining in the random path (black lines) for ten realizations.

### 4.3.2 Minimum Number of Changes

In some cases the number of changes per loop continues to decrease until very few cells change facies values. For those cases, the correlation coefficient does not detect when the image has effectively converged. If a proportion of cells less than a threshold value are changed on a given loop the algorithm is stopped. This value is typically set to 0.01 or 0.02.

### **4.3.3 Maximum Number of Loops**

If the first two stopping criteria are not met over a specified large number of loops, the MPS-GS algorithm is stopped. The other stopping criteria are almost always met between 10 and 30 loops and therefore it makes sense to set the maximum number of loops to 30. This stops the MPS-GS algorithm from becoming trapped for a very long time and wasting CPU resources.

The Markov chain may become trapped in a local area of the state space and cannot escape to properly sample from the joint distribution. It may be necessary to change the parameters to speed convergence.

## **4.4 Simulation Path**

All unsampled locations are visited equally in the MPS-GS algorithm, except when a cell converges locally and is frozen. The order to visit the unsampled locations in each loop is a modeling decision. Two possibilities are considered: a spiral path starting near the conditioning data and a random path.

### **4.4.1 Spiral Path**

A spiral path starts at the locations nearest the hard conditioning data and moves to the locations further away. The justification for this is the idea that the conditioning data should be given additional influence. A spiral path can introduce artifacts into a realization and can take a significant amount of CPU time to calculate for large domains (Zanon and Leuangthong, 2004).

### **4.4.2 Random Path**

A random path is used in a number of simulation algorithms because it avoids biases and artifacts in the realizations. Every unsampled location is assigned a random value and the locations are visited from least to greatest.

### 4.4.3 Conditioning Data Artifacts

Iterative algorithms have some different considerations than sequential algorithms. Using a random initial image may mask the influence of hard conditioning data and lead to artifacts, particularly near strings of data; Figure 4.19 shows three different examples of these types of artifacts. Using multiple grids or local facies proportions can help prevent these types of artifacts, but they remain a possibility. This can be a problem as earth sciences data are often available as strings, such as well logs or core samples.

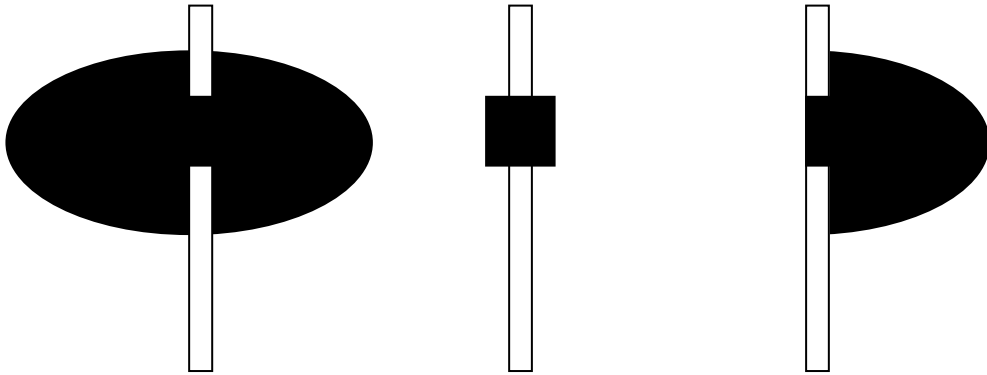


Figure 4.19: Three different types of artifacts seen near strings of conditioning data.

Using a spiral simulation path exacerbates these artifacts. To illustrate this, consider the TI and true data shown in Figure 4.20. The geo-objects are relatively simple ellipsoids and have the same spatial structure in the true data and TI. The two strings of data meant to represent drillholes or wells were taken from the true data.

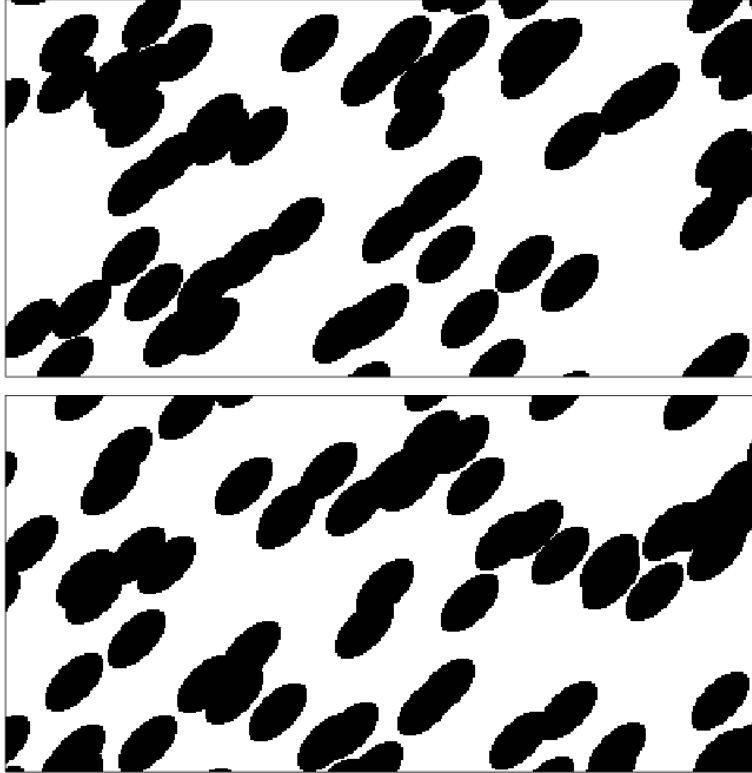


Figure 4.20: Training image (top) and true data (bottom) used to demonstrate conditioning data artifacts.

Figure 4.21 shows three stages of a realization created using the MPS-GS algorithm and a path spiraling away from the conditioning data. The three stages are after 10, 50, and 100 loops and correspond to before the realization has converged, well after convergence, and after the algorithm has been allowed to run for much too long. The artifacts near the conditioning data become progressively worse when the algorithm is allowed to run beyond convergence. Freezing cells as in Section 4.1.4 was not used so as to intensify the artifacts for illustration. These artifacts appear at the boundary between the white and black facies in the conditioning data. Most of the geo-objects are centered on the string data, and this is apparent early in the algorithm even before convergence. This bias in the placement of the geo-objects is a serious problem with using a spiral path because normally there is no reason to believe that the wells or drillholes will sample the center of every body.

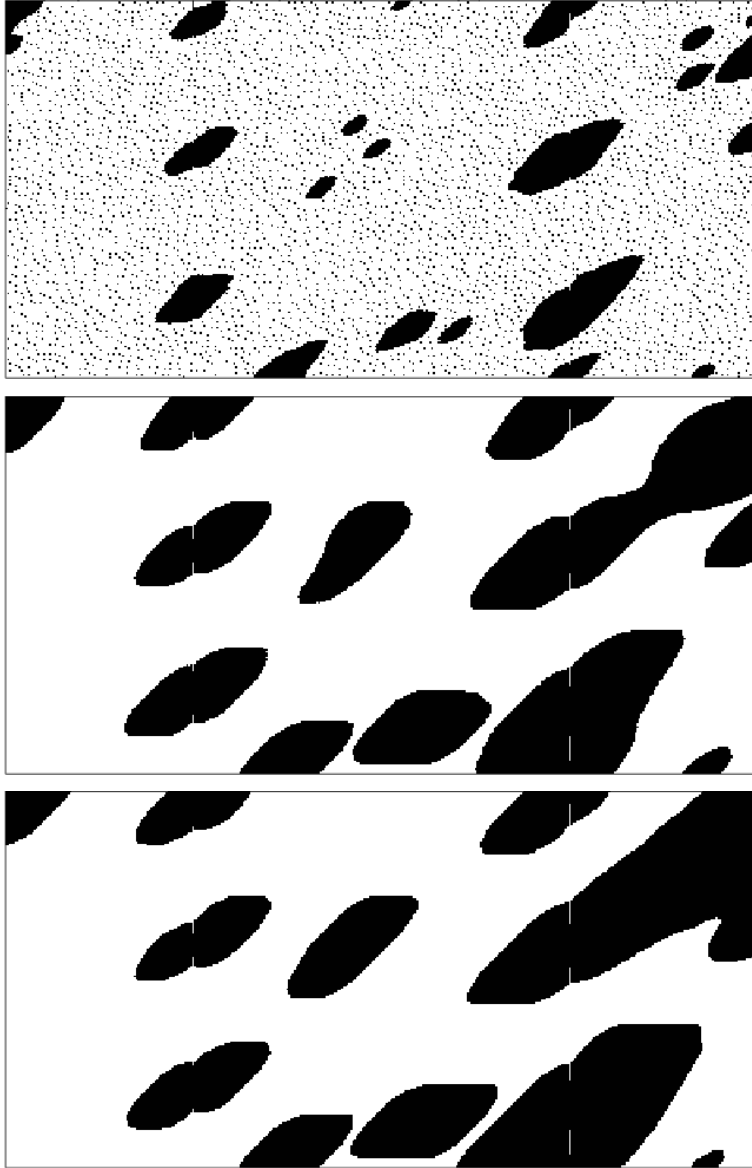


Figure 4.21: An example of the MPS-GS algorithm using a spiral path. One realization is shown after 10, 50, and 100 loops.

Figure 4.22 shows another MPS-GS realization after 10, 50, and 100 loops; this realization uses a random path to visit each location. The geo-objects are randomly distributed about the domain with no visible bias. After 50 loops some artifacts have appeared near the black/white boundaries; these artifacts are clearer after 100 loops. The random simulation path fixes the problem of artifacts near string data, but the example demonstrates that it is important to stop the algorithm once the image has converged (as discussed in Section 4.3) to prevent other artifacts from appearing.

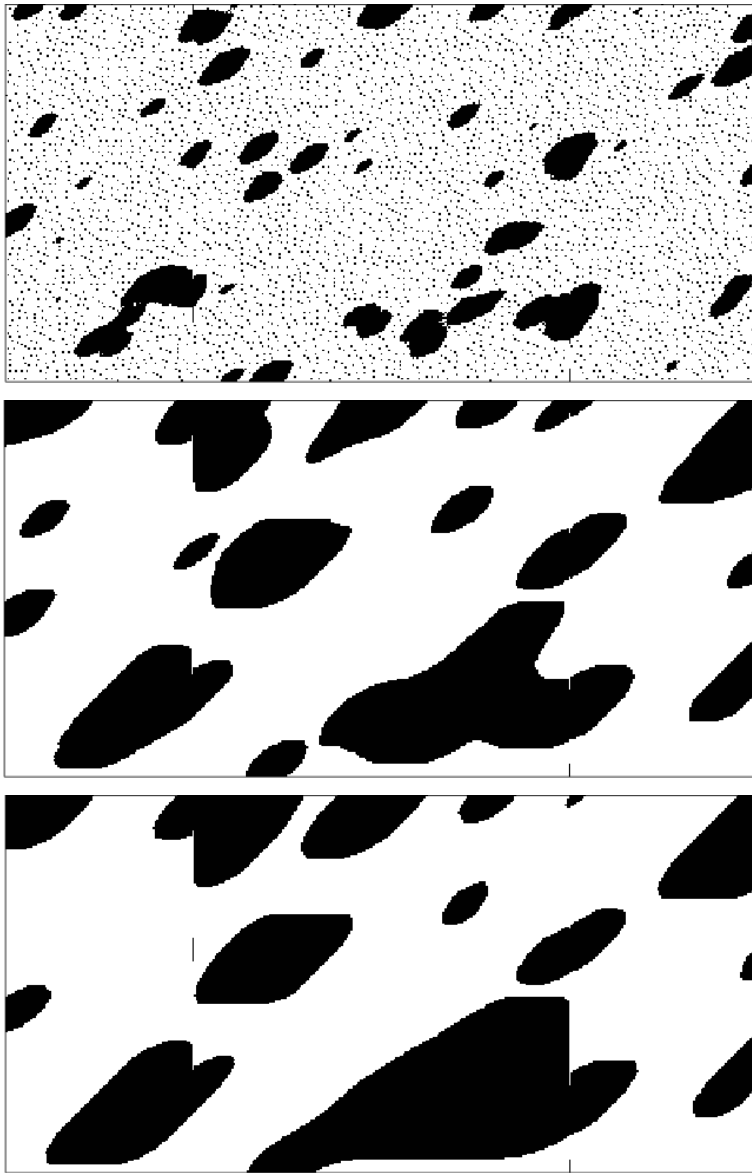


Figure 4.22: An example of the MPS-GS algorithm using a random path. One realization is shown after 10, 50, and 100 loops.

## 4.5 Edge Effects

Iterative algorithms have a number of additional artifacts near the edge of the simulated domain, or edge effects (Deutsch, 1992, Srivastava, 1992). The MPS-GS algorithm has the same problem: near the edge of the domain, the template used for calculation of the conditional distributions cannot be fully informed from the current state of the image.

This causes issues with the algorithm that need to be solved. Figure 4.23 shows an example of an MPS template near the edge of a simulated domain. Figure 4.24 shows an MPS-GS realization created using the TI in Figure 4.8; this realization clearly shows edge effects in the areas where the conditional distributions could not be calculated.

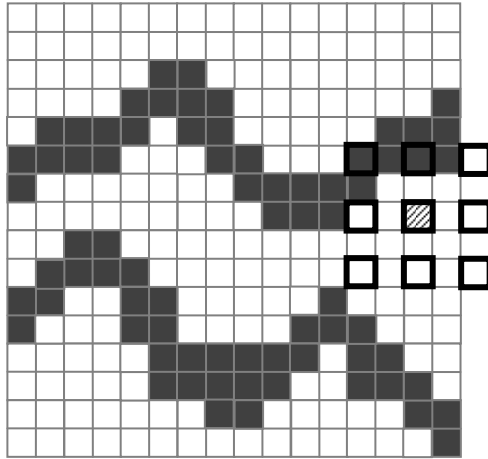


Figure 4.23: An MPS template near the edge of a simulated domain.

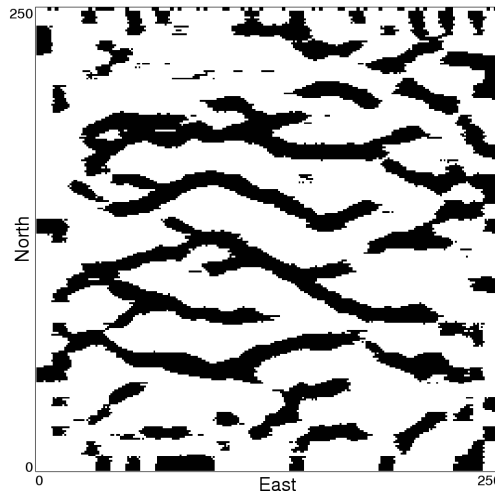


Figure 4.24: An MPS-GS realization with edge effects.

Four solutions to edge effects are considered here: solving a linear set of equations to determine the exact conditional probabilities in the absence of data in some parts of the template; wrapping the grid on itself to fully inform all location in the template; reflecting the grid on itself to full inform all locations in the template; and expanding the grid, then trimming the added locations after simulation.

### **4.5.1 Exact Solutions**

One possible solution to edge effects is to use the available information and exactly solve for the conditional probabilities using that arrangement of MPEs and indicators. Problems with this approach are that there is no easily determined answer of how to rearrange the MPEs to use only the information that is available; the TI would have to be scanned a number of times, when currently it only has to be scanned once; and solving the full system of equations many times is very cumbersome, while it currently only has to be solved once. Solving the full system of MPE covariances takes much longer than the simulation itself and so it is not feasible to solve a number of additional systems for a small portion of the domain. These problems all make using exact solutions computationally inefficient and would not provide enough of an improvement to justify the CPU and memory requirements.

### **4.5.2 Grid Wrapping**

Another possible solution to edge effects is to wrap the grid; that is, to treat the domain as a repeating phenomenon and to use the facies values of cells on the far side of the domain as conditioning information for calculating the conditional probabilities. Figure 4.25 shows an example of an MPS template being wrapped at the edge of a domain. This methodology has the advantage of being computationally fast and easy to perform; the disadvantage is that it leads to wallpaper artifacts. Figure 4.26 shows an MPS-GS realization using the wrapped grid approach, as well as a demonstration of the wallpaper artifact.

The main problem with the wallpaper artifact is that it has long-range effects, particularly in the presence of a trend. The issues that can be caused by wallpaper may not be apparent at first, but the impact on response characteristics or transfer functions can greatly change the uncertainty associated with a model.

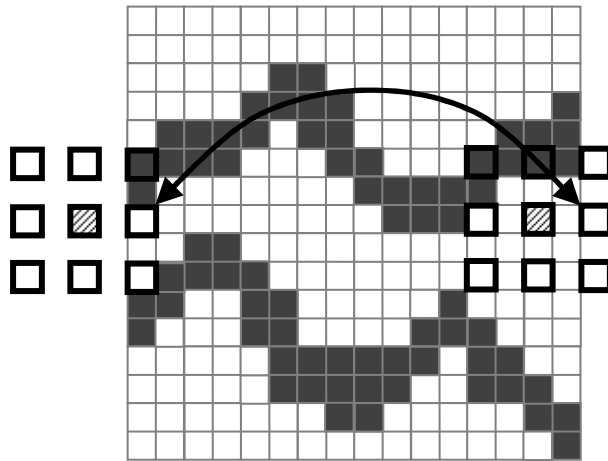


Figure 4.25: An MPS template being wrapped at the edge of a domain.

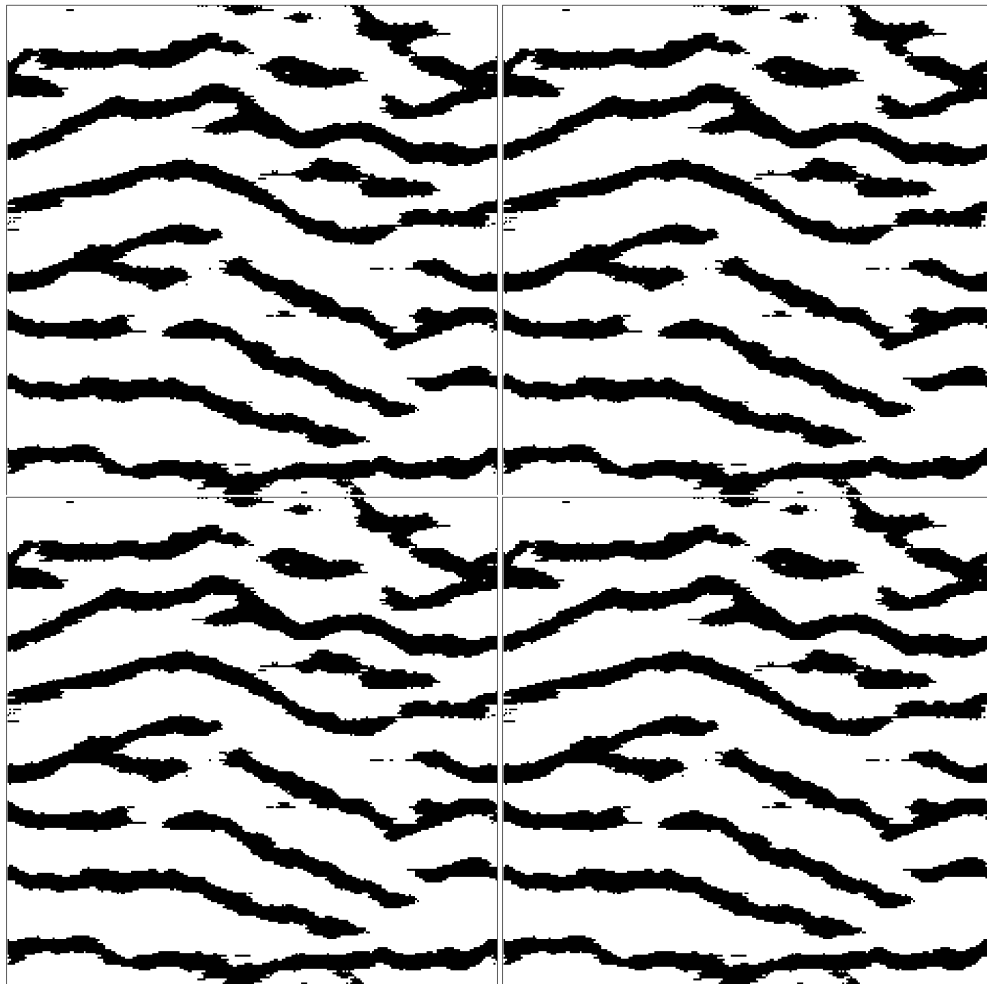


Figure 4.26: An MPS-GS realization using grid wrapping. The same realization is repeated four times to demonstrate the wallpaper artifact.

### 4.5.3 Grid Reflection

Another option for dealing with edge effects is to reflect the grid back on itself. Figure 4.27 shows an example of an MPS template being reflected at the edge of a domain. This can create some of the same problems as wrapping the grid because data values are being used as information in positions that are different than their true locations. The effects of reflecting the grid are shorter range than wrapping the grid, and occur within a single geobody rather than artificially connecting totally separate geobodies at opposite ends of the domain. Figure 4.28 shows an MPS-GS realization that uses the reflected grid method.

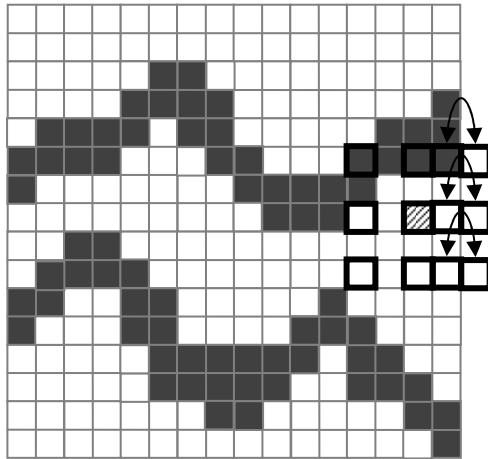


Figure 4.27: An MPS template being reflected at the edge of a domain.

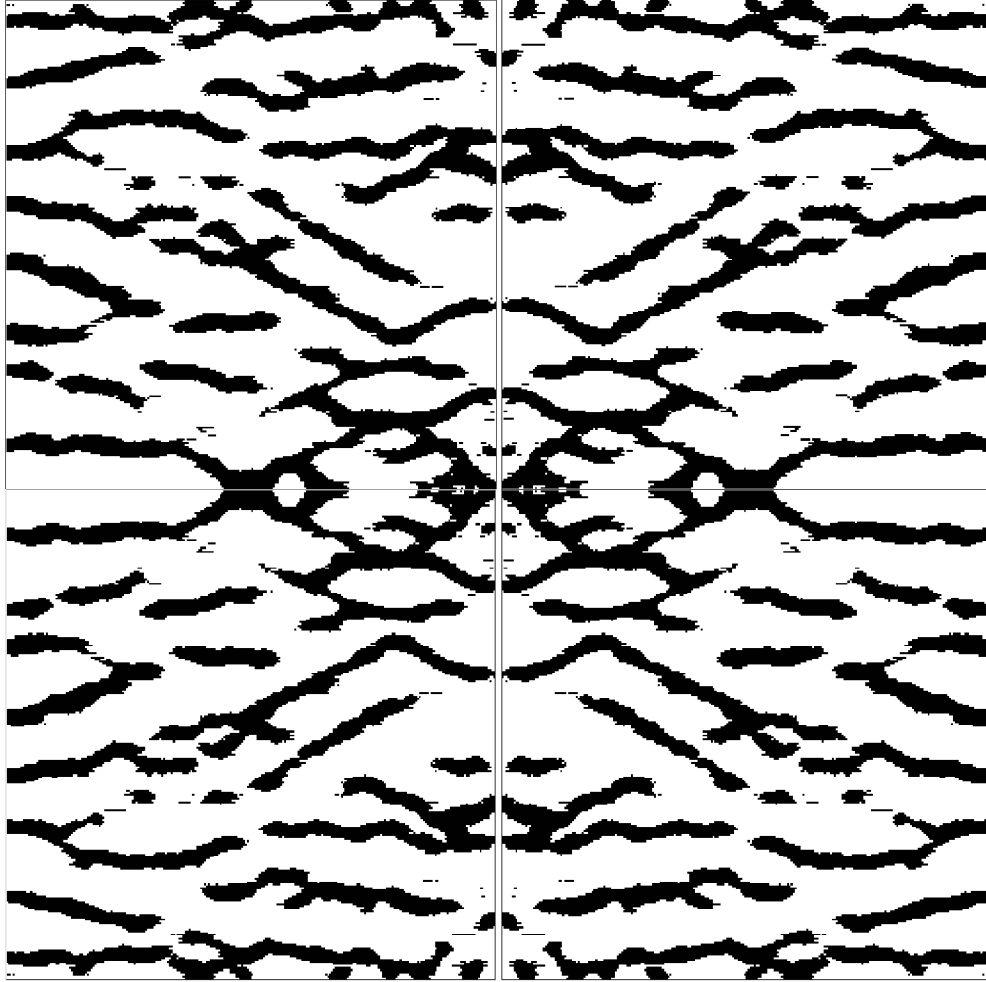


Figure 4.28: An MPS-GS realization using grid reflection (top left). The same realization is mirrored to demonstrate the effects of reflection.

#### 4.5.4 Grid Expansion

The previously mentioned methods to mitigate the problem of edge effects all have significant computational cost or leave artifacts. A way to reduce the impact of the edges of a simulated domain is to increase the effective size of the domain and then trim the expanded portion after the simulation is complete. This increases the computational time because there are more unsampled locations to visit; however, if the expansion of the grid is small relative to the entire domain and the algorithm is sufficiently fast, the increase in CPU time should not be large.

Figure 4.29 shows an MPS-GS realization that was created using a grid that was expanded by the greatest extent of the MPS template in the X and Y directions at the

coarsest grid level. The expanded portion of the domain was previously trimmed off of the realization. The realization also used the reflection of the edge of the grid. Artifacts caused by grid reflection are short-range as noted earlier; trimming the excess cells from the edge of the domain removes any noticeable effect of the reflection. The MPS-GS algorithm uses the expanded grid and reflection approach to eliminate edge effects.

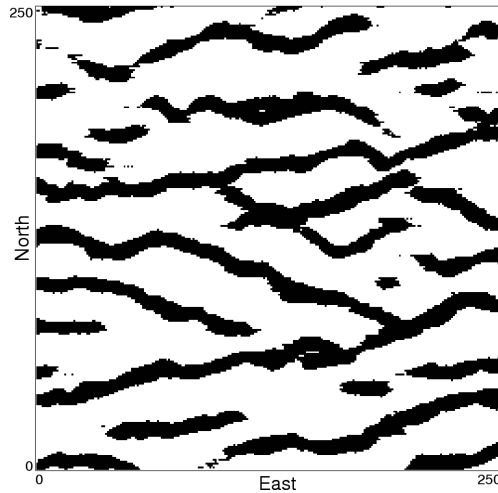


Figure 4.29: An MPS-GS realization using grid expansion and reflection.

## 4.6 Long-term Convergence Properties

As shown above, the MPS-GS algorithm can produce artifacts caused by randomness in the conditional probabilities (Section 4.1.4), conditioning data (Section 4.4.3), or edge effects (Section 4.5). To demonstrate that artifacts are not an issue and also that the stopping criteria in Section 4.3 are sufficient to identify when the image has converged, four conditional MPS-GS realizations were simulated. A total of 100 conditioning data points were used, scattered randomly in the domain. The parameters for each realization were the same:  $M=16$ ,  $N=4$ ,  $G=4$ ,  $\mu=1.0$ ,  $\eta=0.2$ . Each realization was run for a specified number of loops without using stopping criteria. The numbers of loops were 1, 10, 100, and 1000. The four realizations are shown in Figure 4.30.

From Figure 4.30, it may be seen that there is little change from the 10<sup>th</sup> loop to the 1000<sup>th</sup>. The realizations that ran for ten or more loops are similar to the unconditional realization in Figure 4.29, with no obvious edge effects or conditioning artifacts. There is some remaining noise that is not entirely eliminated by the connectivity correction.

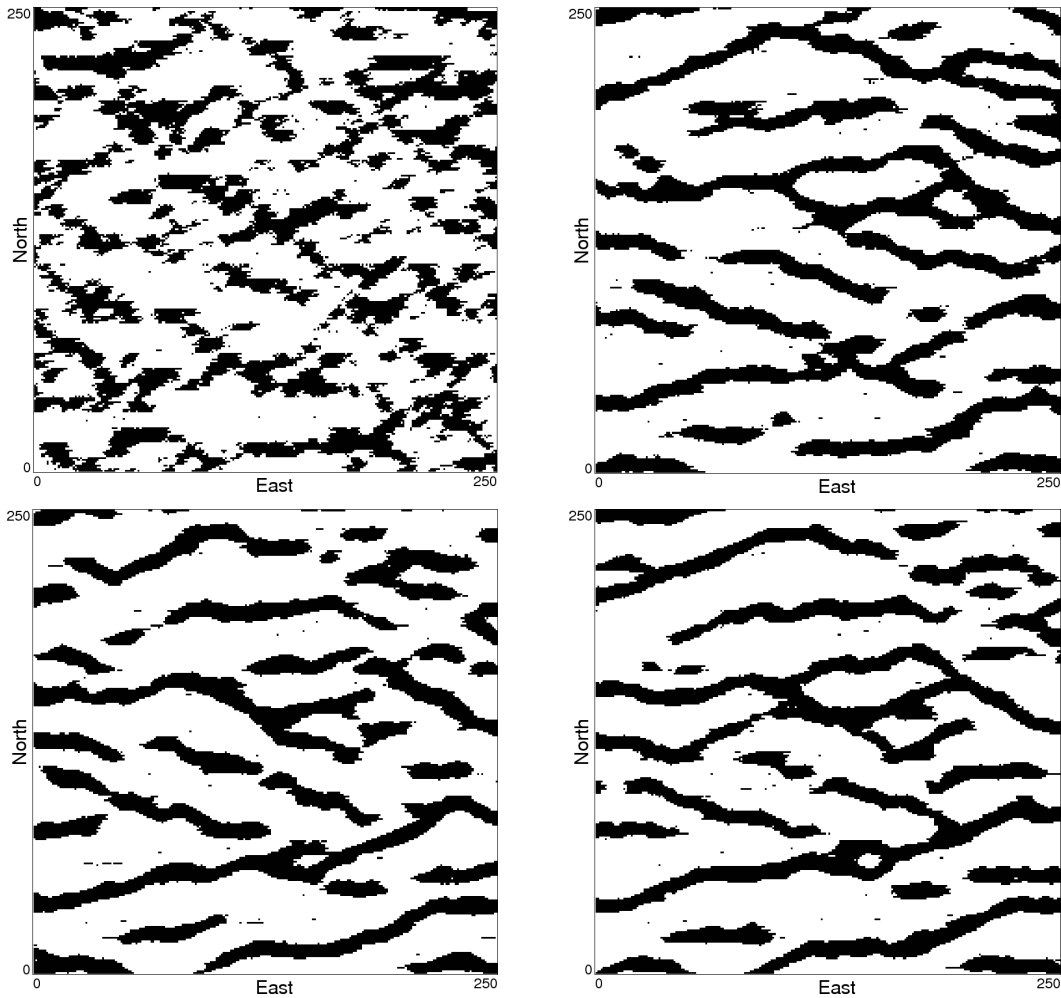


Figure 4.30: Four conditional MPS-GS realizations created using the same parameters and run through a specified number of loops. Top left: 1 loop. Top right: 10 loops. Lower left: 100 loops. Lower right: 1000 loops.

### 4.7 Evaluating Results

A common way of evaluating the quality of MPS algorithms is by visual inspection of the results compared to the appearance of the TI. While visual inspection is useful as a first pass to quality control, it is desirable to have objective statistical measures of quality for the realizations. These measures are used for evaluation of the algorithm, ranking of realizations, comparison of different TIs in a given scenario, and assessing the reproduction of target statistics such as vertical proportion curves.

The most common and simplest measures for evaluating simulation results use low-order statistics. For algorithms that use high-order moments it is logical to use more

sophisticated measures. Uncertainty assessment often necessitates the use of transfer functions or response characteristics to better predict the recoverable resources in deposits.

The criteria used to evaluate a model are subjective and dependent on the purpose for which the model was created. The minimum threshold for acceptance will not be the same for all criteria in all cases. Often a manager or non-technical person will make the final decision as to how much deviation from a target measure is considered acceptable.

#### **4.7.1 Lower-Order Statistics**

The simplest statistical measure in geological models of facies is the univariate proportions of the different facies. Global univariate proportions are generally known more accurately than other statistics and often have a great impact on the results. The simulated facies proportions should match the input quite closely; the actual threshold for how much difference from the target is acceptable is dependent on the relative importance of the different facies and the specific problem.

Local univariate proportions,  $P^{LOC}$ , should also be checked for reproduction of the model. Vertical proportion curves determined from hard data or local proportions from secondary sources such as seismic should be reproduced on average.

Second-order statistics such as variograms should be checked for reproduction. The variogram is a simple spatial statistic to calculate. Comparison of the variogram for each facies is relatively fast and easy. The data variograms and TI variograms should both be used as references, although they should be close to one another for a TI to be justifiable. Cross variograms are more difficult to infer from data but can be used to compare a TI to simulated results.

#### **4.7.2 Multiple-Point Statistics**

The extension of spatial moments to higher orders can be used for both the selection of a TI appropriate for a given scenario and the assessment of the reproduction of the MPS in a TI (Boisvert, 2007, Boisvert et al, 2007b). The simplest MPS that can be used for comparison are runs, particularly when the hard conditioning data are in vertical strings such as wells or drillholes. Other linear arrangements of data are less common but could also be used if available. The comparison of the runs distributions of data, the TI, and the

results of simulation provides a good measurement for the connectivity and continuity of geobodies.

Using a multiple-point histogram (MPH) is more difficult due to the relations between different facies. Linear templates can be used to calculate experimental MPHs from string data, but the extent of this is limited; if the order of the statistics is too high then it is not possible to infer a full MPH even in a limited template. Vertical linear MPH templates with no more than about four points can be used successfully if there are thousands of data points, giving a reference to compare to TIs and simulated realizations.

Connectivity functions are nearly impossible to infer from sample data. The probability of connectivity between two locations can be determined in some cases using well tests or production data; these cases primarily apply to those projects that use flow. The use of connectivity functions mainly applies when comparing TI statistics to unconditional realizations for measuring the quality of different algorithms.

### **4.7.3 Response Characteristics**

Simple statistical measures are useful for fast and easy comparison of algorithms or realizations. However, before model uncertainty to assess the risk in a project, some sort of transfer function or physical simulation is performed. These methods include flow simulation for petroleum reservoirs and mine design for mineral deposits.

## 5 Case Studies

The MPS-GS algorithm can be used for facies modeling in a variety of geological settings. This chapter demonstrates three scenarios: a braided channel system; an eolian sandstone architecture; and a fluvial petroleum reservoir. The results are quantified and compared to SISIM (Deutsch and Journel, 1998).

Common methods are used to compare the results. These methods include a qualitative visual inspection, measurement of the CPU time required, comparison of univariate proportions, and calculation of indicator variograms. More complex measures such as multiple-point histograms are also considered.

### 5.1 Braided Channels

The first scenario considered as a case study is a braided channel system. This type of geology is associated with petroleum reservoirs and features long, continuous high-permeability channels in a background facies of low-permeability shale. The curvilinear connectivity that is seen in channel-type geological structure cannot be characterized by traditional variogram-based geostatistics.

#### 5.1.1 Data and Training Image

Figure 5.1 shows a braided channel training image that is used for this case study. The TI is 250x250 cells and has 30% channel (black) facies and 70% shale (white) facies. If the TI were a real geological body the cell size would be on the order of tens of metres; the overall size of the domain would be 2.5km to 25km. The MPS-GS algorithm works on a cell-by-cell basis and so the size in any specific case does not matter as long as there is consistency between the TI and simulated domain.

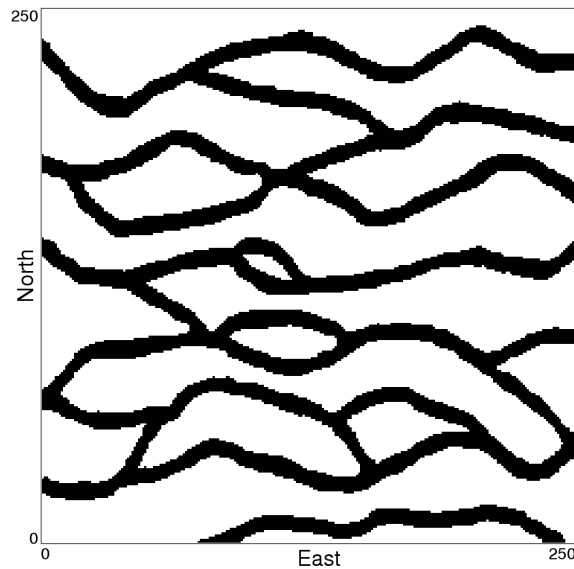


Figure 5.1: The TI used for the braided channel study (Journel, 2004, Liu, 2006, Strebelle, 2002, among others).

To quantify the high-order structure in the TI, a multiple-point histogram was calculated. The template used was nine points in a three-by-three square pattern. Figure 5.2 shows the histogram with the classes sorted from greatest frequency to least; only the 64 classes with frequencies above 0.0001 are shown. The MPH is a useful tool for evaluating the ability of an algorithm to reproduce high-order structure in unconditional realizations.

For this case study, 50 data locations were extracted from the TI to be used in conditional simulation. Figure 5.3 shows a location map of the sample data. A notable feature of the data is the univariate proportions: 35, or 70%, of the samples are channel facies (black); 15, or 30%, are the background facies (white). This is the reverse of the TI proportions and tests the effectiveness of the servosystem. The data were selected to be scattered in a random-looking arrangement and also specifically for the mismatch to the TI univariate proportions.

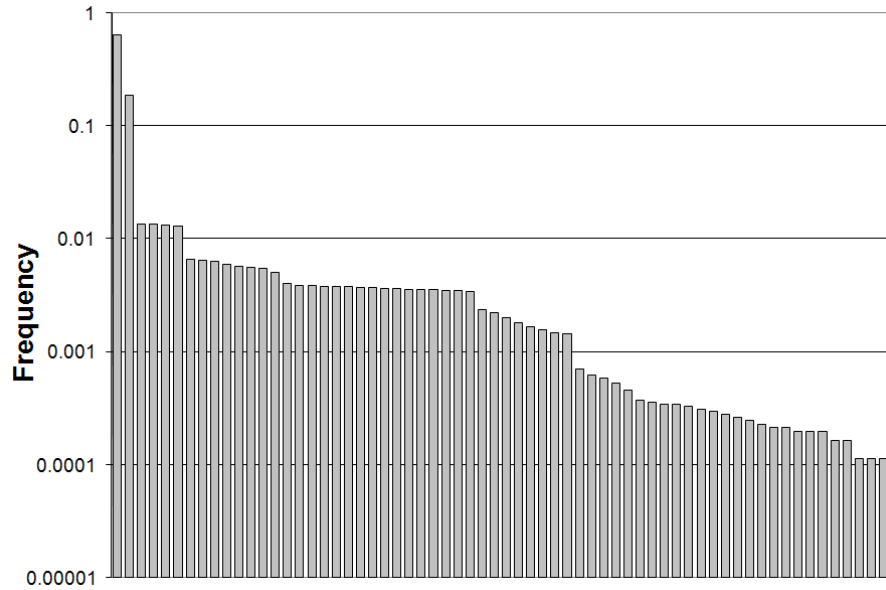


Figure 5.2: The nine-point histogram of the braided channel TI.

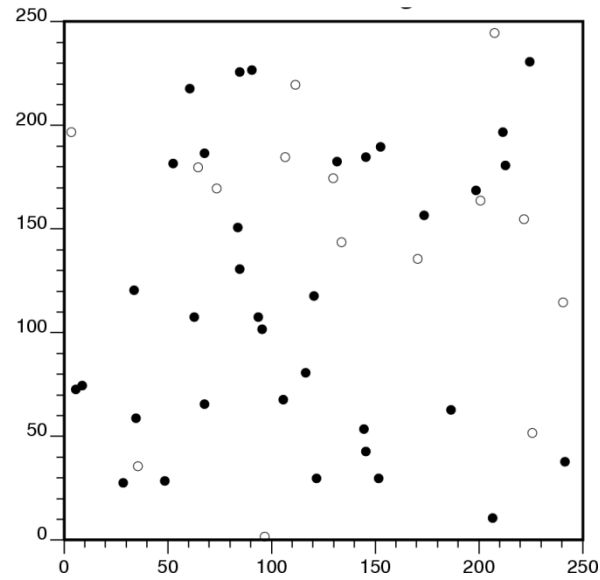


Figure 5.3: 50 data points extracted from the braided channel TI.

A major consideration for the algorithm is the time required for simulation. MPS-GS calculates the optimal linear estimation weights from Equation 4.1 and stores them before proceeding with the simulation. This upfront computational effort is significant and for large MPEs can be greater than the time required for simulation. Table 5.1 shows the CPU time needed to create a template and then scan the TI and solve the system of

equations to find the optimal weights. Four cases are considered:  $M=32$  and  $N=32$ ;  $M=16$  and  $N=4$ ;  $M=10$  and  $N=6$ ;  $M=8$  and  $N=8$ . The scanning of the TI is the driving factor for the smaller MPEs; for eight-point events solving the system of equations is more time-consuming. Four grids were used in simulation and so four systems of equations had to be solved.

Table 5.1: CPU time required to create the templates and calculate MPS for the braided channel study.

Statistics ( $M \times N$ )	Time Required (mm:ss)	
	Template Creation	MPS Calculation
32x2	0:02	2:50
16x4	0:04	2:03
10x6	0:05	2:16
8x8	0:07	6:59

### 5.1.2 Unconditional Simulation

Unconditional simulation was performed using the TI shown in Figure 5.1. Twenty realizations were simulated using the four different MPS templates described above; twenty SISIM realizations were simulated for use as a baseline comparison. Table 5.2 shows the time required for simulation in each case. All simulations were performed using four grids; the MPS-GS realizations used a servosystem parameter of  $\mu=1.0$  and a connectivity correction factor of  $\eta=0.2$ . A maximum of thirty loops was imposed for stopping, but this limit was rarely reached. All realizations are the same size as the TI, 250x250 cells.

Table 5.2: CPU time required to simulate twenty unconditional realizations for the braided channel study.

Statistics ( $M \times N$ )	Time Required (mm:ss)
32x2	1:10
16x4	1:01
10x6	1:00
8x8	1:00
SISIM	0:33

Figures 5.4 through 5.8 show the results of the unconditional simulations, one figure for each case. Each Figure has three parts: (a) two unconditional realizations; (b) the indicator variograms of ten unconditional realizations compared to the TI variograms; (c) a comparison of the TI MPH and the P5, median, and P95 simulated MPH frequencies.

From part (a) of the Figures, it can be seen that the MPS-GS realizations better reproduce the long-range continuity and channel structure than the SISIM realizations.

Comparing the variogram reproduction in part (b) of the Figures, the east-west variograms are reproduced successfully for all cases; the MPS-GS realizations using larger MPEs have slightly too-low variograms but the range and shape are appropriate. The north-south direction shows a clear difference in the variogram reproduction between simulation methods, as MPS-GS successfully reproduces the channel/background repeating pattern and thus has variogram values above the sill. SISIM does not reproduce this pattern.

Part (c) of Figures 5.4 through 5.8 shows the TI MPH from Figure 5.2 and the P5, P50, and P95 frequencies from the simulations. Major similarities and differences between the frequencies can be observed. Figure 5.9 shows a graph of the absolute MPH differences from the TI for the five different cases. The P50 realization values are shown as well as the P5 to P95 range. The MPS-GS realizations match the nine-point TI histogram much better than the SISIM results; the MPS-GS cases have absolute differences in the range of 0.05 to 0.10, while the SISIM realizations have differences of 0.21 to 0.31.

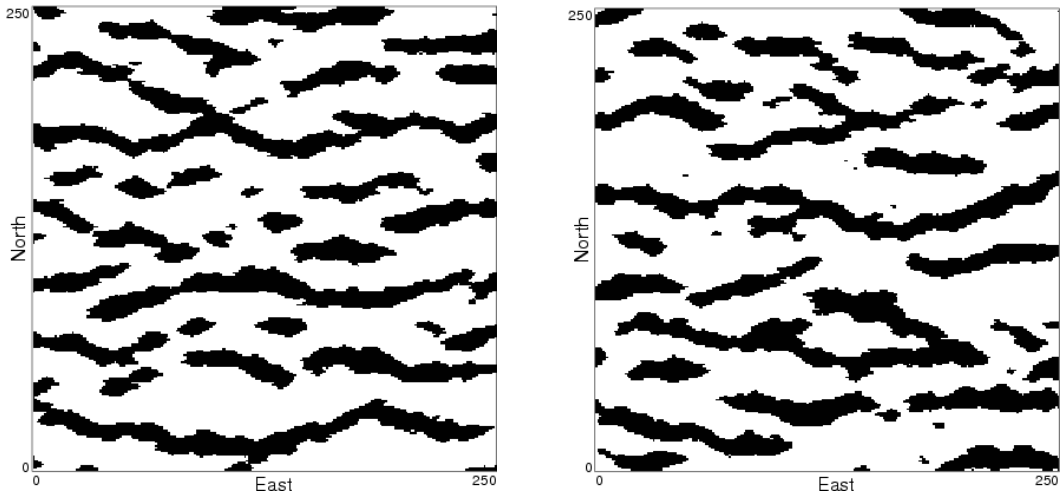


Figure 5.4a: Two unconditional MPS-GS realizations using  $M=32$  and  $N=2$ .

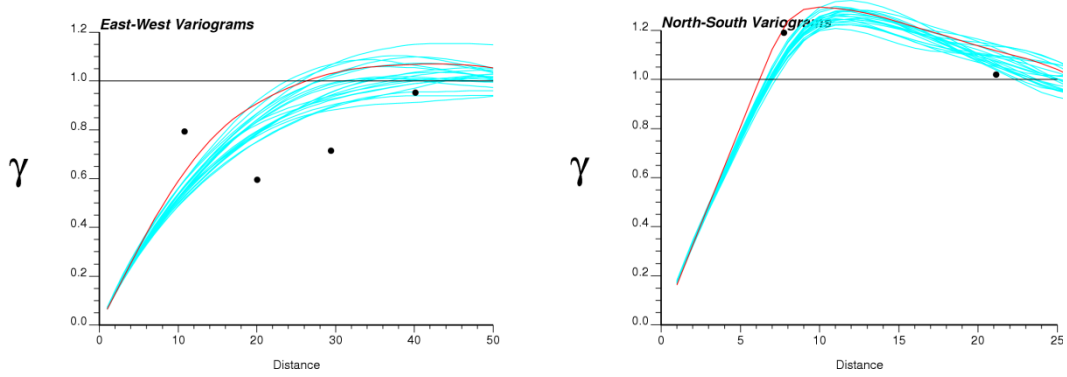


Figure 5.4b: The indicator variograms of the TI (red line), data (black dots) and 20 MPS-GS realizations (blue lines) in the east-west (left) and north-south (right) directions.

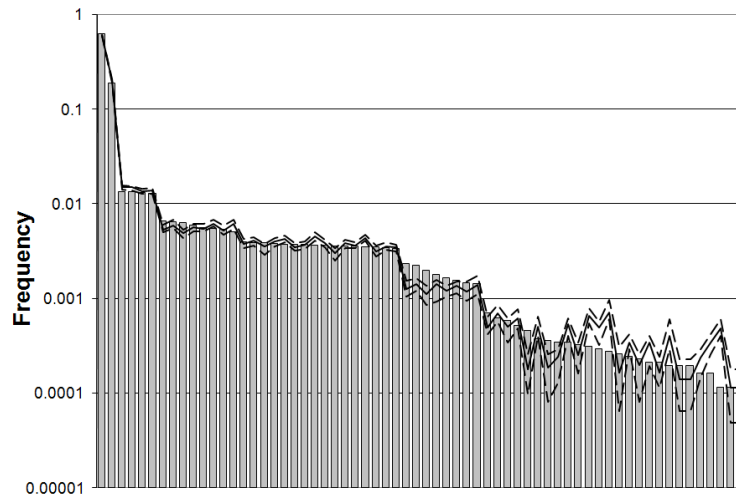


Figure 5.4c: The MPH reproduction of 20 MPS-GS realizations. Bars: reference TI MPH; solid line: median MPH frequencies; dashed lines: P5 and P95 MPH frequencies.

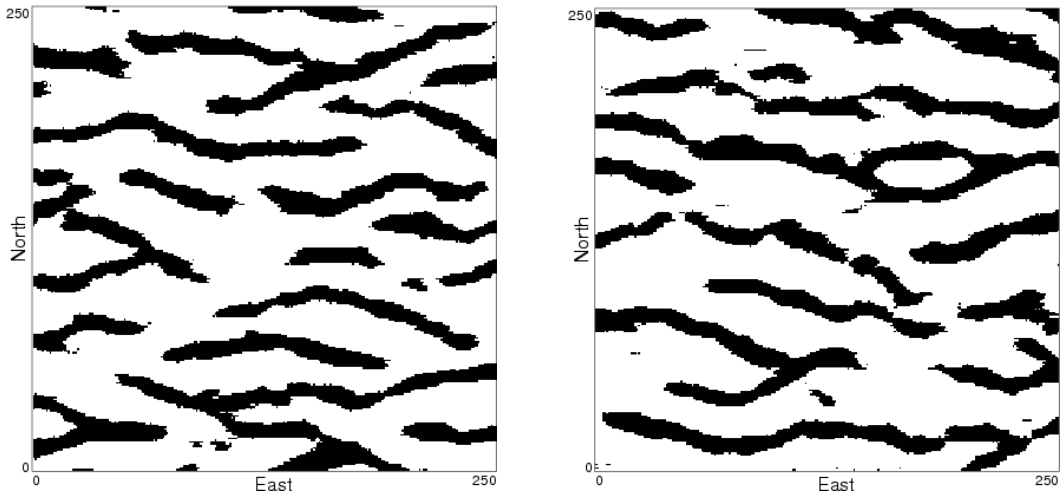


Figure 5.5a: Two unconditional MPS-GS realizations using  $M=16$  and  $N=4$ .

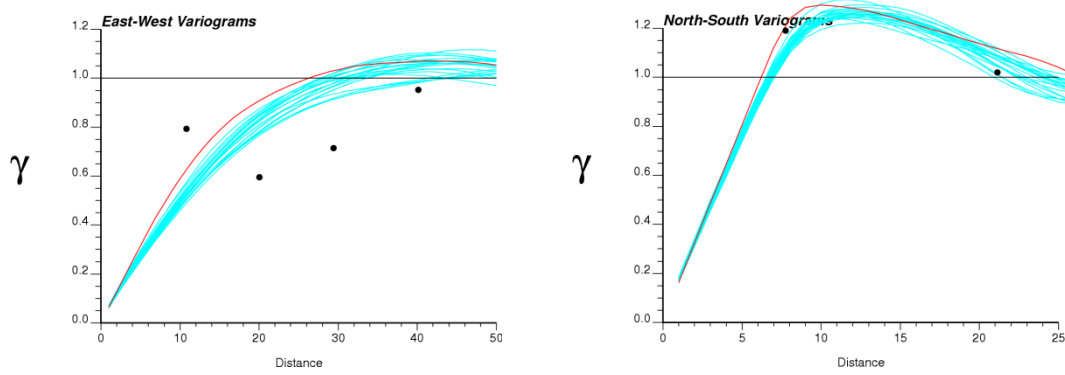


Figure 5.5b: The indicator variograms of the TI (red line), data (black dots) and 20 MPS-GS realizations (blue lines) in the east-west (left) and north-south (right) directions.

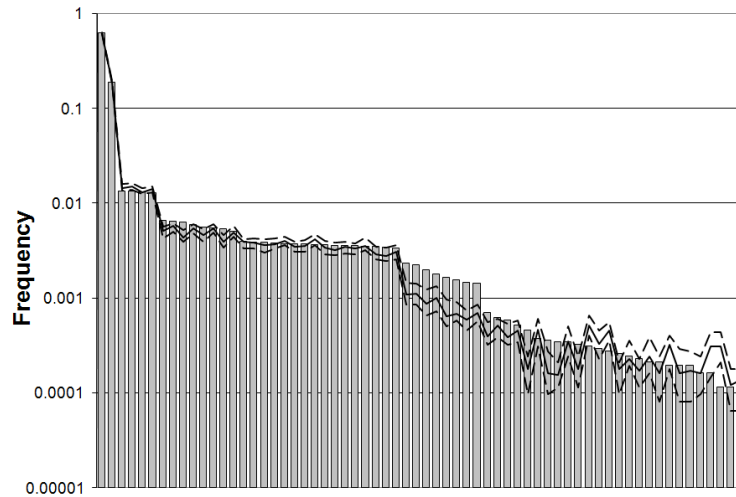


Figure 5.5c: The MPH reproduction of 20 MPS-GS realizations. Bars: reference TI MPH; solid line: median MPH frequencies; dashed lines: P5 and P95 MPH frequencies.

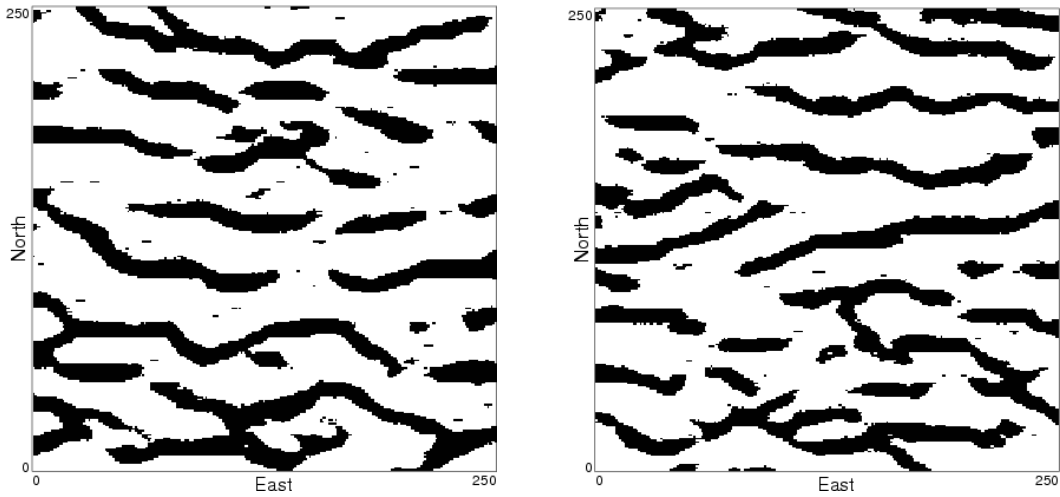


Figure 5.6a: Two unconditional MPS-GS realizations using  $M=10$  and  $N=6$ .

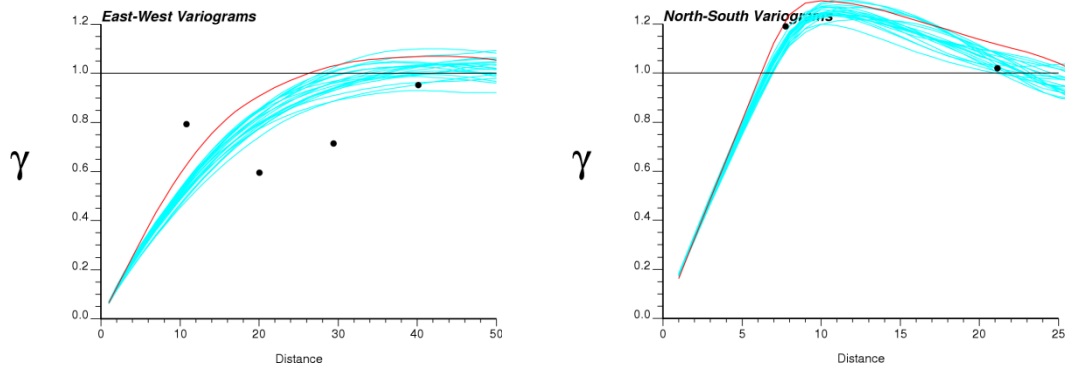


Figure 5.6b: The indicator variograms of the TI (red line), data (black dots) and 20 MPS-GS realizations (blue lines) in the east-west (left) and north-south (right) directions.

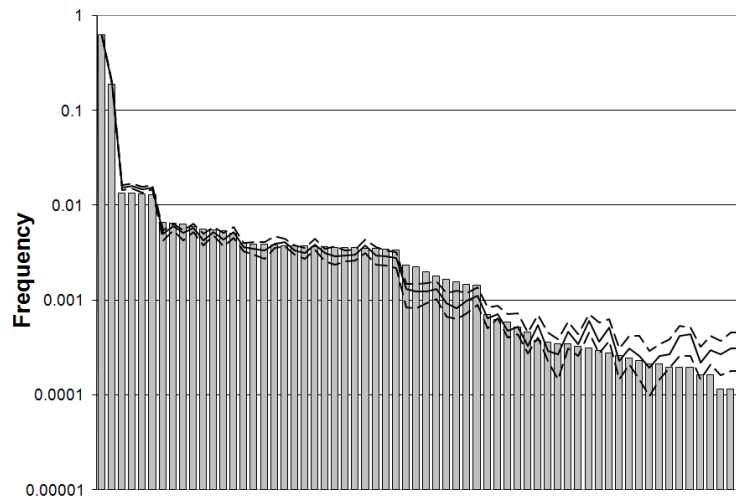


Figure 5.6c: The MPH reproduction of 20 MPS-GS realizations. Bars: reference TI MPH; solid line: median MPH frequencies; dashed lines: P5 and P95 MPH frequencies.

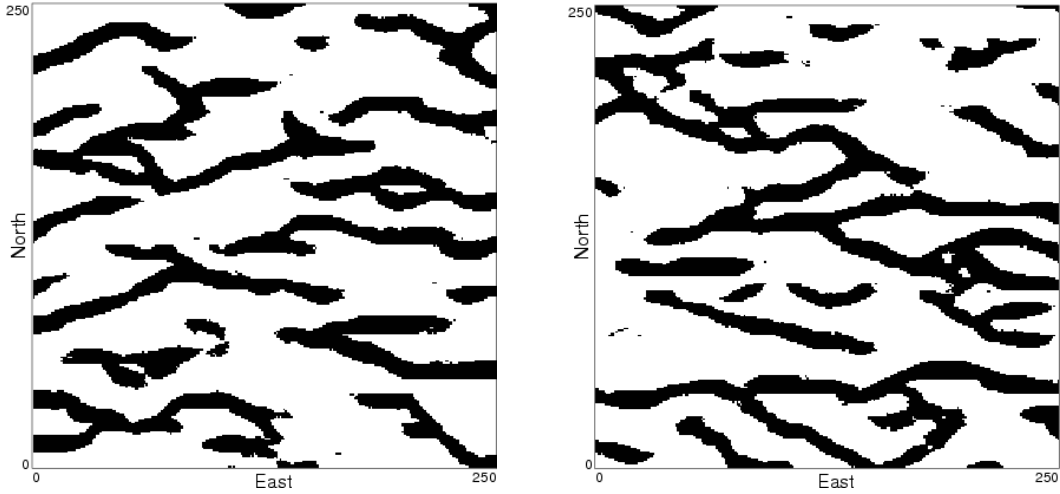


Figure 5.7a: Two unconditional MPS-GS realizations using  $M=8$  and  $N=8$ .

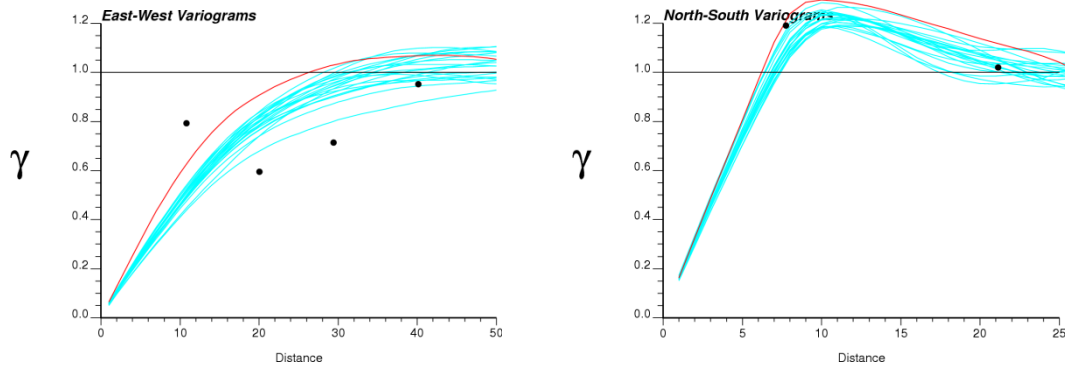


Figure 5.7b: The indicator variograms of the TI (red line), data (black dots) and 20 MPS-GS realizations (blue lines) in the east-west (left) and north-south (right) directions.

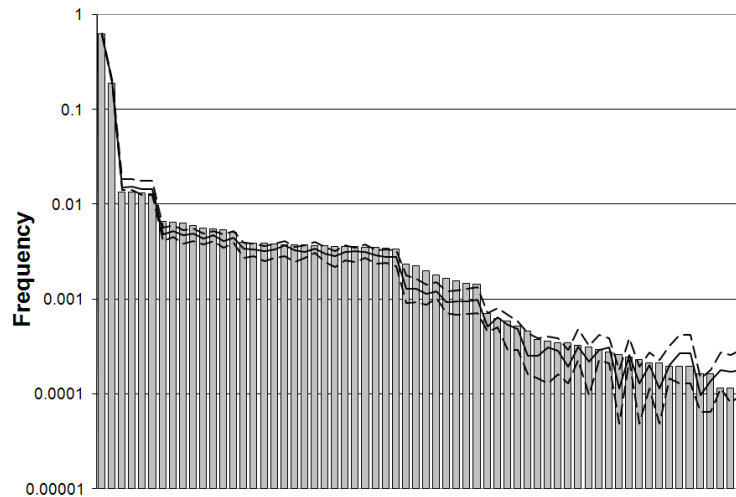


Figure 5.7c: The MPH reproduction of 20 MPS-GS realizations. Bars: reference TI MPH; solid line: median MPH frequencies; dashed lines: P5 and P95 MPH frequencies.

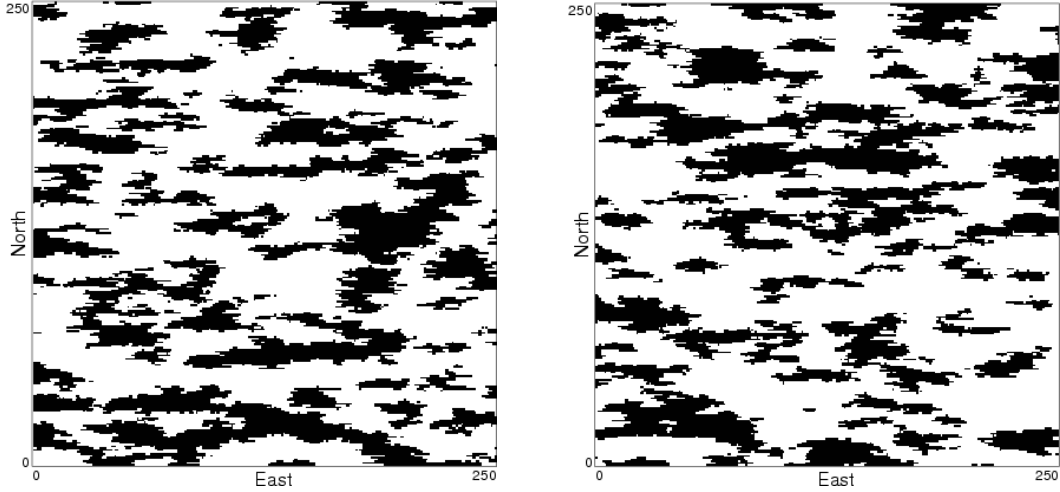


Figure 5.8a: Two SISIM realizations.

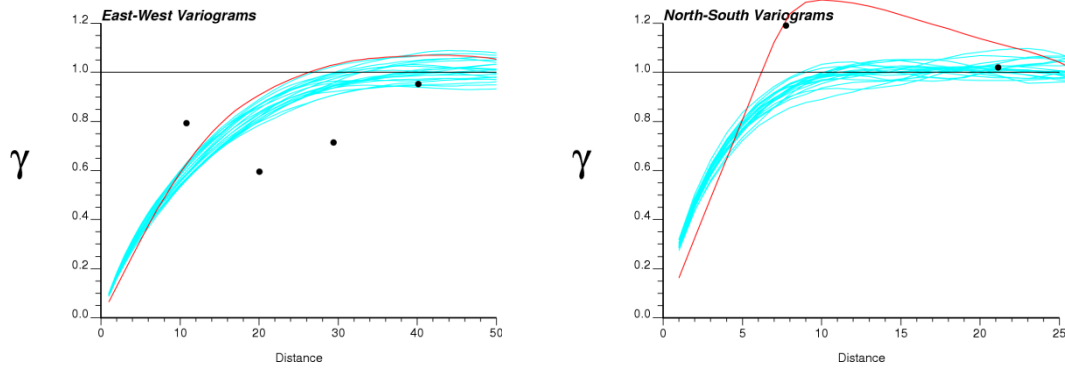


Figure 5.8b: The indicator variograms of the TI (red line), data (black dots) and 20 SISIM realizations (blue lines) in the east-west (left) and north-south (right) directions.

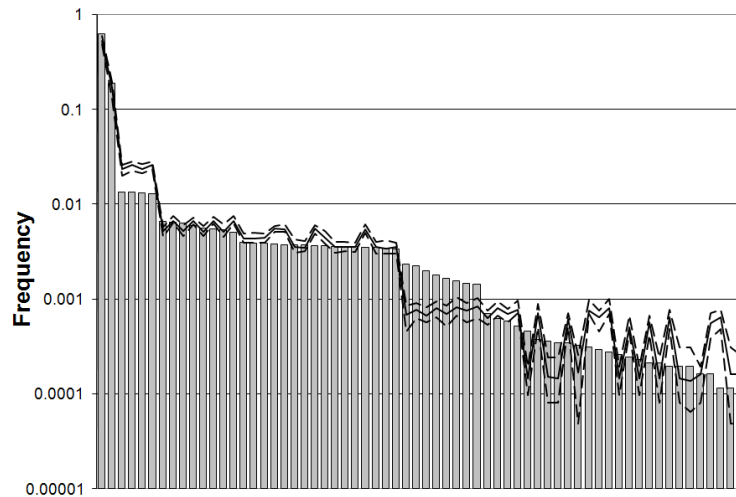


Figure 5.8c: The MPH reproduction of 20 SISIM realizations. Bars: reference TI MPH; solid line: median MPH frequencies; dashed lines: P5 and P95 MPH frequencies.

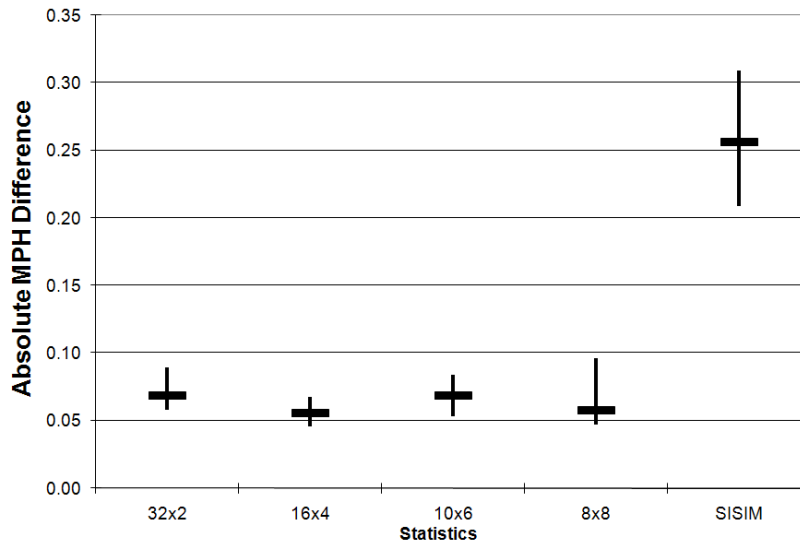


Figure 5.9: A graph of the absolute MPH differences for each case of the braided channel study between twenty realizations and the TI. Bars: P50 realization difference; lines: P5 and P95 realizations.

### 5.1.3 Conditional Simulation

Hard sample data is often available in earth sciences applications. Producing realizations that reproduces this data and the TI is the goal of MPS algorithms such as MPS-GS. Twenty realizations were simulated using the four MPS-GS cases and SISIM. The time required for each set of twenty realizations is shown in Table 5.3; the results are very similar to the unconditional scenario. All parameters were the same as the unconditional case.

Figures 5.10 through 5.14 show the results of the conditional simulations. Each Figure is made up of two parts: (a) two conditional realizations; (b) a map of the simulated probability of channel (black) facies at all locations in the domain. From part (a) it can be seen that the realizations appear much the same as the unconditional realizations shown above; this demonstrates that MPS-GS is capable of using hard data without losing the ability to reproduce the geometric structure of the TI.

Part (b) of Figures 5.10 through 5.14 shows the ranges of uncertainty near the data for the prior structure model used in each case.

Table 5.3: CPU time required to simulate twenty conditional realizations for the braided channel study.

Statistics ( $M \times N$ )	Time Required (mm:ss)
32x2	1:12
16x4	1:04
10x6	1:00
8x8	1:00
SISIM	0:29

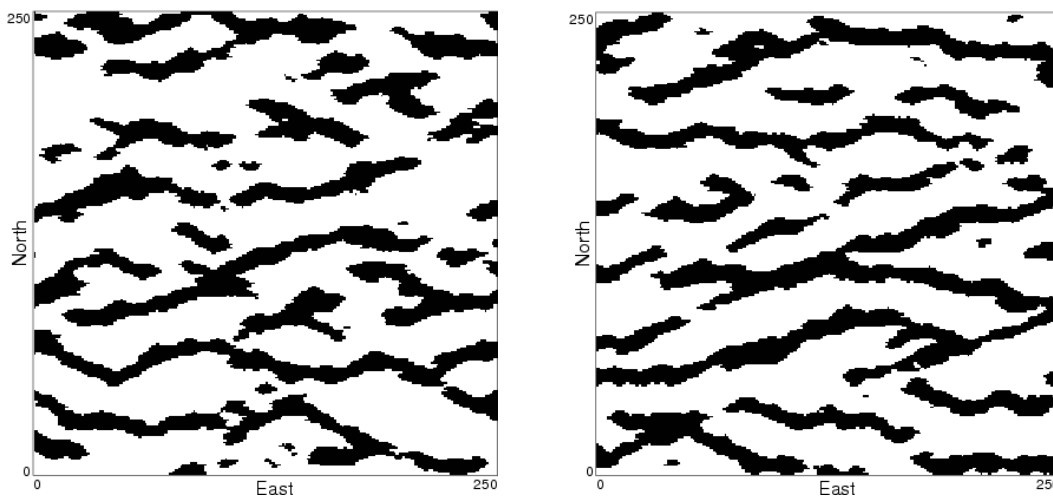


Figure 5.10a: Two conditional MPS-GS realizations using  $M=32$  and  $N=2$ .

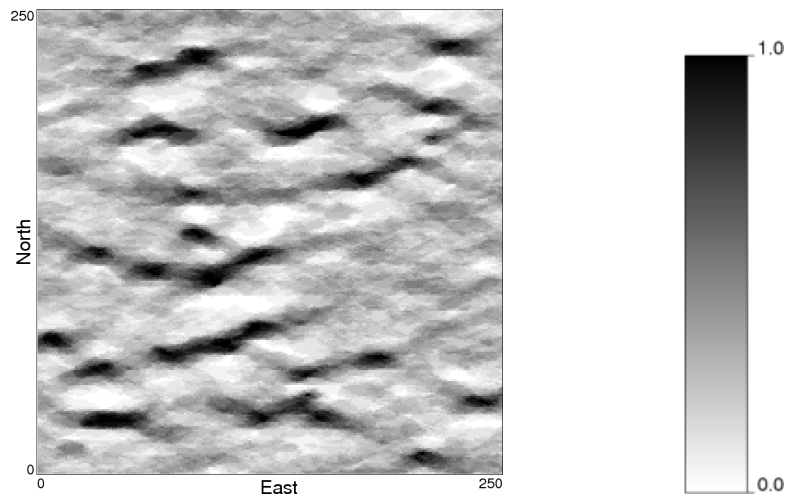


Figure 5.10b: The simulated proportions of sand for 20 conditional MPS-GS realizations.

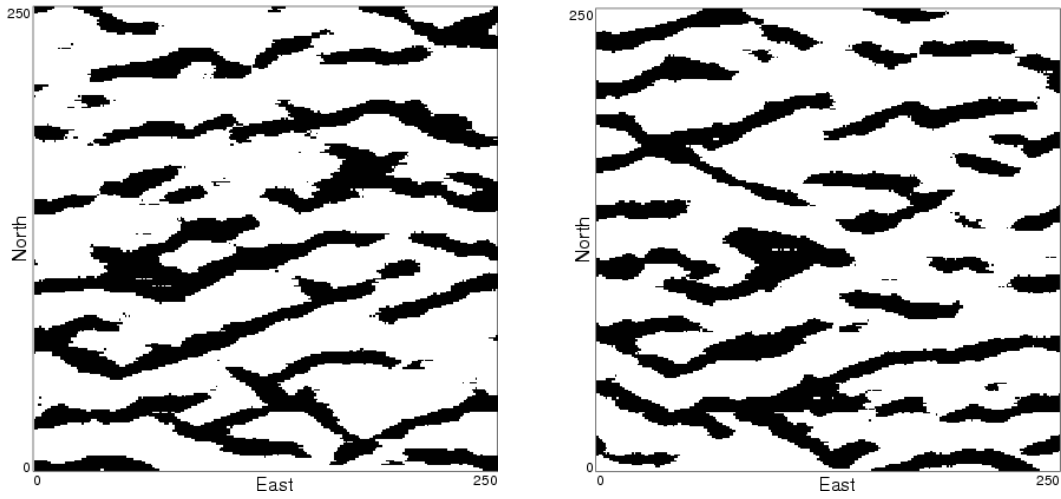


Figure 5.11a: Two conditional MPS-GS realizations using  $M=16$  and  $N=4$ .

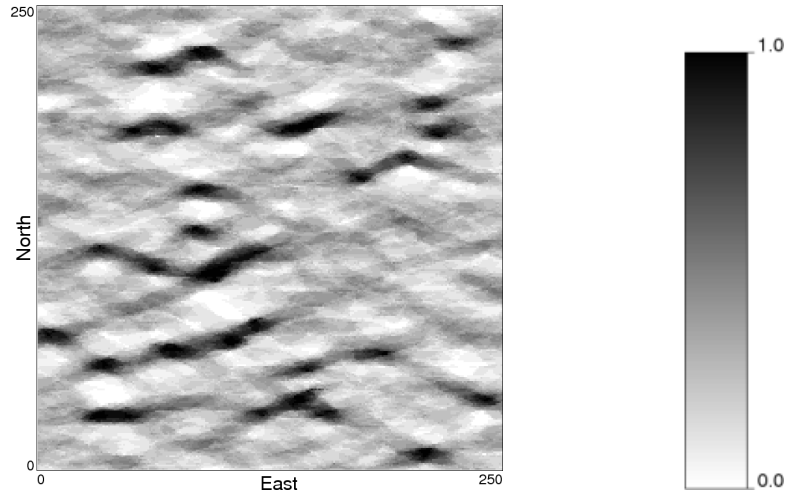


Figure 5.11b: The simulated proportions of sand for 20 conditional MPS-GS realizations.

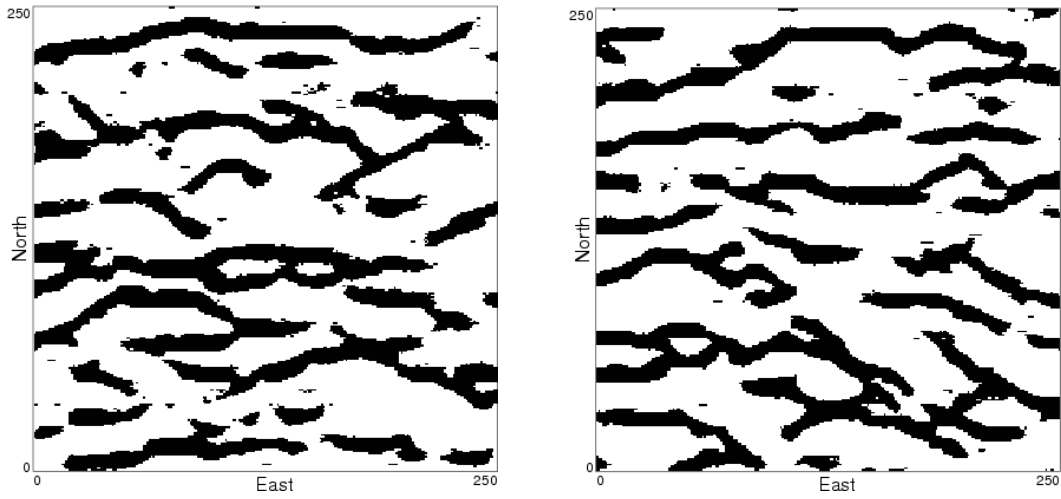


Figure 5.12a: Two conditional MPS-GS realizations using  $M=10$  and  $N=6$ .

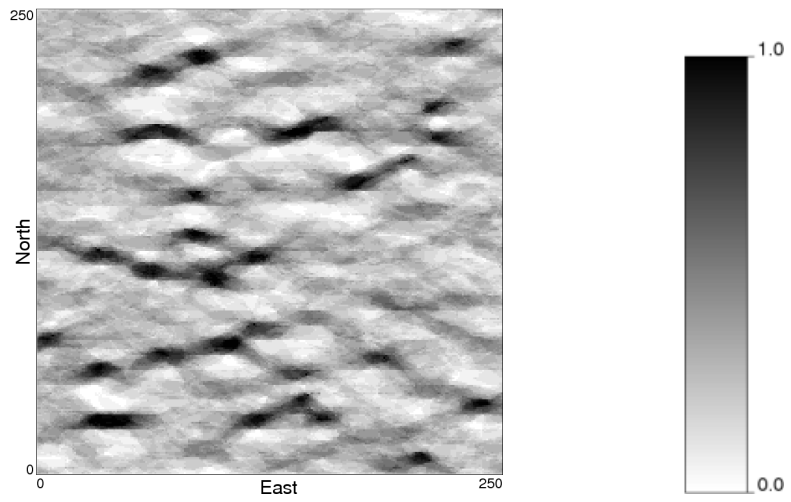


Figure 5.12b: The simulated proportions of sand for 20 conditional MPS-GS realizations.

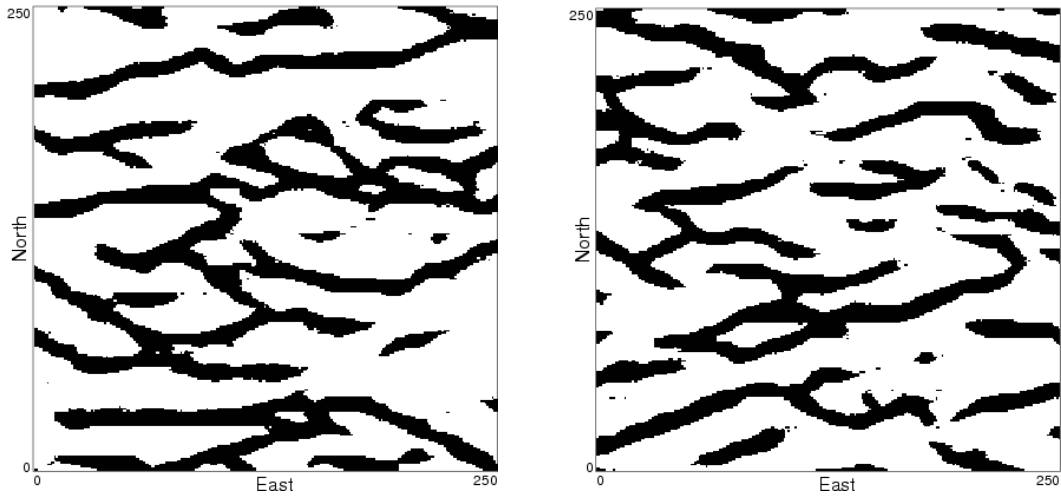


Figure 5.13a: Two conditional MPS-GS realizations using  $M=8$  and  $N=8$ .

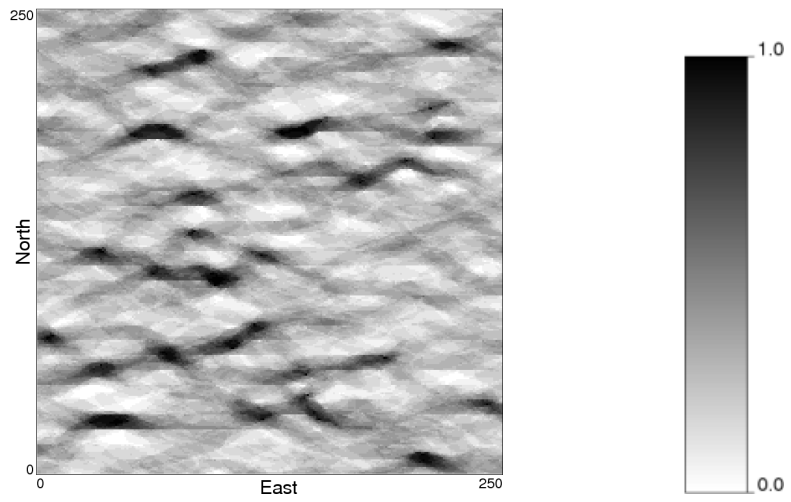


Figure 5.13b: The simulated proportions of sand for 20 conditional MPS-GS realizations.

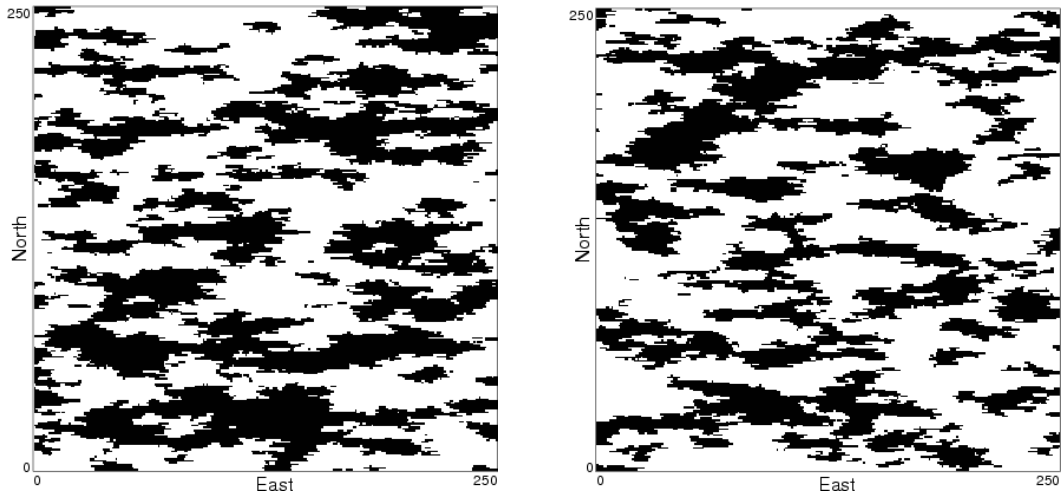


Figure 5.14a: Two conditional SISIM realizations.

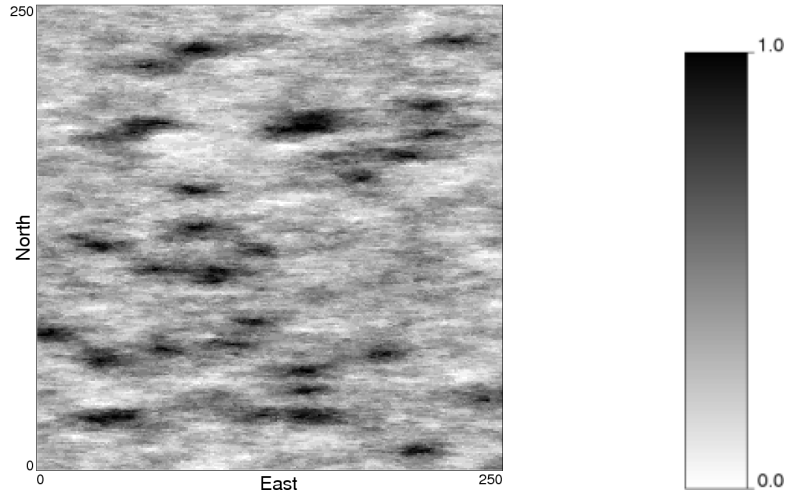


Figure 5.14b: The simulated proportions of sand for 20 conditional SISIM realizations.

The simulated sand proportions from Figures 5.10 through 5.14 were used to measure the accuracy and precision of the different MPS-GS cases and SISIM. Figure 5.15 shows an accuracy plot for the different cases. The horizontal axis is the simulated probability of sand and the vertical axis is the actual probability of finding sand at locations with those simulated probabilities. A perfectly accurate method would show up as a 45-degree line on an accuracy plot, and a totally inaccurate method would have a horizontal line at the global proportion of sand. The five simulation cases considered in this case study cross the 1:1 line at about the global proportion of 30%, and the actual proportion of sand

compared to the simulated probability tends towards the global mean particularly for very high and very low simulated probabilities. The methods are all about equally accurate.

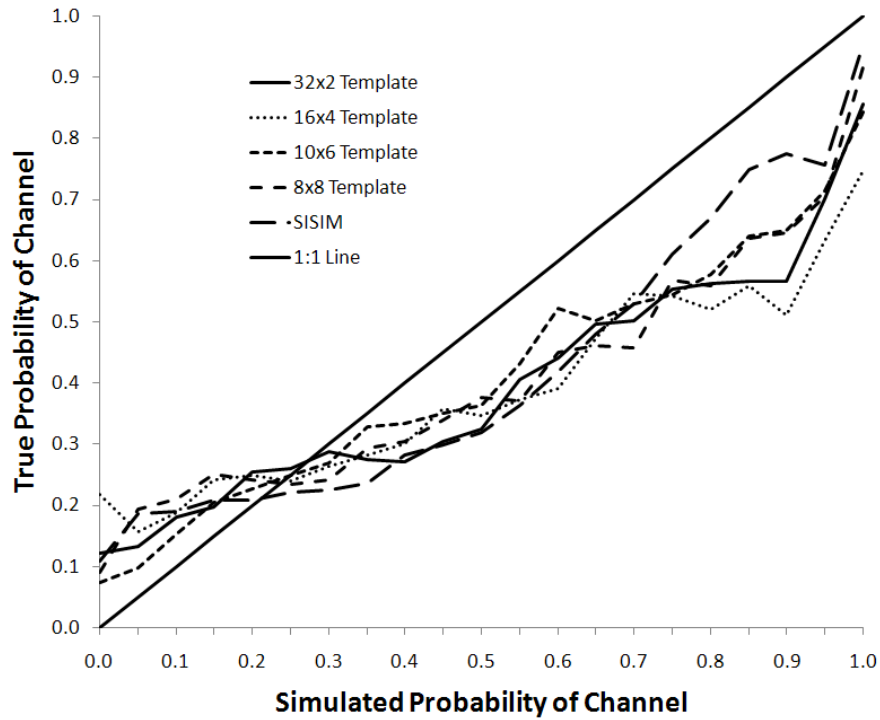


Figure 5.15: Accuracy plot for the braided channel conditional simulations.

A precise facies simulation method has more locations with very high and low simulated probabilities. Figure 5.16 shows the histograms of simulated sand probabilities for each conditional simulated case. Using the spread of the distribution of simulated probabilities as a measure of precision, the MPS-GS case with  $M=32$  and  $N=32$  is the most precise; fewer and larger events leads to less precision and SISIM is the least precise case.

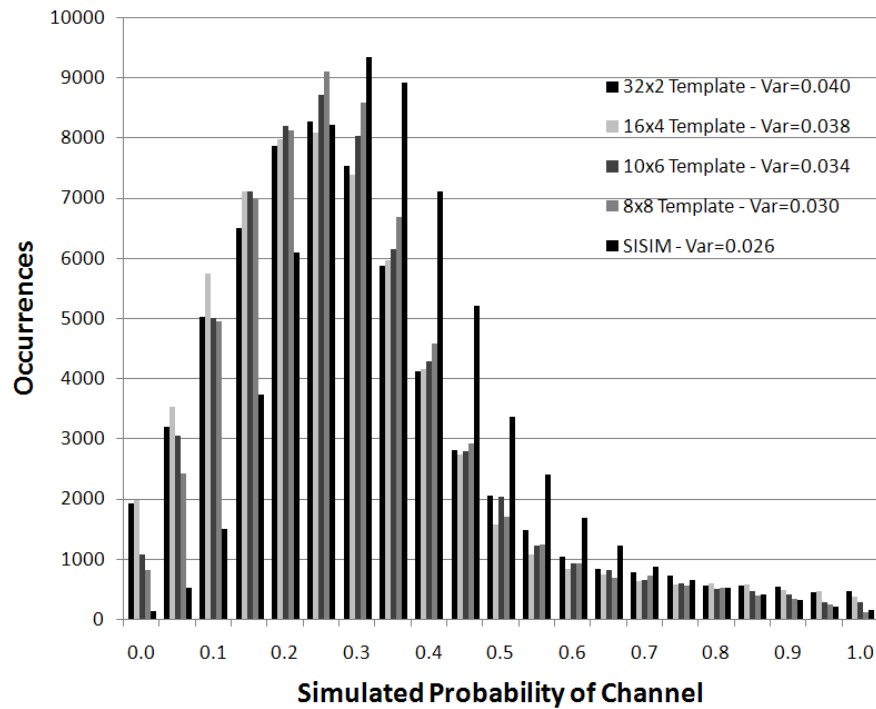


Figure 5.16: Precision of the braided channel conditional simulations.

### 5.1.4 SNESIM Realizations

To better assess the MPS-GS results, the SNESIM algorithm was used to generate twenty unconditional and twenty conditional realizations using the braided channel TI. The version of SNESIM that was used was from the SGeMS software (Remy et al, 2008) that is available as a free download. This comparison was carried out as part of an internship for ConocoPhillips and as such the results will not be shown in great detail.

Figure 5.17 shows the results of unconditional simulation using the SNESIM algorithm. Part (a) shows two unconditional realizations and part (b) shows the variogram reproduction for twenty unconditional realizations. Comparing Figure 5.17a to Figures 5.4a through 5.8a, the SNESIM results have more channels that completely span the domain than the other results; otherwise the realizations appear visually similar to the MPS-GS realizations that use larger events ( $N=6$  and  $8$ ). The variogram reproduction in Figure 5.17b is similar to the MPS-GS realizations. The MPH difference between the unconditional SNESIM realizations and the TI has a P50 of 0.12 with a range from 0.08

to 0.18; comparing that to Figure 5.9, the MPH difference is greater for SNESIM than for MPS-GS but less than for SISIM.

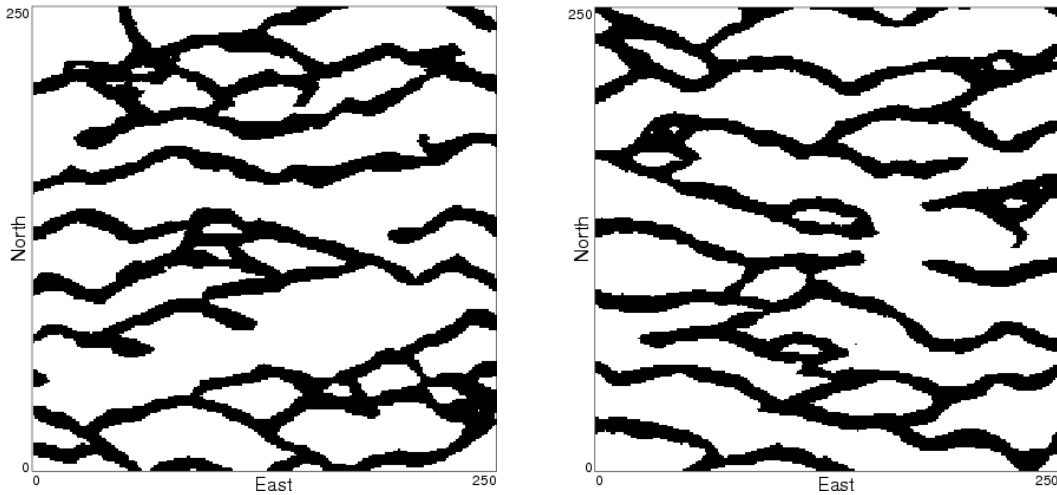


Figure 5.17a: Two unconditional SNESIM realizations.

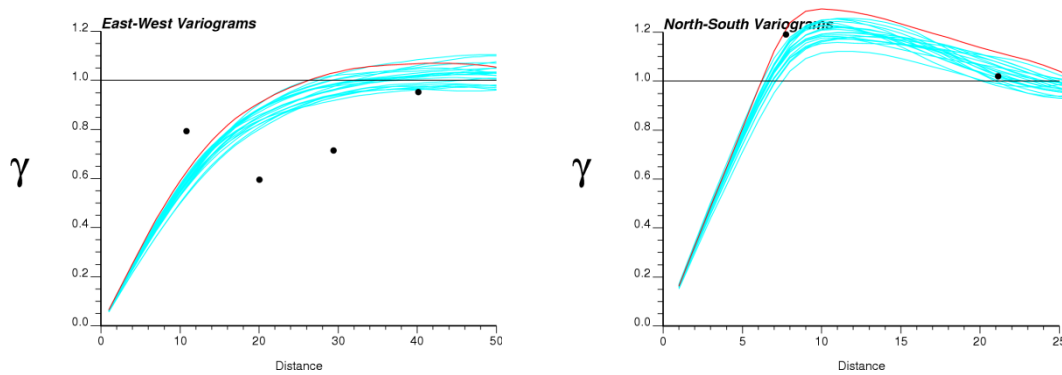


Figure 5.17b: The indicator variograms of the TI (red line), data (black dots) and 20 SNESIM realizations (blue lines) in the east-west (left) and north-south (right) directions.

Figure 5.18 shows the results of conditional SNESIM simulation. Part (a) shows two conditional realizations and part (b) shows the simulated probability of channel facies over twenty realizations. The conditional realizations appear similar to the unconditional results, with only a few small patches of facies that appear out of place near the conditioning data. The accuracy of the conditional realizations is similar to the MPS-GS and SISIM results shown in Figure 5.15. The distributions of simulated channel probabilities has a variance of 0.036, which is in the middle of the pack of the MPS-GS

results; better than the lower-order MPEs but not as high as the large ( $N=6$  and  $N=8$ ) MPEs.

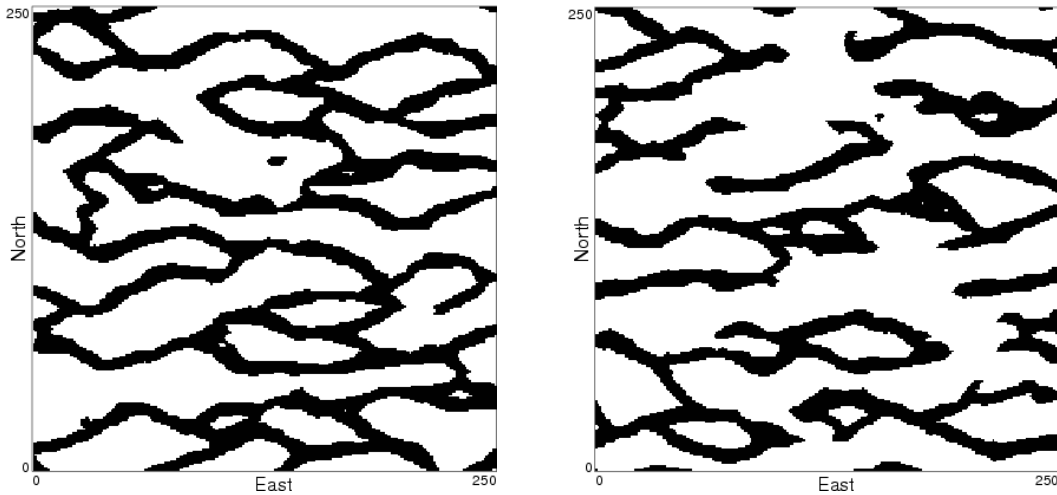


Figure 5.18a: Two conditional SNESIM realizations.

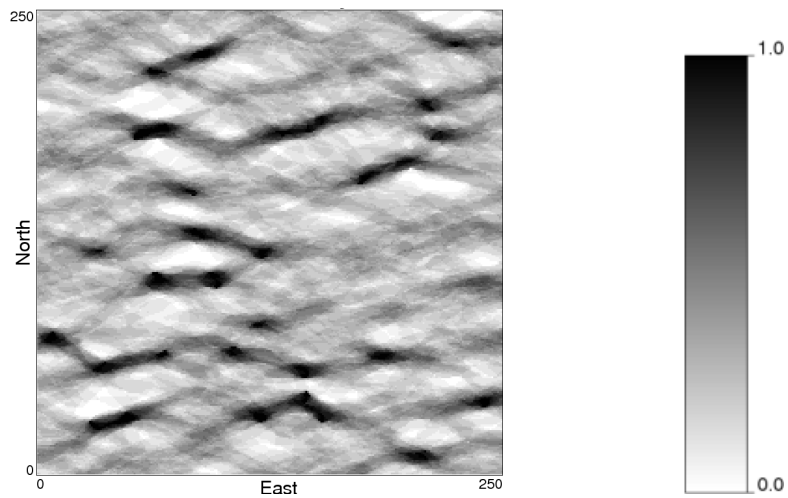


Figure 5.18b: The simulated proportions of sand for 20 conditional SNESIM realizations.

The MPS-GS results compare favourably to SNESIM based on simple statistical measures such as a four-point MPH or local precision; however, the long-range connectivity of the SNESIM realizations would have a significant impact on response characteristics.

## 5.2 Eolian Sandstone

The second case study is a more complex scenario, an eolian sandstone model. The characteristic curved laminae for this type of geology are obvious to a human observer but are very difficult to characterize and reproduce using statistical methods. The data include three facies and the samples are not taken from the TI, resulting in mismatch between the structure of the true values and the TI. In addition, both the true data and the TI are taken from outcrop photographs, increasing the realism of the scenario. The scale of the data is in the order of centimeters for the whole domain.

### 5.2.1 Data and Training Image

The left side of Figure 5.19 shows the reference dataset that was used as the source for the true data (Deutsch, 1992); the right side shows the true data for this case study, which is a categorized, cleaned, and flipped version of the original. The true image is 164x85 cells and has 25% facies 1 (white), 51% facies 2 (grey), and 24% facies 3 (black).

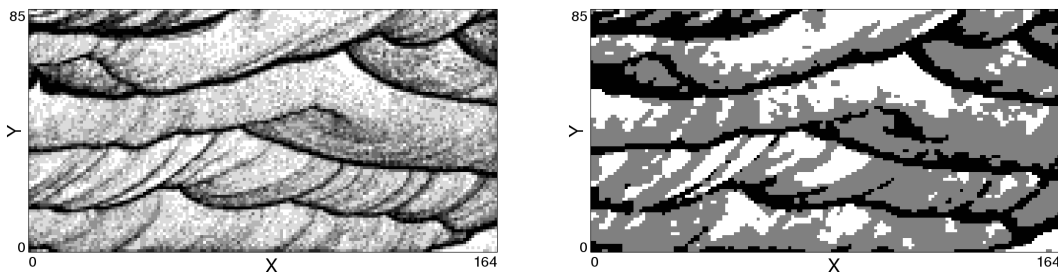


Figure 5.19: The reference dataset (left) and cleaned image (right) used as the true data for the eolian sandstone study.

The top of Figure 5.20 shows another eolian sandstone dataset (Deutsch, 1992); the lower part of Figure 5.20 shows the cleaned version of the image that was used as the TI for this case. The features in the TI are similar to those seen in the true data, but not exactly the same. The dune structure and long-range connectivity in facies 3 is noticeable in both images; nonlinear connectivity is one of the driving properties in a number of applications. The TI is 300x200 cells in size and has 22% facies 1, 56% facies 2, and 22% facies 3. The univariate proportions are similar to the true data.

Figure 5.21 shows 100 sample points that were taken from the true data image. The samples were taken from ten sampling lines. The univariate proportions of the sample data are 25% facies 1, 51% facies 2, and 24% facies 3.

Figure 5.22 shows the indicator variograms for the three facies in the X and Y directions for the true data, TI, and sample data. The variograms are not corrected for differences in univariate proportions. Facies 1 shows a trend in the X direction in the true and sample data sets, but not in the TI. The true and sample data show more cyclicity for all facies in the Y direction than the TI does. These two minor disparities are the only noticeable differences between the TI and true/sample data variograms.

Figure 5.23 shows the four-point histograms of the TI and true data, sorted from greatest to least frequencies in the TI. There are a total of  $3^4=81$  classes; only those with frequencies greater than 0.0001 are shown. The TI and true data histograms are similar, with an absolute difference of 0.142. Several of the lower-frequency classes have differences that appear significant, but because of the logarithmic scale of the MPH the absolute difference is not greatly affected.

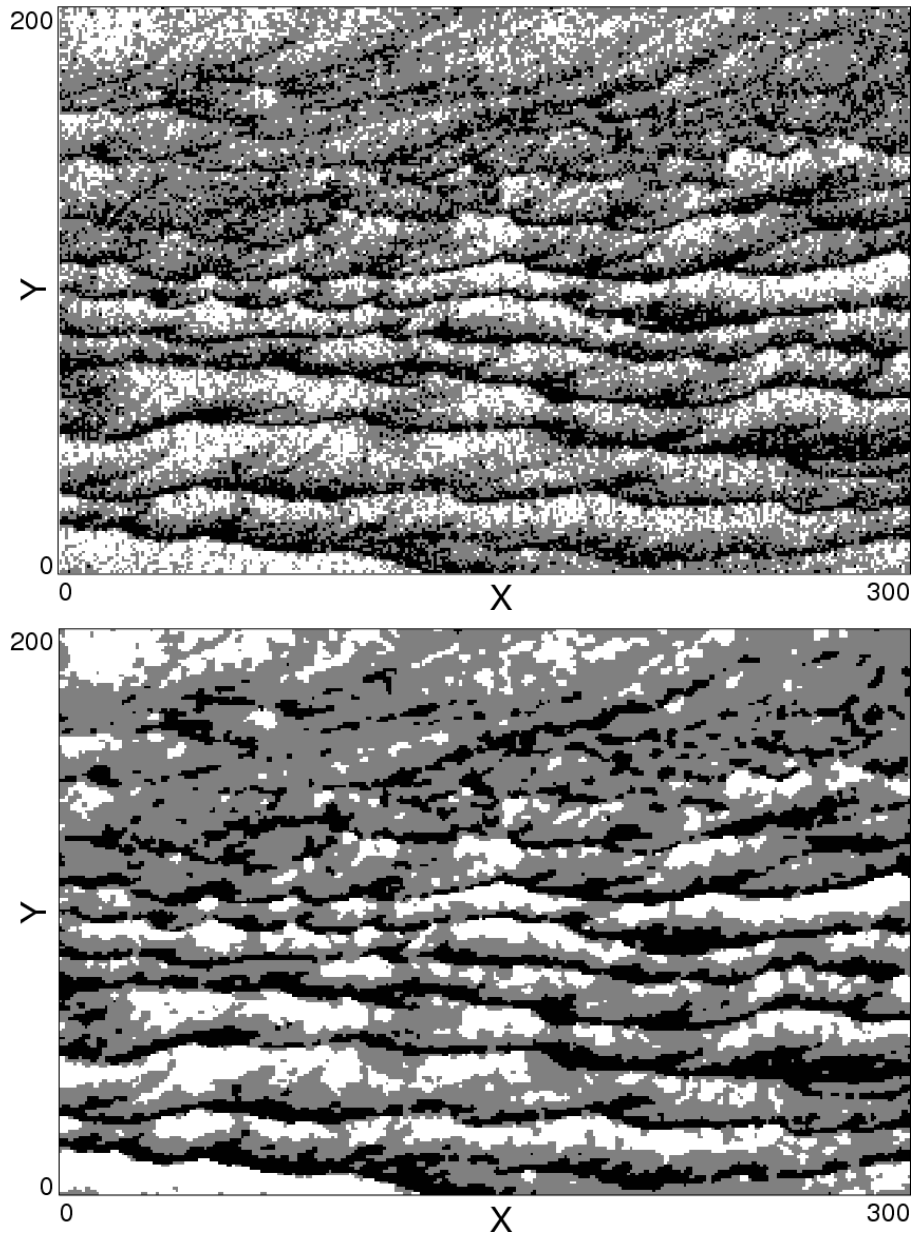


Figure 5.20: The reference dataset (top) and cleaned image (bottom) used as the TI in the eolian sandstone study.

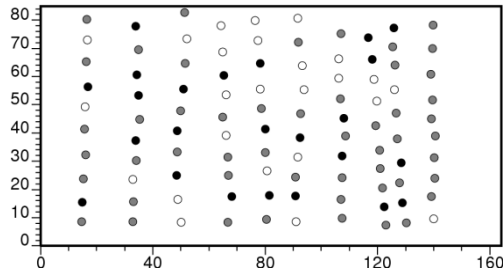


Figure 5.21: 100 data points extracted from the eolian sandstone true dataset.

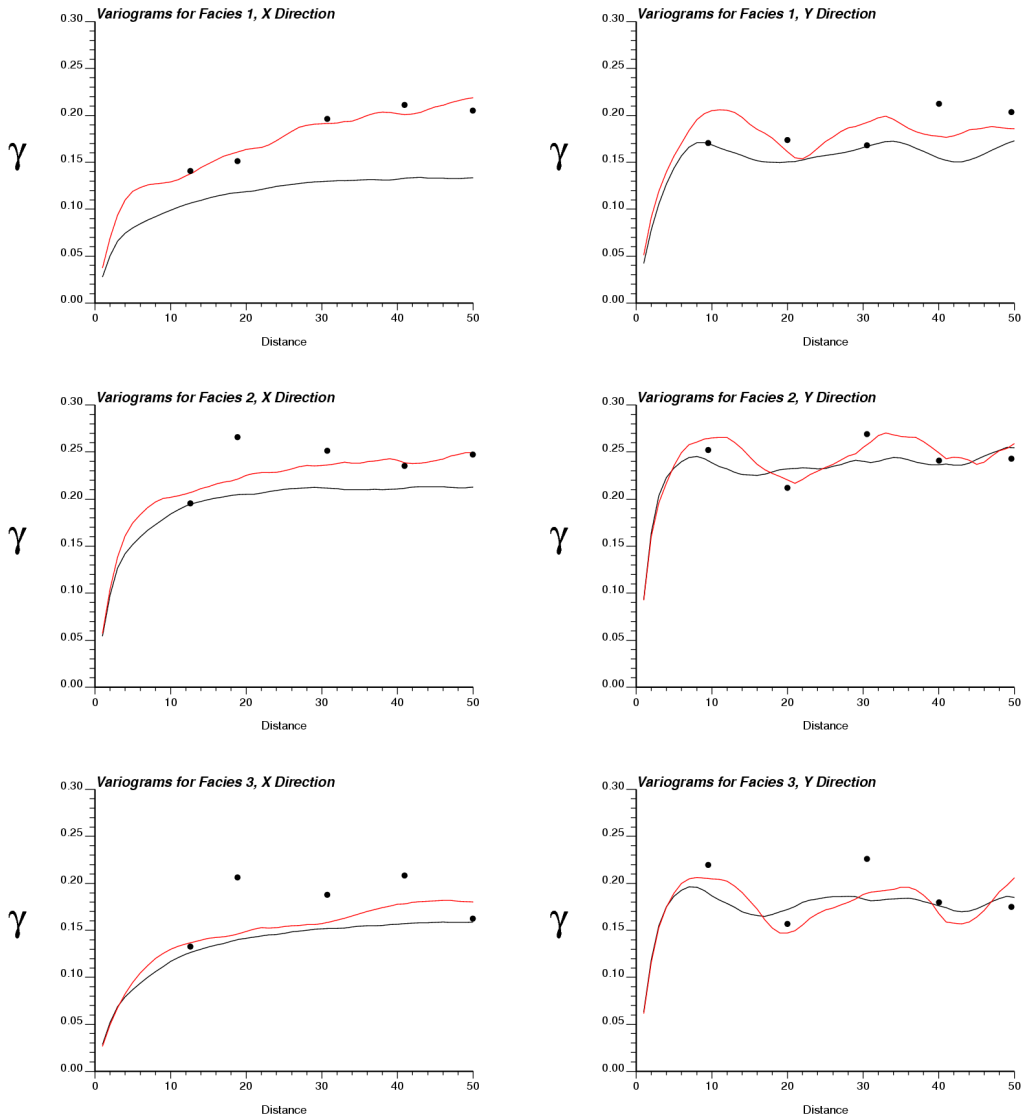


Figure 5.22: Indicator variograms of the eolian sandstone true dataset (red line), sample data (black dots), and TI (black line).

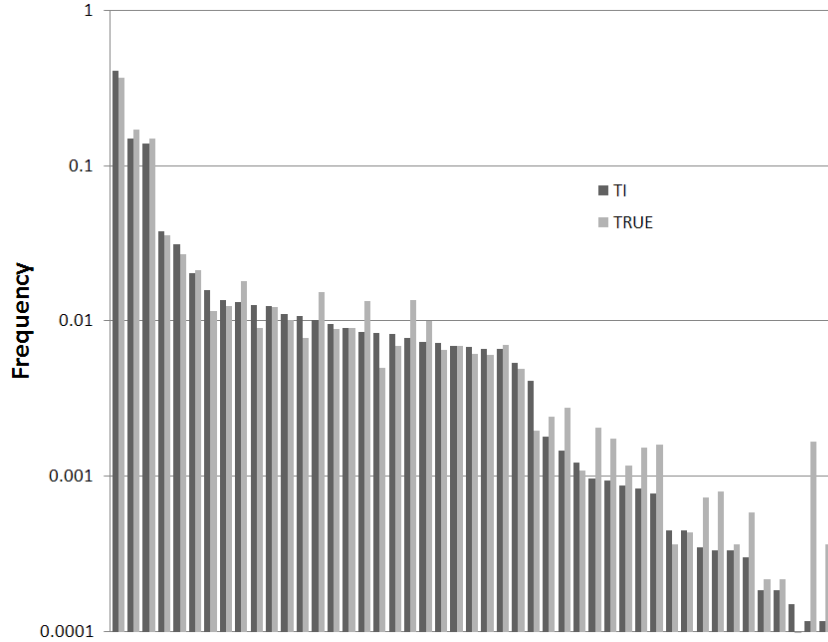


Figure 5.23: The four-point histograms of the true dataset and TI for the eolian sandstone study.

Three cases were considered for the MPS-GS algorithm in this study:  $M=32$  and  $N=2$ ;  $M=16$  and  $N=4$ ;  $M=8$  and  $N=6$ . Eight-point events were not used because of the dimensionality and the resulting size of the LHS matrix. The CPU time required to create the MPS templates and solve the system of equations in the three cases is shown in Table 5.4. The template creation is again very fast; solving the system of equations becomes cumbersome for six-point events, taking nearly three hours. Five grids were used in simulation and so five systems of equations had to be solved.

Table 5.4: CPU time required to create the templates and calculate MPS for the eolian sandstone study.

Statistics ( $M \times N$ )	Time Required (mm:ss)	
	Template Creation	MPS Calculation
32x2	0:02	3:29
16x4	0:04	12:41
8x6	0:05	174:55

## 5.2.2 Unconditional Simulation

Unconditional simulation was performed to test how well the MPS-GS algorithm can reproduce complex features found in the eolian sandstone TI. Twenty realizations were run using each of the three MPS templates described above, as well as twenty SISIM realizations for comparison. Table 5.5 shows the time required to simulate twenty realizations in the four cases. All simulations were performed using five grids; the MPS-GS realizations used a servosystem parameter of  $\mu=1.0$  and a connectivity correction factor of  $\eta=0.1$ . A maximum of thirty loops was imposed for stopping, but this limit was rarely reached. All realizations are the same size as the true data, 164x85 cells.

Table 5.5: CPU time required to simulate twenty unconditional realizations for the eolian sandstone study.

Statistics ( $M \times N$ )	Time Required (mm:ss)
32x2	0:41
16x4	0:38
8x6	0:34
SISIM	0:25

Figures 5.24 through 5.27 show the results of unconditional simulations for the four cases, one case in each Figure. Each Figure has two parts: (a) two unconditional realizations for the case shown in that Figure; (b) the indicator variograms for each of the three facies in the X and Y directions. The variogram sills are not standardized.

Visually comparing the realizations from part (a) of Figures 5.24 to 5.27, the cases using higher-order statistics contain more of the long-range continuity of facies 3 (black) that is seen in the TI; the SISIM is the worst for this type of structure and the 32x2 case is the next worst. The alternating thick and thin sections of facies 3 are evident in the 16x4 and 8x6 cases.

The variograms in part (b) of the Figures show that the second-order statistics are reproduced adequately in all cases. All three facies show cyclicity in the Y direction and the correct range of correlation in the X direction; variations in the sill are caused by slightly different univariate proportions between the realizations and TI.

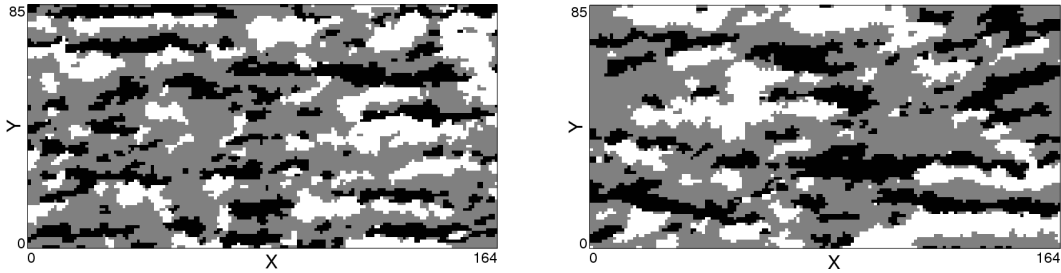


Figure 5.24a: Two unconditional MPS-GS realizations using  $M=32$  and  $N=2$ .

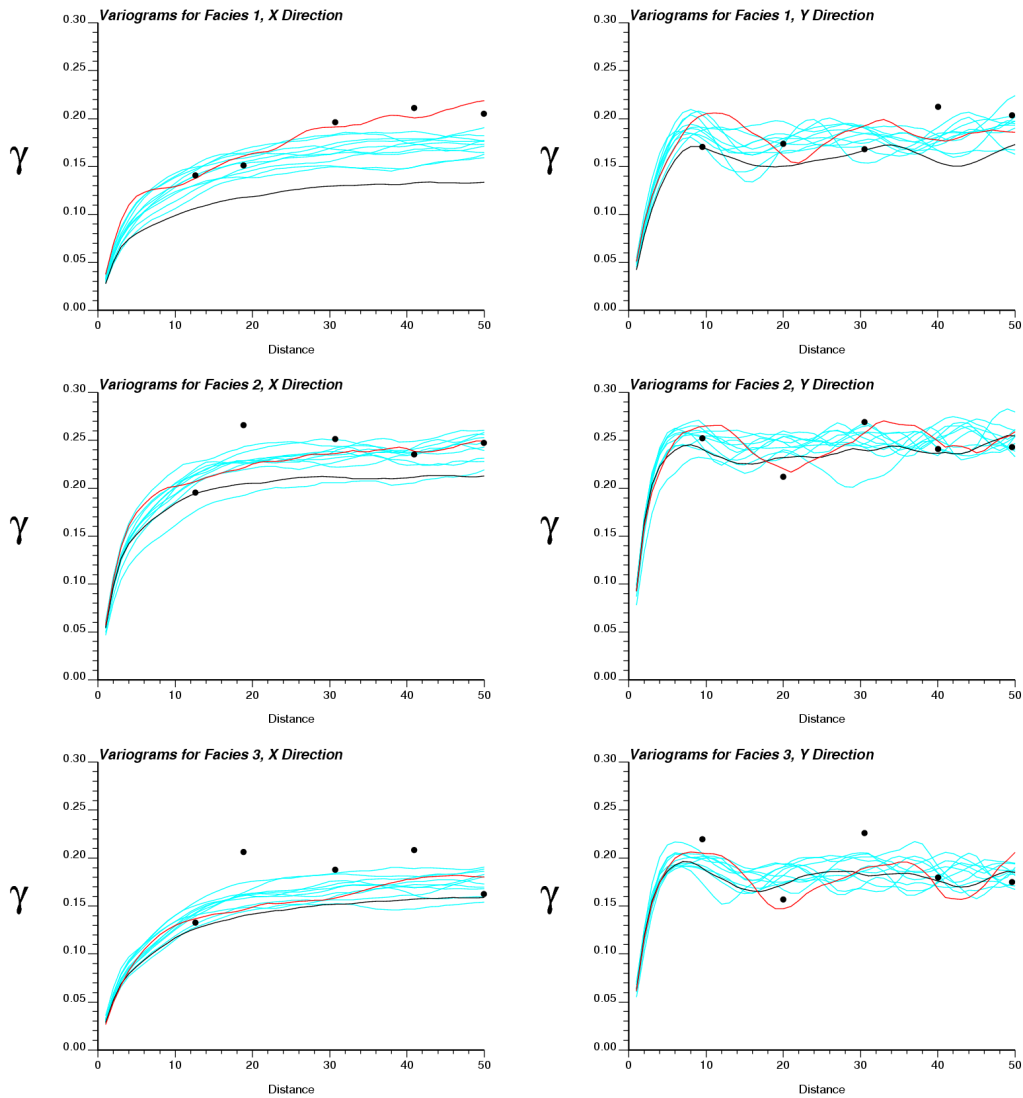


Figure 5.24b: The indicator variograms of the true dataset (red line), sample data (black dots), TI (black line) and 10 MPS-GS realizations (blue lines) in the X (left) and Y (right) directions for facies 1 (top), facies 2 (middle) and facies 3 (bottom).

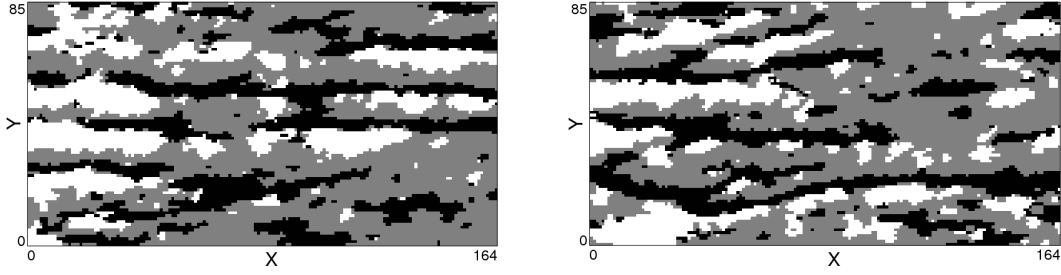


Figure 5.25a: Two unconditional MPS-GS realizations using  $M=16$  and  $N=4$ .

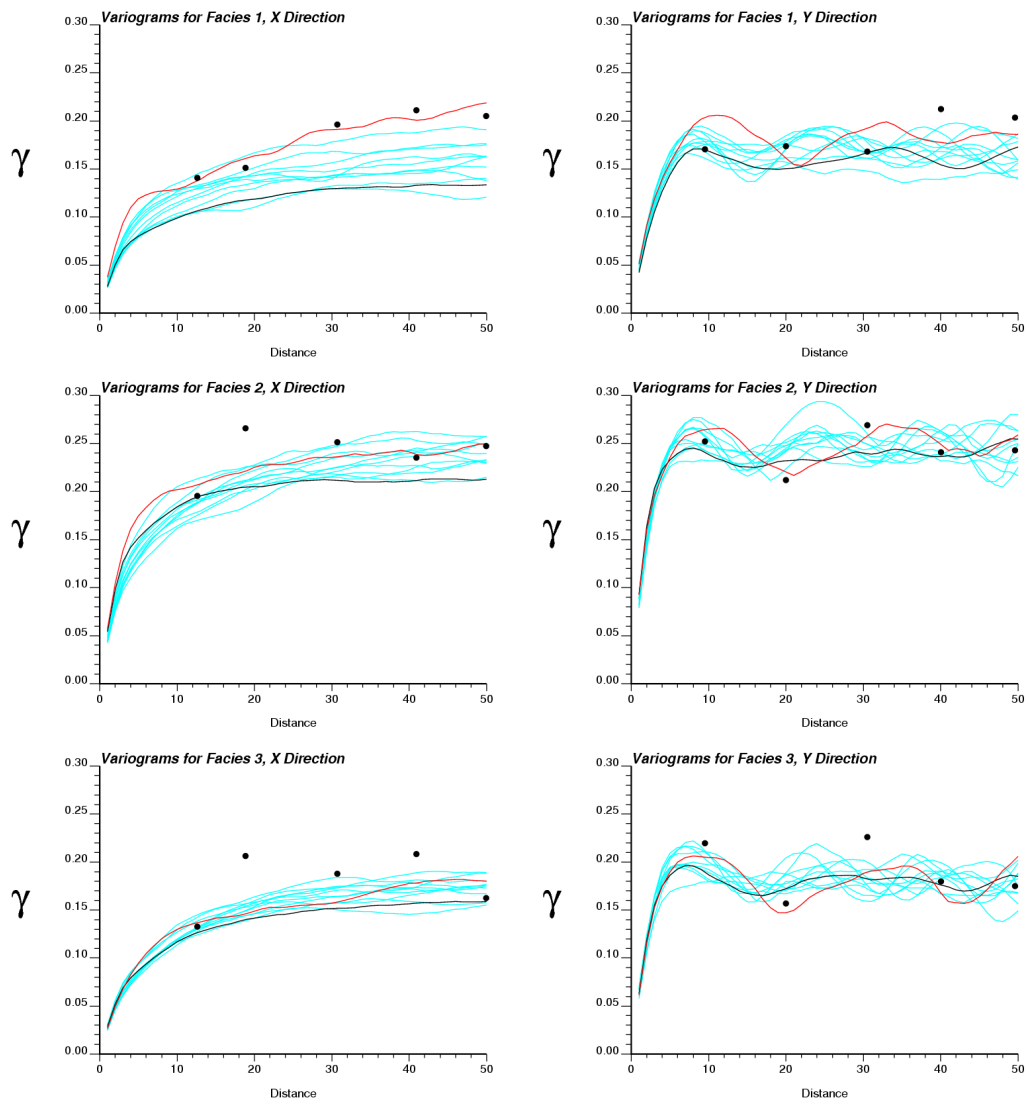


Figure 5.25b: The indicator variograms of the true dataset (red line), sample data (black dots), TI (black line) and 10 MPS-GS realizations (blue lines) in the X (left) and Y (right) directions for facies 1 (top), facies 2 (middle) and facies 3 (bottom).

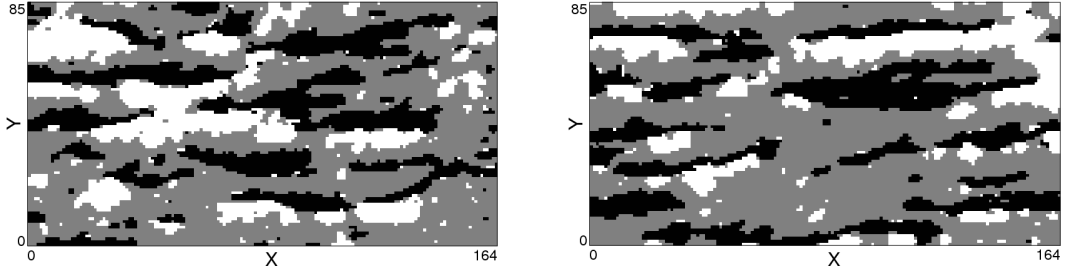


Figure 5.26a: Two unconditional MPS-GS realizations using  $M=8$  and  $N=6$ .

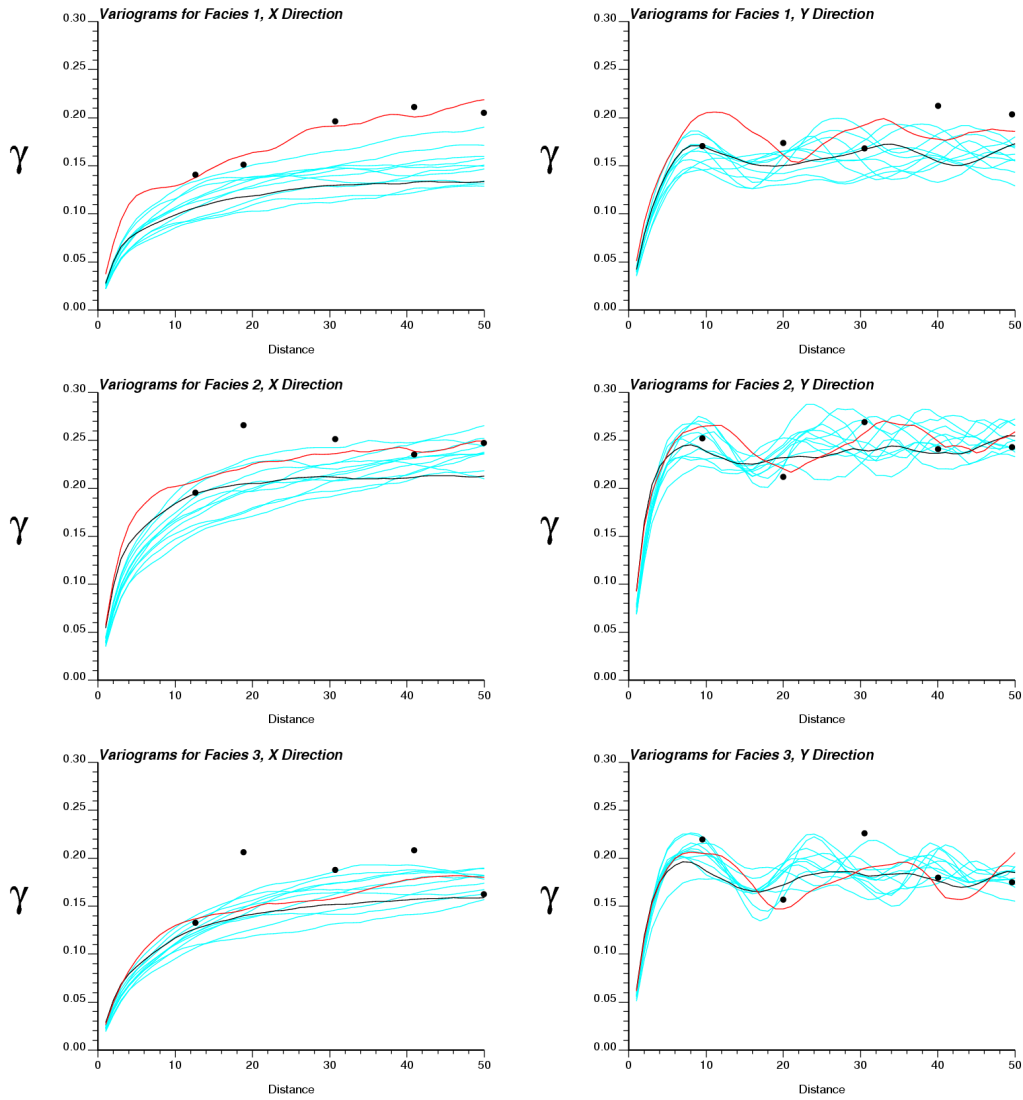


Figure 5.26b: The indicator variograms of the true dataset (red line), sample data (black dots), TI (black line) and 10 MPS-GS realizations (blue lines) in the X (left) and Y (right) directions for facies 1 (top), facies 2 (middle) and facies 3 (bottom).

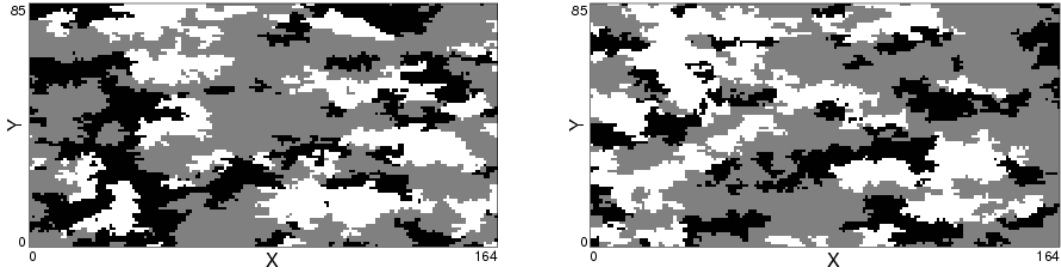


Figure 5.27a: Two unconditional SISIM realizations.

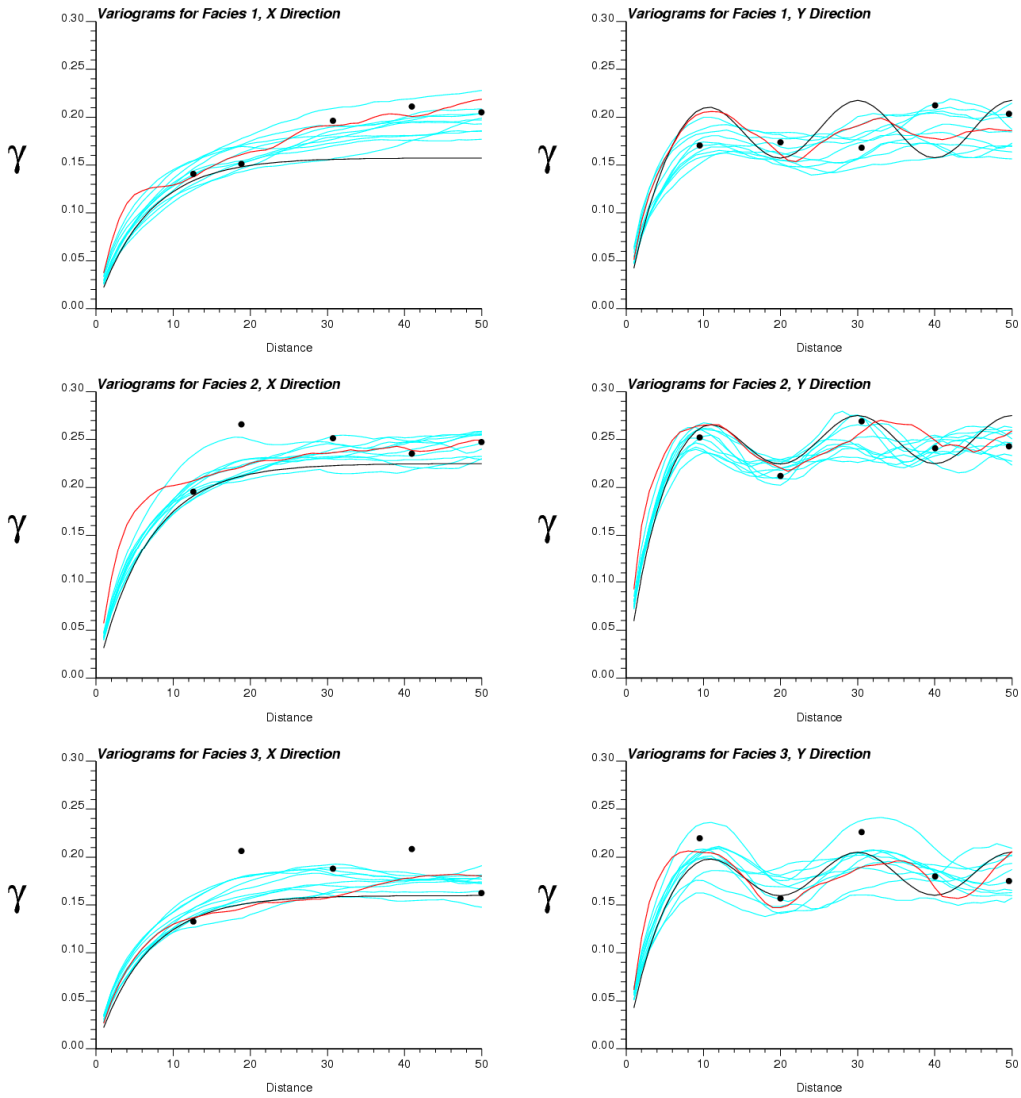


Figure 5.27b: The indicator variograms of the true dataset (red line), sample data (black dots), TI (black line) and 10 SISIM realizations (blue lines) in the X (left) and Y (right) directions for facies 1 (top), facies 2 (middle) and facies 3 (bottom).

Figure 5.28 shows a graph of the absolute MPH differences between the TI MPH shown in Figure 5.23 and the MPHs calculated from the realizations. The 32x2 and 16x4 MPS-GS cases perform the best by this measure, with P50 differences of 0.11. The 8x6 case has a P50 difference of 0.15 and SISIM has a P50 of 0.25. The 16x4 case has less P10-P90 range than the 32x2 case. Four-point MPEs offer the greatest compromise between high-order information content and practicality.

The greater mismatch in high-order statistical reproduction for larger MPEs is caused by the limited TI size, the random initial images used in MPS-GS, and the limitations in solving the system of equations. For three facies and  $N=6$ , each MPE has 729 classes to be informed and with a TI size of 60,000 cells not every class will be informed. A random initial image is necessary in MPS-GS, as was shown in Section 3.4. A random image will have many more uninformed patterns for large MPEs than for smaller ones, causing degradation of the realizations for very large MPEs. The greatest limitation of MPE size is solving the system of equations to determine the optimal linear estimation weights: for  $K=3$ ,  $M=8$ , and  $N=6$ , the maximum size of the system is  $5976 \times 5976$ , and because of currently available CPU speed it must be limited to less than half that size even if more MPEs are informed.

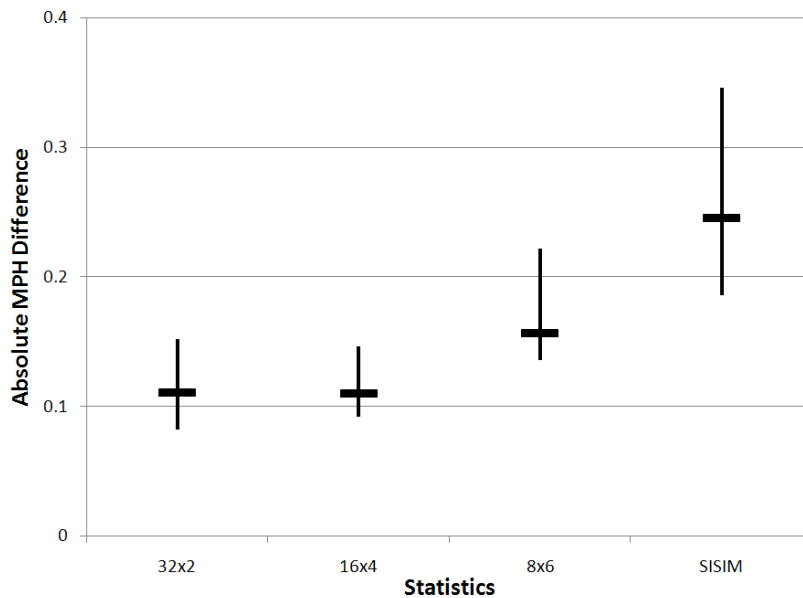


Figure 5.28: A graph of the absolute MPH differences for each case of the eolian sandstone study between twenty realizations and the TI. Bars: P50 realization difference; lines: P5 and P95 realizations.

### 5.2.3 Conditional Simulation

The 100 sample data points shown in Figure 5.20 were used in conditional simulation for the eolian sandstone study. An ideal method would produce realizations that look similar to the true data in Figure 5.18. Twenty realizations were simulated using the three MPS-GS cases and SISIM. The time required for each set of twenty realizations is shown in Table 5.6; the results are very similar to the unconditional scenario. All parameters were the same as the unconditional case.

Table 5.6: CPU time required to simulate twenty conditional realizations for the eolian sandstone study.

Statistics ( $M \times N$ )	Time Required (mm:ss)
32x2	0:41
16x4	0:36
8x6	0:30
SISIM	0:26

Figures 5.29 through 5.32 show the results of the conditional simulations. Part (a) of each Figure shows two conditional realizations for that case; part (b) shows the simulated probability of each facies at all locations in the domain. Visually the conditional realizations in parts (a) look similar to the unconditional realizations for all cases; there are no obvious artifacts or discontinuities. The relationship between facies 2 and 3, with the grey facies on top of the black facies, is seen much more in the MPS-GS realizations than in the SISIM realizations. In part (b) of the Figures the cases using higher-order statistics show more connectivity over all realizations than the lower-order cases, particularly for facies 3. The SISIM and 32x2 case show more “bulls-eyes” around the data locations rather than long continuous structures.

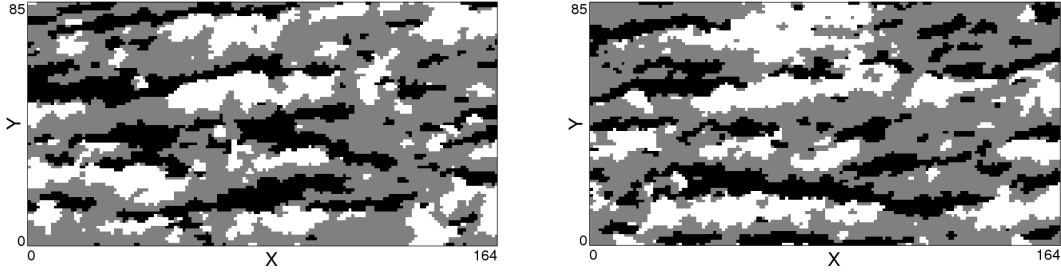


Figure 5.29a: Two conditional MPS-GS realizations using  $M=32$  and  $N=2$ .

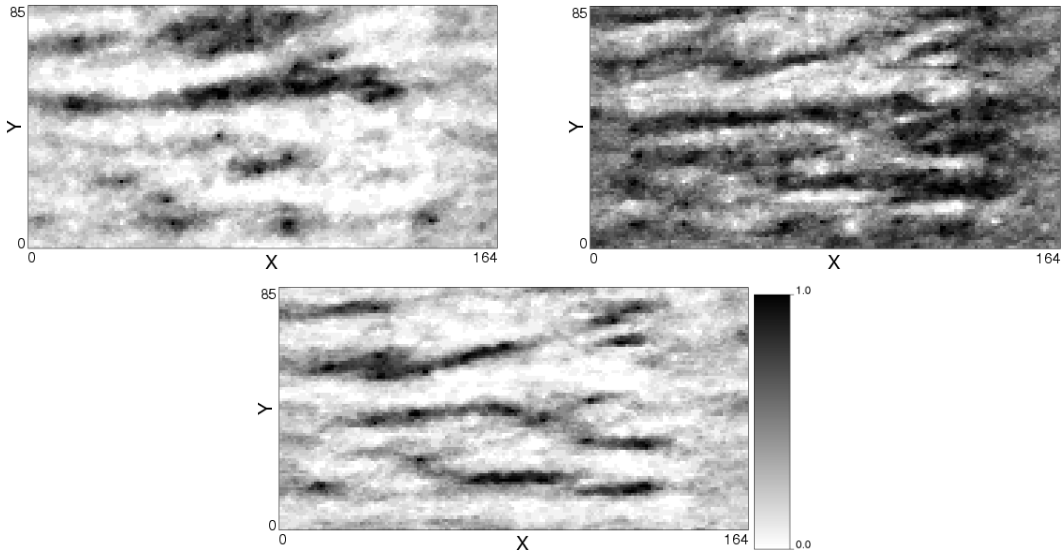


Figure 5.29b: The simulated proportions of facies 1 (top left), facies 2 (top right), and facies 3 (bottom) for 20 conditional MPS-GS realizations.

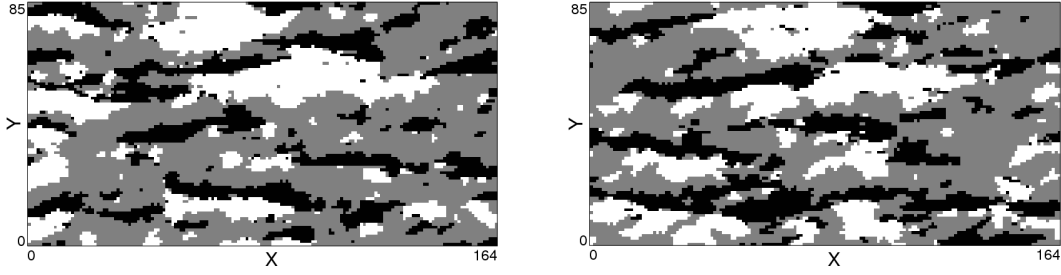


Figure 5.30a: Two conditional MPS-GS realizations using  $M=16$  and  $N=4$ .

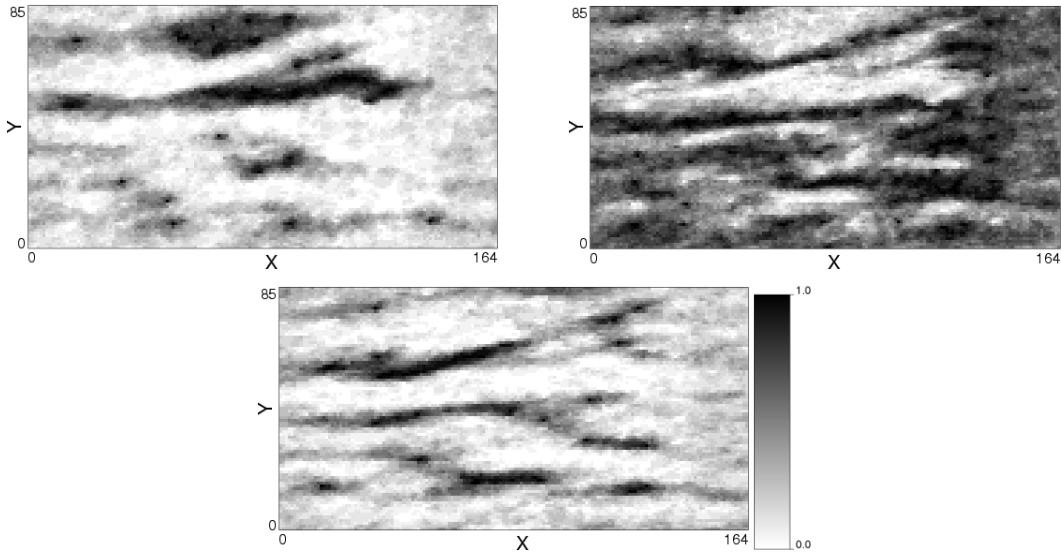


Figure 5.30b: The simulated proportions of facies 1 (top left), facies 2 (top right), and facies 3 (bottom) for 20 conditional MPS-GS realizations.

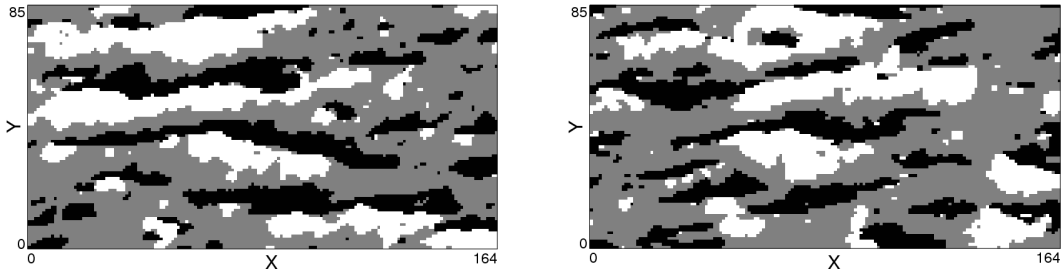


Figure 5.31a: Two conditional MPS-GS realizations using  $M=8$  and  $N=6$ .

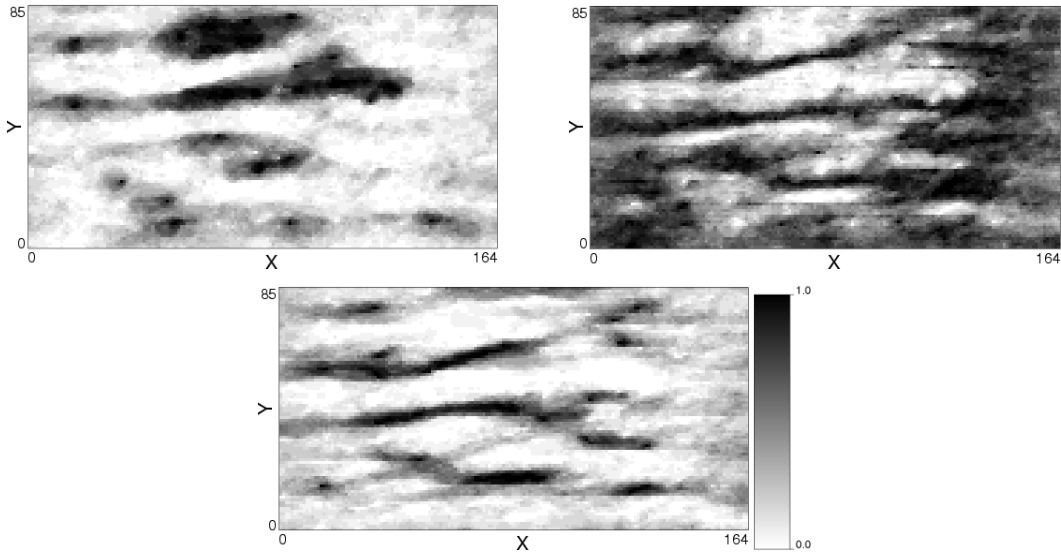


Figure 5.31b: The simulated proportions of facies 1 (top left), facies 2 (top right), and facies 3 (bottom) for 20 conditional MPS-GS realizations.

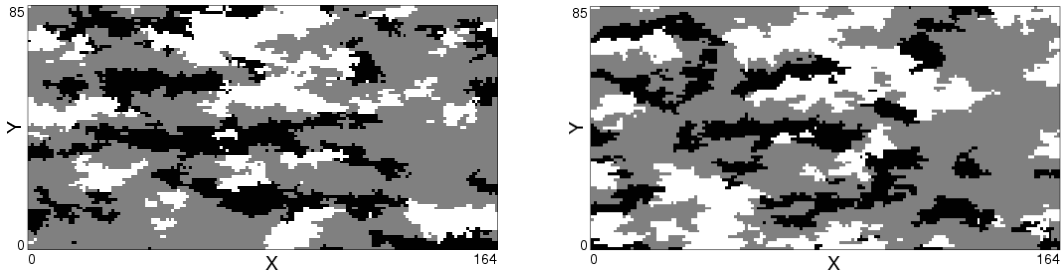


Figure 5.32a: Two conditional SISIM realizations.

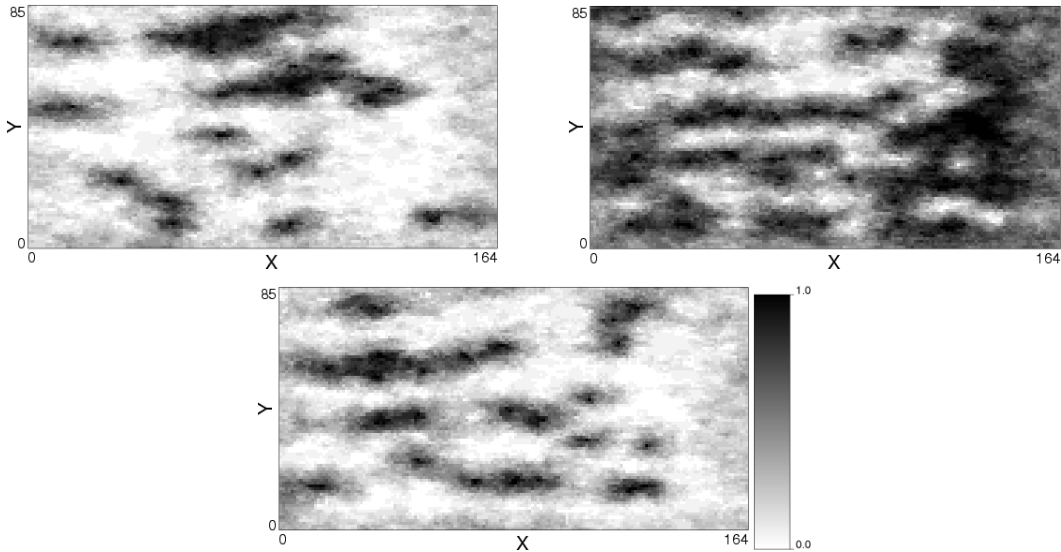


Figure 5.32b: The simulated proportions of facies 1 (top left), facies 2 (top right), and facies 3 (bottom) for 20 conditional SISIM realizations.

The simulated proportions of facies from part (b) of Figures 5.29 to 5.20 and true data from Figure 5.19 were used to assess the accuracy of the simulation methods. Figure 5.33 shows an accuracy plot for the four simulation cases considered. The simulated probability of facies is shown on the horizontal axis, and the actual probability of finding that facies in the true data is shown on the vertical axis. The accuracy of all of the cases is about the same.

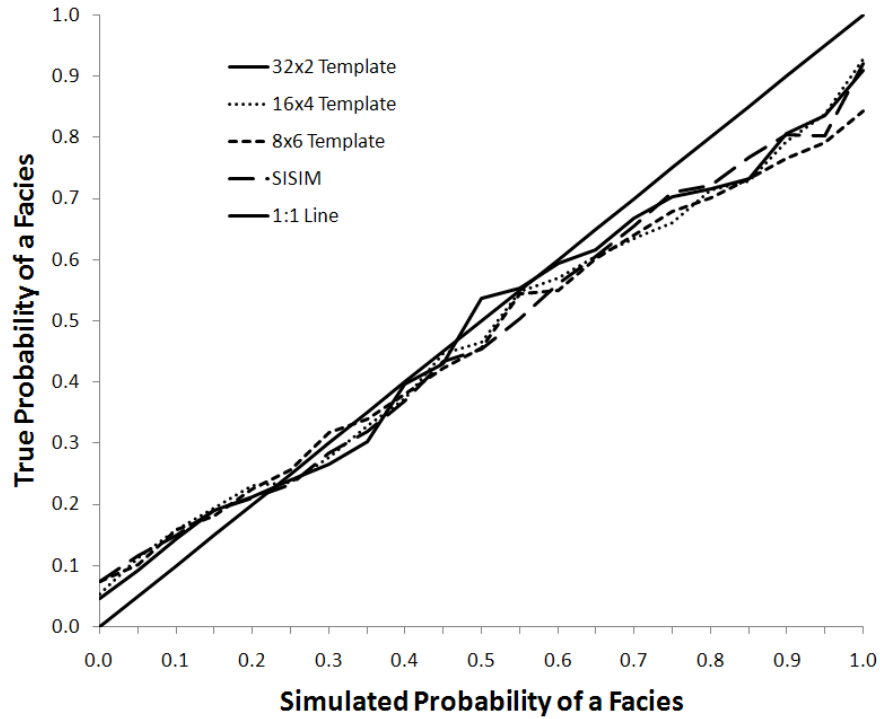


Figure 5.33: Accuracy plot for the eolian sandstone conditional simulations.

The spread of the histogram of simulated facies probabilities was used to measure the precision of the simulation methods. Figure 5.34 shows the histogram of simulated facies probabilities and the variance of each distribution. The greatest precision was attained by the MPS-GS case with  $M=8$  and  $N=6$ ; the least precise case was the MPS-GS simulation using  $M=32$  and  $N=2$ . The number and size of MPEs has a significant impact on the results.

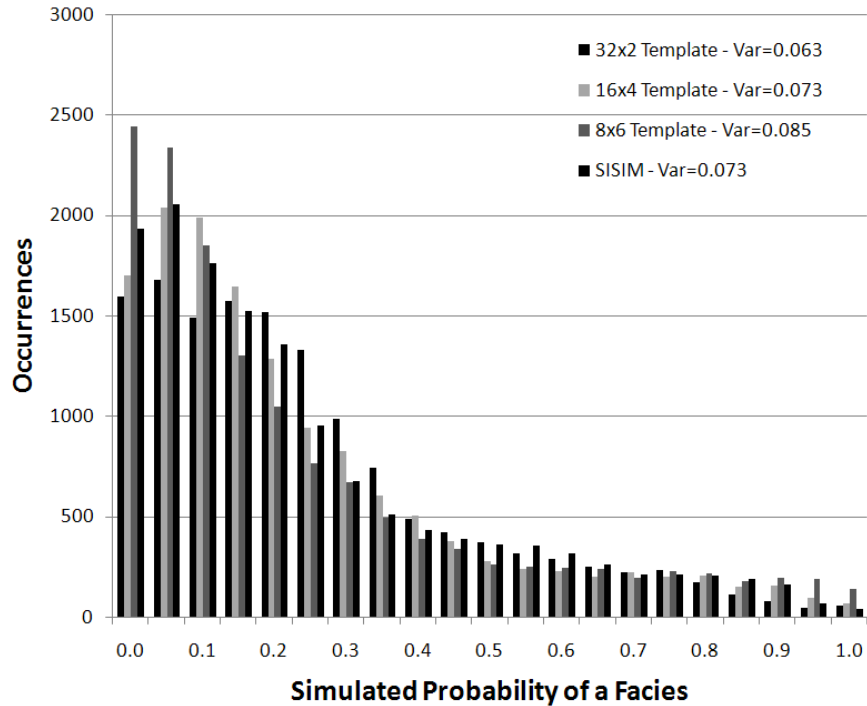


Figure 5.34: Precision of the eolian sandstone conditional simulations.

### 5.3 Petroleum Reservoir

A larger, 3D case study was carried out to test the effectiveness of the MPS-GS algorithm on a real data set that was provided by the ConocoPhillips Company (<http://www.conocophillips.com>). Thirty-three vertical wells from a fluvial petroleum reservoir were used, containing 3449 sample points. An additional 10 wells containing 1116 sample points were not used in the simulation but were used for jackknife cross validation. There are four facies in the reservoir: background shale, low-quality sand, medium-quality sand, and high-quality sand. The global proportions of the facies are 55%, 11%, 14%, and 20% respectively. The major direction of correlation is along the X axis, with less correlation in the Y and Z directions.

There is the most certainty about the structure of facies 1 (white) and facies 4 (black). Facies 1 is background shale. The structure of facies 4 is channels that are high-quality, and relatively large and continuous compared to the facies 2 and 3 geo-objects. Facies 2 (light grey) and 3 (dark grey) are more ambiguous and are closely associated with one another. Facies 3 could be channels or elliptical lobes and facies 2 could be levees or

debris. The major controlling factors associated with the reservoir are the continuity and connectivity of the best (facies 4) and worst (facies 1) quality material.

### **5.3.1 Training Images**

For this case study, there is a large amount of uncertainty associated with the data. There is no definitive answer on what TI is the most appropriate, and for this reason several were considered. The well data and geological setting suggest a fluvial environment, so object-based modeling was used to create unconditional realizations of channel-type systems. Five scenarios are considered as potential TIs:

1. Facies 3 is made up of thinner channels than facies 4, and facies 2 is made up of levees associated with the facies 3 channels.
2. The same case as #1, but with thinner and narrower channels and levees.
3. Facies 3 is made up of thinner channels than facies 4, and facies 2 is made up of lobes of debris within the facies 3 channels.
4. Facies 3 is made up of sandy lobes and facies 2 is lower-quality sand within the lobes.
5. Facies 2 and 3 are made up of similar-sized lobes that are found in close association with one another.

The closest scenario to the conceptual model of geology is #1. A TI was created for each scenario using the object-based modeling in the Petrel software (<http://www.slb.com/content/services/software/geo/petrel/index.asp>). The TIs are all 150x150x75 for a total of 1,687,500 cells, which is larger than the reservoir models. The extra size of the TIs compared to the simulation domain allows better inference of long-range structure. Figures 5.35 through 5.39 show the five TIs. Each Figure has three parts: (a) three slices in each of the XY, XZ, and YZ planes; (b) a graph comparing the MPHs of the well data and the TI; (c) indicator variograms of the well data and TI for the four facies in the X, Y, and Z directions.

Part (a) of the Figures is useful for visualization of the structure of the geo-objects but provides no quantifiable measurement of the statistical closeness of the TIs to the well data. Part (b) offers a quantifiable measure in the form of a MPH. A four-point vertical template was used, for a total of 256 possible classes. From the graphs, TI #2 is clearly a worse match to the well data than the other TIs. A more robust measure than visual inspection is the absolute difference between the MPHs; Table 5.7 shows a

summary of the absolute MPH differences of the TIs from the well data. TIs #3 and 4 are the best by this measure, with TI #1 also being a reasonable choice. TI #2 is clearly the worst and TI #5 is also a poor representation of the spatial statistics. The patterns represented by the MPH classes are shown below the graphs because the vertical template used lends itself to an easier graphical display than most MPH templates.

The variograms in part (c) of the Figures are a good measure for the purpose of rejecting a TI, but cannot be used as the only measure to select the best TI. Like univariate statistics, many TIs may match the variograms but be a poor representation of the connectivity and continuity of the real geology. In this case (and in most real-world applications) the vertical variograms are of particular interest due to the data being obtained from vertical wells. TIs #1, 3, 4, and 5 all match the vertical variograms for all four facies to within a close tolerance; only TI #2 is clearly not a good choice based on the variograms. All of the channel-type facies in the TIs show cyclicity in the X direction because of the perfectly repeating patterns used, and so the variograms return to values of zero at the wavelength lag distance. Deviations from an ideal sinusoid in the realizations will come from the simulation algorithm instead of the inferred statistics.

Based on the conceptual geology, variograms, and MPHs, TIs #1, 3, and 4 were used for simulation with the MPS-GS algorithm in this case study. The results using each TI were compared, and taken together can be used to assess the full range of uncertainty; in this case there is uncertainty in the TI as well as ergodic fluctuations in the simulated realizations.

All of the TIs were used to create templates and calculate optimal linear weights using the parameters  $M=12$ ,  $N=4$ , and  $G=4$ . With four facies, four points is the largest practical size for a MPE as there are a possible 256 classes in the MPH for each event. Using twelve MPEs gives a potential for over 3000 informed classes. Trimming uninformed or low-frequency classes must be done to limit the size of the matrices to be inverted. Table 5.8 shows the CPU time required to create the templates and solve the systems of equations for each TI. The template creation is fast at less than a minute and a half. Solving the systems of equations takes over an hour in all three cases and is related to the randomness and hence the number of informed classes. TI #1 is the fastest case while TI #4 is the slowest due to the smaller structures and the greater number of informed classes.

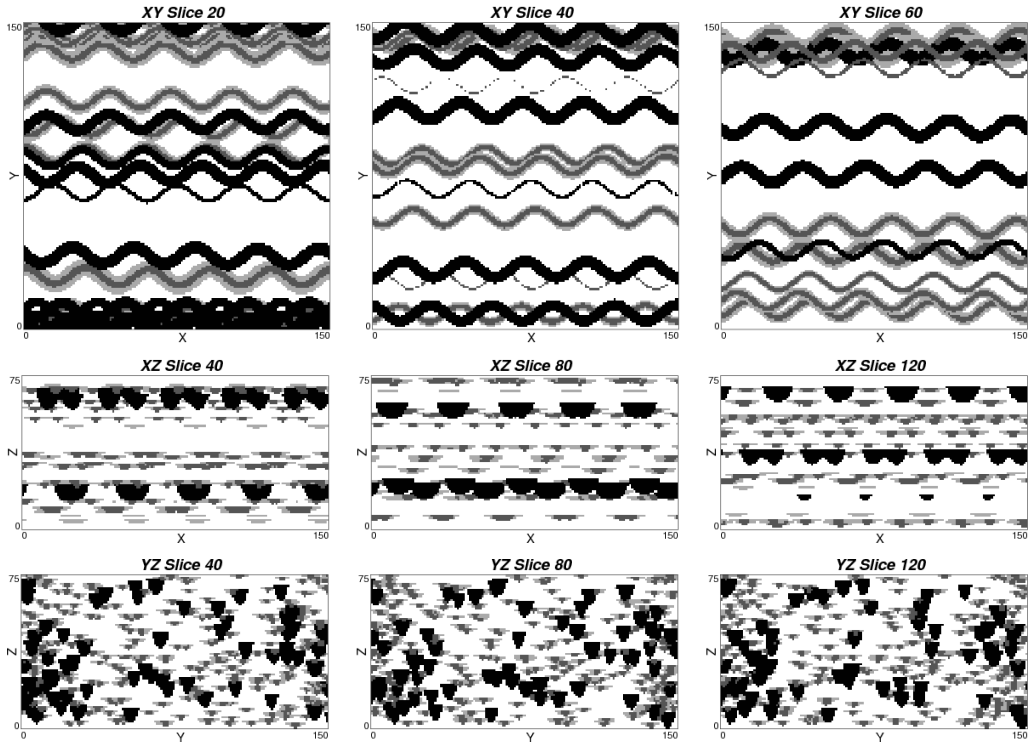


Figure 5.35a: TI #1 for the petroleum reservoir case study.

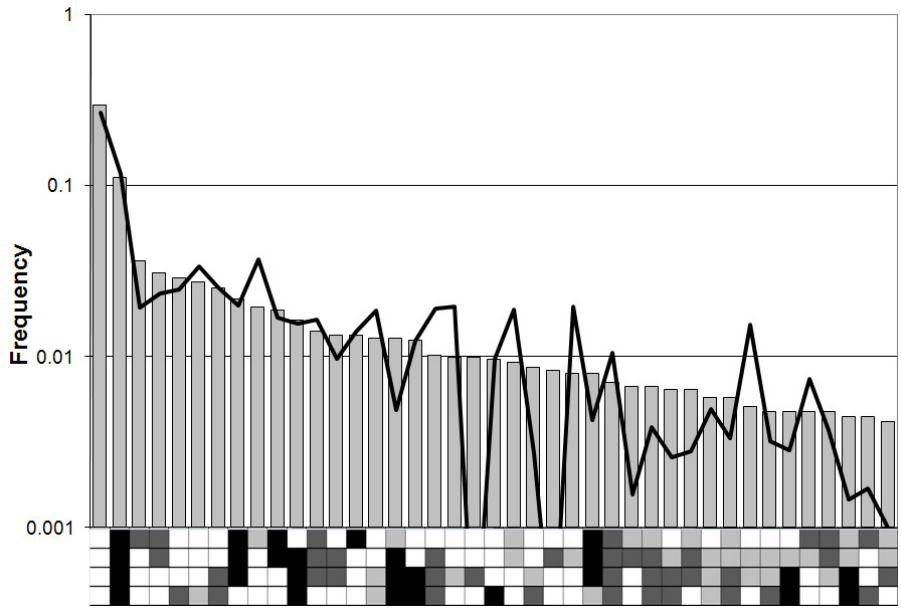


Figure 5.35b: The MPH of the well data (bars) and TI #1 (line). The MPH patterns are shown under the horizontal axis.

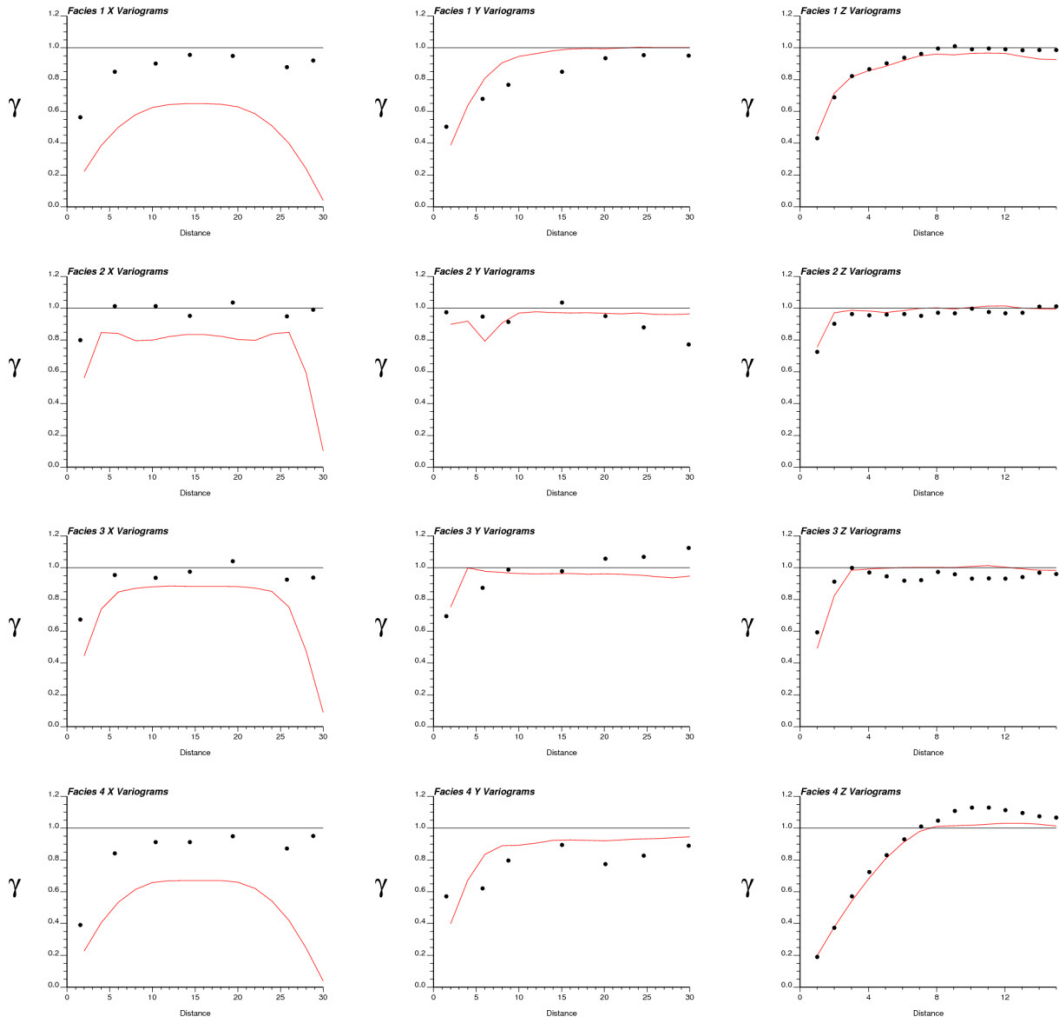


Figure 5.35c: Indicator variograms for the well data (points) and TI #1 (line) in the X, Y, and Z directions (left to right) for the four facies, top to bottom: facies 1 (white), facies 2 (light grey), facies 3 (dark grey), and facies 4 (black).

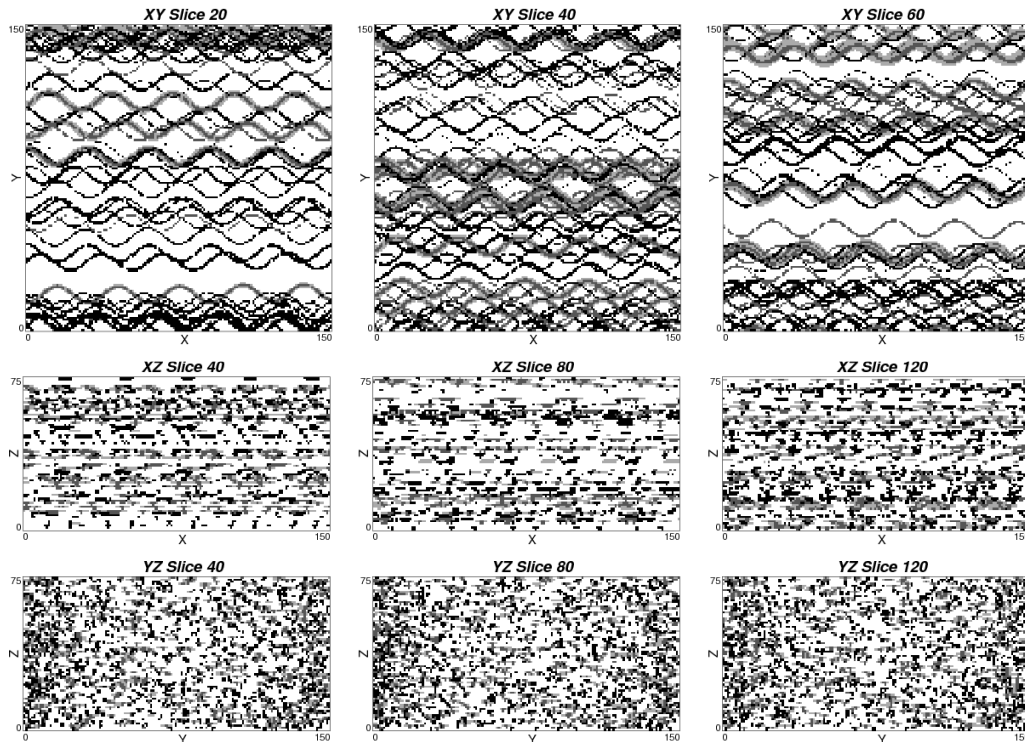


Figure 5.36a: TI #2 for the petroleum reservoir case study.

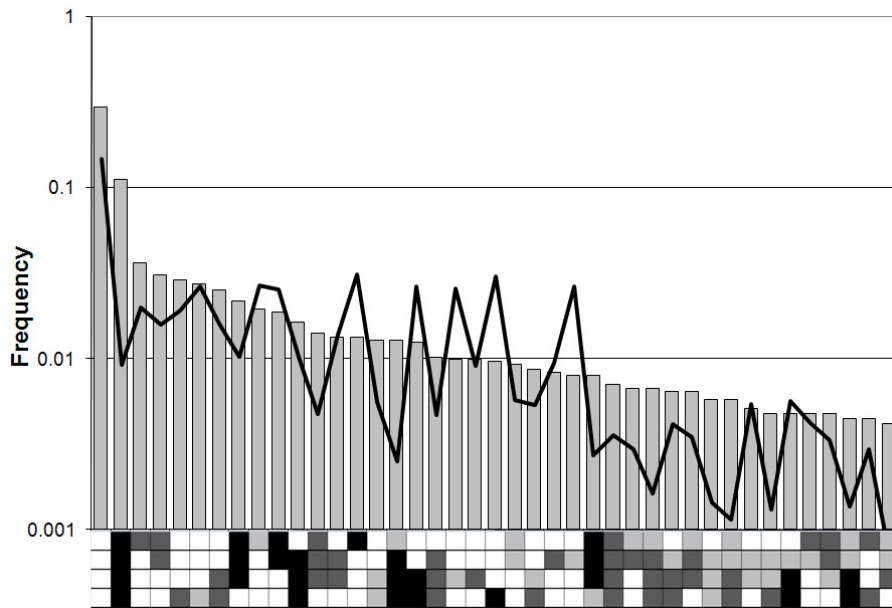


Figure 5.36b: The MPH of the well data (bars) and TI #2 (line). The MPH patterns are shown under the horizontal axis.

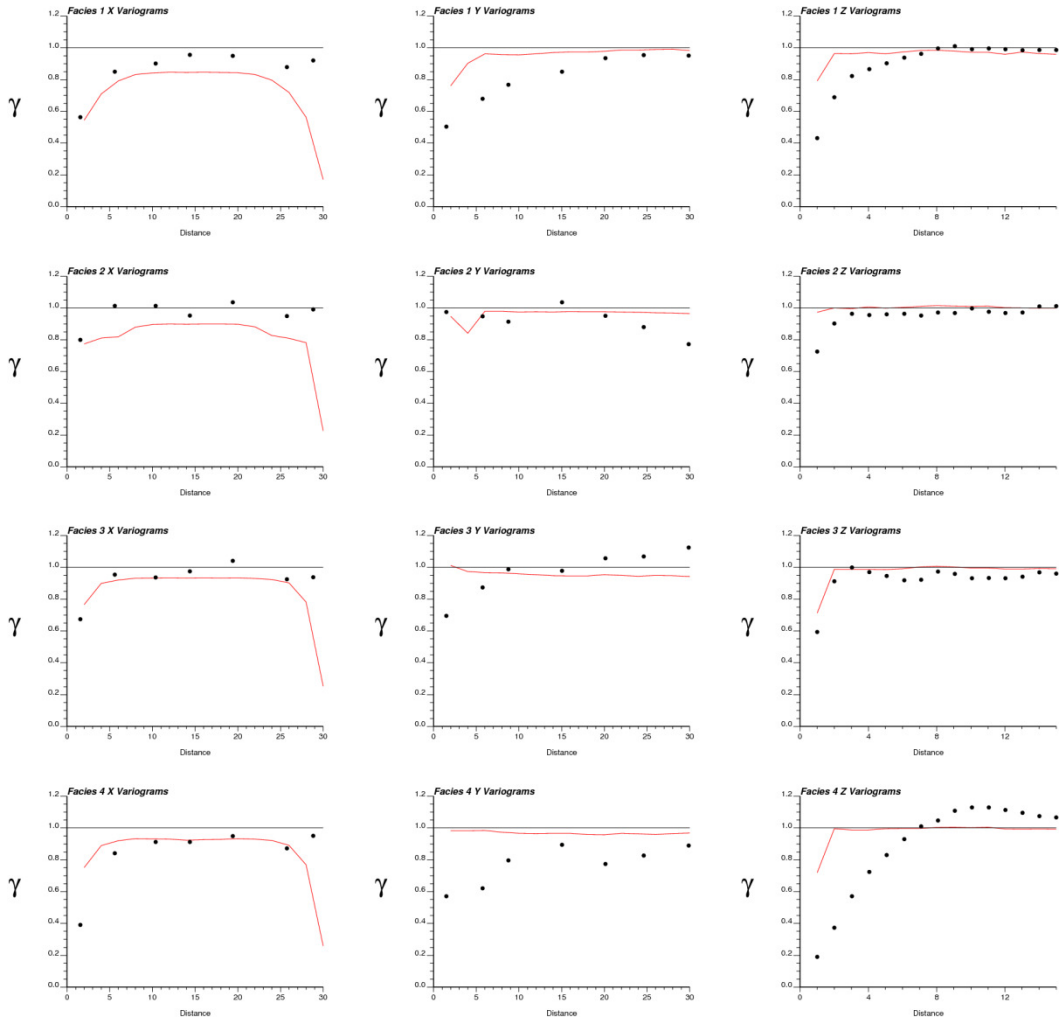


Figure 5.36c: Indicator variograms for the well data (points) and TI #2 (line) in the X, Y, and Z directions (left to right) for the four facies, top to bottom: facies 1 (white), facies 2 (light grey), facies 3 (dark grey), and facies 4 (black).

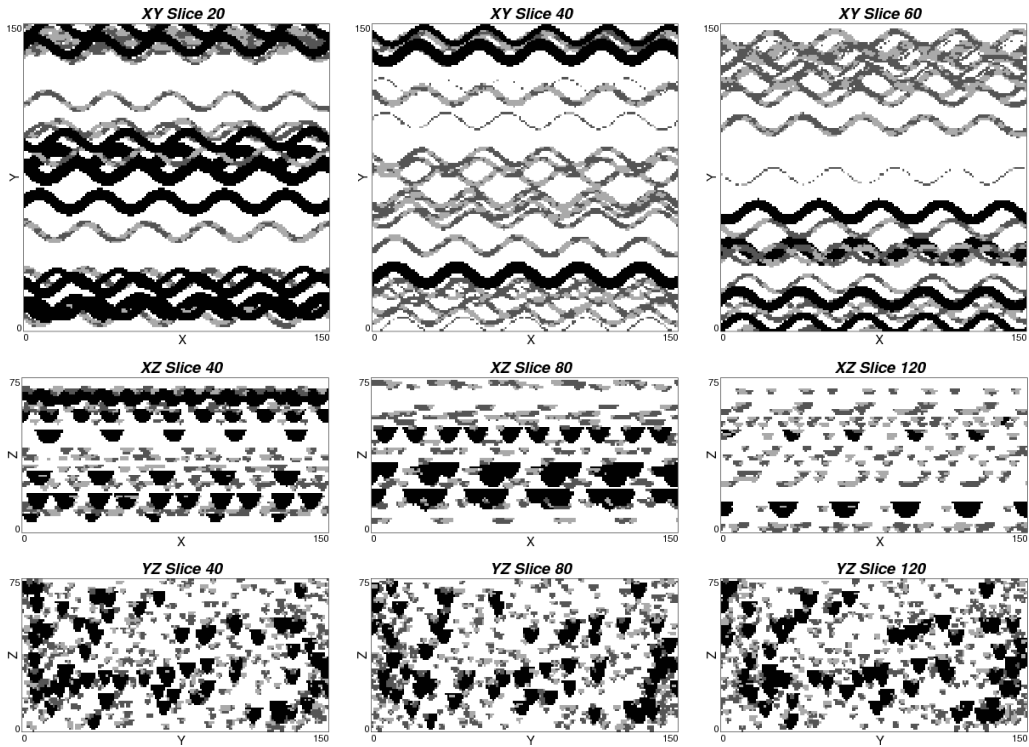


Figure 5.37a: TI #3 for the petroleum reservoir case study.

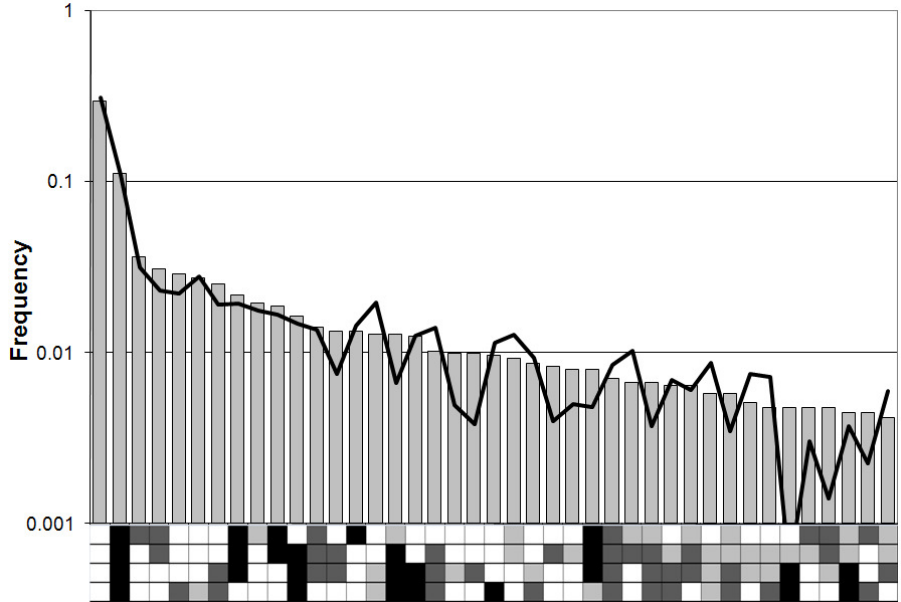


Figure 5.37b: The MPH of the well data (bars) and TI #3 (line). The MPH patterns are shown under the horizontal axis.

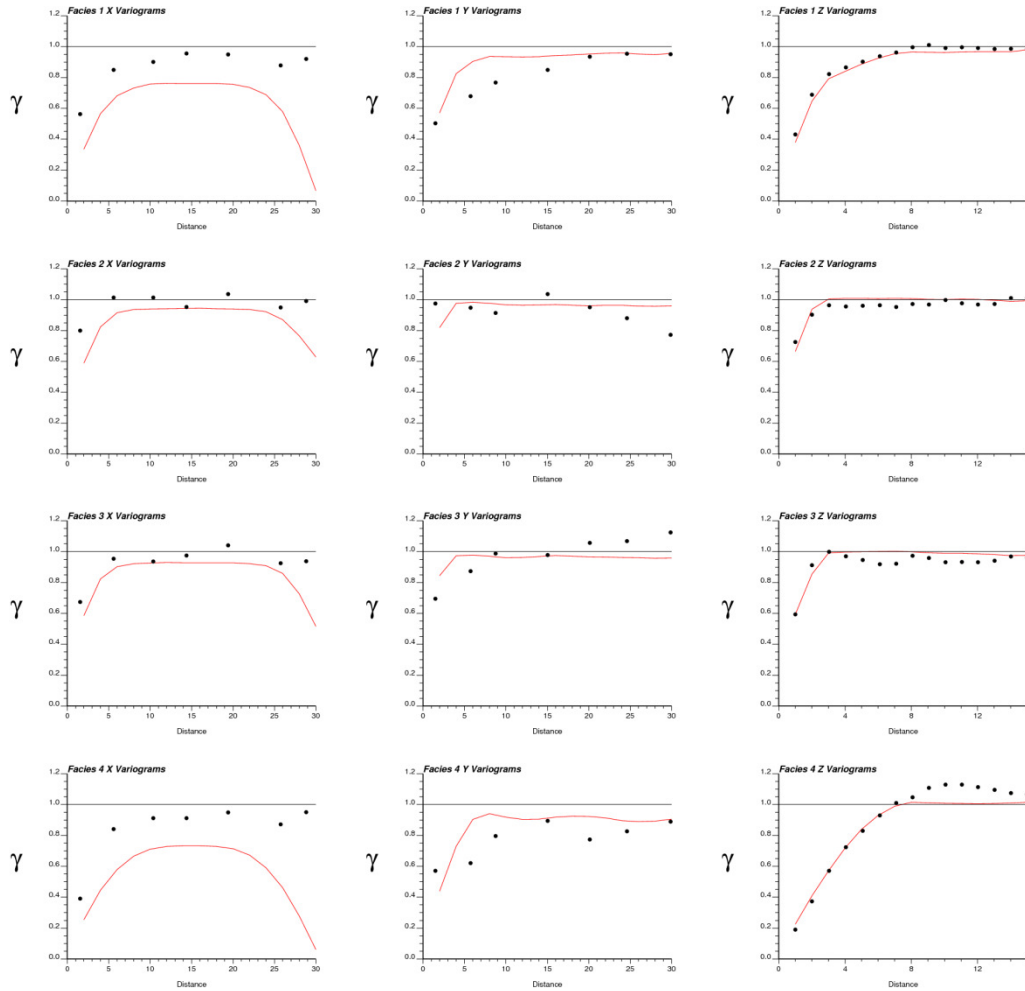


Figure 5.37c: Indicator variograms for the well data (points) and TI #3 (line) in the X, Y, and Z directions (left to right) for the four facies, top to bottom: facies 1 (white), facies 2 (light grey), facies 3 (dark grey), and facies 4 (black).

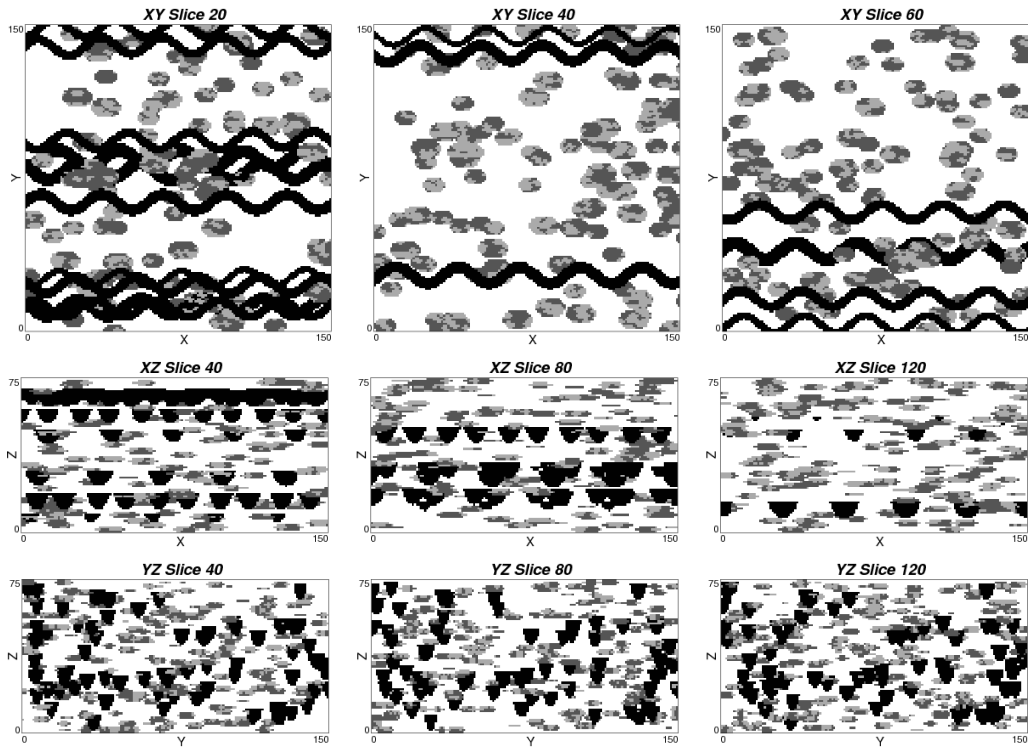


Figure 5.38a: TI #4 for the petroleum reservoir case study.

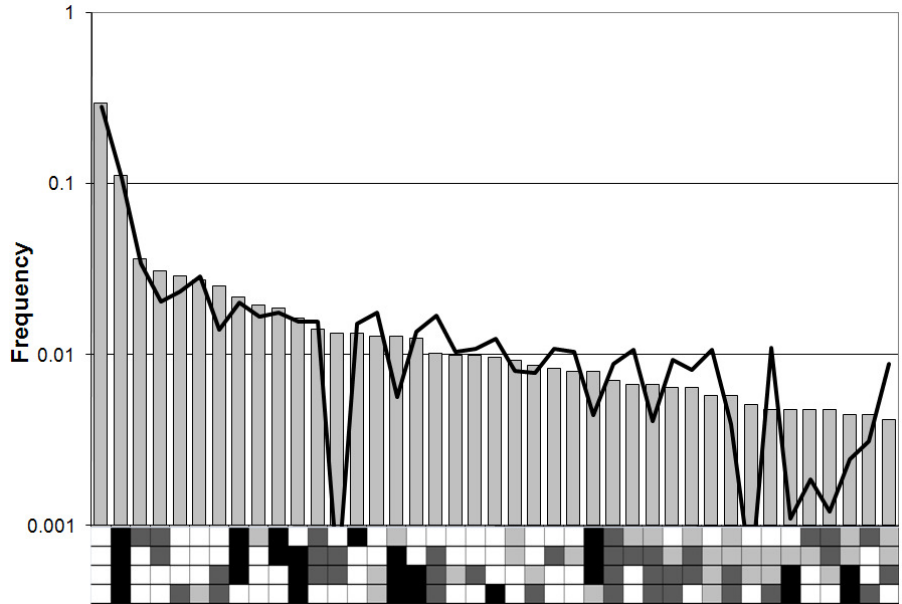


Figure 5.38b: The MPH of the well data (bars) and TI #4 (line). The MPH patterns are shown under the horizontal axis.

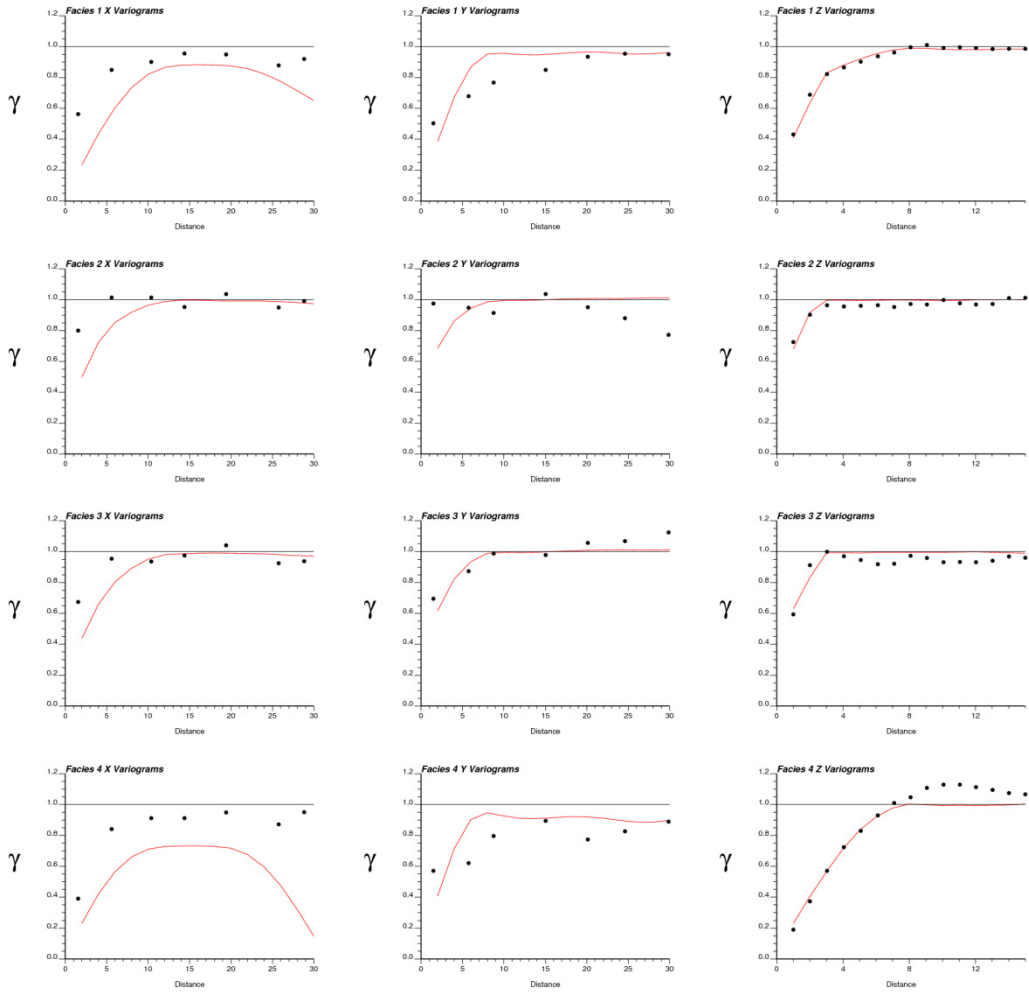


Figure 5.38c: Indicator variograms for the well data (points) and TI #4 (line) in the X, Y, and Z directions (left to right) for the four facies, top to bottom: facies 1 (white), facies 2 (light grey), facies 3 (dark grey), and facies 4 (black).

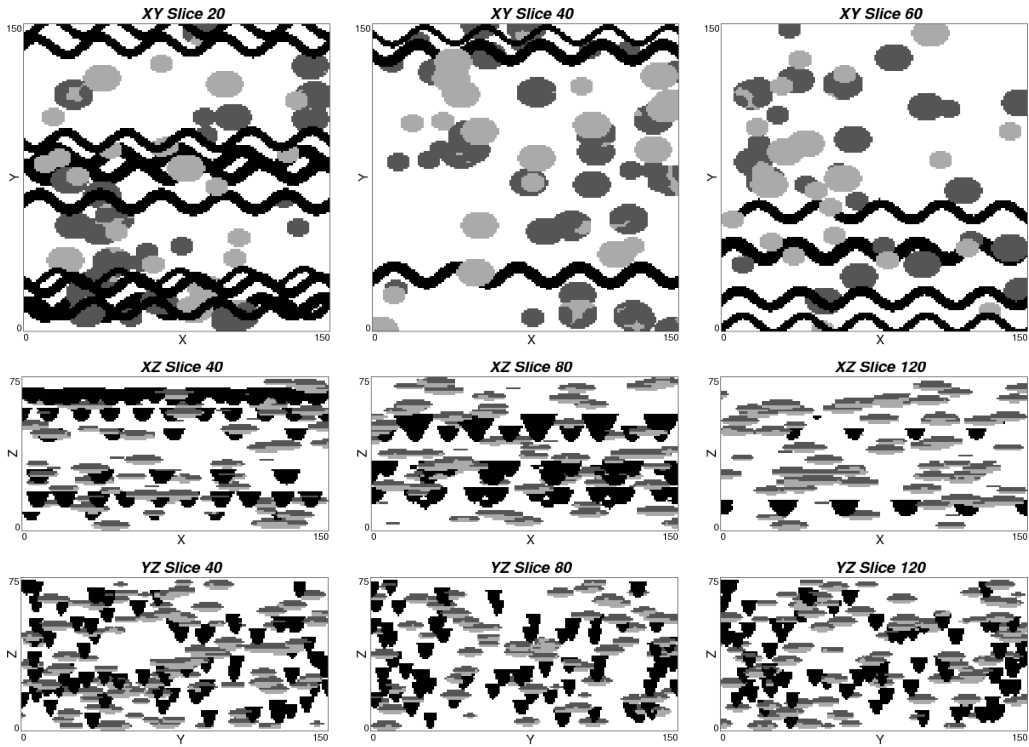


Figure 5.39a: TI #5 for the petroleum reservoir case study.

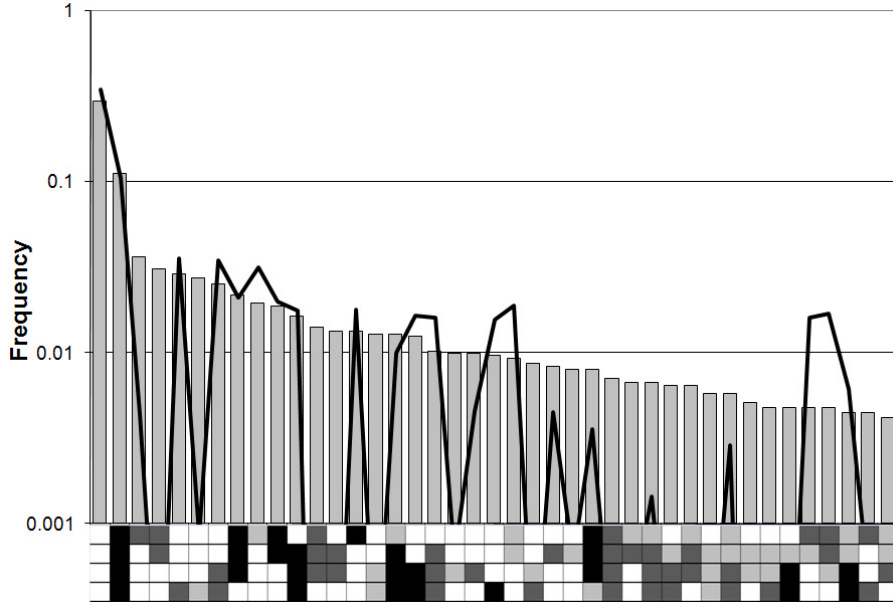


Figure 5.39b: The MPH of the well data (bars) and TI #5 (line). The MPH patterns are shown under the horizontal axis.

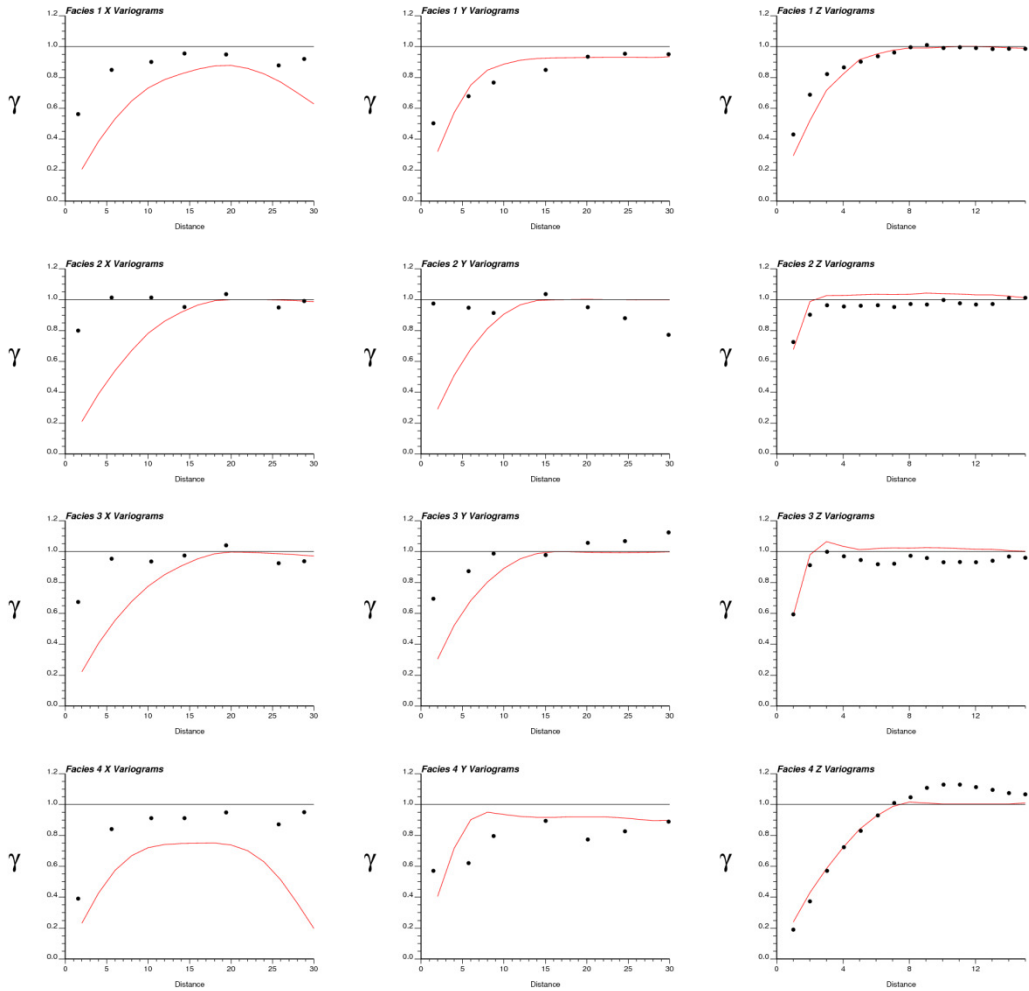


Figure 5.39c: Indicator variograms for the well data (points) and TI #5 (line) in the X, Y, and Z directions (left to right) for the four facies, top to bottom: facies 1 (white), facies 2 (light grey), facies 3 (dark grey), and facies 4 (black).

Table 5.7: Absolute MPH differences of the petroleum reservoir TIs from the well data.

Training Image	Absolute MPH Difference
1	0.352
2	0.870
3	0.257
4	0.283
5	0.606

Table 5.8: CPU time required to create the templates and calculate MPS for the petroleum reservoir case study.

Training Image	Time Required (mm:ss)	
	Template Creation	MPS Calculation
TI #1	1:26	60:19
TI #3	1:22	63:18
TI #4	1:24	74:55

### 5.3.2 Unconditional Simulation

Unconditional simulation was used to assess the reproduction of features in the TIs. The three cases for MPS-GS were considered and SISIM was used for a comparison to a standard geostatistical method. Table 5.9 shows the time required for simulating ten realizations of the four cases. All simulations were performed using five grids; the MPS-GS realizations used a servosystem parameter of  $\mu=1.0$  and a connectivity correction factor of  $\eta=0.1$ . A maximum of thirty loops was imposed for stopping, but this limit was rarely reached. The SISIM realizations use a variogram model that was inferred from the data rather than from one of the TIs. All realizations are 68x56x112 for a total of 426,496 cells; recall that the TIs are 150x150x75 cells, so the cell sizes in the figures are different between the TIs and realizations.

Table 5.9: CPU time required to simulate ten unconditional realizations for the petroleum reservoir study.

Training Image	Time Required (mm:ss)
TI #1	8:52
TI #3	9:55
TI #4	9:03
SISIM	2:27

Figures 5.40 through 5.43 show the results of unconditional simulation from each of the four cases. The Figures have two parts: (a) nine slices from the realization, three in each plane; (b) the indicator variograms of five realizations in the X, Y, and Z directions

for each of the four facies. No MPH was used to compare the unconditional realizations because there is no standard for comparison.

Some notable observations from the realizations:

- The sinusoidal channel features for facies 4 are apparent in the MPS-GS realizations, although the relatively large size of the channel structures compared to the simulation domain largely eliminates the repeating nature of the patterns;
- The channel cross-sections for facies 4 are reproduced in all MPS-GS cases, with flat tops and the correct cross-sectional shape and size;
- Facies 2 and 3 are properly associated with one another in the MPS-GS realizations;
- The TI #1 case reproduces the channel features of facies 3 and the associated levees of facies 2;
- The TI #3 case has the worst reproduction of the facies 2 and 3 structure, caused by the separated nature of the individual facies bodies within the channels. In this case the two should be combined in to a single channel architecture;
- The TI #4 case reproduces the facies 2 and 3 lobes well;
- SISIM does not reproduce any of the geological features seen in the TIs or presumed to be represented by the data;
- All MPS-GS cases have indicator variograms that are too low at short ranges. This could be caused by the relatively small size of the domain reducing the repeating nature of the pattern;
- The variograms do not show the perfect cyclicity seen in the TI variograms, but rather continue increasing to the sill values.

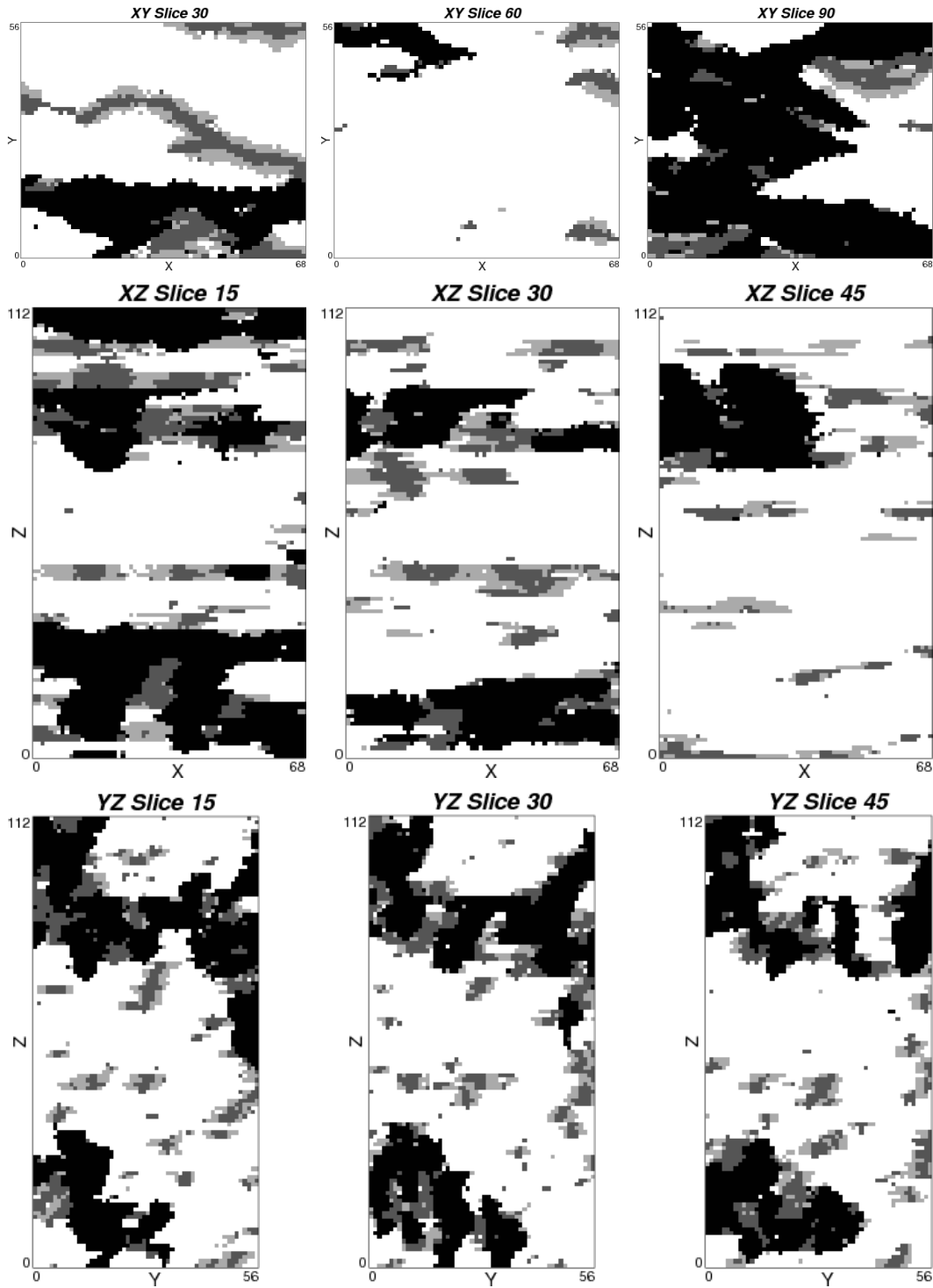


Figure 5.40a: Slices from one unconditional MPS-GS realization created using TI #1 in the petroleum reservoir case study.

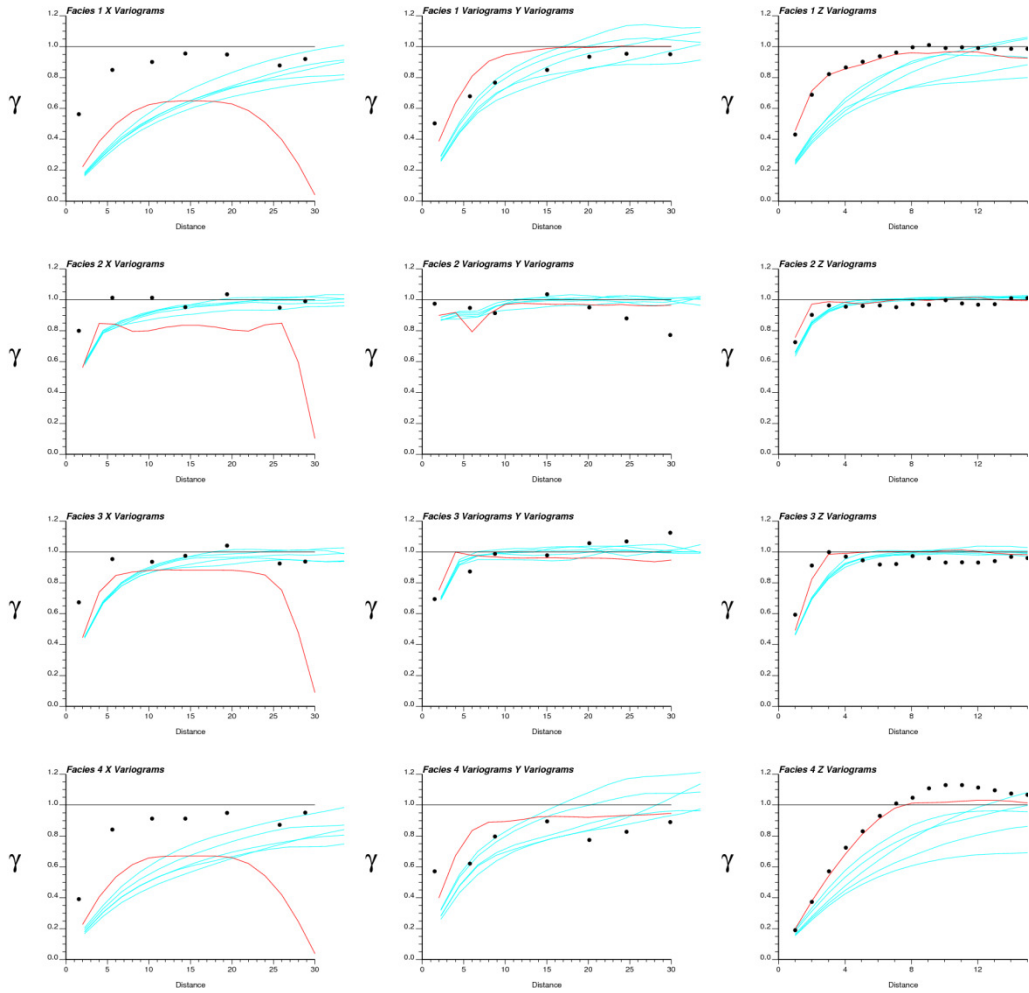


Figure 5.40b: The indicator variograms of TI #1 (red line), sample data (black dots), and 5 MPS-GS realizations (blue lines) in the (left to right) X, Y, and Z directions for (top to bottom) facies 1, facies 2, facies 3, and facies 4.

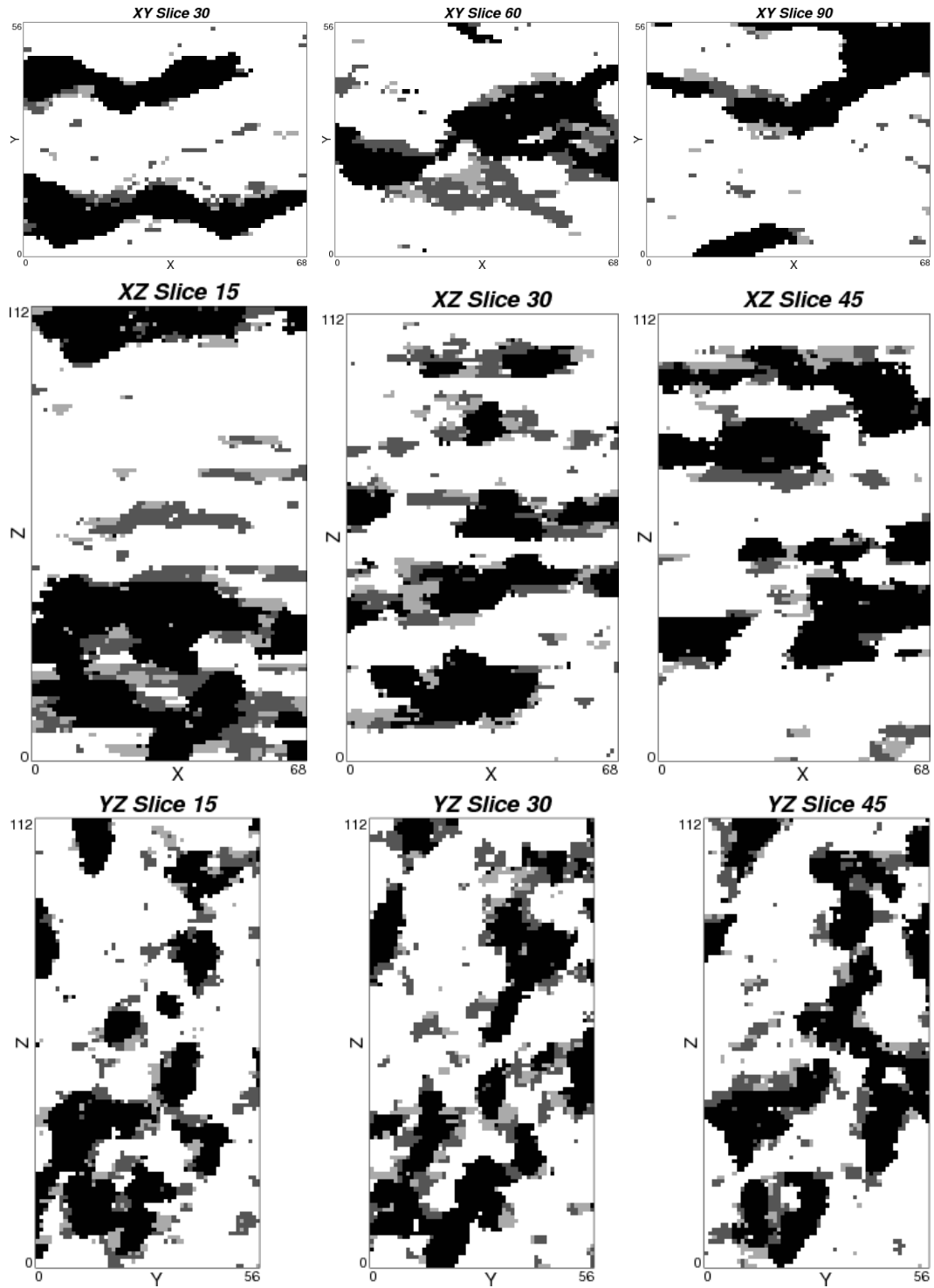


Figure 5.41a: Slices from one unconditional MPS-GS realization created using TI #3 in the petroleum reservoir case study.

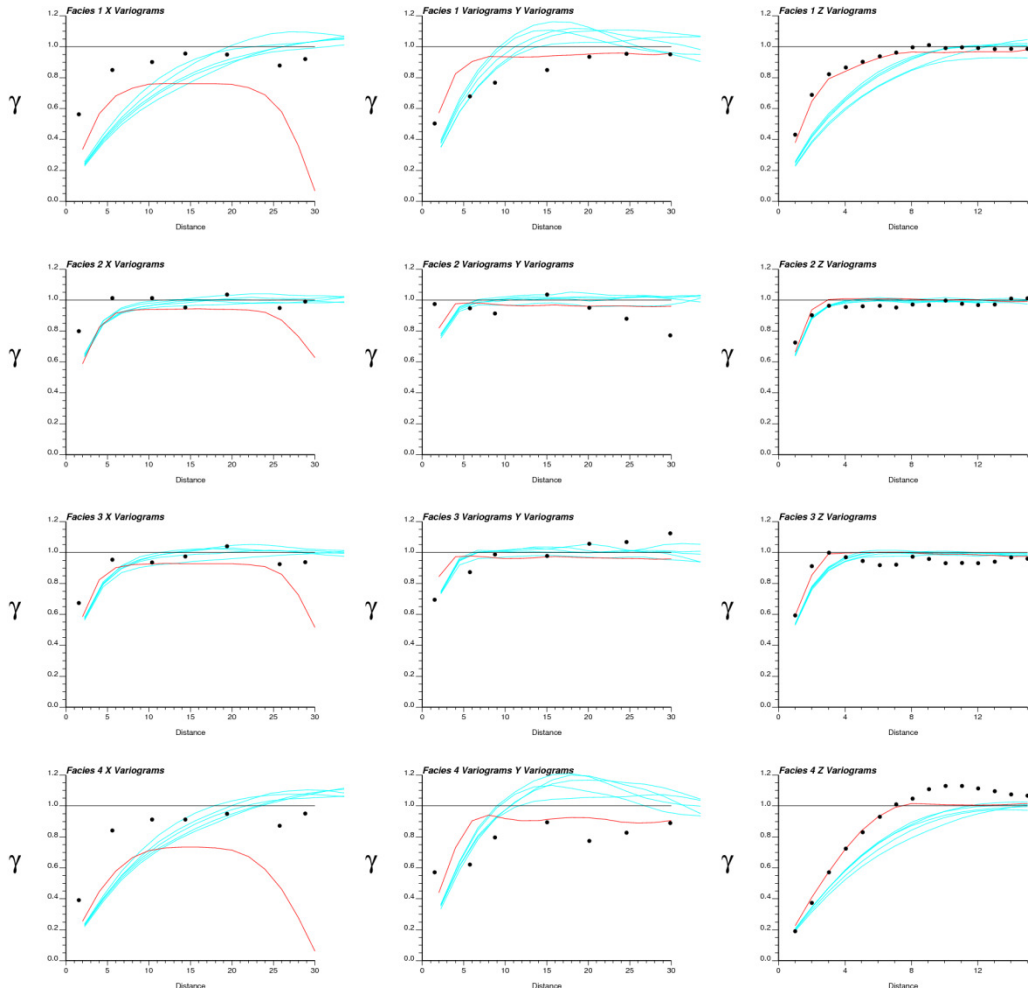


Figure 5.41b: The indicator variograms of TI #3 (red line), sample data (black dots), and 5 MPS-GS realizations (blue lines) in the (left to right) X, Y, and Z directions for (top to bottom) facies 1, facies 2, facies 3, and facies 4.

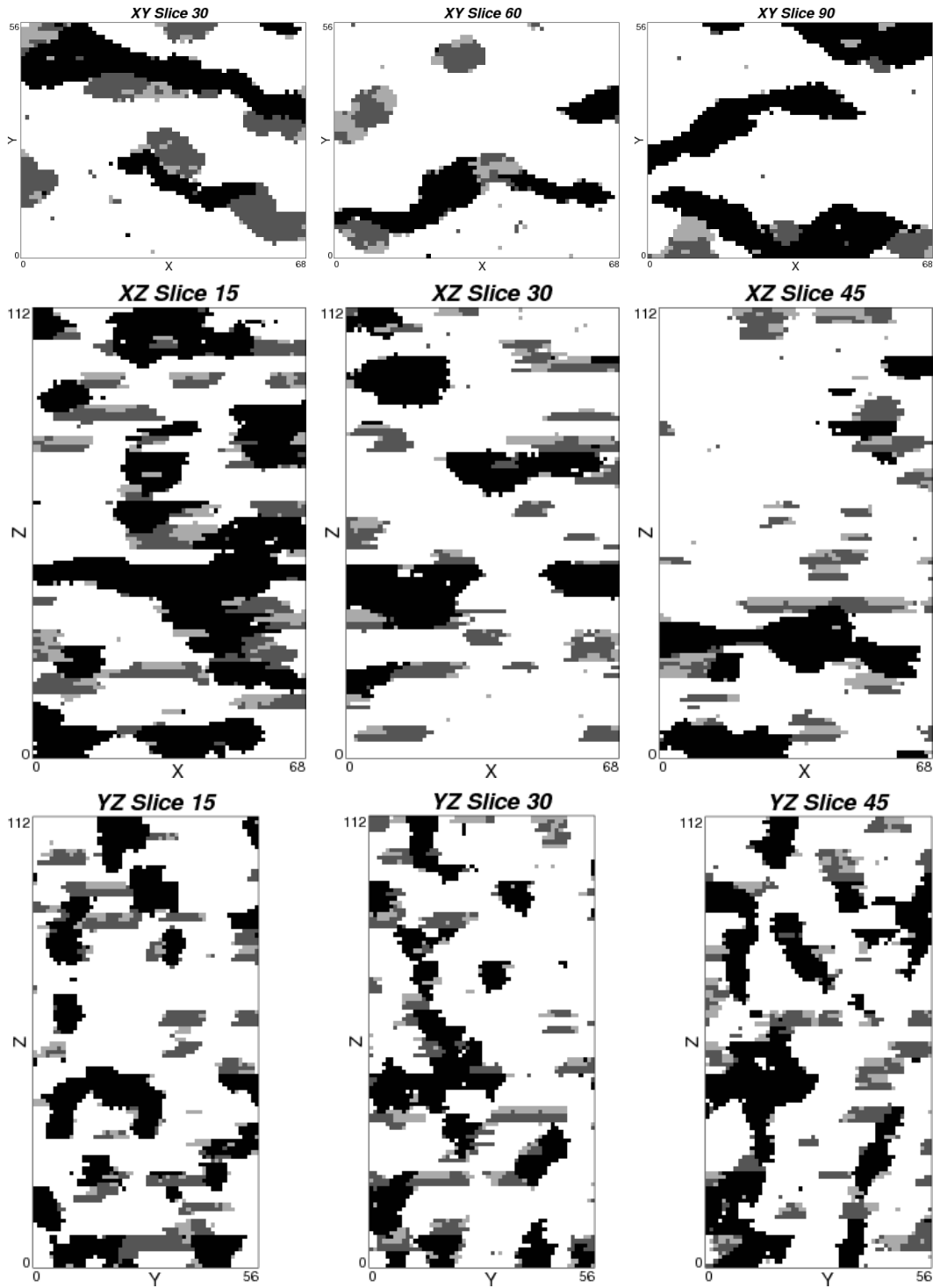


Figure 5.42a: Slices from one unconditional MPS-GS realization created using TI #4 in the petroleum reservoir case study.

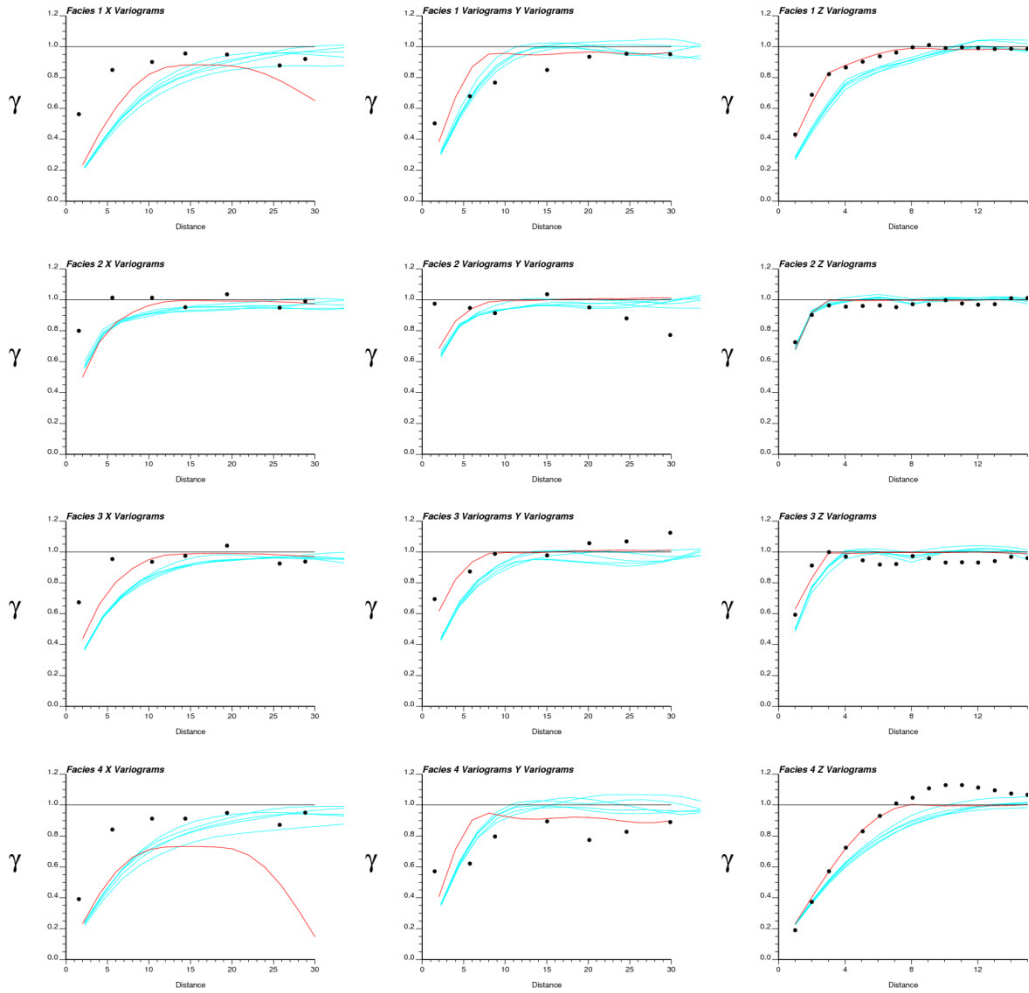


Figure 5.42b: The indicator variograms of TI #4 (red line), sample data (black dots), and 5 MPS-GS realizations (blue lines) in the (left to right) X, Y, and Z directions for (top to bottom) facies 1, facies 2, facies 3, and facies 4.

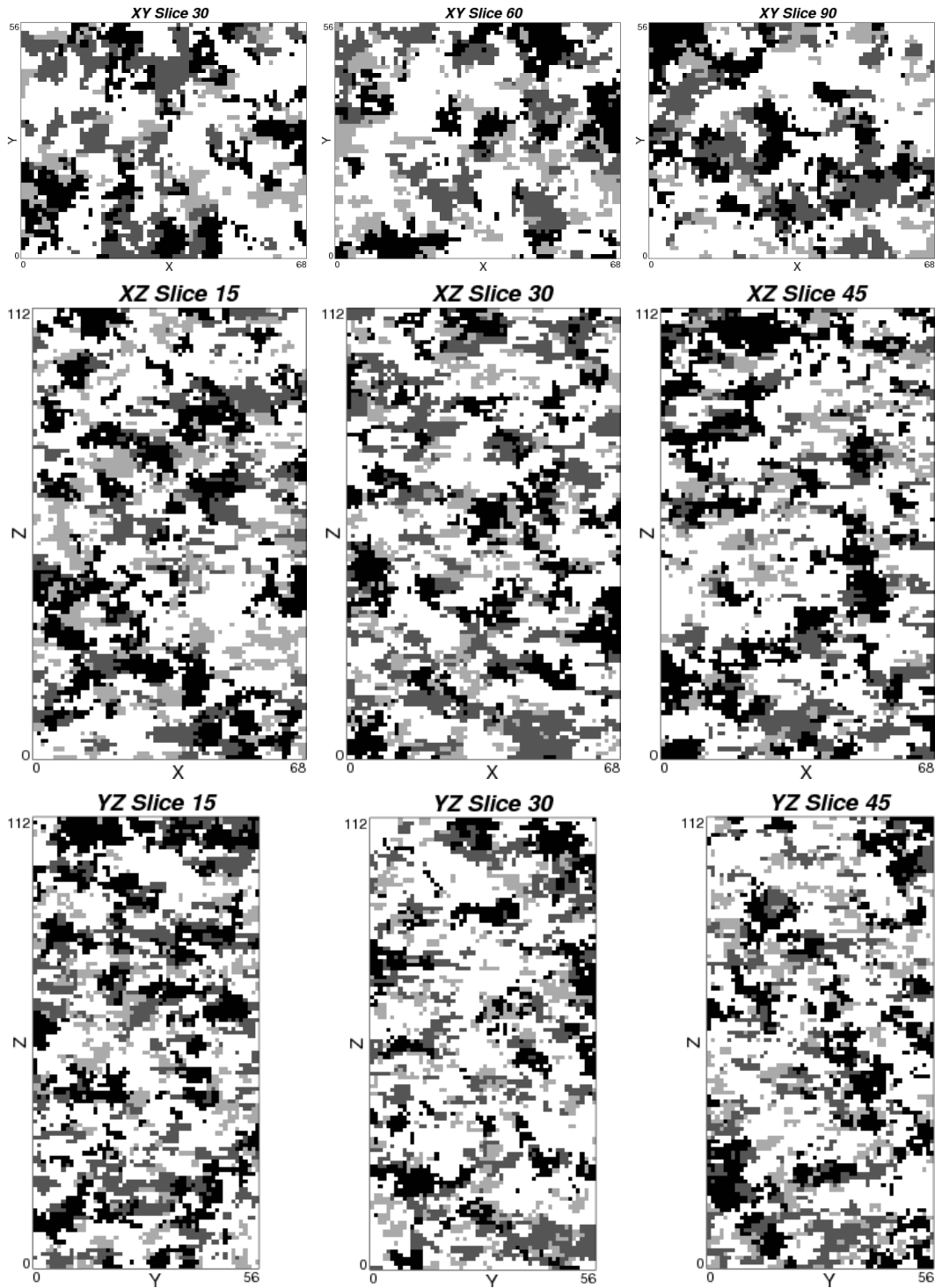


Figure 5.43a: Slices from one unconditional SISIM realization in the petroleum reservoir case study.

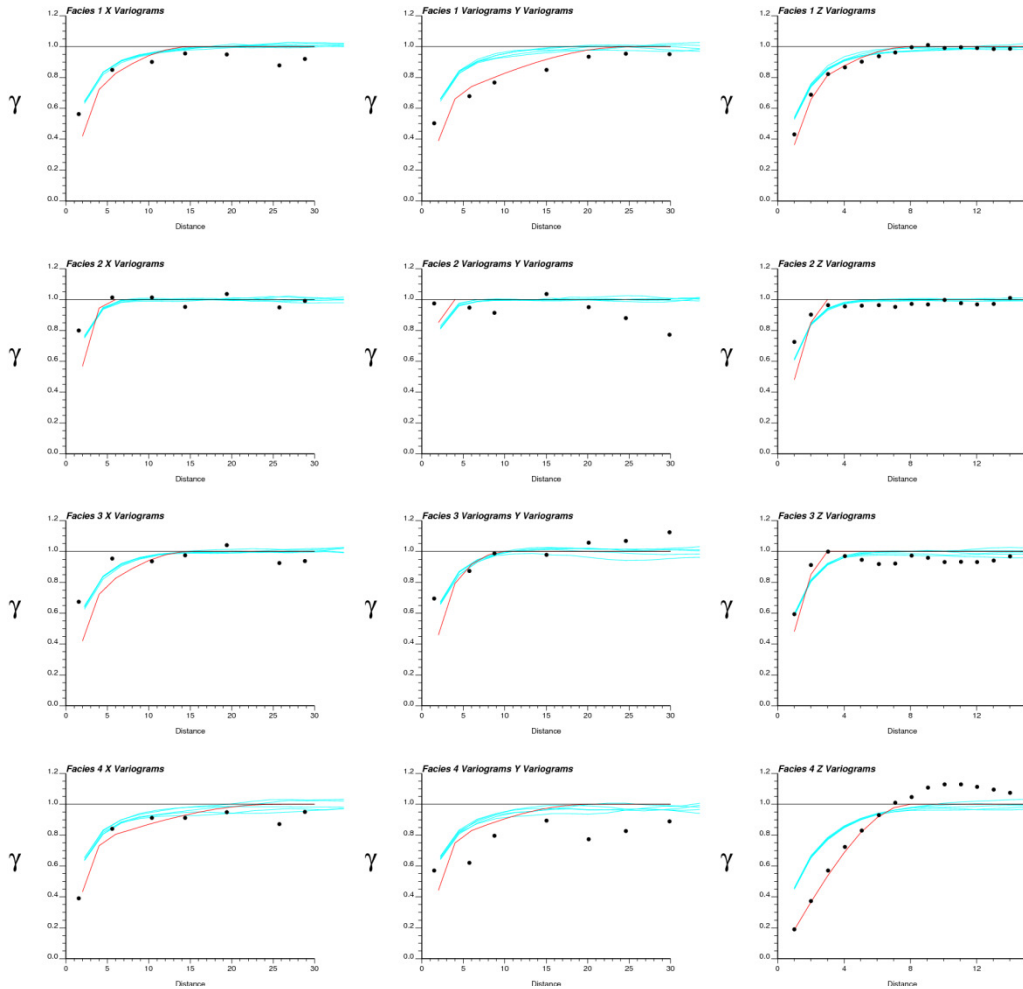


Figure 5.43b: The modeled indicator variograms, sample data (black dots), and 5 SISIM realizations (blue lines) in the (left to right) X, Y, and Z directions for (top to bottom) facies 1, facies 2, facies 3, and facies 4.

### 5.3.3 Conditional Simulation with a Vertical Trend

The available well data were used for simulation to assess the ability of MPS-GS to integrate real information that does not necessarily follow an idealized model of geology. The 33 wells were used as hard conditioning information and a vertical trend was modeled from the well data and used as locally varying facies proportions. There are distinct variations in the proportions at different horizontal layers; Figure 5.44 shows the modeled vertical trend. There are five distinct zones: three with higher net sands proportions (top, middle and bottom) and two with higher shale proportions (upper and lower). The middle high net zone has a greater proportion of facies 4 and is thin while the

upper and lower high net zones have relatively high proportions of facies 2 and 3 and are thicker than the middle zone. Each of the 112 layers has its own set of facies proportions and areal trends were not considered.

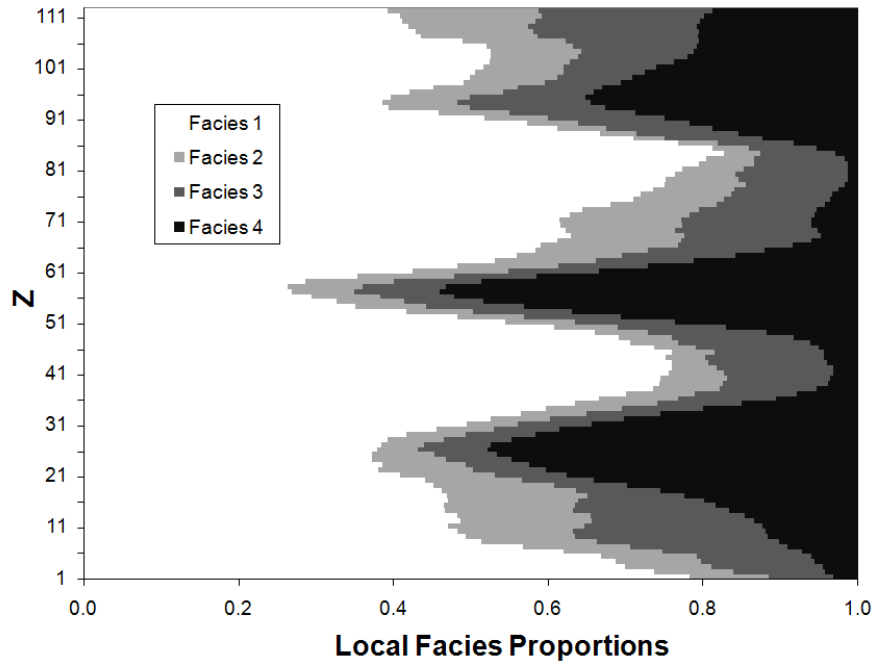


Figure 5.44: Vertical trend model used in the petroleum reservoir case study.

The parameters and domain size for the simulations were the same as the unconditional case. Table 5.10 shows the time required to simulated ten realizations for each of the cases.

Table 5.10: CPU time required to simulate ten conditional realizations for the petroleum reservoir case study.

Training Image	Time Required (mm:ss)
TI #1	10:30
TI #3	10:34
TI #4	9:48
SISIM	2:32

Figures 5.45 through 5.48 show the results of the conditional simulations. Each Figure shows nine slices from one realization. Figure 5.49 shows the reproduction of the vertical trend model of each facies in the four cases.

Some observations from these results:

- All of the comments from the unconditional cases still apply. Using hard and soft data does not significantly change the overall structure produced;
- Some of the well data appear as discontinuities where there are sudden changes from one facies structure to another and in areas of facies proportions significantly different than the global TI proportions. This is visible in all cases;
- The high and low net zones appear to be reproduced on visual inspection;
- From Figure 5.49 the methods all reproduce the vertical trend model. Facies 2 and 3, with the lowest proportions, show the greatest variation from the target;
- MPS-GS appears to slightly overshoot the very high and low target facies proportions while SISIM undershoots;
- Facies 2 and 3 are underrepresented by MPS-GS, particularly in the zones of very low proportions.

Using the 10 wells reserved for jackknife cross-validation, the accuracy of the simulation cases was assessed. Figure 5.50 shows an accuracy plot of the four cases: the simulated probability of a facies is shown on the horizontal axis and the actual probability of finding that facies is shown on the vertical axis. The MPS-GS case using TI #1 and SISIM are more accurate than the TI #3 and TI #4 cases for simulated facies probabilities above 0.4, and all four cases are comparable below that threshold. Training image #1 is the closest to the conceptual model of geology and this is the likely cause of the improved accuracy.

The precision of the cases was measured using the histograms of the simulated facies proportions. Figure 5.51 shows the results. The three MPS-GS cases have very similar histograms and variances of 0.098 while SISIM has a variance of only 0.048 and a noticeably different histogram, in particular a spike at a simulated proportion of 0.2. The SISIM results have little local precision and as a result the realizations would all be more similar in terms of response characteristics.

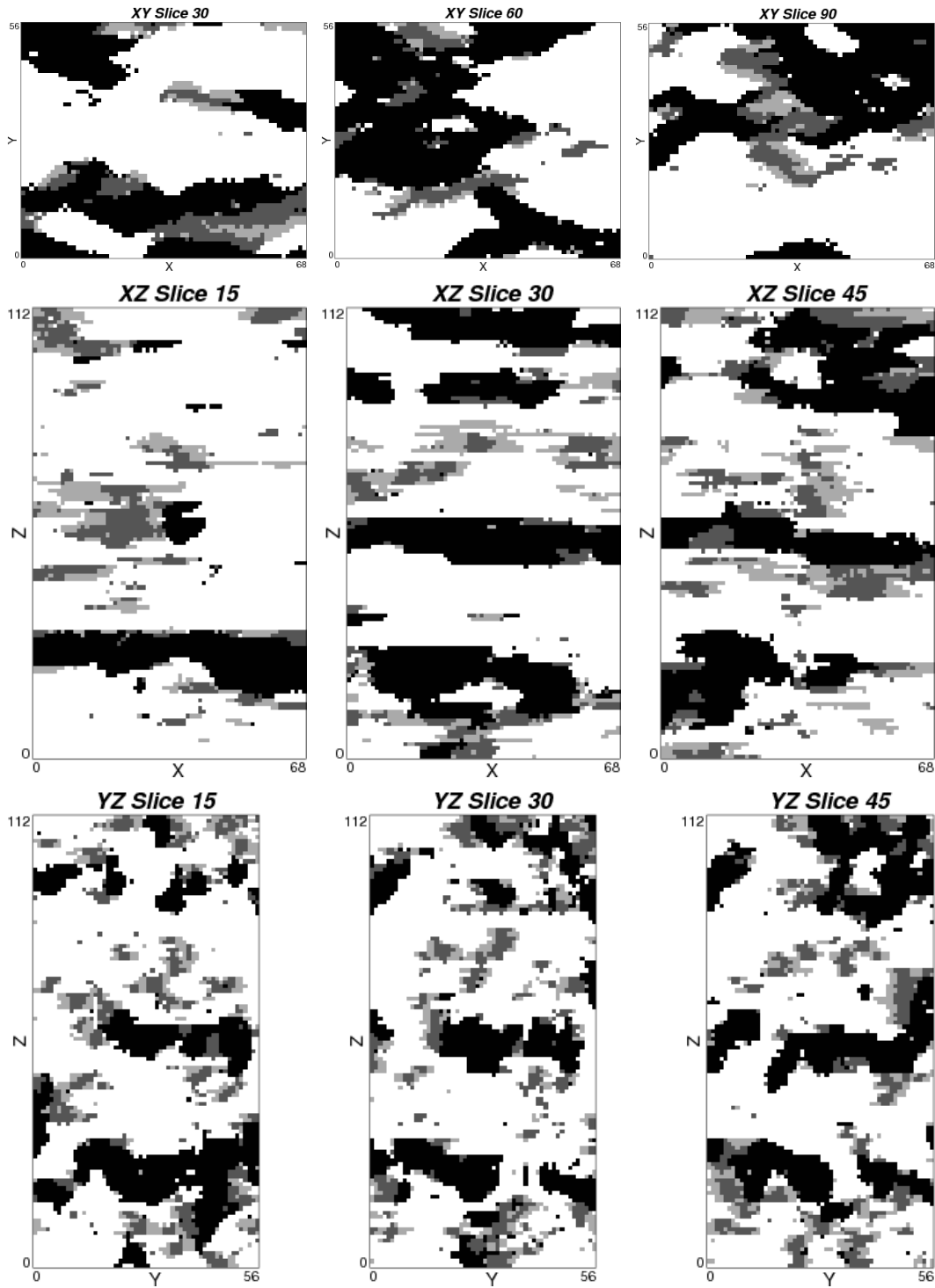


Figure 5.45: Slices from one conditional MPS-GS realization created using TI #1 in the petroleum reservoir case study.

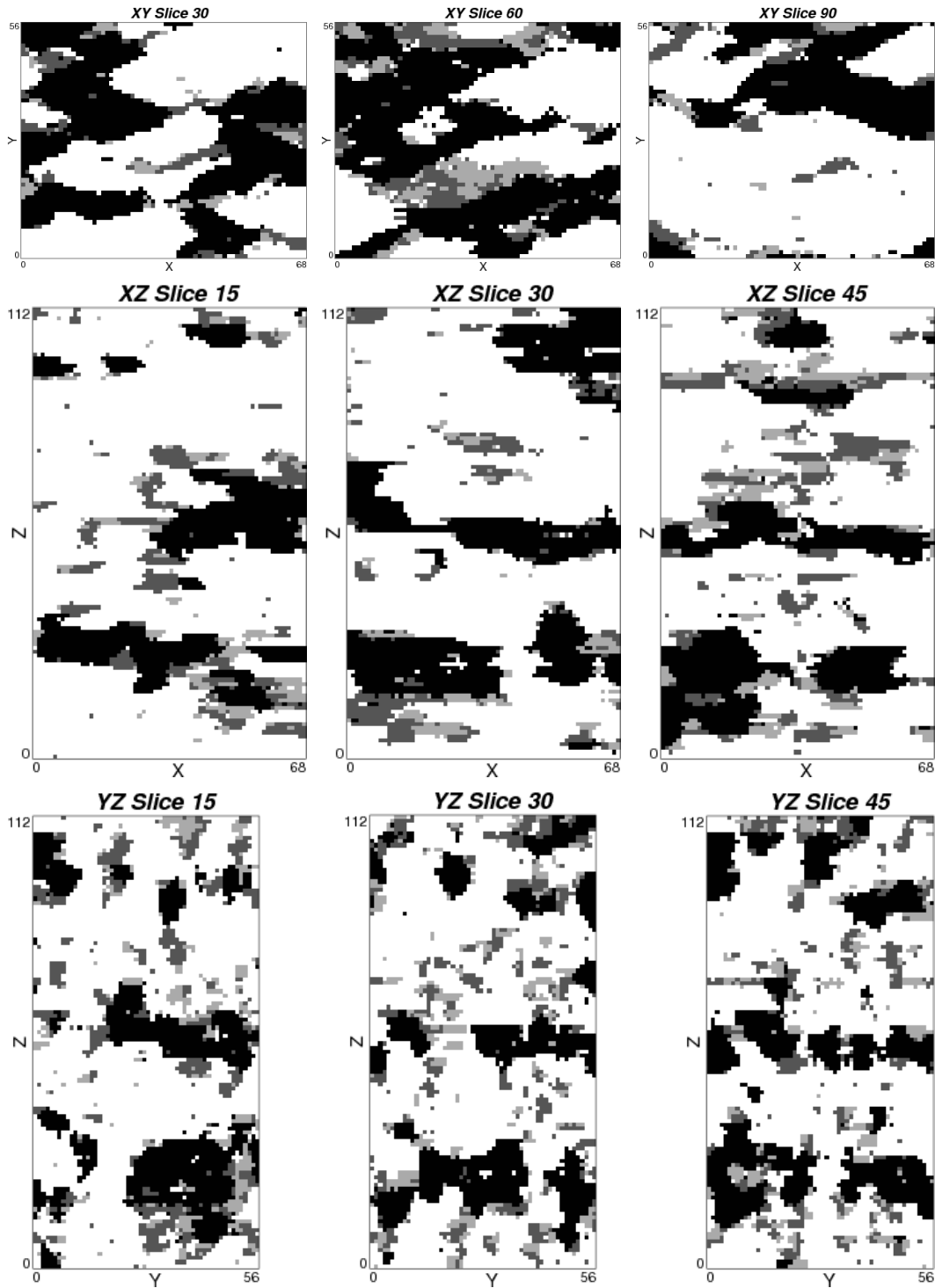


Figure 5.46: Slices from one conditional MPS-GS realization created using TI #3 in the petroleum reservoir case study.

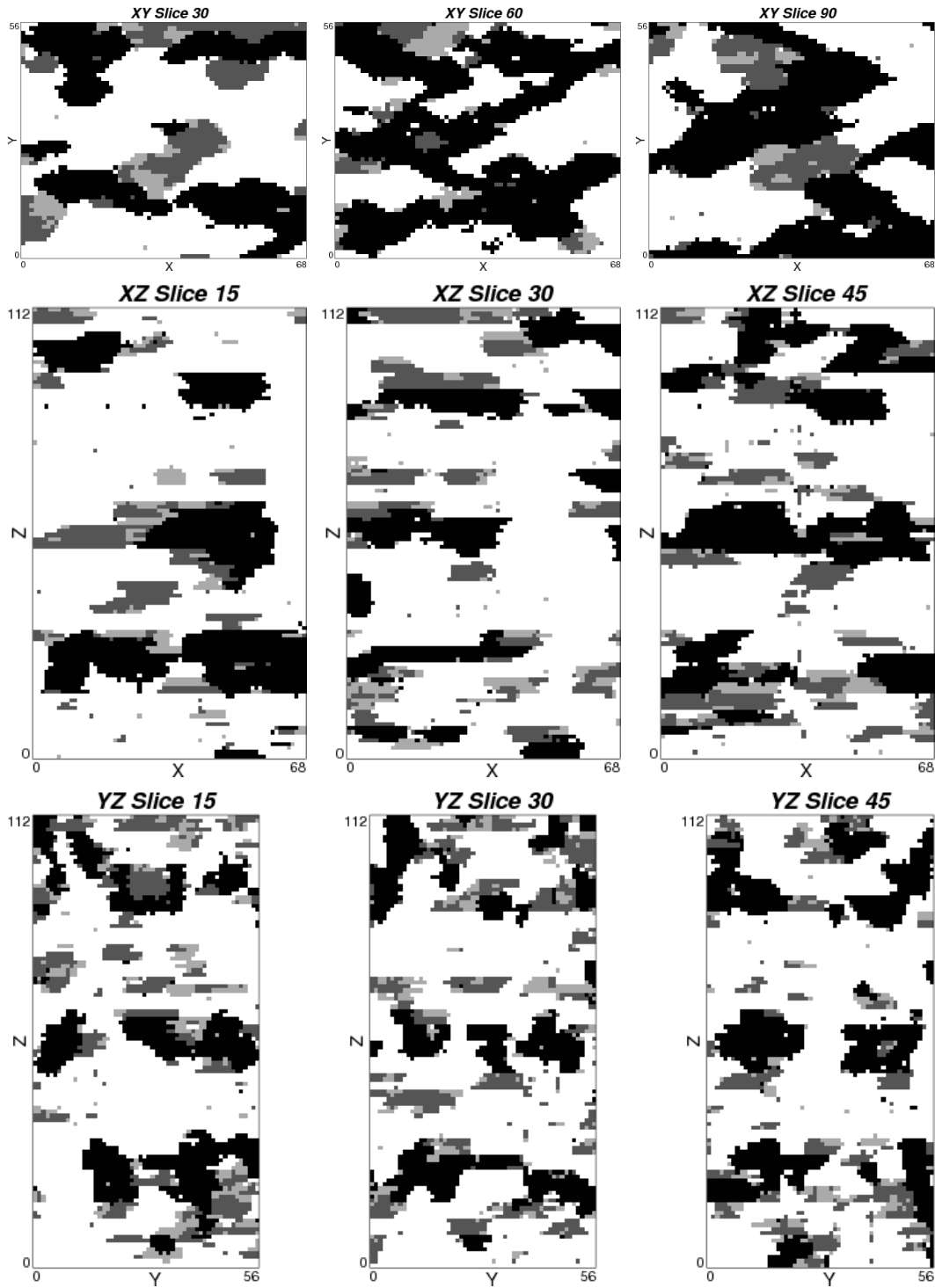


Figure 5.47: Slices from one conditional MPS-GS realization created using TI #4 in the petroleum reservoir case study.

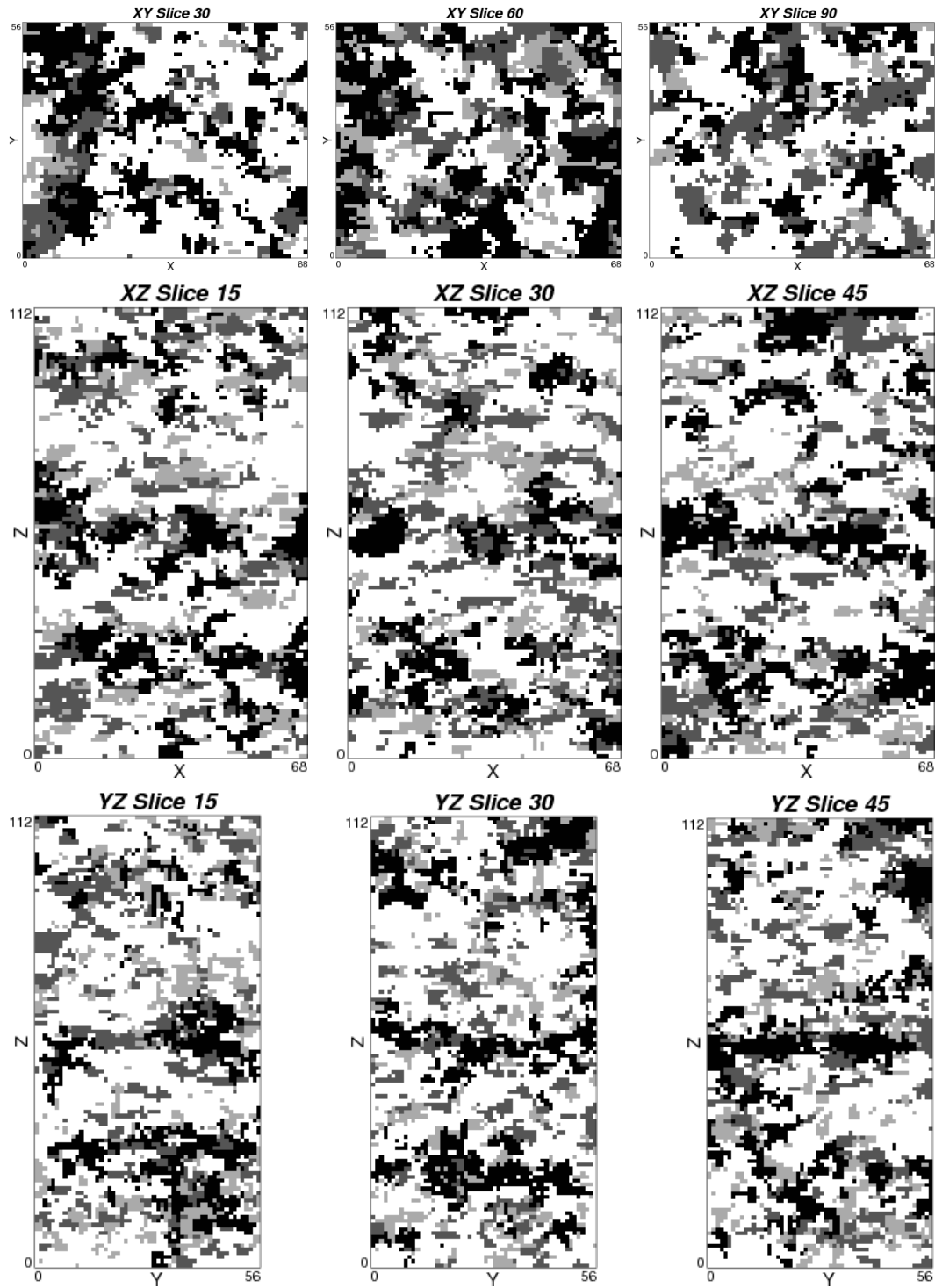


Figure 5.48: Slices from one conditional SISIM realization in the petroleum reservoir case study.

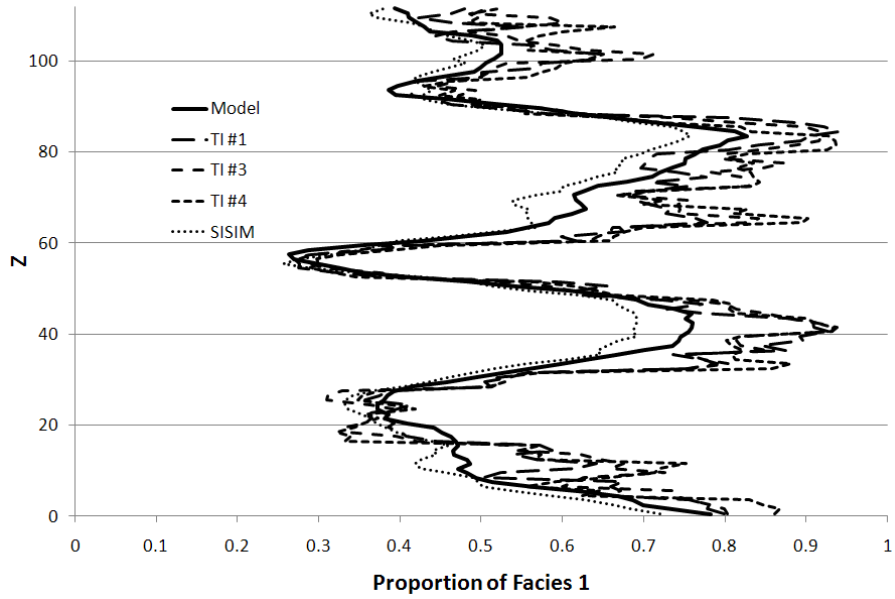


Figure 5.49a: Trend model reproduction of the conditional simulations for facies 1 in the petroleum reservoir case study.

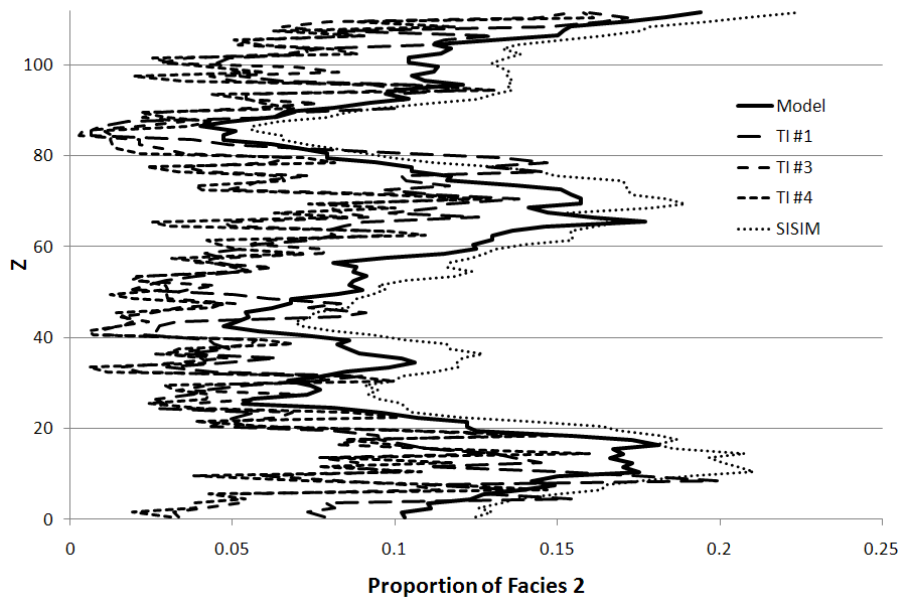


Figure 5.49b: Trend model reproduction of the conditional simulations for facies 2 in the petroleum reservoir case study.

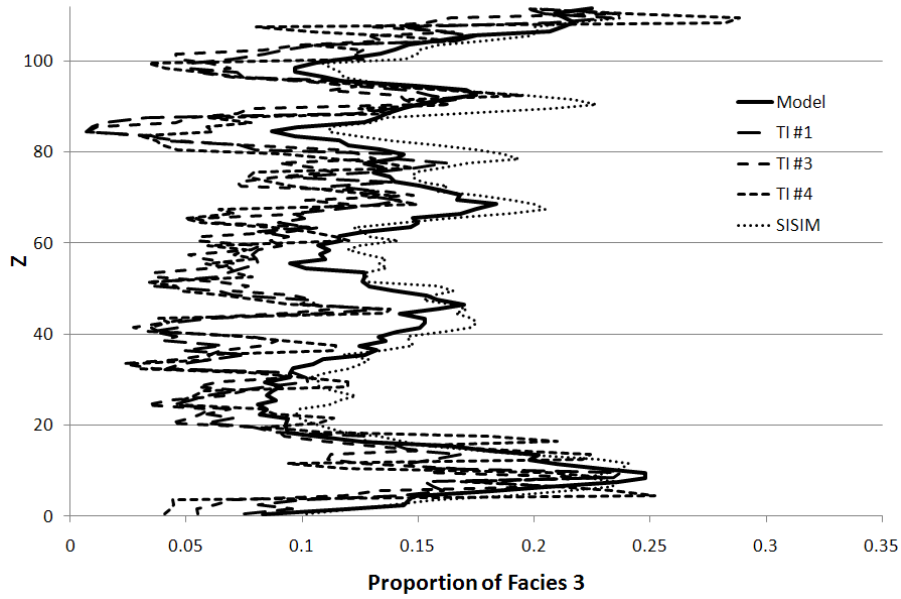


Figure 5.49c: Trend model reproduction of the conditional simulations for facies 3 in the petroleum reservoir case study.

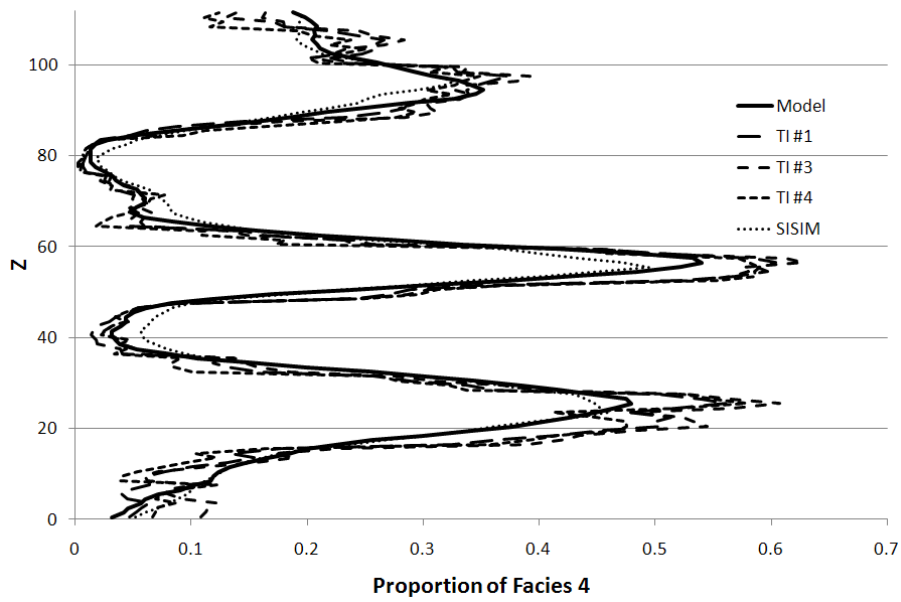


Figure 5.49d: Trend model reproduction of the conditional simulations for facies 4 in the petroleum reservoir case study.

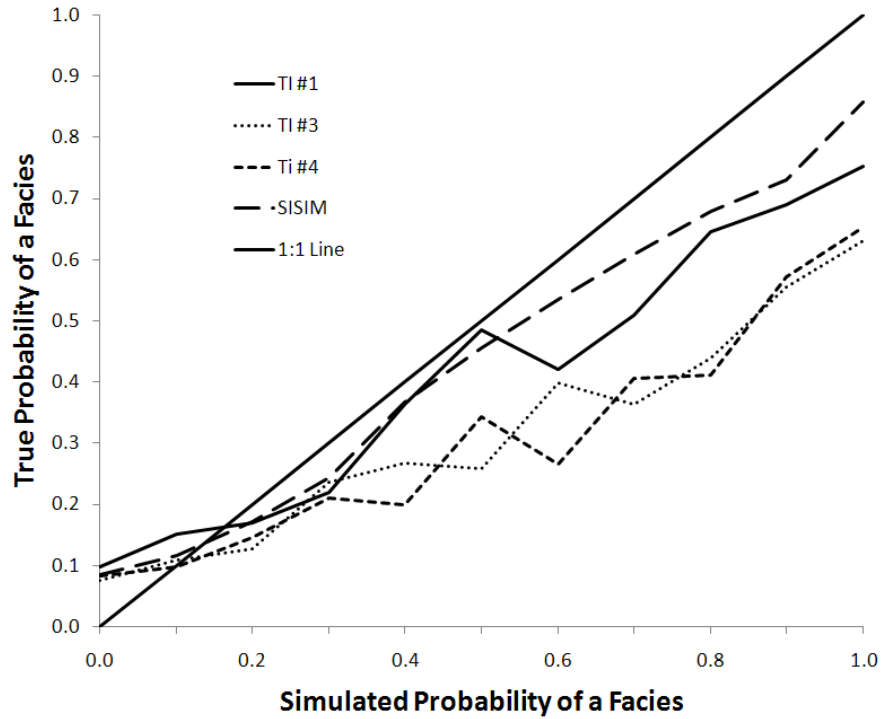


Figure 5.50: Accuracy plot of the petroleum reservoir conditional simulations based on the jackknife cross-validation data.

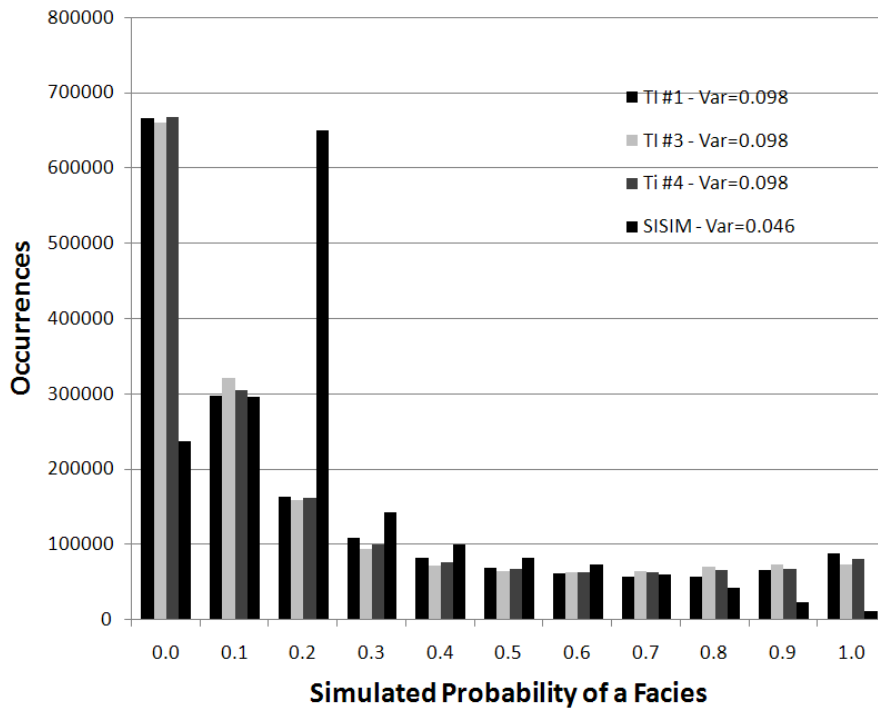


Figure 5.51: Precision of the petroleum reservoir conditional simulations.

## 5.4 Conclusions

The MPS-GS algorithm was compared to SISIM for three different geologic scenarios. Different templates and TIs were used for MPS-GS to examine the effects of changing these parameters. The MPS-GS algorithm was found to be as accurate as SISIM. The precision of MPS-GS is greater than SISIM in most cases, and no worse in other cases.

The best results for MPS-GS are generally found using MPEs of about size  $N=4$ . Higher-order statistics give better results in some cases, but with three or more facies the TIs that are available are usually insufficient for adequate statistical inference, and solving the large systems of equations takes significantly longer without a corresponding gain in quality of realizations.

Using different TIs for quantification of global uncertainty represents the uncertainty in the conceptual model of geology. Multiple realizations represent ergodic fluctuations inherent to stochastic simulation. Comparing a variety of scenarios also allows for the identification of statistically good and poor choices for a TI.

## 6 Conclusions

The subject of multiple-point statistics (MPS) within the field of geostatistics has seen significant development since the early 1990s. Traditional variogram-based geostatistics cannot produce realizations that are consistent with curvilinear or highly structured conceptual models of geology. Object- or process-based methods have difficulty integrating all available hard and soft data. Algorithms using MPS have been developed to reproduce both a training image (TI) and all available data. Other areas of MPS such as TI creation and selection and evaluation of results have seen less research. The overall field of multiple-point geostatistics continues to evolve.

This research develops a new Gibbs sampler framework for generating categorical variable models using MPS, lower-order statistics, hard sample data, and secondary information. The approach is flexible enough to use dense sample data. Multiple-point events (MPEs) are used to mitigate the problem of dimensionality while using higher-order spatial statistics.  $M$  multiple-point events of order  $K^N$  are used rather than a single large template of order  $K^{MN}$ . The approach taken in the MPS-GS algorithm has the advantage of only requiring the inverse of a single matrix to solve for all possible conditional distributions.

The Gibbs sampler has advantages and drawbacks common to iterative methods. A number of features were implemented to maximize the advantages and work around the disadvantages: the use of multiple grids for long-range structure reproduction; a servosystem for matching target global and local univariate distributions; image cleaning through either a noise reduction factor or a correction to match the connectivity of the TI; and several stopping criteria to recognize the different conditions that indicate convergence.

## 6.1 Areas of Application

MPS-GS is a newly-developed approach for the simulation of categorical variables. In some cases it is better to use a traditional variogram-based method or object-based modeling. In other cases categorical modeling is not necessary at all. For modeling of categorical variables such as facies, the categories should largely control the petrophysical or mineralogical characteristics of interest in the geology. There should also be a clear spatial structure in the categories, as interpreted by an expert. The structure may be simple, but for the application of MPS-GS typically complex nonlinear structure is considered. For practical purposes the number of categories should be limited to no more than five.

Using the MPS-GS algorithm for categorical simulation requires that a TI be available. A TI may come from outcrop mapping, interpretation, or unconditional object-based or process-based simulation. There must be enough geological and statistical information available to justify the TI(s) used. The TI is a subjective decision and is a matter of expert interpretation. If categorical simulation is needed and an appropriate TI is available, then MPS-GS may be applied.

Depending on the use of the model and the categorization of the variables into facies or other divisions, the cell size for MPS-GS can vary greatly. Pore space modeling at a micrometer scale is an application that has been explored by others using different simulation methods, including SNESIM. Micromodeling is used to determine a porosity-permeability relationship.

Mineralogical modeling within rock types at a millimeter scale is another application where MPS-GS can provide categorical models. The relations between different minerals are often too complex for traditional geostatistical methods and are important when considering ore recovery or contamination.

Rock type modeling within facies groups at a centimeter to decimeter scale is considered when considering the relationship between a modeled cell size and the permeability distribution of the categories. Highly shaley rock types can control the effective permeability of a facies, even in small proportions.

Facies modeling is the most common application for MPS and the MPS-GS algorithm. Facies modeling may be done at a variety of scales for different purposes, such as high-resolution flow simulation with a vertical resolution of decimeters; low-resolution

flow simulation at a vertical scale of meters; and reservoir or mine planning at a scale of tens of meters.

Large scale applications are feasible using MPS-GS. Modeling an entire lease using a cell size of tens to hundreds of meters can be used during exploration to quantify the wide range of uncertainty in a number of potential mineral projects. Regional modeling with a cell size of hundreds of meters is another application, modeling stratigraphy or geological units as the categories.

## **6.2 Future Areas of Research**

The approach developed here is not the only methodology for using MPS. Moreover, the approach has not been explored exhaustively. There are a variety of areas for future research.

Extending the MPS from conditioning information to the quantities being estimated was derived as pattern simulation in Section 3.5. This concept allows for the patching of entire MPEs into a simulated domain instead of single locations at a time and could improve the reproduction of high-order structure inferred from the TI.

Accounting for nonstationarity in MPS-GS is accomplished by forcing local proportions to be reproduced. The MPS used to estimate the conditional probabilities still contain the global univariate proportions in the TI. Scaling the MPS to different univariate proportions could be applied rather than the servosystem method to account for the changes to high-order structure caused by nonstationarity. Alternatively, different TIs could be used to account for nonstationarity in the geological structure and not just the univariate proportions.

The Gibbs sampler framework developed for MPS-GS could be applied to continuous variables such as porosity or grade instead of facies proportions. This would require research into how to determine the conditional distributions but the iterative scheme and convergence properties still apply.

As with all simulation methods, there remains room for improvement in the computational efficiency and programming of the code. A move to a more sophisticated programming language such as C++ and the effort of a more experienced programmer could significantly improve the CPU and memory requirements.

A number of the implementation aspects developed in this work could be utilized in other Markov chain Monte Carlo methods. The use of MPEs for determining conditional facies probabilities could be applied in a Metropolis-Hastings framework or a simulated annealing algorithm, or some combination. Future work on MPS-GS includes the addition of an accept/reject step found in Metropolis-Hastings or simulated annealing.

# Bibliography

- [1] Allard, D., Froidevaux, R., and Biver, P. (2004) Accounting for Non-stationarity and Interactions in Object Simulation for Reservoir Heterogeneity Characterization. Leuangthong, O. and Deutsch, C.V., Editors, *Geostatistics Banff 2004*, Springer, pp 155-164.
- [2] Anderson, E., Bai, Z., Bischof, C., Blackford, S., Demmel, J., Dongarra, J., Du Croz, J., Greenbaum, A., Hammarling, S., McKenney, A., Sorensen, D. (1999) *LAPACK User's Guide, 3<sup>rd</sup> Ed.* Society for Industrial and Applied Mathematics, Philadelphia, PA, 429 p.
- [3] Arpat, G.B. and Caers, J. (2004) A Multiple-scale, Pattern-based Approach to Sequential Simulation. Leuangthong, O. and Deutsch, C.V., Editors, *Geostatistics Banff 2004*, Springer, pp 255-264.
- [4] Arpat, G.B. and Caers, J. (2007) Conditional Simulation with Patterns. *Mathematical Geology*, Vol. 39, No. 2, Feb. 2007, pp 177-203.
- [5] Barrera, A.E., Ni, J., and Srinivasan, S. (2004) Multiple Point Geostatistics: Optimal Template Selection and Implementation in Multi-Threaded Computational Environments. Leuangthong, O. and Deutsch, C.V., Editors, *Geostatistics Banff 2004*, Springer, pp 621-630.
- [6] Boisvert, J.B. (2007) *Mineral Deposit Modeling with Pseudo-Genetically Constructed Training Images*. M.Sc. Thesis, University of Alberta, 72 p.

- [7] Boisvert, J.B., Lyster, S., and Deutsch, C.V. (2007) Constructing Training Images for Veins and Using Them in Multiple-Point Geostatistical Simulation. *APCOM 2007*, Santiago, Chile, Apr. 2007, pp 113-120.
- [8] Caers, J. (2001) Geostatistical Reservoir Modelling Using Statistical Pattern Recognition. *Journal of Petroleum Science and Engineering*, Vol. 29, No. 3, May 2001, pp 177-188.
- [9] Caers, J. (2003) History Matching Under Training-Image-Based Geological Model Constraints. *SPE Journal*, Sept, 2003, pp 218-226. SPE #74716.
- [10] Caers, J. and Journel, A.G. (1998) Stochastic Reservoir Simulation Using Neural Networks Trained on Outcrop Data. *SPE Annual Technical Conference and Exhibition*, New Orleans, Oct. 1998, pp 321-336. SPE #49026.
- [11] Casella, G. and George, E.I. (1992) Explaining the Gibbs Sampler. *The American Statistician*, Vol. 46, No. 3, Aug. 1992, pp 167-174.
- [12] Chiles, J.P. and Delfiner, P. (1999) *Geostatistics: Modeling Spatial Uncertainty*. Wiley-Interscience, New York, 720 p.
- [13] Chong, E.K.P. and Zak, S.W. (2001). *An Introduction to Optimization, 2<sup>nd</sup> Edition*. Wiley-Interscience, New York, 496 p.
- [14] Cojan, I., Fouche, O., Lopez, S., and Rivoirard, J. (2004) Process-based Reservoir Modelling in the Example of Meandering Channel. Leuangthong, O. and Deutsch, C.V., Editors, *Geostatistics Banff 2004*, Springer, pp 611-619.
- [15] ConocoPhillips (2009). <http://www.conocophillips.com>. Accessed Feb. 2009.
- [16] Daly, C. (2004) High Order Models using Entropy, Markov Random Fields and Sequential Simulation. Leuangthong, O. and Deutsch, C.V., Editors, *Geostatistics Banff 2004*, Springer, pp 215-224.
- [17] Deutsch, C.V. (1992) *Annealing Techniques Applied to Reservoir Modeling and the Integration of Geological and Engineering (Well Test) Data*. Ph.D. Thesis, Stanford University, 304 p.

- [18] Deutsch, C.V. (2002) *Geostatistical Reservoir Modeling*. Oxford University Press, New York, 376 p.
- [19] Deutsch, C.V. and Journel, A.G. (1998) *GSLIB: Geostatistical Software Library and User's Guide, 2<sup>nd</sup> Ed.* Oxford University Press, New York, 368 p.
- [20] Deutsch, C.V. and Tran, T.T. (2002) FLUVSIM: A program for Object-based Stochastic Modeling of Fluvial Depositional Systems. *Computers & Geosciences*, Vol. 28, No. 4, May 2002, pp 525-535.
- [21] Deutsch, C.V. and Wang, L. (1996) Hierarchical Object-Based Modeling of Fluvial Reservoirs. *Mathematical Geology*, Vol. 28, No. 7, Oct. 1996, pp 857-880.
- [22] Emery, X. (2007) Using the Gibbs Sampler for Conditional Simulation of Gaussian-Based Random Fields. *Computers & Geosciences*, Vol. 33, No. 4, May 2007, pp 522-537.
- [23] Eskandaridavand, K. (2008) *Growthsim: A complete framework for integrating static and dynamic data into reservoir models*. Ph.D. Thesis, University of Texas at Austin, 199 p.
- [24] Gelfand, A.E. and Smith, A.F.M. (1990) Sampling-Based Approaches to Calculating Marginal Densities. *Journal of the American Statistical Association*, Vol. 85, No. 410, June 1990, pp 398-409.
- [25] Geman, S. and Geman, D. (1984) Stochastic Relaxation, Gibbs Distributions, and the Bayesian Restoration of Images. *IEEE Transactions on Pattern Analysis and Machine Intelligence*, No. 6, Nov. 1984, pp 721-741.
- [26] Goovaerts, P. (1997) *Geostatistics for Natural Resources Evaluation*. Oxford University Press, New York, 483 p.
- [27] Goovaerts, P. and Journel, A.G. (1996) Accounting for Local Probabilities in Stochastic Modeling of Facies Data. *SPE Journal*, March 1996, pp 21-29. SPE #29230.

- [28] Guardiano, F.B. and Srivastava, M.R. (1992) Borrowing Complex Geometries from Training Images: The Extended Normal Equations Algorithm. *Stanford Center for Reservoir Forecasting*, No. 5, 15 p.
- [29] Guardiano, F.B. and Srivastava, R.M. (1993) Multivariate Geostatistics: Beyond Bivariate Moments. Soares, A., Editor, *Geostatistics Troia '92*, Vol. 1, pp 133-144.
- [30] Harding, A., Strebelle, S., Levy, M., Thorne, J., Xie, D., Leigh, S., Preece, R., and Scamman, R. (2004) Reservoir Facies Modelling: New Advances in MPS. Leuangthong, O. and Deutsch, C.V., Editors, *Geostatistics Banff 2004*, Springer, pp 559-568.
- [31] Hastings, W.K. (1970) Monte Carlo sampling methods using Markov chains and their applications. *Biometrika*, Vol. 57, No. 1, pp 97-109.
- [32] Hoffman, B.T., Wen, X.H., Strebelle, S., and Caers, J. (2005) Geologically Consistent History Matching of a Deepwater Turbidite Reservoir. *SPE Annual Technical Conference and Exhibition*, Dallas, TX, October 2005, 12 p. SPE #95557.
- [33] Holden, L, Hauge, R. Skare, O., and Skorstad, A. (1998) Modeling of Fluvial Reservoirs with Object Models. *Mathematical Geology*, Vol. 30, No. 5, July 1998, pp 473-496.
- [34] Isaaks, E.H. and Srivastava, R.M. (1990) *Introduction to Applied Geostatistics*. Oxford University Press, New York, 592 p.
- [35] Journel, A. (2002) Combining Knowledge from Diverse Sources: An Alternative to Traditional Data Independence Hypotheses. *Mathematical Geology*, Vol. 34, No. 5, July 2002, pp 573-596.
- [36] Journel, A.G. (2004) Beyond Covariance: The Advent of Multiple-Point Geostatistics. Leuangthong, O. and Deutsch, C.V., Editors, *Geostatistics Banff 2004*, Springer, pp 225-233.

- [37] Journel, A., and Alabert, F. (1989) Non-Gaussian Data Expansion in the Earth Sciences. *Terra Nova*, Vol. 1, No. 2, March 1989, pp 123-134.
- [38] Journel, A. and Deutsch, C.V. (1993) Entropy and Spatial Disorder. *Mathematical Geology*, Vol. 25, No. 3, April 1993, pp 329-355.
- [39] Journel, A. and Huijbregts, Ch. (1978) *Mining Geostatistics*. Blackburn Press, Caldwell, NJ, 600 p.
- [40] Journel, A., and Zhang, T. (2006) The Necessity of a Multiple-Point Prior Model. *Mathematical Geology*, Vol. 38, No. 5, July 2006, pp 591-610.
- [41] Kindermann, R., and Snell, J.L. (1980) *Markov Random Fields and Their Applications*. American Mathematical Society, 142 p.
- [42] Krishnan, S. and Journel, A.G. (2003) Spatial Connectivity: From Variograms to Multiple-Point Measures. *Mathematical Geology*, Vol. 35, No. 8, Nov. 2003, pp 915-925.
- [43] Lawler, G.F. (2006) *Introduction to Stochastic Processes, 2<sup>nd</sup> Ed.* Chapman & Hall/CRC, Boca Raton, FL, 234 p.
- [44] Liu, Y. (2004) An Information Content Measure Using Multiple-point Statistics. Leuangthong, O. and Deutsch, C.V., Editors, *Geostatistics Banff 2004*, Springer, pp 1047-1056.
- [45] Liu, Y. (2006) Using the Snesim Program for Multiple-Point Statistical Simulation. *Computers & Geosciences*, Vol. 32, No. 10, Dec. 2006, pp 1544-1563.
- [46] Liu, Y., Harding, A., Gilbert, R., and Journel, A.G. (2004) A Workflow for Multiple-point Geostatistical Simulation. Leuangthong, O. and Deutsch, C.V., Editors, *Geostatistics Banff 2004*, Springer, pp 245-254.
- [47] Maharaja, A. (2004) Stochastic Modeling of the Rhine-Meuse Delta using Multiple-point Geostatistics. Leuangthong, O. and Deutsch, C.V., Editors, *Geostatistics Banff 2004*, Springer, pp 653-659.

- [48] Maharaja, A., and Journel, A. (2005) Hierarchical Simulation of Multiple-Facies Reservoirs Using Multiple-Point Geostatistics. *SPE Annual Technical Conference and Exhibition*, Dallas, Oct. 2005, 15 p. SPE #95574.
- [49] Metropolis, N., Rosenbluth, A.W., Rosenbluth, M.N., Teller, A.H., and Teller, E. (1953) Equations of State Calculations by Fast Computing Machines. *Journal of Chemical Physics*, Vol. 21, No. 6, pp 1087-1091.
- [50] Okabe, H., and Blunt, M.J. (2004) Multiple-point Statistics to Generate Pore Space Images. Leuangthong, O. and Deutsch, C.V., Editors, *Geostatistics Banff 2004*, Springer, pp 763-768.
- [51] Okabe, H., and Blunt, M.J. (2005) Pore-space reconstruction using multiple-point statistics. *Journal of Petroleum Science and Engineering*, Vol. 46, No. 1-2, Feb. 2005, pp 121-137.
- [52] Ortiz, J.M. (2003) *Characterization of High Order Correlation for Enhanced Indicator Simulation*. Ph.D. Thesis, University of Alberta, 255 p.
- [53] Ortiz, J.M. and Deutsch, C.V. (2004) Indicator Simulation Accounting for Multiple-Point Statistics. *Mathematical Geology*, Vol. 36, No. 5, July 2004, pp 545-565.
- [54] Ortiz, J.M. and Emery, X. (2004) Integrating Multiple-point Statistics into Sequential Simulation Algorithms. Leuangthong, O. and Deutsch, C.V., Editors, *Geostatistics Banff 2004*, Springer, pp 969-978.
- [55] Ortiz, J.M., Lyster, S., and Deutsch, C.V. (2006) Scaling Multiple-Point Statistics to Different Univariate Proportions. *Computers & Geosciences*, Vol. 33, No. 2, Feb. 2007, pp 191-201.
- [56] Petrel Seismic-to-Simulation Software, Schlumberger (2009) <http://www.slb.com/content/services/software/geo/petrel/index.asp>. Accessed Feb. 2009.
- [57] Pyrcz, M.J. (2004) *The Integration of Geologic Information into Geostatistical Models*. Ph.D. Thesis, University of Alberta, 250 p.

- [58] Pyrcz, M.J. and Deutsch, C.V. (2004) Conditioning Event-based Fluvial Models. Leuangthong, O. and Deutsch, C.V., Editors, *Geostatistics Banff 2004*, pp 135-144.
- [59] Pyrcz, M.J., Boisvert, J., and Deutsch, C.V. (2008) A Library of Training Images for Fluvial and Deepwater Reservoirs and Associated Code. *Computers & Geosciences*, Vol. 34, No. 5, May 2008, pp 542-560.
- [60] Pyrcz, M.J., Catuneanu, O., and Deutsch, C.V. (2005) Stochastic surface-based modeling of turbidite lobes. *AAPG Bulletin*, Vol. 89, No. 2, Feb. 2005, pp 177-191.
- [61] Remy, N., Boucher, A., Wu, J., Li, T., Rajiv, J., and Sharps, M. (2008) SGeMS – Geostatistics Software. <http://sgems.sourceforge.net/> Accessed June 2008.
- [62] Ren, W., Cunha, L.B., and Deutsch, C.V. (2004) Preservation of Multiple Point Structure when Conditioning by Kriging. Leuangthong, O. and Deutsch, C.V., Editors, *Geostatistics Banff 2004*, Springer, pp 643-652.
- [63] Robert, C.P. and Casella, G. (2004) *Monte Carlo Statistical Methods*. Springer Science + Business Media, New York, 645 p.
- [64] Smith, A.F.M. and Gelfand, A.E. (1992) Bayesian Statistics without Tears: A Sampling-Resampling Perspective. *The American Statistician*, Vol. 46, No. 2, May 1992, pp 84-88.
- [65] Srivastava, M. (1992) Iterative Methods for Spatial Simulation. *Stanford Center for Reservoir Forecasting*, No. 5, 24 p.
- [66] Strebelle, S. (2002) Conditional Simulation of Complex Geological Structures Using Multiple-Point Statistics. *Mathematical Geology*, Vol. 34, No. 1, Jan. 2002, pp 1-21.
- [67] Strebelle, S. (2005) Building Geologically Realistic Reservoir Models Using the MPS/FDM Workflow. *Proceedings of IAMG '05: GIS and Spatial Analysis*, Vol. 1, pp 25-35.

- [68] Strebelle, S. and Journel, A.G. (2000) Sequential Simulation Drawing Structures from Training Images. Kleingeld, W.J. and Krige, D.G., Editors, 6<sup>th</sup> *International Geostatistics Congress*, 12 p.
- [69] Strebelle, S. and Journel, A.G. (2001) Reservoir Modeling Using Multiple-Point Statistics. *SPE Annual Technical Conference and Exhibition*, New Orleans, Oct. 2001, 11 p. SPE #71324.
- [70] Strebelle, S., and Remy, N. (2004) Post-processing of Multiple-point Geostatistical Models to Improve Reproduction of Training Patterns. Leuangthong, O. and Deutsch, C.V., Editors, *Geostatistics Banff 2004*, Springer, pp 979-988.
- [71] Strebelle, S., and Zhang, T. (2004) Non-stationary Multiple-point Geostatistical Models. Leuangthong, O. and Deutsch, C.V., Editors, *Geostatistics Banff 2004*, Springer, pp 235-244.
- [72] Strebelle, S., Payrazyan, K., and Caers, J. (2002) Modeling of a Deepwater Turbidite Reservoir Conditional to Seismic Data Using Multiple-Point Geostatistics. *SPE Annual Technical Conference and Exhibition*, San Antonio, TX, Sept.-Oct. 2002, 10 p. SPE #77425.
- [73] Strebelle, S., Payrazyan, K., and Caers, J. (2003) Modeling of a Deepwater Turbidite Reservoir Conditional to Seismic Data Using Principal Component Analysis and Multiple-Point Geostatistics. *SPE Journal*, Sept. 2003, pp 227-235. SPE #85962.
- [74] Tjelmeland, H., and Besag, J. (1998) Markov Random Fields with Higher-order Interactions. *Scandinavian Journal of Statistics*, Vol. 25, Iss. 3, Sept. 1998, pp 415-433.
- [75] Wackernagel, H. (2003) *Multivariate Geostatistics, 3<sup>rd</sup> Ed.* Springer, Berlin, 403 p.
- [76] Wang, L. (1996) Modeling Complex Reservoir Geometries with Multiple-Point Statistics. *Mathematical Geology*, Vol. 28, No. 7, Oct. 1996, pp 895-907.

- [77] Wu, J., Boucher, A., and Zhang, T. (2008a) A SGeMS code for pattern simulation of continuous and categorical variables; FILTERSIM. *Computers & Geosciences*, DOI <http://dx.doi.org/10.1016/j.cageo.2007.08.008>.
- [78] Wu, J., Zhang, T., Journel, A. (2008b) Fast FILTERSIM Simulation with Score-based Distance. *Mathematical Geosciences*, Vol. 40, No. 7, Oct. 2008, pp 773-788.
- [79] Xu, W. (1996) Conditional Curvilinear Stochastic Simulation Using Pixel-Based Algorithms. *Mathematical Geology*, Vol. 28, No. 7, Oct. 1996, pp 937-949.
- [80] Zanon, S. and Leuangthong, O. (2004) Implementation Aspects of Sequential Simulation. Leuangthong, O. and Deutsch, C.V., Editors, *Geostatistics Banff 2004*, Springer, pp 543-548.
- [81] Zhang, T. (2002) *Multiple-Point Simulation of Multiple Reservoir Facies*. M.Sc. Thesis, Stanford University, 159 p.
- [82] Zhang, T., Switzer, P., and Journel, A. (2004) Sequential Conditional Simulation Using Classification of Local Training Patterns. Leuangthong, O. and Deutsch, C.V., Editors, *Geostatistics Banff 2004*, Springer, pp 265-274.
- [83] Zhang, T., Bombarde, S., Strebelle, S., and Oatney, E. (2006a) 3D Porosity Modeling of a Carbonate Reservoir Using Continuous Multiple-Point Statistics Simulation. *SPE Journal*, Sept. 2006, pp 375-379. SPE #96308.
- [84] Zhang, T., Switzer, P., and Journel, A. (2006b) Filter-Based Classification of Training Image Patterns for Spatial Simulation. *Mathematical Geology*, Vol. 38, No. 1, Jan. 2006, pp 63-80.

# A Symbols and Selected Terms

This Appendix contains definitions for words, symbols, and variables used throughout this dissertation that may not be straightforward to the reader.

$B_k$	Bin of a local facies proportion at a location $\mathbf{u}$
$Cov\{I(k;\mathbf{u}), I(k;\mathbf{u} + \mathbf{h})\}$	Covariance of an indicator variable $I$ between two locations separated by lag vector $\mathbf{h}$
$Cov\{Z(\mathbf{u}), Z(\mathbf{u} + \mathbf{h})\}$	Covariance of a variable $Z$ between two locations separated by lag vector $\mathbf{h}$
$Cov\{E_i^\alpha, E_j^\beta\}$	Covariance between multiple-point events $E_i^\alpha$ and $E_j^\beta$
$Cov\{E_i^\alpha, k\}$	Covariance between multiple-point event $E_i^\alpha$ and facies $k$
$Cov\{I_u^\kappa, I_v^\psi\}$	Covariance between facies $\kappa$ and $\psi$ at template points $u$ and $v$
$C_k$	Connectivity of facies $k$ as defined in Section 4.1.4
$\chi_{u,\kappa}^k$	Linear estimation weight assigned to facies $\kappa$ at template point $u$ for the conditional distribution of facies $k$
$d$	Discretization of multiple grids; the proportion between the number of cells in one dimension of one grid and the next coarser grid
$D$	Set of conditioning data
Dimensionality:	The property of having dimensions. In the field of multiple-point statistics, dimensionality is often used to describe the problem of having too many dimensions for practical purposes.

$E_i^\alpha$	Multiple-point event with offsets $i$ and an arrangement of facies corresponding to multiple-point histogram class $\alpha$
$E_0^\gamma$	Multiple-point event in the center of a template and an arrangement of facies corresponding to multiple-point histogram class $\gamma$
$\varepsilon_t$	Movement component of a random walk at time $t$
$\varepsilon$	Small value added to the denominator in local proportion binning to prevent undefined values
$\phi(k;N)$	Connectivity function for facies $k$ and $N$ points
$[ \varphi_\alpha ]$	Initial state of a Markov chain
$g$	Integer value of current grid
$G$	Number of multiple grids
Gibbs sampler (GS):	A Markov chain Monte Carlo method that uses conditional distributions to explore a state space.
$\gamma(k;\mathbf{h})$	Variogram value at lag $\mathbf{h}$ for indicator function of variable $k$
$\mathbf{h}$	Lag vector
$H_{\mathbf{u}}$	Spatial entropy between the null vector and location $\mathbf{u}$
$H_i$	Multiple-point spatial entropy of event $i$
$\eta$	Connectivity correction control parameter
$I(k;\mathbf{u})$	Indicator function of facies $k$ at location $\mathbf{u}$
$I^*(k;\mathbf{u})$	Estimated value of indicator function of facies $k$ at location $\mathbf{u}$
$I(k;\mathbf{u} + \mathbf{h})$	Indicator function of facies $k$ at location $\mathbf{u} + \mathbf{h}$
$I(E_i^\alpha)$	Indicator of multiple-point event $E_i^\alpha$
$[ I ]$	Row vector of indicators of multiple-point events

Initial image (initial state): The starting value of a Markov chain variable before simulation commences. In MPS-GS, the starting facies values in the simulated domain.

$k$  A particular facies value

$K$  The number of possible facies values

$k; \mathbf{u}$  The facies value at location  $\mathbf{u}$

$k(n)$  The facies value at template point  $n$

$\lambda_i$  Linear estimation weight assigned to data location  $i$

$\lambda_{i,\alpha}^k$  Linear estimation weight assigned to class  $\alpha$  of multiple-point event  $i$  for the conditional distribution of facies  $k$

$\left[ \begin{array}{c} LHS \end{array} \right]$  The left-hand-side covariance matrix in a system of linear equations

$\left[ \begin{array}{c} \lambda \end{array} \right]$  Column vector of optimal linear estimation weights

$m_z$  Mean value of variable  $z$

$M$  Number of multiple-point events used in MPS-GS

$\mu$  Servosystem control parameter

Markov chain: A sequence of states for a variable where the value of the next state depends only on the current value and earlier states are irrelevant.

Markov chain Monte Carlo (MCMC): A family of statistical methods that use Markov chains in a stochastic fashion.

Multiple-point event (MPE): A defined set of  $N$  spatial offsets from the null vector that is used as a template.

Multiple-point histogram (MPH): A set of frequencies for all possible combinations of categories within a specified template.

Multiple-point histogram class: A specific pattern or arrangement of categories within a template.

Multiple-point statistics (MPS): Statistical moments of order greater than two; also used to describe geostatistical methods that use high-order moments.

$n$	Number of data used in kriging
$N$	Number of points per multiple-point event in MPS-GS
$N_{xyz}$	Number of cells in a three-dimensional domain
$N_{ti}$	Number of cells in a training image
$N_B$	Number of bins for discretizing local facies proportions
$NRF$	Noise reduction factor
$Nch_i$	Number of facies value changes on loop $i$ in MPS-GS
$O$	Objective function in simulated annealing
$P(k)$	Global proportion of facies $k$
$P_k$	Alternate notation for global proportion of facies $k$
$P^*(k)$	Estimated proportion of facies $k$ at the current location in the simulation path, $\mathbf{u}$
$P^+(k)$	Base estimate for facies $k$ as defined in Section 4.1.2
$P'(k)$	Updated estimate of facies $k$ at the current location accounting for the servosystem
$P''(k)$	Updated estimate of facies $k$ at the current location accounting for noise reduction or the connectivity correction
$P^{TI}(k)$	Global proportion of facies $k$ in a training image
$P^{SIM}(k)$	Current simulated global proportion of facies $k$
$P^{SIM}(k; B_k)$	Current simulated proportion of facies $k$ within local proportion bin $B_k$
$P^{LOC}(k)$	Local proportion of facies $k$ at the current location in the simulation path, $\mathbf{u}$

$P^{TARG}(k)$	Target global proportion of facies $k$
$P^{MIN}(k)$	Minimum nonzero local proportion of facies $k$
$P^{MAX}(k)$	Maximum local proportion of facies $k$ less than one
$P_{kk'}$	Probability of facies $k$ at the null vector and facies $k'$ at a specified offset
$P(E_i^\alpha)$	Global probability of multiple-point event $E_i^\alpha$
$P(E_0^\gamma)$	Global probability of multiple-point event $E_0^\gamma$
$P_{\alpha\beta}$	Transition probability of a Markov chain moving from state $\alpha$ to state $\beta$ in a single step
$P_{\alpha\beta}^t$	Transition probability of a Markov chain moving from state $\alpha$ to state $\beta$ in exactly $t$ steps
$\begin{bmatrix} P_{\alpha\beta} \end{bmatrix}$	Transition matrix of a finite Markov chain
$[P_k]$	Row vector of the global facies proportions
$[P]$	Row vector of global probabilities of multiple-point events
$[P^*]$	Row vector of estimated conditional facies probabilities
$[\pi_\alpha]$	Stationary distribution of a Markov chain
$\begin{bmatrix} RHS \end{bmatrix}$	Right-hand-side covariance matrix in a system of linear equations
$\sigma_E^2$	Error variance of a linear estimate
$\sigma_k^2$	Global variance of the indicator variable of facies $k$

$\sigma_y^2$  Global variance of Gaussian variable  $y$

$\sigma_z^2$  Global variance of variable  $z$

Servosystem: A correction applied to conditional distributions in a simulation algorithm to improve the ultimate match to a global distribution.

Single-point indicator: An indicator variable at a specified location within a template.

State: A value that a variable can take.

State space: The set of all possible values that can be taken by a variable.

$T$  Temperature control parameter in simulated annealing

$\tau$  Control parameter for conditional independence / tau model

Template: A specified arrangement of points in space that is used to calculate and store multiple-point statistics.

Training image (TI): A conceptual model of geology used to infer multiple-point statistics.

$\begin{bmatrix} V \end{bmatrix}$  Matrix of orthonormal eigenvectors

$X_t$  Value of a Markov chain at time  $t$

$Y(\mathbf{u})$  Gaussian variable  $Y$  at location  $\mathbf{u}$

$Y^*(\mathbf{u})$  Estimated value of Gaussian variable  $Y$  at location  $\mathbf{u}$

$Z(\mathbf{u})$  Variable  $Z$  at location  $\mathbf{u}$

$Z^*(\mathbf{u})$  Estimated value of variable  $Z$  at location  $\mathbf{u}$

$\begin{bmatrix} \omega \end{bmatrix}$  Matrix with eigenvalues on the diagonal and zeros elsewhere

$$\left[ \begin{array}{c} 1/\omega \end{array} \right]$$

Matrix with inverse eigenvalues on the diagonal and zeros elsewhere

## B MPS-GS Software

To develop and test the MPS-GS algorithm, a GSLIB-style (Deutsch and Journel, 1998) program was developed in FORTRAN. The program is called MPESIM. This chapter describes the structure of the program and the files necessary for its use. Section B.1 reviews the GSLIB standard conventions for data files and geometry. Section B.2 presents the workflow of MPESIM. Section B.3 explains the user-specified parameters used by MPESIM. Section B.4 explains the format of files used by MPESIM for storing the template and statistics. Section B.5 lists the FORTRAN files necessary to compile the MPESIM program. Section B.6 presents a brief example to help users confirm successful compilation of the program.

The MPESIM program was written as research code. Some effort has been made for user friendliness, stability, and flexibility; however, there no support and bugs may be present in the code.

### B.1 GSLIB Conventions

The GSLIB suite of software is documented extensively in Deutsch and Journel, 1998. It is a library of geostatistical software that can be used for a variety of tasks such as data analysis, plotting, estimation, and simulation.

An example of a data file in GSLIB format is shown in Table B.1. The Line labeled 1 is the header and is used as a description or title. Line 2 contains an integer value that is the number of columns in the file, three in the example; each column contains one variable. Line 3 identifies the first variable name or column description. Each column/variable has one line in this section. From label 4 and below contains the data, with the specified number of columns. Each column must be present on every row; negative number placeholders such as -99 or -1 are used for missing values.

Table B.1: An example GSLIB data file.

1	Header of File		
2	3		
3	Variable 1		
	Variable 2		
	Variable 3		
4	1.001	2.359	15
	0.995	1.837	15
	0.982	2.105	13
	...		

Data files such as the example in Table B.1 can contain scattered data that have coordinates as variables. The coordinates are Euclidean X,Y,Z, although for two-dimensional cases one of the coordinates may be omitted and the physical meaning of the coordinates can be specified by the user (such as northing, easting, elevation).

An exhaustive block model is specified with no coordinates necessary in the file; rather, there are  $N_{xyz}$  lines. The origin of the block model is in the lower-left corner (minimum X, Y, and Z values) and cycles in the X, then Y, then Z directions. Note that in GSLIB convention the Z coordinates increase upwards. The cells are numbered from (1,1,1) to  $(nx,ny,nz)$ . Figure B.1 shows an example of the grid indexing in GSLIB.

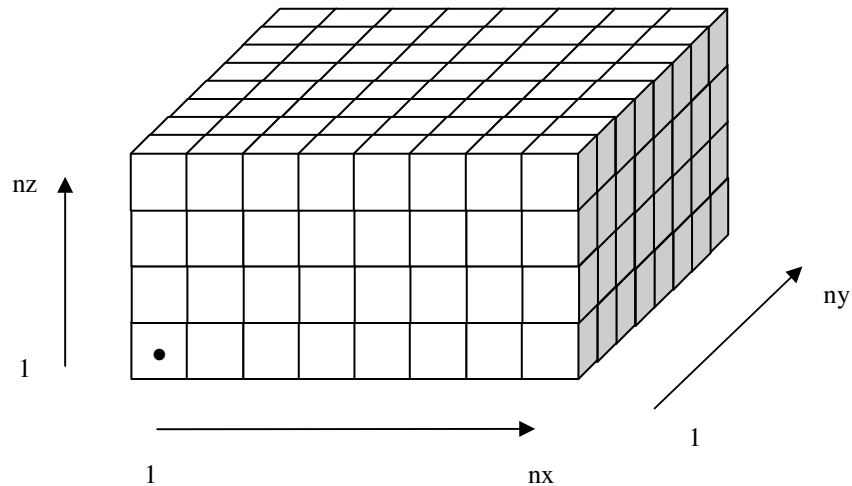


Figure B.1: An example of GSLIB grid indexing. The origin cell is marked with a dot.

To use both scattered data and a block model, the geometry of the cells must be specified. The grid definitions in GSLIB are based on  $nx$ ,  $xmin$ , and  $xsiz$  (with y or z replacing x in the other directions). The  $nx$  variable is the number of cells in the X

direction;  $xmin$  is the X coordinate of the center of the origin cell; and  $xsiz$  is the size of the cells in the X direction. The edge of the block model is  $xmin-(xsiz/2)$  and the size of the model is  $xsiz*nx$ . An example of the cell geometry for a two-dimensional model is shown in Figure B.2.

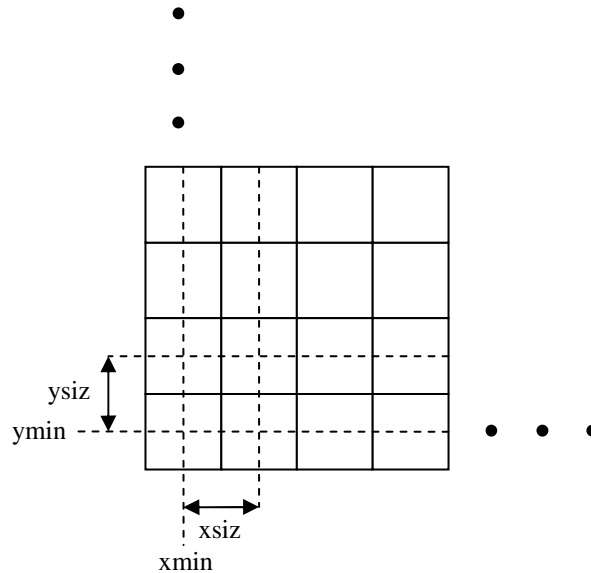


Figure B.2: An example of GSLIB cell geometry definitions.

## B.2 Workflow

The MPESIM program follows the workflow of the MPS-GS algorithm described in Chapter 3, with the features mentioned in Chapter 4. MPESIM will use the user-specified TI and automatically create a template and calculate the optimal linear weights in Equation 4.1. Figure B.3 shows a flowchart of the initial state of MPESIM, where the parameter, template, and MPS files are either read as input (if they exist) or created. The workflow in Figure B.3 is used as the setup before simulation. The program will stop after each step to allow the user to review the results.

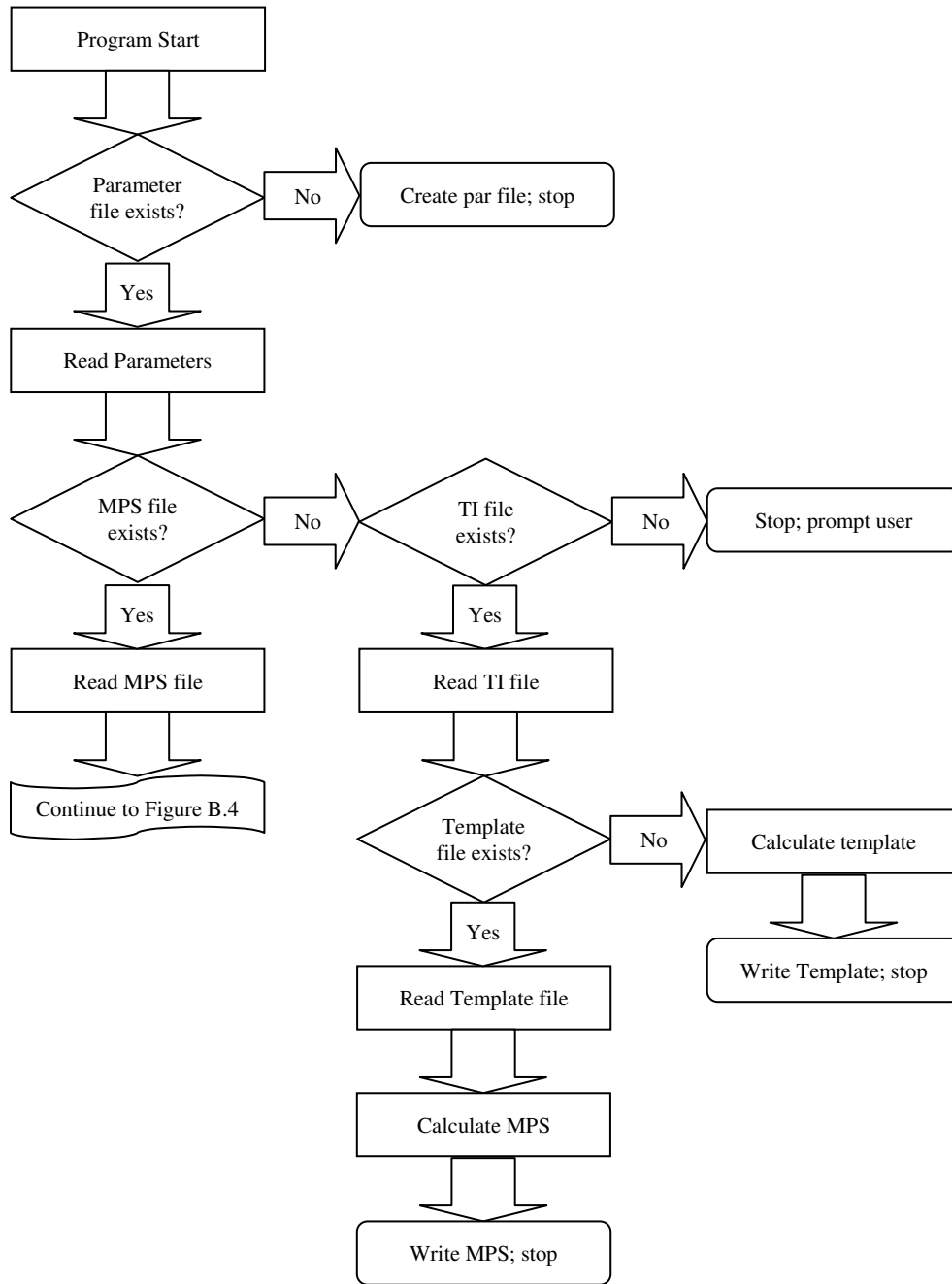


Figure B.3: MPESIM workflow for creating a template and calculating MPS.

Once the statistics have been calculated and written to a file, the preparation stage of MPESIM proceeds. This part of the workflow is shown in a flowchart in Figure B.4. At this stage the program reads in any hard data and local proportions and discretizes the local proportions if necessary. The output files is opened and the header written.

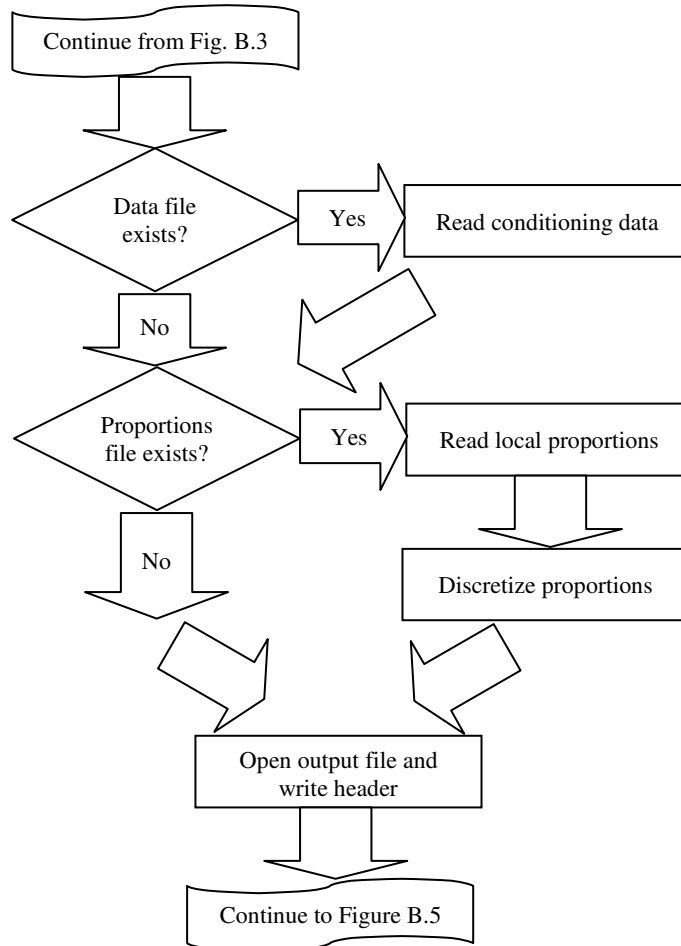


Figure B.4: MPESIM workflow for preparing for simulation.

Figure B.5 shows a flowchart for the simulation portion of MPESIM. The program follows the Gibbs sampler algorithm outlined in Chapter 3 and uses stopping criteria as specified in Chapter 4.

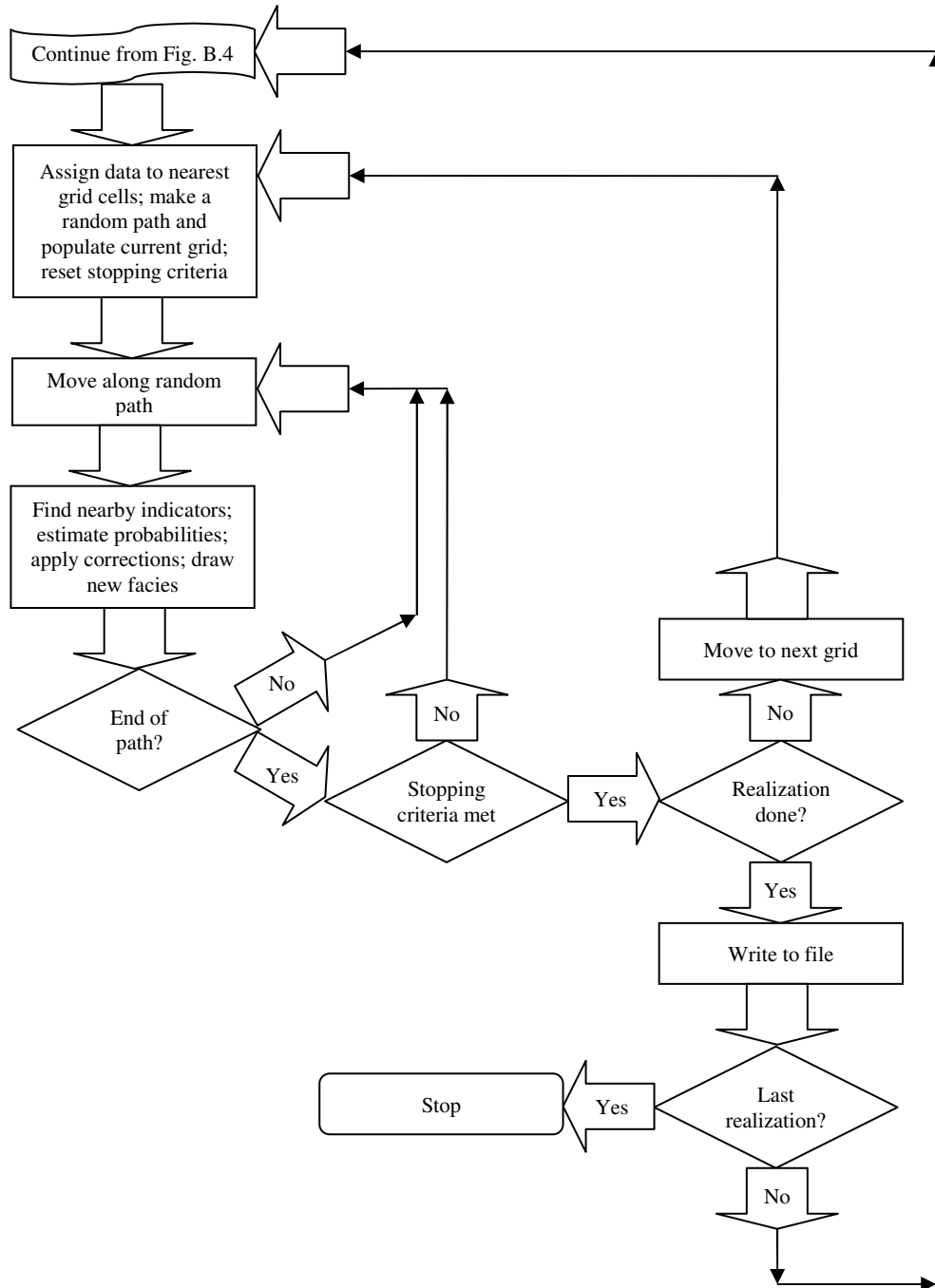


Figure B.5: MPESIM workflow for performing simulation.

### B.3 Parameter File

Several text files are used by the MPSEIM2 program. The first is a GSLIB-style parameter file. If no parameter file is found on the program execution then a default

parameter file is created. Table B.2 shows a default parameter file. Line 1 is the name of the file containing the MPS; if this file exists it will be read in, if not it will be created (see Figure B.3). Lines 2 through 4 define the MPS to use in simulation; the number of grids to use ( $G$ ), the number of MPEs for the template ( $M$ ), and the points per event ( $N$ ). The  $M$  and  $N$  values must agree with the MPS file, and  $G$  must be no greater than that contained in the file (the simulation cannot use more grids than the MPS have been calculated for). Line 5 defines the minimum frequency of a MPE class to consider. A higher value on Line 5 will reduce the size of the system to solve but will also ignore more MPEs.

Lines 6 to 8 define the TI file. Line 6 is the filename; Line 7 is the column containing the facies information; and Line 8 is the size of the TI field ( $X$ ,  $Y$ , and  $Z$ ). No TI file is needed if the MPS file (Line 1) already exists.

Lines 9 through 11 define the template to calculate the MPS within, if necessary. Line 9 is the name of the file containing the template offsets; if this file exists it will be read, otherwise it will be created. Line 10 is the columns containing the  $X$ ,  $Y$ , and  $Z$  offsets for each point in the template. Line 11 is the maximum offsets in the  $X$ ,  $Y$ , and  $Z$  directions if a template is to be created. These lines are irrelevant if the MPS file already exists, but must be present in the parameter file. If the simulation is 2D, the  $Z$  offset column may be set to 0.

Lines 12 through 14 define the indicators for the facies. Line 12 specifies the number of facies,  $K$ ; Line 13 provides the integer codes defining the facies and must have  $K$  values; and Line 14 defines the global target proportions of the facies and must also have  $K$  values.

Lines 15 and 16 specify the hard conditioning data file. Line 15 is the file name, and Line 16 identifies the columns for the  $X$ ,  $Y$ ,  $Z$ , and facies information. If the data set is 2D the  $Z$  column may be set to 0. If the conditioning data file is not found then the realizations will be unconditional.

Lines 17 through 23 define the output. Line 17 is the name of the file to write the results to; this file will be in standard GSLIB format with one column. Line 18 is the number of realizations to generate. Lines 19 to 21 are the grid definitions in the standard GSLIB format. Line 22 specifies the stopping criteria for the realizations, with a stopping number (typically left as 1 except for research); a minimum proportion of cell values to change in each loop (if less than, say, 0.1% of all values change the image is assumed to

have converged); and the maximum number of loops to allow before stopping. Line 23 is the debugging output file; this file will provide a record of the output to the screen during simulation and will contain the parameters used, the number of changes in each loop, and the univariate proportions in each loop.

Lines 24 to 26 define the local proportion information. Line 24 is the file name (if the file does not exist no local proportions will be used); Line 25 provides the  $K$  columns for the local data; and Line 26 specifies the discretization of the local proportions, or number of bins  $B_k$ . If local proportion data exists then the global proportions are not used.

Line 27 specifies the servosystem and connectivity correction control parameters. Line 28 is the random number seed value.

Table B.2: An example parameter file for MPESIM.

Parameters for MPESIM *****	
	START OF PARAMETERS:
1	mpstats.mps -File for MPS
2	4 -Number of grids to use
3	8 -Number of MP events to consider
4	4 -Number of points per event
5	1.0e-6 -Minimum MP frequency to consider
6	tifile.dat -File for Training Image
7	1 -Column for TI data
8	256 256 128 -Size of TI field
9	template.temp -File containing point offsets
10	1 2 3 -Columns for X,Y,Z offsets
11	5 5 3 -Maximum point offsets
12	5 -Number of codes/facies
13	0 1 2 4 5 -Indicators for codes/facies
14	0.4 0.2 0.2 0.1 0.1 -Global pdf values
15	data.dat -File for conditioning data
16	1 2 3 4 -X,Y,Z,Data columns
17	MPESIM.out -File for output
18	1 -Number of realizations
19	256 0.5 1.0 -nx,xmin,xsiz
20	256 0.5 1.0 -ny,ymin,ysiz
21	128 0.5 1.0 -nz,zmin,zsiz
22	1 0.05 30 -Stopping number,threshold,max loops
23	MPESIM.dbg -File for debugging
24	pdf.dat -File for local proportions
25	1 2 3 4 5 -Columns for all indicators
26	4 -Discretization of local pdf
27	1.0 0.1 -Servosystem, connectivity factors
28	6744889 -Random number seed value

## B.4 Template and MPS Files

Using the TI and the defined parameters, the MPESIM program will calculate the optimal MPS template and weights used in MPS-GS, as shown in Figure B.3. These two calculations are stored in files for checking by the user and for later use without recalculation.

Table B.3 shows an example of a template file. Line 1 defines the parameters for the template:  $G$ ,  $M$ , and  $N$ . Line 1 is also the GSLIB-style header line for the file. Line 2 is the number of columns in the file; if the template is created by MPESIM this is always 3. The Lines numbered 3 in Figure 5 are the header lines and there is one for each column in the file; in this case, one each for the X, Y, and Z offsets. The Lines numbered as 4 define the offsets in the template from the central location of (0,0,0). There are  $GMN$  lines in the file, with  $N$  cycling the fastest, then  $M$ , then  $G$ , so the first  $N$  lines define the first MPE in the first grid and the  $(MN+1)$  to  $(MN+N)$  lines define the first MPE in the second grid. In the example template file two grids were used with four, four-point MPEs in each grid for a template size of 16 points and 32 lines in the file.

Table B.4 shows an example of an MPS file. The dots “...” represent lines that have been removed to shorten the file to a single page for this example. Line 1 is the header line; note the MPS file is no longer GSLIB-standard, but is unique to the MPESIM program. Line 2 contains the parameters for the MPS in the file, with four numbers:  $G$ ,  $M$ ,  $N$ , and  $K$  (these letters are shown in order on Line 1). These parameters must agree with the parameter file used, though grids may be dropped from MPS calculation to simulation.

The Lines labeled as 3 are the headers for each grid and there are  $G$  of these lines. After the grid header there is a Line 4 (again one for each grid) that defines the global proportions for this grid,  $P_k$ ,  $k=1, \dots, K$ . Note that these numbers vary slightly from grid to grid due to the range of the search for each grid; these very small fluctuations can have a significant impact on the multiple-point covariance matrix. After each Line 4 there is a group of Lines, labeled 5 here, for each grid. There are seven lines and they define the connectivity values  $P(C_k)$   $k=1, \dots, K$ ; each line defines one connectivity value from  $C_k=0$  to  $C_k=6$ . These are the connectivity values as used in Equation 11.

After the grid header lines there is the header for the first MPE on that grid. Line 6 is the header for each MPE and there are  $M$  of these lines for each grid. After Line 6 is the

group of Lines 7 that specify the point offsets for the MPE. There are  $N$  of these lines for each event. The set of Lines 8 are the statistics calculated for the indicators in the MPE. Each line specifies the class  $\alpha$ , the global proportion of that class,  $P(E_i^\alpha)$ , and weight assigned to the indicator of that class for each facies,  $\lambda_{i,\alpha}^k$ ,  $k=1,\dots,K$ . There are a maximum of  $K^N$  of these lines; one for every possible class. Classes that are below the cutoff proportion are not included. Lines 6 through 8 are repeated  $M$  times for each grid. The weights assigned to the univariate indicators are at the end of each grid. There are  $MNK$  lines in this part of the MPS file.

After the univariate indicators portion of the file, Lines 3 through 10 repeat again for each of the remaining grids. Line 11 defines the end of the MPS file.

Table B.3: An example template file for MPESIM.

<b>1</b>	Template of points G M N	2	4	4
<b>2</b>	3			
<b>3</b>	X offset			
	Y offset			
	Z offset			
<b>4</b>	1 0 0			
	-1 0 0			
	2 0 0			
	-2 0 0			
	0 1 0			
	0 -1 0			
	1 -1 0			
	-1 1 0			
	1 1 0			
	-1 -1 0			
	2 1 0			
	-2 -1 0			
	2 -1 0			
	-2 1 0			
	1 -2 0			
	-1 2 0			
	2 0 0			
	-2 0 0			
	4 0 0			
	-4 0 0			
	0 2 0			
	0 -2 0			
	2 -2 0			
	-2 2 0			
	2 2 0			
	-2 -2 0			
	4 2 0			
	-4 -2 0			
	4 -2 0			
	-4 2 0			
	0 4 0			
	0 -4 0			

Table B.4: An example MPS file for MPESIM.

1	MPS file for MPESIM v2 G M N K					
2	2	4	4	2		
3	GRID		1			
4	0.696324		0.303676			
5	0.000187		0.000000			
	0.002355		0.001886			
	0.040112		0.087176			
	0.127551		0.313561			
	0.829794		0.597377			
	0.000000		0.000000			
	0.000000		0.000000			
6	EVENT		1			
7	1	0	0			
	-1	0	0			
	2	0	0			
	-2	0	0			
8	1	0.642467	-0.334973	0.334973		
	5	0.012859	-0.258374	0.258374		
	6	0.025718	-0.073913	0.073913		
	...					
6	EVENT		2			
7	0	1	0			
	0	-1	0			
	1	-1	0			
	-1	1	0			
8	1	0.565051	-0.250738	0.250738		
	2	0.006898	-0.231665	0.231665		
	...					
	...					
9	UNIVARIATE INDICATORS					
10	1	0	0	0	0.328335	-0.328335
	1	0	0	1	-0.328335	0.328335
	-1	0	0	0	0.340872	-0.340872
	-1	0	0	1	-0.340872	0.340872
	...					
3	GRID		2			
4	0.691189		0.308811			
5	0.000628		0.000000			
	0.008791		0.004129			
	0.081122		0.163299			
	...					
6	EVENT		1			
7	2	0	0			
	-2	0	0			
	4	0	0			
	-4	0	0			
8	1	0.589871	0.062044	-0.062044		
	2	0.001790	-0.055254	0.055254		
	3	0.001872	-0.074566	0.074566		
	...					
	...					
9	UNIVARIATE INDICATORS					
10	2	0	0	0	0.205283	-0.205283
	2	0	0	1	-0.205283	0.205283
	-2	0	0	0	0.189959	-0.189959
	-2	0	0	1	-0.189959	0.189959
	...					
11	END					

## B.5 FORTRAN Files

There are 81 files of FORTRAN code needed to compile the MPESIM program. The majority of these are from the LAPACK suite of subroutines (Anderson et al, 1999). A full list of these files is shown in Table B.5. There is the main file, MPESIM.f; a group of GSLIB and similarly-styled files; and a variety of LAPACK and BLAS (Basic Linear Algebra Subprograms) subroutines.

Table B.5: A list of the FORTRAN files required for MPESIM.

<b>Main File</b>						
MPESIM.f						
<b>GSLIB and Similar Files</b>						
chknam.for	getclass.for	makeevents.for	readstats.for			
convmat.for	getcodes.for	makepar.for	readtemp.for	writeevents.for		
convtemp.for	getconn.for	mpstatcalc.for	readti.for	writetemp.for		
dsortem.for	getindx.for	pickem.for	sortem.for			
<b>LAPACK Subroutine Files</b>						
dlacpy.f	dlaed4.f	dlaeda.f	dlarf.f	dlaset.f	dorm2r.f	dsterf.f
dlae2.f	dlaed5.f	dlaev2.f	dlarfb.f	dlasr.f	dormql.f	dsyevd.f
dlaed0.f	dlaed6.f	dlamrg.f	dlarfg.f	dlasrt.f	dormqr.f	dsytd2.f
dlaed1.f	dlaed7.f	dlanst.f	dlarft.f	dlassq.f	dormtr.f	dsytrd.f
dlaed2.f	dlaed8.f	dlansy.f	dlartg.f	dlatrd.f	dstedc.f	
dlaed3.f	dlaed9.f	dlapy2.f	dlascl.f	dorm2l.f	dsteqr.f	
<b>LAPACK Auxiliary Files</b>						
dlamch.f	ieeek.f	ilaenv.f	iparmq.f	lsame.f	xerbla.f	
<b>BLAS1 Files</b>						
daxpy.f	ddot.f	drot.f	dswap.f	idamax.f		
dcopy.f	dnrm2.f	dscal.f				
<b>BLAS2 Files</b>						
dgemv.f	dger.f	dsymv.f	dsyr2.f	dtrmv.f		
<b>BLAS3 Files</b>						
dgemm.f	dsyr2k.f	dtrmm.f				

## B.6 Example

To confirm the successful compilation and execution of the MPESIM program, consider the eolian sandstone case study from Section 5.2. The true data, sample data, and training image are stored in ASCII files names TRUE.DAT, DATA.DAT, and TI.DAT, respectively. The data are in GSLIB standard format for gridded data (true.dat and ti.dat) or scattered data (data.dat). Figure B.6 shows the true, sample, and TI data sets for reference.

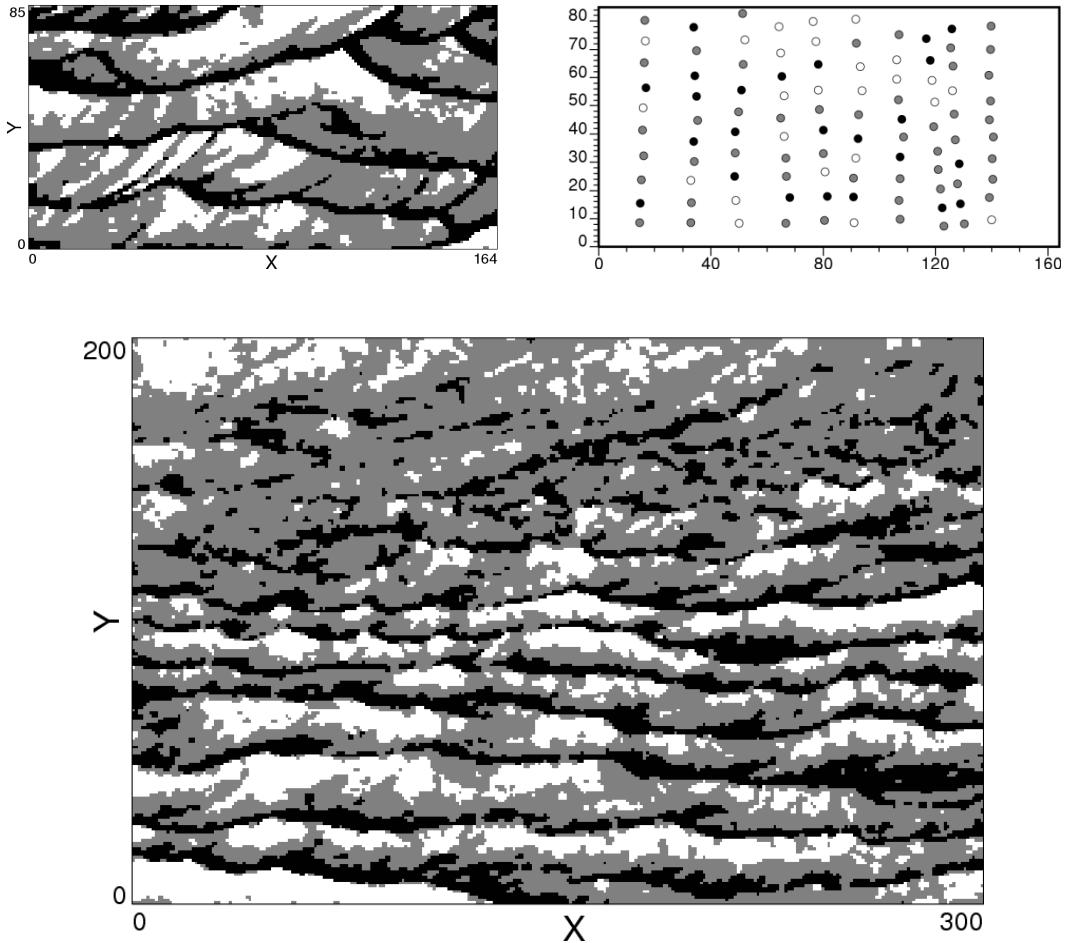


Figure B.6: The data in TRUE.DAT (top left), DATA.DAT (top right), and TI.DAT (bottom).

Compiling the MPESIM program with the files from Table B.5 produces the MPESIM.EXE executable file. Running the executable with no parameter file will create the default parameter file shown in Table B.2. If the parameter file is modified to use the parameters shown in Table B.6, then when MPESIM.EXE is run again it will produce the files 16x4.temp and MPS-GS.DBG. Running the executable again will create the file 16x4.mps and overwrite MPS-GS.DBG. Note that the TI.DAT file must be in the same folder as MPESIM.EXE.

At this point the simulation case is ready to be run. Running the executable file one more time will create MPS-GS.OUT, containing twenty conditional realizations of the eolian sandstone case study. The DATA.DAT file must be in the same folder as MPESIM.EXE for the realizations to be conditional; if it is not found the program will

automatically generate unconditional realizations instead. Different realizations may be created by modifying the random number seed value. Using the default random number seed, the first two conditional realizations are shown in Figure B.7. These are the same as the two conditional realizations from Section 5.2.

Table B.6: The MPESIM parameter file used in the example.

Parameters for MPESIM *****	
START OF PARAMETERS:	
16x4.mps	-File for MPS
5	-Number of grids to use
16	-Number of MP events to consider
4	-Number of points per event
1.0e-5	-Minimum MP frequency to consider
ti.dat	-File for Training Image
1	-Column for TI data
300 200 1	-Size of TI field
16x4.temp	-File containing point offsets
1 2 0	-Columns for X,Y,Z offsets
5 3 0	-Maximum point offsets
3	-Number of codes/facies
1 2 3	-Indicators for codes/facies
0.25 0.51 0.24	-Global pdf values
data.dat	-File for conditioning data
1 2 0 3	-X,Y,Z,Data columns
mps-gs.out	-File for output
20	-Number of realizations
164 0.5 1.0	-nx,xmin,xsiz
85 0.5 1.0	-ny,ymin,ysiz
1 0.5 1.0	-nz,zmin,zsiz
1 0.02 30	-Stopping number,threshold,max loops
mps-gs.dbg	-File for debugging
pdf.dat	-File for local proportions
1 2 3 4 5	-Columns for all indicators
4	-Discretization of local pdf
1.0 0.1	-Servosystem, connectivity factors
6744889	-Random number seed value

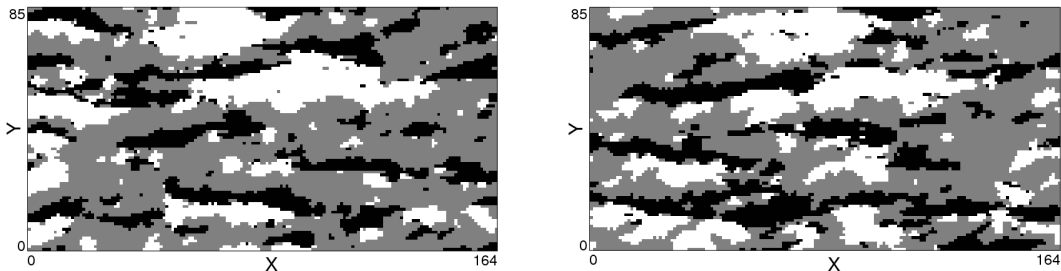


Figure B.7: The first two realizations produced by MPESIM using the data in Figure B.6 and the parameters in Table B.6.